UNIVERSIDADE DE LISBOA
FACULDADE DE CIÊNCIAS
DEPARTAMENTO DE FÍSICA

Calibration and Performance of the Tile Calorimeter of ATLAS with cosmic ray muons

João Gentil Mendes Saraiva

DOUTORAMENTO EM FÍSICA

2010

UNIVERSIDADE DE LISBOA
FACULDADE DE CIÊNCIAS
DEPARTAMENTO DE FÍSICA

Calibration and Performance of the Tile Calorimeter of ATLAS with cosmic ray muons

Dissertação submetida por

João Gentil Mendes Saraiva

com o grau de Mestre em Física
como requesito parcial para a obtenção do grau de
Doutor em Física

Dissertação orientada por:
Prof. Doutora Amélia Arminda Teixeira Maio
e
Dr. José Carvalho Maneira

DOUTORAMENTO EM FÍSICA

2010

Agradecimentos

Não posso deixar de agradecer a todos os que ajudaram na execução desta tese. As contribuições para o trabalho e também aquelas que me afastaram dele, sem as quais teria sido muito mais difícil esta tese ter chegado a bom porto. Os nomes não são segredo nenhum, mas também apenas só interessam a mim, por isso curiosos da vida alheia vão ter que ler outra tese.

Agradeço o apoio da Prof. Amélia Maio que embora sempre muito ocupada, não deixa de se preopocupar com todos os seus alunos, e parece por vezes ter mais energia (muito mais do que 14 TeV!) e entusiasmo que todo o grupo de ATLAS junto.

Agradeço ao José Maneira todo o apoio e paciência durante estes anos de tese, e toda a ajuda disponibilizada na realização do trabalho que agora com a escrita desta tese viu o seu fim.

Agradeço ainda ao Nuno Ribeiro, que queria ser teórico quando fosse grande (mas ele já é grande?!) e ao recentemente chegado Mário Sousa, pela grande ajuda que deu o primeiro e tem dado agora o segundo nas análises de dados.

Agradeço a todos os que gostaram de fazer um pequeno intervalo no seu dia de trabalho para tomaram café comigo.

Agradeço a todos os meus colegas do grupo de ATLAS no LIP que ajudaram de uma ou outra forma para que esta tese estivesse escrita hoje a um mês do centenário da implantação da republica.

Por fim agradeço aos meus pais o apoio que me tem dado ao longo destes intermináveis anos de estudante.

Agradeço á FCT pela bolsa SFRH/BD/27416/2006.

Contents

List of Figures

List of Tables

Sumário

A instalação do detector ATLAS na caverna experimental, decorreu entre 2005 e 2009. Durante este período, técnicos, engenheiros e físicos trabalharam arduamente na preparação do detector para o seu principal objectivo: estudar a física de altas energias nas novas fronteiras definidas pela mais elevada energia de centro de massa (14 TeV) e alta luminosidade ($10^{34} cm^{-2} s^{-1}$ nominal) em experiências de colisionadores. Esta tese inscreve-se no contexto deste ambiente intenso e motivador que envolveu todos os membros de ATLAS na preparação do detector para colisões protão-protão i.e. durante o periodo de certificação com muões de radiação cósmica e os sistemas de calibração e monitorização do detector. Em 2008 durante o período conhecido como *singlebeam* muões resultantes da colisão de um feixe protões contra colimadores do LHC, foram utilizados para avaliar o desempenho do detector. Este trabalho foi fundamental para preparar o detector para as primeiras colisões no LHC que começaram em Novembro de 2009.

Antes das colisões começarem, as únicas partículas de altas energias disponíveis para estudar o desempenho dos detectores do LHC eram os muões produzidos na interacção das partículas cósmicas com os mais altos estratos da atmosfera. Estes muões cósmicos são as únicas partículas que é possível detectar e que chegam à superfície terrestre em número suficiente para poderem ser utlizadas em estudos de desempenho dos diferentes sub-sistemas do detector ATLAS. O trabalho desenvolvido por mim durante o meu doutoramento e que será detalhadamente neste documento foca a calibração em energia e sincronização do calorímetro hadrónico de telhas cintilantes de ATLAS (TileCal) utilizando os muões cósmicos. Estes dois tópicos de estudo são agora apresentados sumáriamente:

Contribuição para a calibração em energia do calorímetro TileCal

A escala de energia electromagnetica foi determinada durante os testes com feixes de partículas utilizando apenas 12% do número total de módulos. De forma a medir com um método independente a escala de energia electromagética e avaliar a resposta do detector em função de η e ϕ, aplicado agora a todos os módulos do calorímetro TileCal, são utilizados muões cósmicos. A minha contribuição consistiu em validar a escala de energia global e a uniformidade da resposta em energia em ϕ utilizando o algoritmo TileMuonFitter. O método descrito neste documento permitiu validar a escala de energia, inter-calibrada com o sistema de calibração com césio, com uma precisão melhor que 5% e medir uma uniformidade também melhor que 5%. Uma diferença de 3% entre a camada radial A e a camada radial D foi medida, indicando a necessidade de prosseguir os estudos da escala de energia utilizando agora muões isolados. Estes resultados obtidos com um método independente estão consistentes com uma análise anterior, descrita no artigo de *readiness* para colisões do calorímetro TileCal [18]. Embora os calorímetros não sejam desenhados e construídos para detectarem muões, estas partículas elementares são de uma grande importância não só para a certificação dos detectores do LHC mas também no programa de física do LHC. Antes de chegarem às camâras do espectrómetro de muões, os muões produzidos como resultado das colisões protão-protão (p-p) do LHC vão perder energia nos calorímetros, sendo necessário introduzir correcções nos algoritmos de reconstrução. Estas correcções são aplicadas a todos os muões que atravessam o calorímetro e em particular em processos fundamentais para a calibração de alto nível do detector que inclui a reconstrução de objectos complexos como o bosão Z no seu decaimento para dois muões. Técnicas de isolamento são utilizadas no designado canal-de-ouro para a descoberta do bosão de Higgs, em que o bosão de Higgs decai para quatro leptões $H \rightarrow ZZ \rightarrow 4l$ e onde o isolamento de muões utilizando os calorímetros desempenha um papel importante na eliminação do fundo de QCD. A resposta do TileCal a muões poderá ter um impacto relevante na descoberta de nova física para além do modelo padrão, como a de modelos Super-Simétricos, e em particular nos testes de modelos onde se inclui a procura de partículas estáveis e de massa elevada, sendo que é esperado que algumas destas partículas massivas,

devido à sua elevada massa, tenham um desempenho semelhante ao dos muões. O trabalho desenvolvido com muões cósmicos não só é importante para a certificação do detector como pode ainda ser relevante para a física do LHC no detector ATLAS. Compreeder a resposta dos muões no calorímetro TileCal assim como ter sob controlo a escala de energia electromagnetica são pontos fundamentais para se obter o melhor desempenho do detector ATLAS.

Sincronização do calorímetro TileCal

A sincronização do calorímetro TileCal foi efectuada durante 2008 combinando medições do sistema de calibração com laser e com partículas de alta energia: muões cósmicos e muões de colisões do feixe com colimadores do LHC *single beam*. No meu trabalho de tese realizei estudos com os muões provenientes destas tuas fontes mas com diferentes objectivos. Utilizando dados do *single beam* mediram-se correcções à velocidade de propagação da luz nas fibras ópticas, um dos parâmetros utilizados na sincronização com laser. O valor medido de 18.5 cm/ns levou a uma actualização deste parâmetro do sistema de calibração com laser. O trabalho realizado com muões cósmicos consistiu na determinação das correcções de tempo quer para torres (agrupamento de células) quer para células individuais. Estas correcções não são mais do que os desvios de tempo que ainda existem mesmo após a a sincronização com o sistema de laser. Os resultados finais mostraram que as medições com os muões cósmicos e com o *single beam* têm um acordo melhor do que 2 ns. A medição do tempo de um evento é fundamental para o funcionamento do detector e todos os sistemas tem que estar internamente sincronizados e sincronizados externamente com o relógio do LHC ($f = \frac{1}{25\ ns}$ dado pelo cruzamento de pacotes do feixe p-p). No calorímetro TileCal o tempo tem um papel importante na reconstrução em energia devido aos constrangimentos severos de operação do LHC que apenas permitem uma iteração na reconstrução do sinal. O tempo de cada um dos 10000 canais do TileCal tem de ser conhecido com a precisão de alguns nanosegundos de forma que os coeficientes correctos sejam utilizados pelo algoritmo de *Optimal filter* na única iteração disponível. A medição do tempo é tambem importante para: seleccionar partículas que vêm de colisões p-p, definir a qualidade de um evento e é ainda a quantidade mais sensível para a descoberta de partículas lentas e de massa muito elevada que são previstas

em modelos para além do modelo padrão.

Esta tese divide-se em 7 capítulos. O primeiro é introdutório e apresenta o acelerador *Large Hadron Collider*, o detector ATLAS e os objectivos globais de física. No segundo capítulo o calorímetro TileCal é descrito com algum promenor apresentado a geometria, os sistemas de calibração e os resultados de desempenho em testes com feixes de partículas. O terceiro capítulo apresenta as motivações para a análise desenvolvida centrando a discussão na escala de energia e sincronização em tempo do calorímetro TileCal. Para além do interesse intrínseco para o próprio calorímetro TileCal, também é discutido o papel que estas quantidades têm no funcionamento de todo o detector, assim como em alguns canais de física particulares. No Capítulo 4 a fase de certificação do detector é apresentada, focando algumas das actividades desenvolvidas neste período, com destaque naquelas em que dei a minha contribuição durante o desenvolvimento do meu trabalho de tese. A parte central do trabalho de tese encontra-se nos dois capítulos seguintes. No Capítulo 5 são apresentados os resultados sobre a escala de energia electromagnética e uniformidade em ϕ utilizando o algoritmo TileMuonFitter. O Capítulo 6 é dedicado aos metodos utilizados na sincronização do detector com dados de muões cósmicos e respectivos resultados. Por fim no Capítulo 7 são apresentadas as conclusões do trabalho desenvolvido.

Palavras chave: calorimetria, commissioning, muões, uniformidade, sincronização

Summary

The installation of the ATLAS detector in the experimental cavern, took place from 2005 until 2009. During this period, technicians, engineers and physicists have been intensively working on the preparation of the detector for its main objective: probing the new frontiers of high energy physics with the LHC, the particle collider with the largest center of mass energy (14 TeV nominal) and very high luminosities($10^{34} cm^{-2} s^{-1}$ nominal). The context of this thesis was this challenging environment that involved all ATLAS members in the preparation of the detector for collisions during the period of the detector commissioning with cosmic ray muons and with calibration and monitoring systems. In 2008 during a short period of time single beam data was available and was used to study the detector response. This large effort was fundamental to prepare the detector for the first collisions at the LHC that started in November 2009.

Before collisions started, the only high energy particles available for studies with the LHC detectors were the muons produced by the interaction of cosmic particles in the atmosphere. These cosmic ray muons are the only detectable particles reaching the earth surface in quantities large enough to study the performance of the different sub-systems of the ATLAS detector. The work I have developed during my PhD and that will be detailed in this document is centered on the energy calibration and synchronization of the Tile Calorimeter, the barrel hadronic calorimeter of ATLAS, using cosmic ray muons. The two main topics of study are now summarized:

Contribution to the energy calibration of the Tile Calorimeter

A electromagnetic energy scale was set in testbeam using high energy particles for 12% of the Tile Calorimeter modules. My contribution was centered in the validation of the global energy scale algorithm and the detector's energy response uniformity in ϕ using the TileMuonFitter. The results presented in this document have shown that both the energy scale application, from testbeam to all modules in the experimental cavern, and the energy uniformity in ϕ are better than 5%. A difference between radial layers A and D of 3% is measured and it is something not completely understood and must be studied later using e.g. isolated muons from collisions. The used data stream and method, still have shown that a full coverage in ϕ can be achieved for these measurements. These results obtained with an independent method are consistent with an earlier analysis, reported in the readiness paper of the Tile Calorimeter [18]. Calorimeters are not designed and developed for the detection of muons however they play an important role on the commissioning of the LHC detectors and physics program. Before reaching the muon chambers the muons produced in collisions will lose energy in the calorimeter volume. Corrections on the energy loss in the calorimeters are necessary to improve the precision of the muon momentum measurement. This correction mus be applied to any muons crossing the calorimeter volume and in particular in fundamental processes used on the final calibration of the detector which includes complex objects as the Z boson decaying to two muons. Lepton isolation techniques are used in the so called golden-channel for the Higgs boson discovery, the decay to four leptons $H \rightarrow ZZ \rightarrow 4l$, for the rejection of QCD background. The Tile Calorimeter performance with muons can have an important impact in physics beyond the standard model, such as Super-Symmetry, for instance on the search for stable massive particles, since some of these massive particles are characterized by having an energy loss in the calorimeter similar to muons. The work developed with cosmic muons can also be applied later using muons produced in collisions to monitor the EM scale during the LHC operation. So the work developed with cosmic ray muons is not only important for the commissioning of the detector but can also be relevant for the physics of the LHC to be done with the ATLAS detector. Understanding the response

of the Tile Calorimeter to muons as well as to have under control the EM energy scale are fundamental to achieve the best performance of the ATLAS detector.

Synchronization of the Tile Calorimeter

The Tile Calorimeter synchronization was established during 2008 combining measurements with the laser system and high energy particles: cosmic ray muons and muons from single beam. The work presented in this thesis uses both types of muons, but with different objectives in mind. Using the single beam data were measured corrections to the velocity of propagation of light in the clear fibers, a parameter used in the laser synchronization. The measured value of 18.5 cm/ns resulted in the update of this parameter in the laser calibration system. The work done with cosmic muons consisted in the determination of the time offsets of the Tile Calorimeter measured both for towers and individual cells. The time offsets were calculated as the residuals after the synchronization made with the laser system. The final results have shown that the cosmic ray muons and single beam data agree within less than 2 ns. The timing is fundamental for the operation of the detector and all systems must be internally synchronized and externally synchronized with the LHC clock ($f = \frac{1}{25\ ns}$ given by the bunch crossing). The timing plays an important role in the energy measurement due to the stringent operation conditions of the LHC that require the online signal reconstruction for the Tile Calorimeter channels to be done without iterations. The time of each channel must be known with a precision of the order of a few nanoseconds so that the correct parameters are chosen for the online reconstruction method. Time is also used to select particles that come from p-p collisions, to provide quality factors on the selection of events, and it is the most sensitive quantity for the discovery of slow long lived particles, also called stable massive particles, that are predicted in models beyond the Standard Model.

This thesis is divided in 7 chapters. The first is introductory and presents the Large Hadron Collider, the ATLAS detector and its physics goals. In Chapter 2 the Tile Calorimeter is described in some detail presenting the geometry, calibration systems and performance

features obtained from the last testbeam results. The following chapters are dedicated to the commissioning of the Tile Calorimeter with cosmic ray muons. The third chapter presents the motivations for the work developed, focusing on the energy scale and synchronization of the Tile Calorimeter. These quantities are of course important in the overall detector performance and have also a larger importance in specific physics channels. Chapter 4 introduces the commissioning and gives a brief overview of the activities during this stage, it is mostly descriptive but also reporting with some detail the activities in which I contributed during the development of my thesis work. The main contributions to the Tile Calorimeter commissioning is included in the next two chapters. Chapter 5 presents the results on the energy scale and uniformity in ϕ using the TileMuonFitter. Chapter 6 is dedicated to the methods and results for synchronization with cosmic ray muons data. Finally in Chapter 7 conclusions are given.

Keywords: calorimetry, commissioning, muons, uniformity, synchronization

1 Introduction

This thesis is focused on studies with cosmic ray muons of the performance of the hadronic barrel calorimeter of the ATLAS experiment [1], built to detect high energy events at the Large Hadron Collider [2] at CERN. This chapter presents the main elements that build up the background in which my work fits in and the global motivations for the development and construction of this collider and these experiments. Later and in a dedicated chapter (Chapter 3) the direct motivations of my work for the ATLAS experiment are discussed.

1.1 The Large Hadron Collider at CERN

The LHC collider and detectors are the largest and most complex scientific experiment, that was ever built by mankind. The number of people involved, hardware parameters, and goals are well above those of any others experiments that built until now. All this to explore the structure of matter and explain the interactions of the elementary particles by colliding bunches of protons from where physicists may reach for an answer to the still open questions in the field of particle physics.

1.1.1 The accelerator

The accelerators complex that produces the 450 GeV beam injected in the Large Hadron Collider (LHC) is shown in Figure 1.1. The LHC is a two-ring-superconducting-hadron accelerator and collider installed in the $\sim 27\ km$ tunnel that, between 1989 and 2000, hosted the LEP e^+e^- accelerator. This is a particle-particle collider and two rings with counter-rotating beams are required unlike particle-antiparticle colliders that need only one ring. Figure 1.2

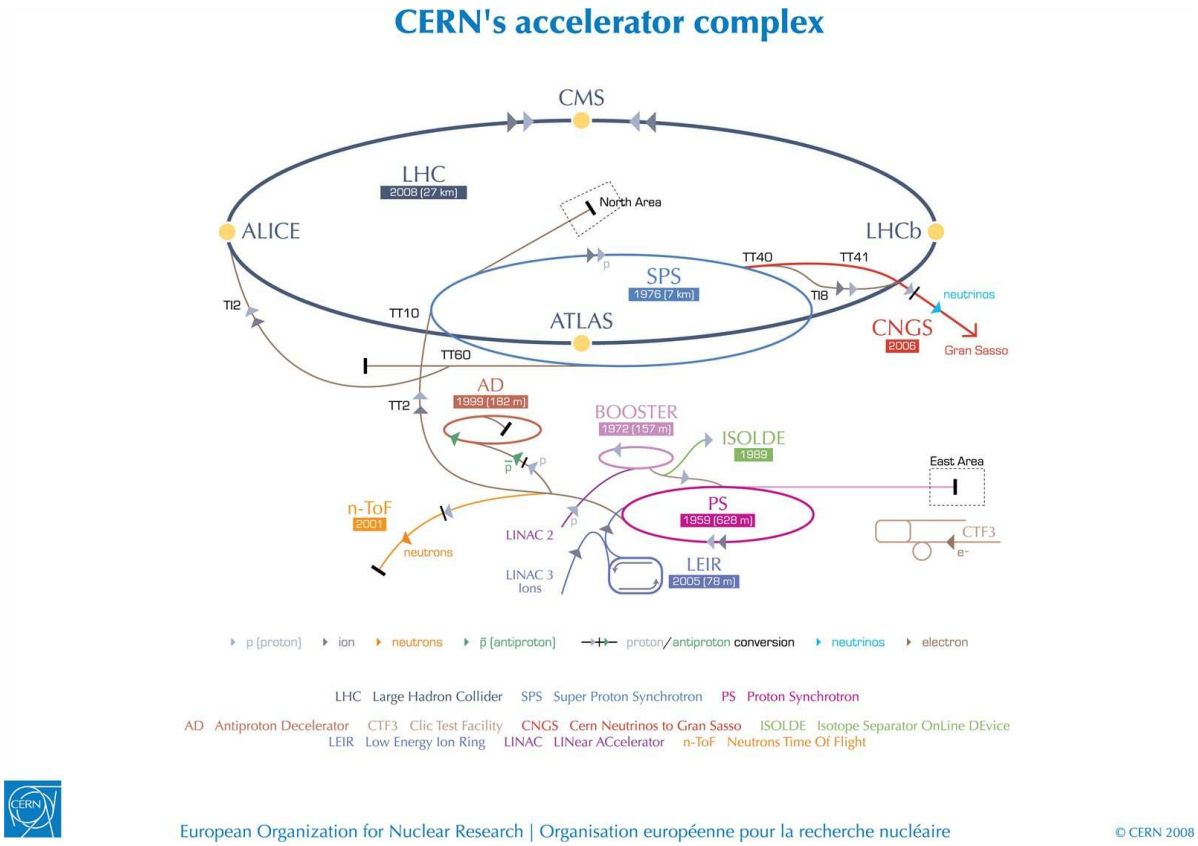

Figure 1.1: The LHC complex where are visible the different stages of preparation of the LHC beam: Linac → Booster → PS → SPS → LHC. The beams are injected in the LHC ring with an energy of 450 GeV.

illustrates this feature by showing the clockwise beam in red and the anti-clockwise beam in blue. Other technical aspects are also indicated such as the injections points where the 450 GeV beam is introduced in the LHC rings, cleaning regions and dumping exits.

The LHC was designed to operate in proton-proton collisions with center of mass energies of up to 14 TeV and luminosities up to $L = 10^{34} cm^{-2} s^{-1}$. Each beam can have up to 2808 bunches (+ 756 empty bunches), each bunch has 1.15×10^{11} protons and a length of 7.55 cm. The crossing angle between beams is 285 μrad. For a fill with the nominal design parameters, the beam bunches collide every 25 ns and give rise to an average of 23 inelastic collisions per bunch.

The rate of events produced in a collision can be calculated as:

$$N_{event} = L \sigma_{event}$$

where σ_{event} is the cross section of the relevant physics process and L is the machine luminosity. The luminosity can be calculated from machine parameters as:

$$L = \frac{N_b^2 \, n_b \, f_{rev} \, \gamma_r}{4 \, \pi \, \epsilon_n \, \beta_*} \cdot F$$

where N_b is the number of particles per bunch, n_b the number of bunches per beam, f_{rev} the revolution frequency, γ_r the relativistic gamma factor, ϵ_n the normalized transverse beam emittance, β_* the beta function at the collision point, and F the geometric luminosity reduction factor due to the crossing angle at the interaction point (IP). This last factor is

$$F = \left(1 + \left(\frac{\theta_c \, \sigma_z}{2 \, \sigma_*} \right)^2 \right)^{-1/2}$$

where θ_c is the full crossing angle at the IP, σ_z the RMS bunch length, and σ_* the transverse RMS beam size at the IP.

Protons are not elementary particles so in the inelastic collisions the particles the interacting will be its constituents the partons (quarks, gluons). An effective center of mass

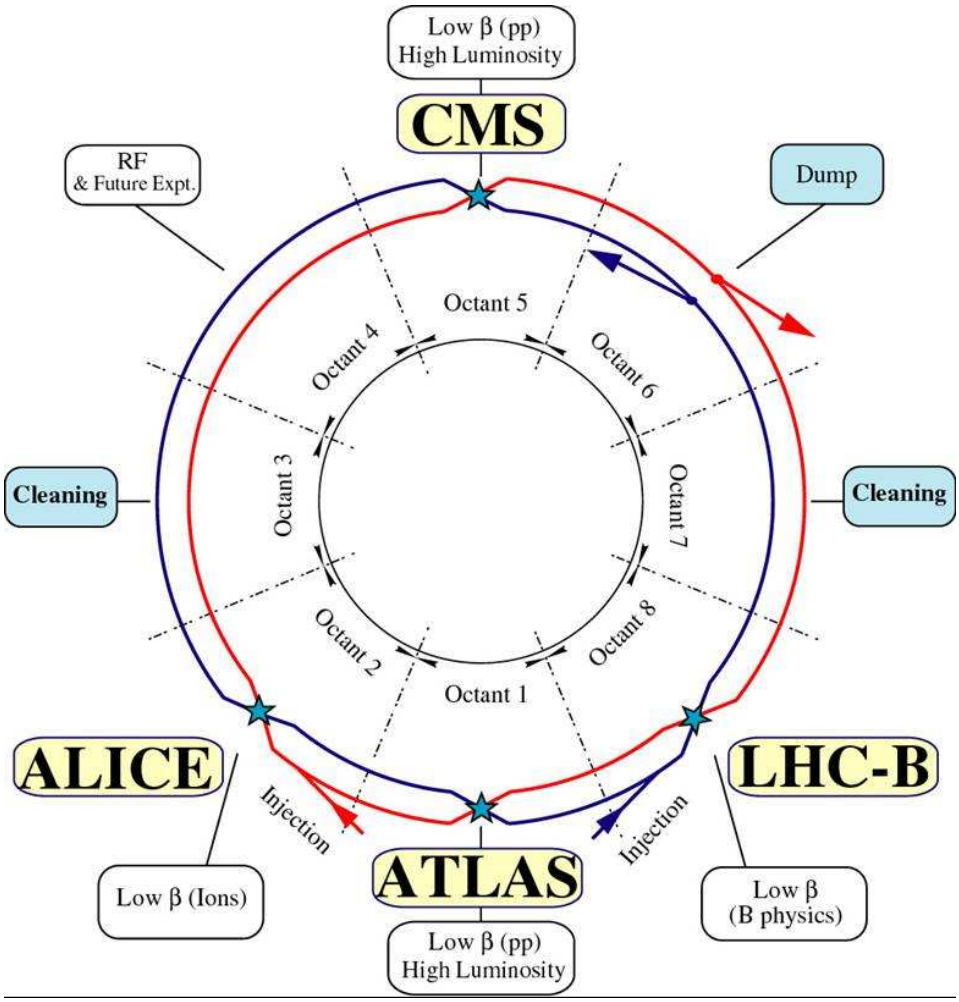

Figure 1.2: A scheme of the LHC accelerator showing the main characteristics of the two circulating beams: one circulating clockwise and the other anti-clockwise in two separate rings. Close to each of the interaction points there are 140 m long ring segments that are used by both beams.

energy must be defined:

$$\sqrt{s}_{eff} = 2\, x_1\, x_2\, \sqrt{s}$$

where x_i the fraction of momentum carried by each parton.

1.1.2 The detectors

The LHC has two general-purpose and high luminosity experiments ATLAS and CMS having a peak luminosity of $L = 10^{34} cm^{-2} s^{-1}$ and three low luminosity experiments LHCb with $L = 2 \times 10^{32} cm^{-2} s^{-1}$, TOTEM with $L = 2 \times 10^{29} cm^{-2} s^{-1}$ and LHCf optimized for operation below $L < 10^{30} cm^{-2} s^{-1}$ for p-p collisions at $\sqrt{s} = 14\ TeV$. It has still one experiment dedicated to ion collisions that aims at $L = 10^{27} cm^{-2} s^{-1}$ for nominal lead-lead ion operation. For the ion-ion collisions the center of mass energy is of $\sqrt{s} = 5.5\ TeV$ per nucleon

ATLAS and CMS are competing experiments, since their global objectives are the same. Although competitive, both experiments require that when a measurement is observed in one of them, a confirmation is required from the other. So both must be complementary in order and specially to evaluate any discovery. It is common to refer them as experiments with a general purpose and their physics goals are presented later in this chapter. This designation is attributed in opposition to the other LHC experiments:

- LHCb that is dedicated to the precise measurement of CP-violation in the B-meson system.
- TOTEM that is dedicated to the measurement of the total cross section of elastic proton scattering, with an absolute error of 1 mb, and diffractive dissociation over a wide range of momentum transfer.
- LHCf that is dedicated to the measurement of neutral particles emitted in the very forward region of $|\eta| > 8.4$ with the goal of providing data for calibrating the hadron interaction models that are used in the study of Extremely High-Energy Cosmic-Rays.
- ALICE was designed for ion-ion collision and will have as main focus the study of the physics of strongly interacting matter at extreme energy densities (quark-gluon plasma)

and provide a deeper understanding of quantum chromodynamics. However, ALICE also proposes to use proton-proton collisions, both to compare with the ion collisions as well as in physics areas where it can be competitive with the other LHC experiments.

1.1.3 Present status

The operating conditions for the present year (2010) and until the end of 2011 are a center of mass energy of $\sim 7\ TeV$ and a luminosity of the order of $10^{31}\ cm^{-2}\ s^{-1}$. At the time of writing 162×10^9 collisions have occurred and a integrated luminosity of $\sim 2.3\ pb^{-1}$ have been accumulated.

1.2 The ATLAS detector

ATLAS is one of the general purpose detectors built for the LHC experiment. The detector is divided in four main units as is characteristic of most high energy particle detectors: a magnetic field, an inner tracker, a calorimeter and a outer tracker. Each one of these units has a set of sub-systems that are responsible for a specific task. Figure 1.3 shows a cut-view of the full detector, from where the different elements mentioned can be depicted. ATLAS measures 44 m in length and 25 m in height and weighs about 7000 tonnes.

1.2.1 Magnetic field systems

The magnetic field in ATLAS is produced by the composition of three systems: the solenoid, the barrel toroid and the end-cap toroid. Their main characteristics are summarized in Table 1.1. The magnetic field will deflect particle's trajectories according to their mass and charge, this is fundamental for an unambiguous determination of the particle's type and charge. The solenoid encloses the ATLAS inner trackers and has a magnetic field peak strength of about 2 Tesla.

The two toroids systems are located outside the calorimeters and between the muon chambers that are the sensitive parts of the outer tracker. The combination of these two systems builds up what is called the muon spectrometer and is mainly used for the reconstruction of

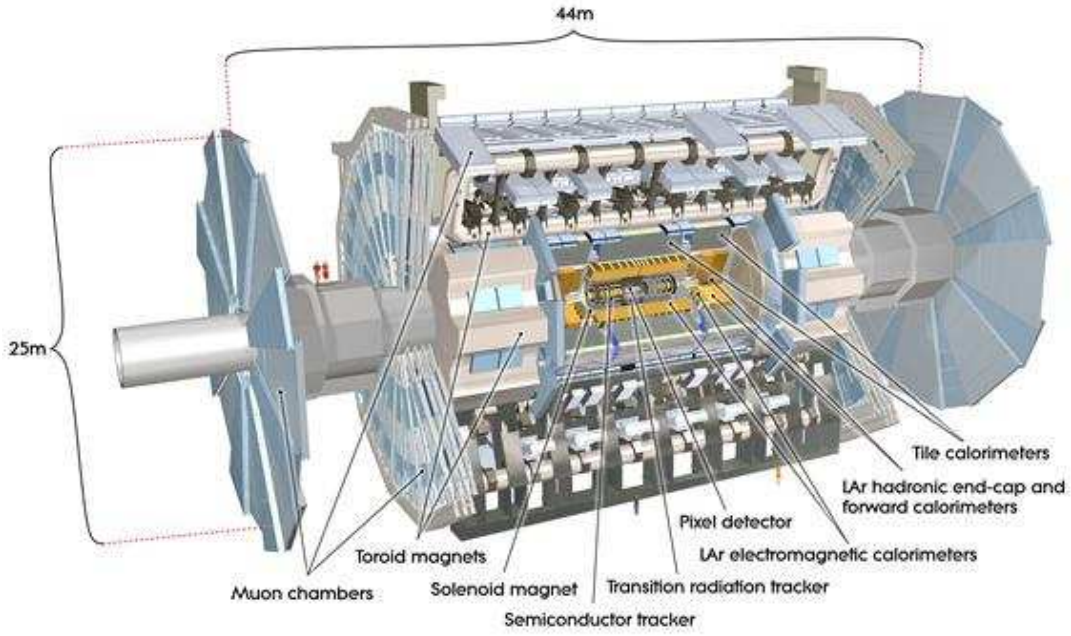

Figure 1.3: A cut-view scheme of the ATLAS detector showing its main elements and dimensions.

muons and their characterization. However, some models beyond the standard model predict the existence of exotic particles of either electromagnetic or hadronic nature, that may reach the outer parts of the ATLAS detector and leave hits in the muon chambers.

1.2.2 Inner tracker

The ATLAS inner tracker is composed of three different detectors: the silicon pixel tracker (Pixels), the transition radiation tracker (TRT) and the semiconductor tracker (SCT), shown in Figure 1.4. The three systems combined cover a region of $|\eta| < 2.5$ and have a target resolution for the momentum of

$$\frac{\sigma(p_T)}{p_T} = 0.05\%\, p_T \oplus 1\%$$

To identify tracks and measure their momentum, are challenging tasks under the high multiplicity environment of p-p collisions at nominal LHC luminosity. With an average of 23 collisions more than 1000 particles are produced each bunch-crossing (every 25 ns),

	Solenoid	Barrel Toroid	End-cap Toroid
Length	5.3 m	25.3 m	5 m
Outer Diameter	2.63 m	20.1 m	10.7 m
Coils	1 coil	8 coils with individual cryostat	2×8 coils with common cryostat
Nominal current	7.73 kA	20.5 kA	20.5 kA
Peak filed strength	2 T	3.9 T	4.1 T
Stored energy	39 MJ	1100 MJ	2×250 MJ
Thickness	0.66 X_0	—	—

Table 1.1: ATLAS magnetic field main characteristics

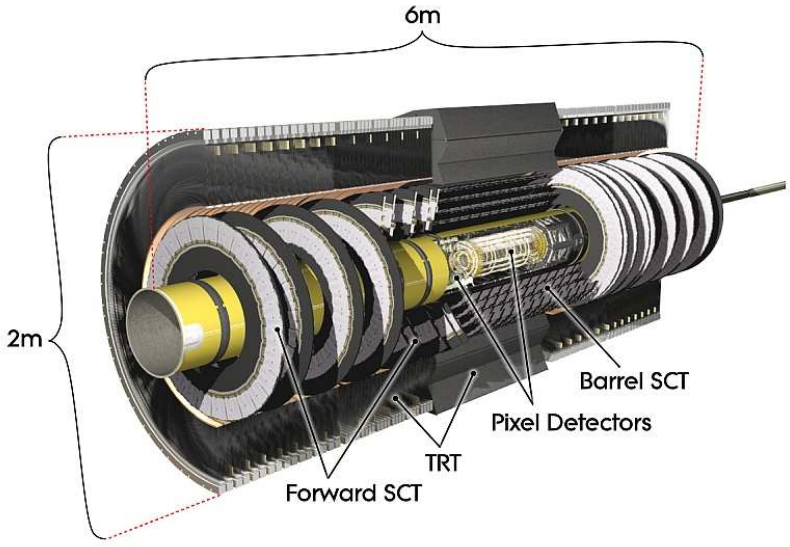

Figure 1.4: The inner detector of ATLAS: Pixels detector, Semiconductor Tracker and Transition Radiation Tracker.

producing a high track density that must be scrutinized to identify the tracks belonging to the interesting event. In addition, the inner detector has the task of measuring the position of event vertex and contribute to the electron identification.

The precision tracking detectors, the **SCT** (6.3 million channels) and **Pixels** (80.4 million channels), cover the region of $|\eta| < 2.5$. Their arrangement varies depending on the position in η and they are segmented in $R-\phi$ and z. Closer to the interaction point they are arrange in concentric cylinders around the beam axis while in the end-cap regions they are located on disks perpendicular to the beam axis. The intrinsic accuracies for the Pixels are: in the barrel 10 μm in $R-\phi$ and 115 μm in z and in the end-cap 10 μm in $R-\phi$ and 115 μm in R. For the SCT the intrinsic accuracies are: in the barrel 17 μm in $R-\phi$ and 580 μm in z and in the end-cap 17 μm in $R-\phi$ and 580 μm in R. Typically the Pixels have three space points per track and the SCT 4 space points.

In the **TRT** (315000 channels) typically 36 hits per track are produced that enables track reconstruction up to $\eta < 2.0$. These are 4 mm straw tubes: 144 cm long positioned parallel to the beam axis in the barrel region and 37 cm arranged radially in wheels perpendicular to the beam axis. The intrinsic accuracy is of 130 μm per straw.

1.2.3 Calorimeters

The electromagnetic calorimeter is used to stop and detect the electromagnetic components of the particle's decays and measure showers produced electrons and photons. This is crucial for the separation of particles that produce electromagnetic showers from the ones producing hadronic jets. The latter are stopped and their properties measured using the hadronic calorimeters. In most cases the deposited energy by hadrons is divided between the two calorimeter systems and a combined reconstruction is necessary.

The **electromagnetic calorimeter** is a sampling calorimeter using Liquid Argon (LAr) as the sensitive material and lead as the absorber. It has an accordion (Figure 1.6) geometry motivated by the desire to eliminate projective azimuthal cracks that contribute to the constant term of the electromagnetic energy resolution. An early design requisite was a constant term

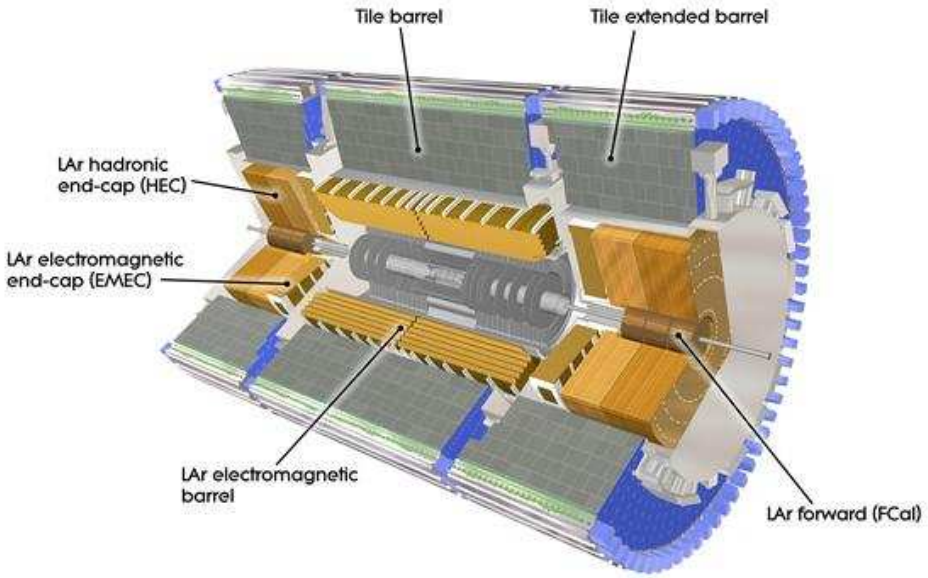

Figure 1.5: The ATLAS calorimeters

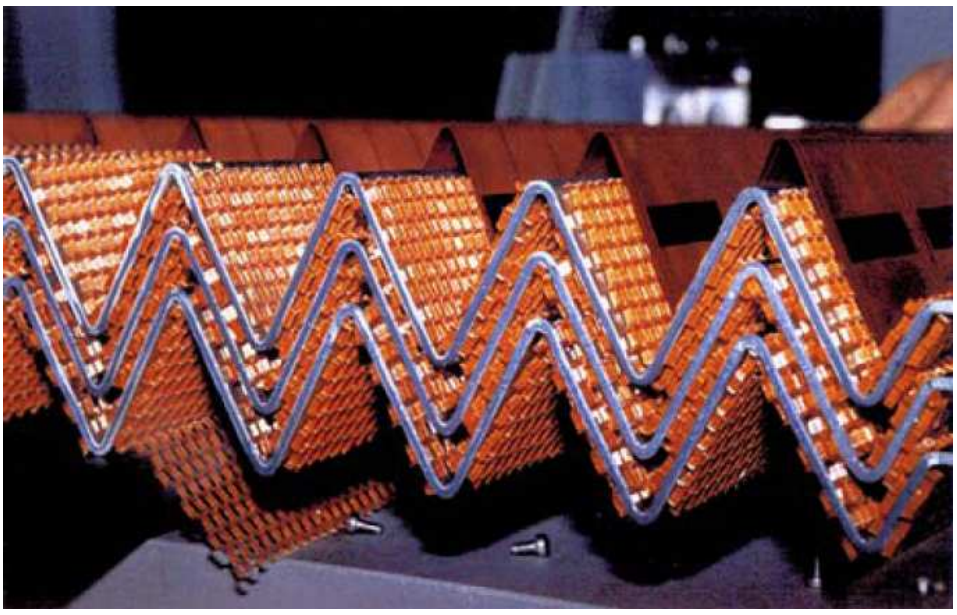

Figure 1.6: The accordion geometry of the absorber plates and the honeycomb spacers of the LAr barrel electromagnetic calorimeter.

of 0.7% or less to provide the best possible energy resolution for high-energy electromagnetic objects, as was the case for the $H^0 \to \gamma\gamma$ channel. Currently in the Higgs boson mass searches this is not the most sensitive discovery channel due to the limits set to the Higgs boson searches at LEP. The design resolution is

$$\frac{\sigma(E)}{E} = \frac{10\%}{\sqrt{E}} + 0.7\%$$

It has 3 longitudinal samples covering a region of $|\eta| < 2.5$ and a preshower detector covering a region of $|\eta| < 1.8$. It has 173 000 channels in the readout.

The **hadronic calorimeter** uses two different technologies to sample the signal from hadronic jets. In the barrel, covering a region of $|\eta < 1.7|$, is the scintillator tile calorimeter (Tile Calorimeter) that has 3 mm scintillating tiles as the sensitive medium and steel as the absorber, using approximately 10 000 channels in the readout (more details are given on the Tile Calorimeter in the dedicated Chapter 2). The end-cap and forward hadronic calorimeters that cover the region of $|\eta| > 1.7$ use the same technologies as the electromagnetic calorimeter but with copper (Cu) as the absorber, in the end-cap region and tungsten (W) as the absorber in the forward region. The end-cap has 4 longitudinal samples and the forward 3 longitudinal samples and they have approximately 10 000 channels in the readout. The design resolution for the hadronic calorimetry depends on the $|\eta|$ region and are defined based on performance requirements for the ATLAS physics goals on the reconstruction of jets:

$$\frac{\sigma(E)}{E} = \frac{50\%}{\sqrt{E}} + 3\% \qquad \eta < 3$$

and

$$\frac{\sigma(E)}{E} = \frac{100\%}{\sqrt{E}} + 10\% \qquad \eta > 3$$

The calorimeters are readout by the Level 1 trigger to define regions-of-interest that are later communicated to the Level 2 trigger.

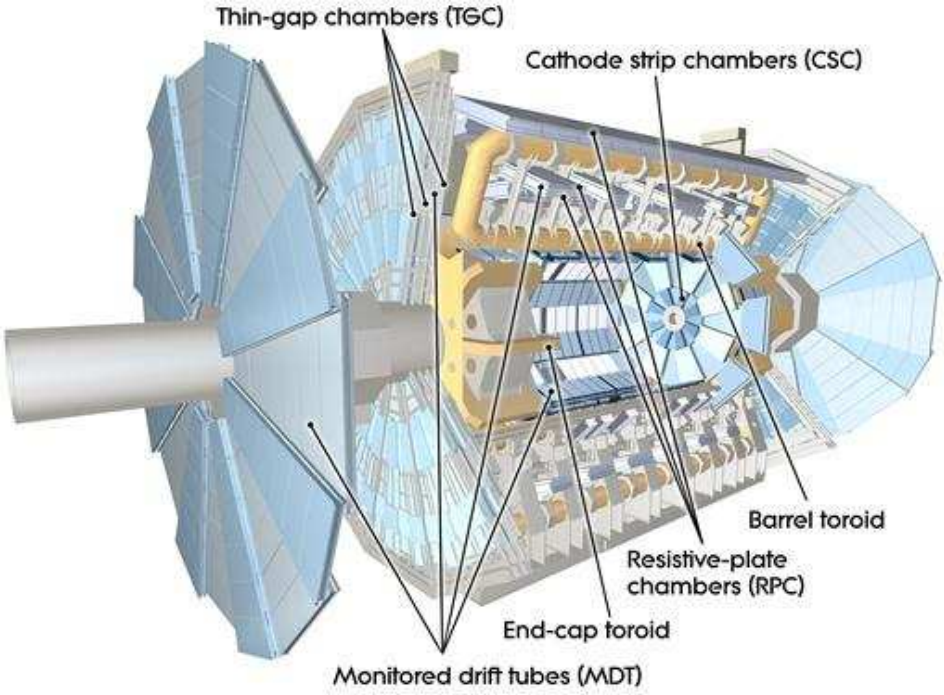

Figure 1.7: The muons spectrometer of the ATLAS detector. The different sub-systems are evidenced the MDT, CSC, RPC and TGC.

1.2.4 Muon Spectrometer

The outermost detector is used for the collection of the charged particles that escape the calorimeter volume. Within the present knowledge of particle physics the only particles reaching these chambers produced in proton-proton collisions are the muons from decays of the collisions products. The measurement and identification is made combining the muon chambers with the barrel toroid magnetic field in $|\eta| < 1.4$ and the end-cap toroid in $|\eta| > 1.6$. The intermediate region uses the combination of the two magnetic fields to bend the particles. The design momentum resolution requirement for muons is

$$\frac{\sigma_{p_T}}{p_T} = 10\% \qquad at \qquad p_T = 1TeV$$

The **muon spectrometer** is divided in two main parts: the high precision tracker systems and the triggering systems. The characteristic parameters of these systems are listed in Table 1.2 The precision trackers include the Monitored drift tubes (MDT) for most of the η

MDT	Coverage	$\eta < 2.7$ (innermost layer: $\eta < 2.0$)
	Number of chambers	1150
	Number of channels	354 000
	Function	Precision tracking
CSC	Coverage	$2.0 < \eta < 2.7$
	Number of chambers	32
	Number of channels	31 000
	Function	Precision tracking
RPC	Coverage	$\eta < 1.05$
	Number of chambers	606
	Number of channels	373 000
	Function	Triggering, second coordinate
TGC	Coverage	$1.05 < \eta < 2.7$ (2.4 for triggering)
	Number of chambers	3588
	Number of channels	318 000
	Function	Triggering, second coordinate

Table 1.2: Parameters of the muon spectrometer.

range and Cathode strip chambers (CSC) for $2 < |\eta| < 2.7$. The latter have a larger granularity, necessary to handle the larger rate of particles in the forward region. In the triggering systems, providing bunch crossing identification and well defined p_T thresholds, are the Resistive plate chambers (RPC) in the barrel region and the Thin gap chambers (TGC) in the end-cap region covering the region of $|\eta| < 2.4$. These chambers still contribute to the track reconstruction and momentum measurement by measuring the muon coordinate in the direction orthogonal to the one determined by the precision tracking chambers.

1.2.5 Trigger and DAQ system

The trigger system is divided in three levels: L1, L2 and event filter. The L1 selection is hardware based but the other two are already software based.

The collisions occur every 25 ns which means that the L1 trigger will receive data at a rate of 40 MHz. The L1 trigger combines the information from calorimeters (L1-Calo) and

the muon spectrometer (L1-Muon). It will search for high transverse momentum muons, electrons, photons, jets, and τ-leptons as well as a large missing and total transverse energy. The L1 defines one or more regions of interest in (η, ϕ) that later are passed to the next trigger levels. It is required that the L1 trigger takes a decision in 2.5 μs reducing the rate to 75 kHz. The L2 trigger uses the ROIs defined by the L1 trigger, runs its algorithms and with its event selection, should reduce the trigger rate to approximately 3.5 kHz, with an average event processing time of 40 ms. The event filter will make the last event selection reducing the event rate down to 200 Hz. Each selected event is approximately 1.3 Mbyte in size.

1.3 The Standard Model of particles physics

The standard model (SM) describes the electromagnetic, weak and strong interactions between elementary particles. These interactions are theoretically described with the combination of the gauge symmetry groups $SU(3) \times SU(2) \times U(1)$. The elementary particles if the spin is half-integer are called fermions and if the spin is integer are called bosons. To any elementary particle is associated an anti-particle that has the same mass and lifetime but with opposite charge. The fermions are divided in a set of free particles the leptons and another set of particles that are not free, i.e. only existing as bounded states of more complex and non-elementary particles as the proton and the neutron (quark trios - baryons) or pions and kaons (quark and anti-quark mesons), and these are called the quarks. The only stable lepton is the electron, both the μ and τ are not stable and both decay to electrons with life-times of 2.2×10^{-6} s for the muons and of 2.9×10^{-13} s for the τ. For the quark bounded states there is only one stable particle, the proton that is build up from the u and d quark (uud).

The bound states of the quarks lead to the hypothesis of a new property only associated to these particles that it is called colour. The colour of particles is not visible i.e. directly measured. This property can also summarized by saying that all visible particles are colourless. Although not visible the experimental results have shown e.g. that the difference between the number of hadronic decays of the Z boson are larger than the ones observed for leptonic decays in a such a way that confirms the existence of 3 color quantum numbers that

leptons	charge	quarks	charge
e	1	u	$\frac{2}{3}$
μ	1	d	$-\frac{1}{3}$
τ	1	c	$\frac{2}{3}$
ν_e	0	s	$-\frac{1}{3}$
ν_μ	0	t	$\frac{2}{3}$
ν_τ	0	b	$-\frac{1}{3}$

bound the quarks.

Bosons have a fundamental role on the theory since they are the carriers of the different interaction. The photon is the carrier of the electromagnetic force such as in processes like the photoelectric effect, the Compton effect or pair production. The $W^{\pm}$ and Z^0 are the carriers of the weak force such as in any process where neutrinos take part (beta decay). The gluon is the carrier of the strong force and describes the interactions between gluons and quarks. Particles with electric charge can interact through the electromagnetic force, the strong force requires the existence of colour and so only gluons and quarks can interact but all fermions can interact through the weak force.

For all the above particles there is experimental data that directly or indirectly confirms their existence however the model is still not fully summarized. There is a quantity that is used to characterize particles and, in first order, distinguish them, that is the particles mass.

In the SM, the particle masses are introduced together with a new particle, the Higgs boson. The masses of all the particles are free parameters, that must be determined experimentally, and that it is included in the theory by the mechanism of spontaneous electroweak symmetry breaking giving then mass to all elementary particles. The particles mass depends on the strength of the coupling between the Higgs boson and the particle and this justify the difference of masses for the different elementary particles. Something that distinguishes this particle from the all others is that this one has not been observed in experiments. This is the missing block necessary to fully validate the particle physics SM.

The interactions of particles are constrained by principles of conservation like the leptonic flavour number, baryonic flavour number, charge conservation, colour conservation. From experiment it is known that all these are conserved for the electromagnetic and strong

interactions. However weak interactions have been observed to fail the conservation of the baryonic flavour number in a manner that is described the Cabbibo-Koboyashi-Maskawa mixing matrix and of the leptonic flavour number, now that neutrinos oscillations have been experimentally confirmed. Another principle of conservation is the CPT-invariance, for which the main test is confirm that particles and anti-particles have an equal mass and life-time. Until now there is no evidence of CPT violation [3]. However CP-violation has been observed (which is equivalent to T-violation given CPT-invariance) in kaons decays and B-mesons decays.

The Standard Model (SM) of particle physics has been along the years a very successful model with several experiments verifying its predictions. Although the LHC experiments want to discover what is beyond, the SM main results measured for the last collider experiments are references for the comprehension and calibration of the different detectors. This is the present stage of the LHC detectors operation, measuring well known quantities to verify the performance of the detectors. This is the subject of the next section.

1.3.1 Standard Model latest experimental results

This section concludes by briefly mentioning selected results from recent high energy physics experiments, including the results from the collider experiments at:

1. LEP with the Aleph, Delphi, L3 and Opal detectors.
2. Tevatron with the CDF and D0 detectors.
3. Stanford Linear Collider (SLC) with the SLD detector.

The LEP and SLC are lepton-positron colliders and the Tevatron is a proton-antiproton collider.

The Z^0 boson mass and width and the number of light neutrinos [4]

The first phase of LEP (LEP-I, 1989-1995) was dedicated to the study of the Z^0 boson properties in processes like $e^+e^- \rightarrow f\overline{f}$ with a center of mass energy of 91 GeV. Figure 1.8 shows the final results for the mass and width of this boson combining all the four LEP experiments. A

mass $M_Z = 91.1875 \pm 0.0021$ GeV and a width of $\Gamma_Z = 2.4952 \pm 0.0023$ are the most precise measurements achieved for these properties of the Z^0 boson.

The Z^0 decays will occur in a pair of particle and anti-particle to conserve the electric charge, lepton number, baryonic number and colour. The only invisible decays should be the decays to pairs of neutrinos. Figure 1.9 shows the dependence of the hadronic cross section for the Z^0 boson decays which is extremely sensitive on the number of light neutrinos. The experimental results follow very well the cross-section curve that corresponds to the existence of 3 families of light neutrinos. The measured number was $N_\nu = 2.9840 \pm 0.0082$, in agreement with the three observed generations of fundamental fermions.

W boson mass and width [5]

The W mass was measured both during the second phase LEP (LEP-II, 1996-2000) when the center of mass energy was increased up to 161 GeV first and 209 GeV later to study processes of the type $e^+e^- \rightarrow W^+W^-$, and at the Tevatron (1985-Today) that is a proton-antiproton collider running at FermiLab and that has been operating with center of mass energies of 1.96 TeV. The most recent combination of the results of the two accelerators for the mass and width of the W boson are in Figure 1.10. A global average of $M_W = 80.399 \pm 0.023$ GeV and $\Gamma_W = 2.085 \pm 0.042$ GeV are the last public results.

Top mass

The top quark is the heaviest elementary particle and was the last quark to be experimentally detected. Indirect predictions of its mass have been produced already at LEP and SLC but its direct measurement was only made at the Tevatron. The result gives a top quark mass of $M_{top} = 173.3 \pm 1.10$ GeV [6].

Higgs boson mass searches

The limits on the searches of the Higgs boson have been set also by LEP and the Tevatron. In Figure 1.12 the shaded regions represent the exclusion limits for the Higgs boson masses.

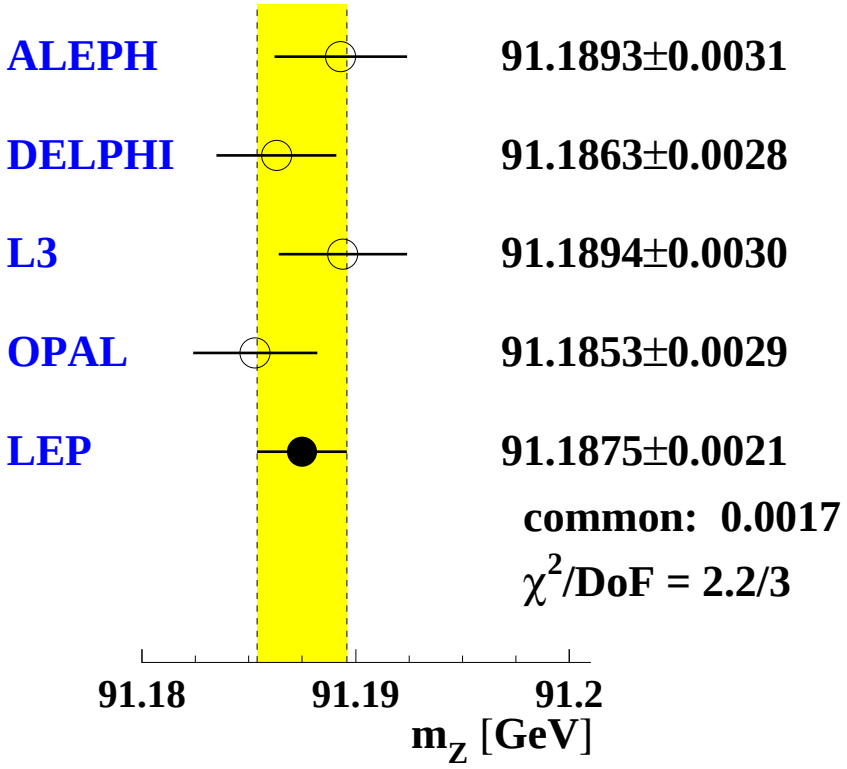

(a) Z boson mass

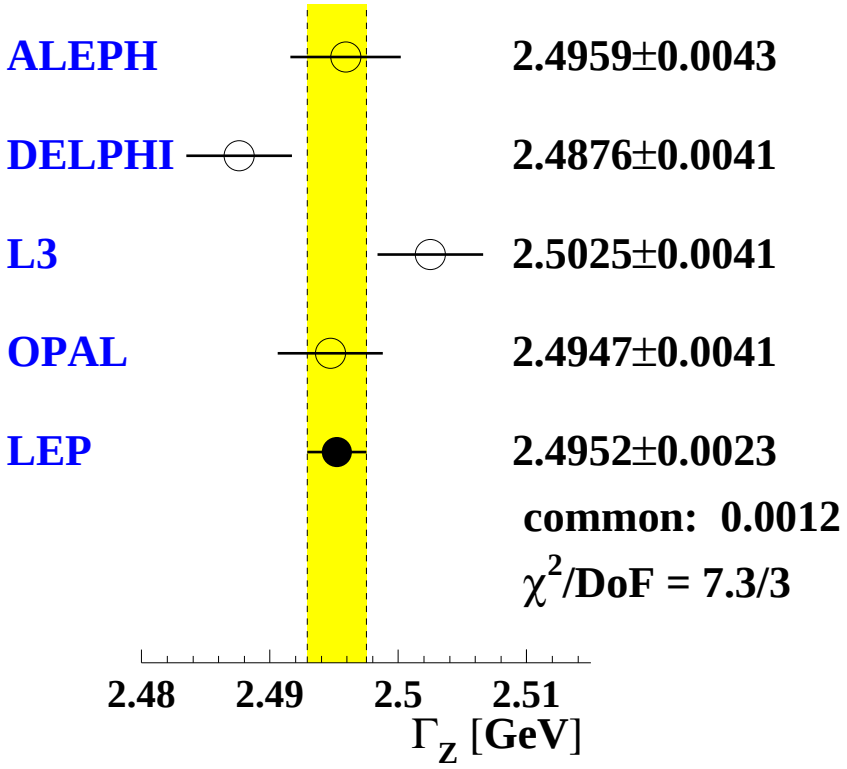

(b) Z boson width

Figure 1.8: The Z^0 boson average mass and width results from LEP-I experiments.

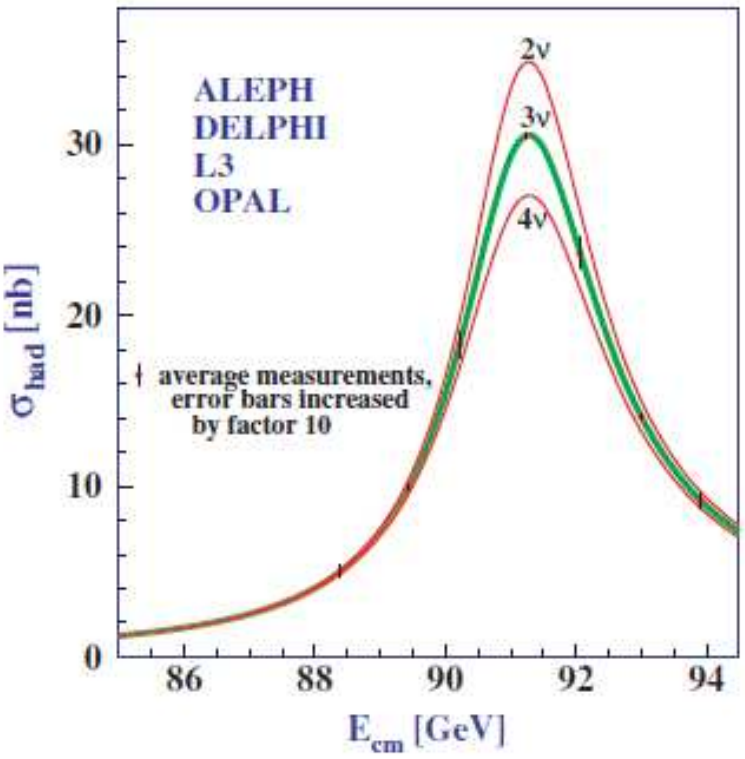

Figure 1.9: The hadronic cross section dependence on the number of light neutrinos families. The experimental results fit well to the 3ν case which validates that the number of light neutrinos is three.

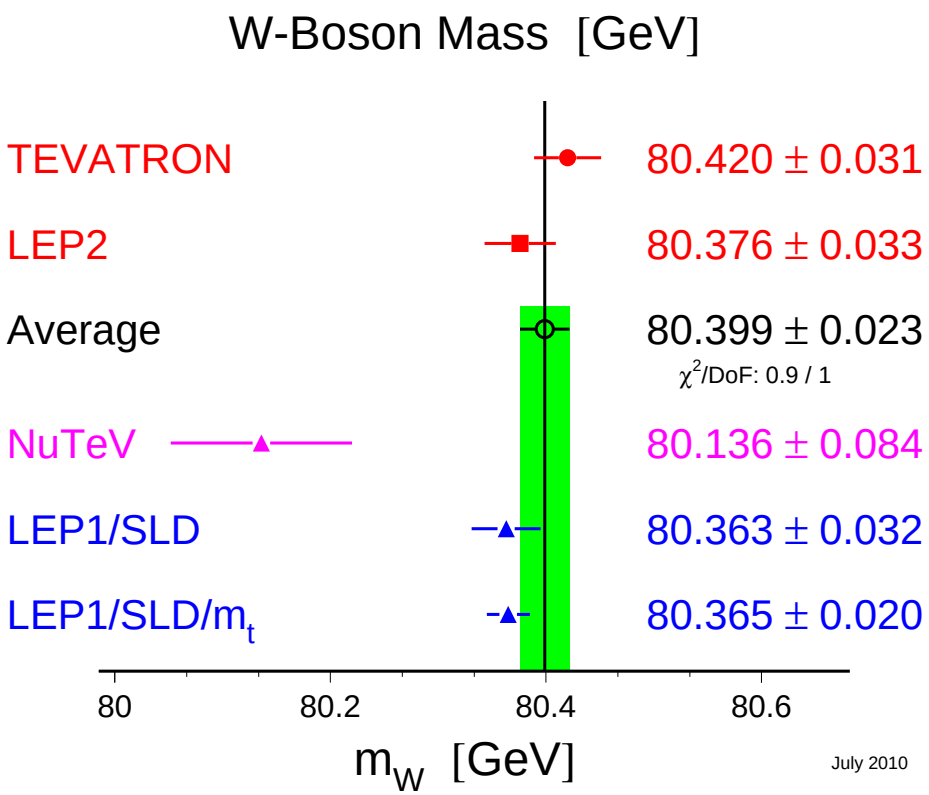

(a) W mass

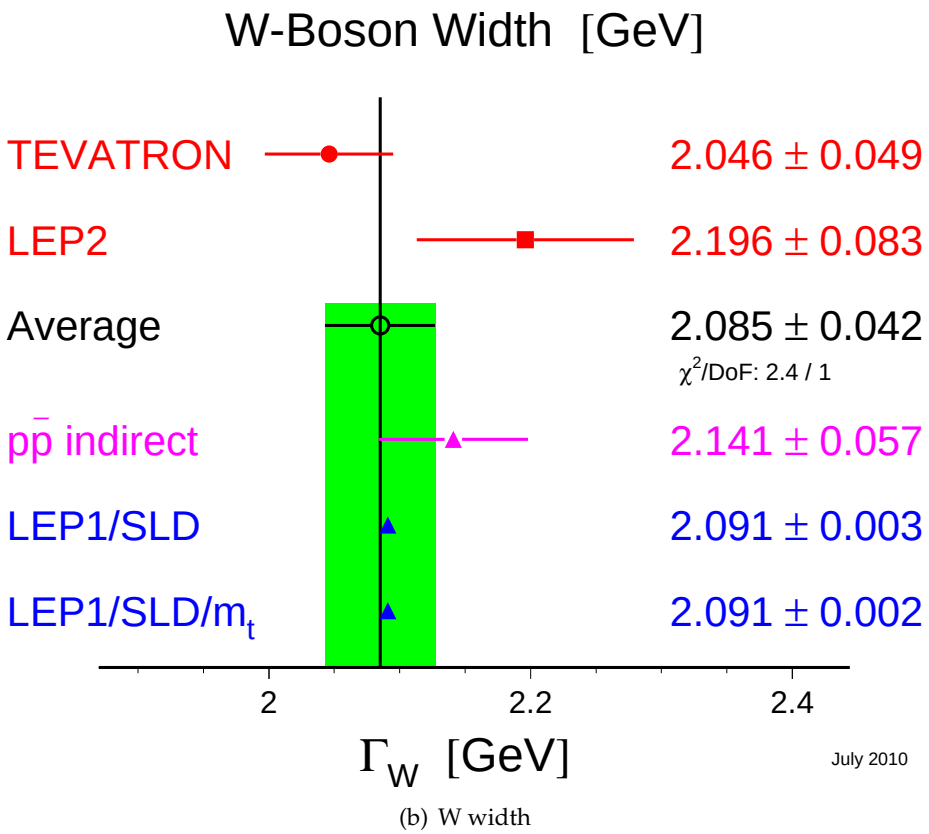

(b) W width

Figure 1.10: W boson mass and width world average from LEP-II.

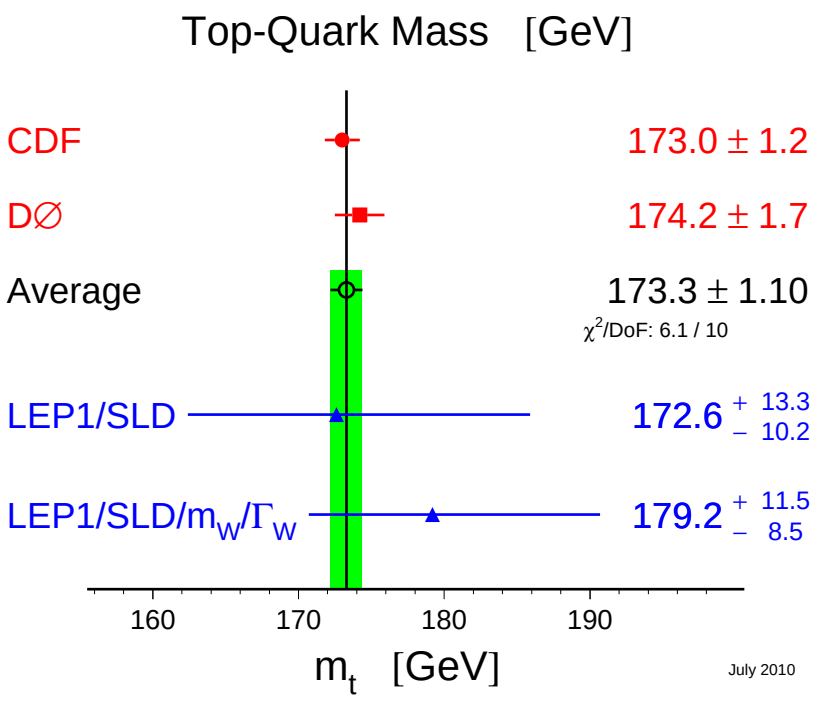

Figure 1.11: Top quark mass direct measurement from the Tevatron. Other experiments only have indirect measurement.

The LEP have made direct searches of the Higgs boson and established the lower limit of 114 GeV for the mass of the Standard Model Higgs boson. The Tevatron has advertised last year a small exclusion interval of 162 $GeV < M_H < 166\ GeV$ [8]. However from this year summer conferences the Tevatron has presented preliminary results extending this exclusion interval for masses between 158 GeV and 175 GeV [7]. This high mass measurement results from using the decay of the Higgs boson to a pair of W bosons.

1.4 The Physics goals of ATLAS/LHC

The standard model (SM) has had along the years a large number of predictions experimentally confirmed. With the start of the LHC collisions with a center of mass energy $\sqrt{s} = 7\ TeV$ the experiments will be in conditions to start searching answers to the still open questions in the field of particle physics.

The search for the Higgs boson is one of the main objectives for the LHC experiments. ATLAS as been designed aiming the discovery of this particle that in the SM gives masses to all

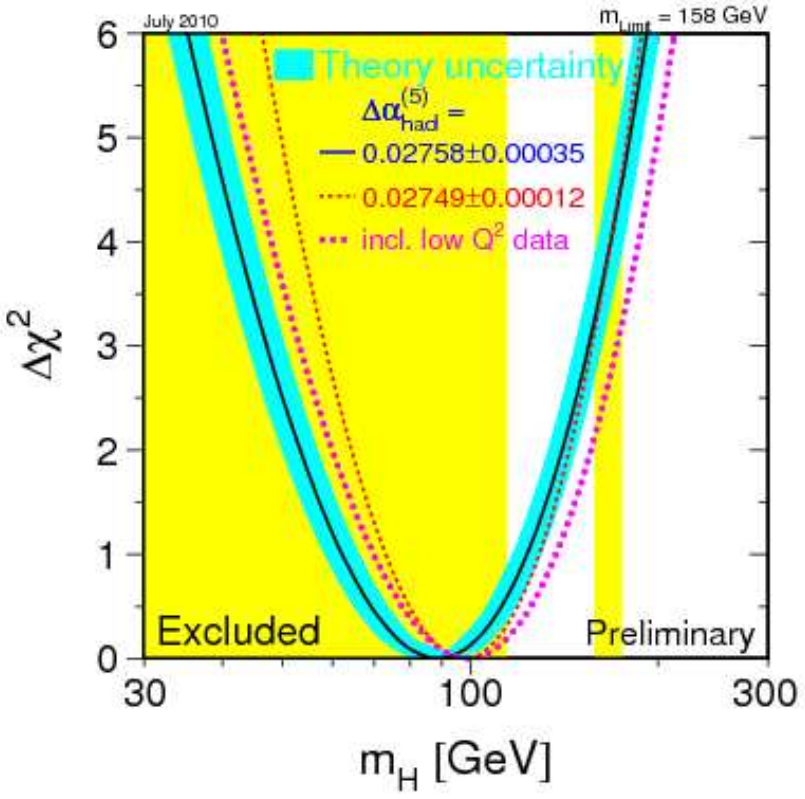

Figure 1.12: Higgs boson mass limits. The shaded bands represent exclusion regions for the Standard Model Higgs boson mass: M_H <114 GeV at LEP experiments [9] and 158 GeV < M_H < 175 GeV [7] from TEVATRON at Fermi Lab.

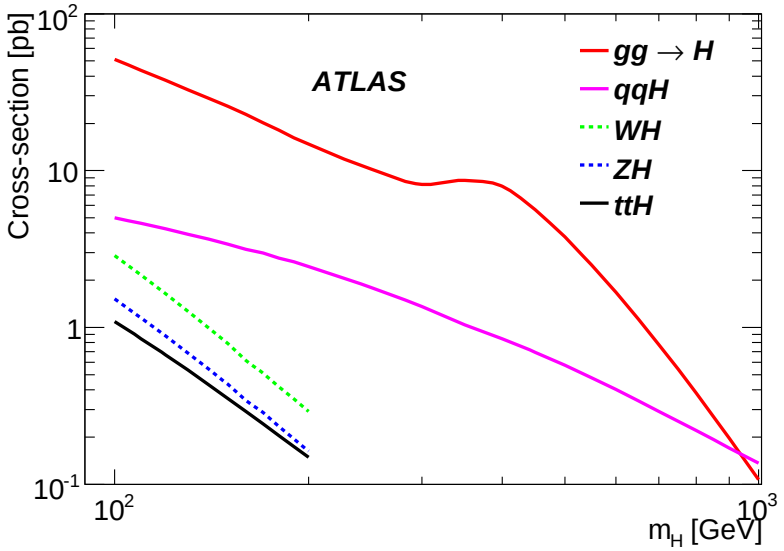

Figure 1.13: Cross-section for the production of the Higgs boson as function of its mass for the LHC with $\sqrt{s} = 14\,TeV$.

particles. The Higgs boson is fundamental to complete the SM as it is know today. If it exists it will be produced in several processes as the ones of Figure 1.13 [10] where the cross-section of the Higgs boson production is presented as function of its mass. The most sensitive decay for the Higgs boson will change also with its mass as shown in Figure 1.14 [10].

The LHC will be a top quark *factory*, producing millions of $t\bar{t}$ pairs in a sample of 10 fb^{-1}. The top quark has a mass of about 173 GeV measured at the Tevatron with a precision of the order of 1 GeV [6]. Its mass is unexpectedly high when compared to the other elementary particles, mainly the other quarks, and so some models predict it should have a different role. The very high top quark mass sets a large number of questions, for example: if the top quark mass is generated by the Higgs mechanism as the Standard Model predicts and if its mass is related to the top-Higgs Yukawa coupling, or if it does play a more fundamental role in the electroweak symmetry breaking mechanism [10]. The search for anomalies in top quark production and decays could lead to first evidence of new physics. From experimental point of view this particle will also be challenging since most part of the ATLAS subsystems must be used in its detection.

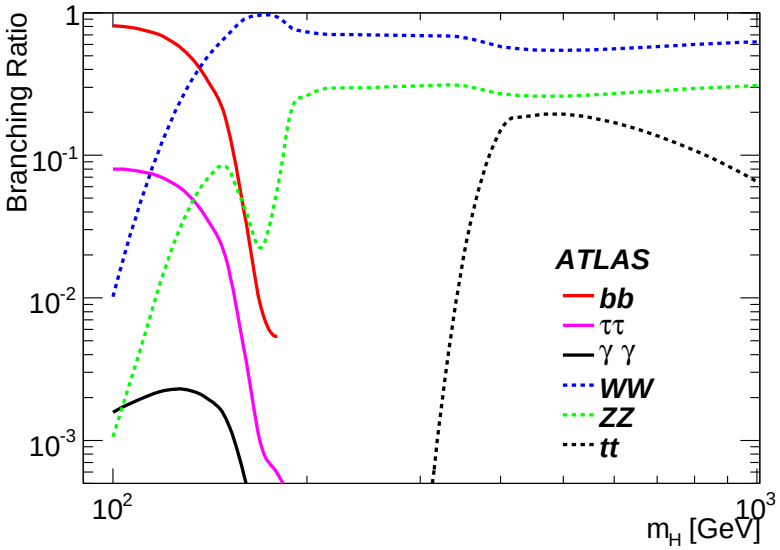

Figure 1.14: Branching ratio of the Higgs boson decays as function of its mass for the LHC with $\sqrt{s} = 14\,TeV$.

If the Higgs boson does not exist, it will be necessary some other particle or process to stabilize the top quark and W boson masses which in the SM have a direct dependence on the Higgs boson mass. The large center of mass energy of the LHC will also allow the search for new particles at the TeV scale that can give answers to open questions in the SM such as the hierarchy problem, the nature of dark matter etc. The most popular models for physics beyond the SM are in Super-Symmetric theories (SUSY). In SUSY models with R-parity conservation, it is predicted that the lightest super-symmetric particle will be stable and weakly interacting. These two characteristics make the LSP a good dark matter candidate.

The LHC and its experiments are considered the final test to a SM with a mechanism of electroweak symmetry breaking with and a particle with the characteristics of the Higgs boson. There are strong theoretical motivations to expect that new physics will be present at the TeV scale and within reach of the LHC experiments. The LHC has started very successfully, with the early measurement of several resonances as well as the first Z and W bosons decays; what its achievements will be cannot be exactly predicted, but the next few years will be extremely exciting for all particle physicists.

2 The ATLAS hadronic Tile Calorimeter

The performance of the hadronic scintillating tile calorimeter of ATLAS is the sub-system of ATLAS whose performance is discussed in the analyses presented in Chapter 5 and Chapter 6. In what follows is presented and overview of the Tile Calorimeter detector, including the calibration and monitoring tools necessary to guarantee the stability of its performance. Results from testbeam periods conclude this chapter since they represent the experimental status of the Tile Calorimeter prior to the phase of commissioning in the experimental cavern with cosmic muons.

2.1 Tile Calorimeter description

The coordinates system of ATLAS defines z as the axis along the beam pipe, the y-axis point upwards and the x-axis points to the center of the LHC accelerator ring. To define the geometry and elements in the detector volume both the cartesian and the spherical coordinates systems are used. It is also usual to use the pseudo-rapidity that is defined as $\eta = -ln\left(tan\left(\frac{\theta}{2}\right)\right)$.

The Tile Calorimeter [15] is the hadronic barrel calorimeter of the ATLAS [1] detector in the region $|\eta| < 1.7$. It is a sampling calorimeter with scintillating tiles as the active medium and steel as the absorber. The calorimeter structure is characterized by a periodic structure along z of 18 mm where steel and scintillator plates are intercalated. These results in an innovative geometry with the scintillating tiles positioned perpendicular to the beam axis. The Tile Calorimeter main purpose is to stop and characterize the hadrons produced in collisions or from the decay of other particles. A more developed discussion on the role of the Tile Calorimeter in physics analyses is covered in Chapter 3. In the following the detector

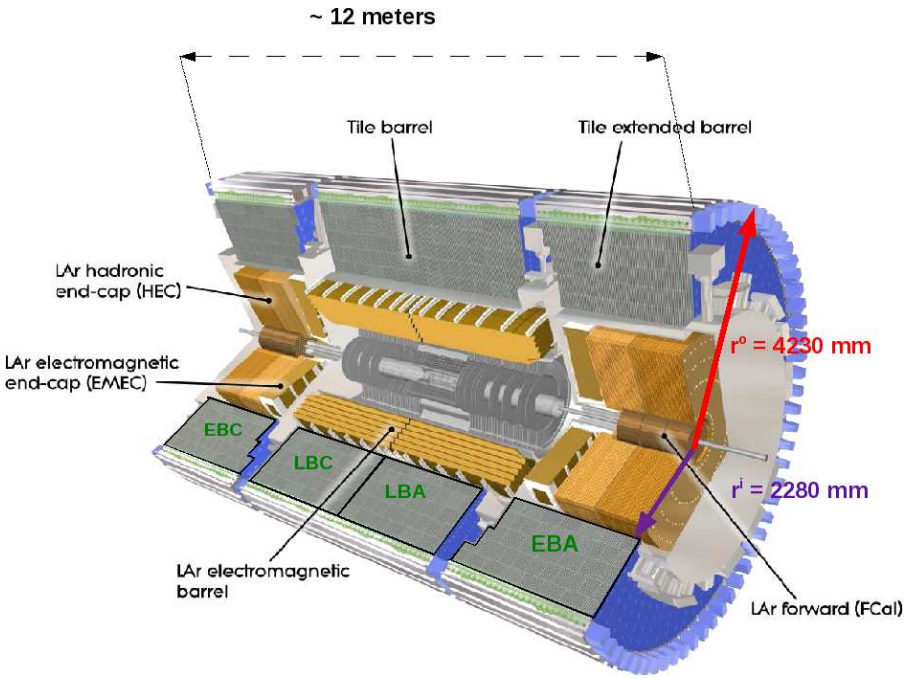

Figure 2.1: The Tile Calorimeter partitions: EBA, LBA, LBC and EBC

geometry, readout principle and signal reconstruction are briefly described.

2.1.1 Tile Calorimeter Geometry

The Tile Calorimeter is composed of three cylinders positioned along the beam axis (z-axis) with an inner radius of 2.28 m and an outer radius of 4.23 m. Along Z it has a length of approximately 12 m covering the region of pseudo-rapidity $|\eta| < 1.7$. In the hardware labeling convention of ATLAS detector the region with $\eta < 0$ is designated as the C side and $\eta > 0$ as the A side. The central cylinder is the Long Barrel (LB = LBA+LBC) that covers the region $|\eta| < 1.0$. Adjacent to the two lateral ends of the LB there are the Extended Barrels (EBA and EBC) covering the region $0.8 < |\eta| < 1.7$. Between each cylinder there is a gap required for the distribution of services (cabling, cooling) to the most internal detectors, the LAr electromagnetic barrel calorimeter and the Inner Detector. The structure of the calorimeter is shown in Figure 2.1 where the four hardware partitions EBC, LBC, LBA and EBA are identified. The Tile Calorimeter readout includes also the gap, crack and minimum bias trigger scintillators (MBTS). The gap scintillators (E1 and E2) are located in the $1.0 < |\eta| < 1.2$

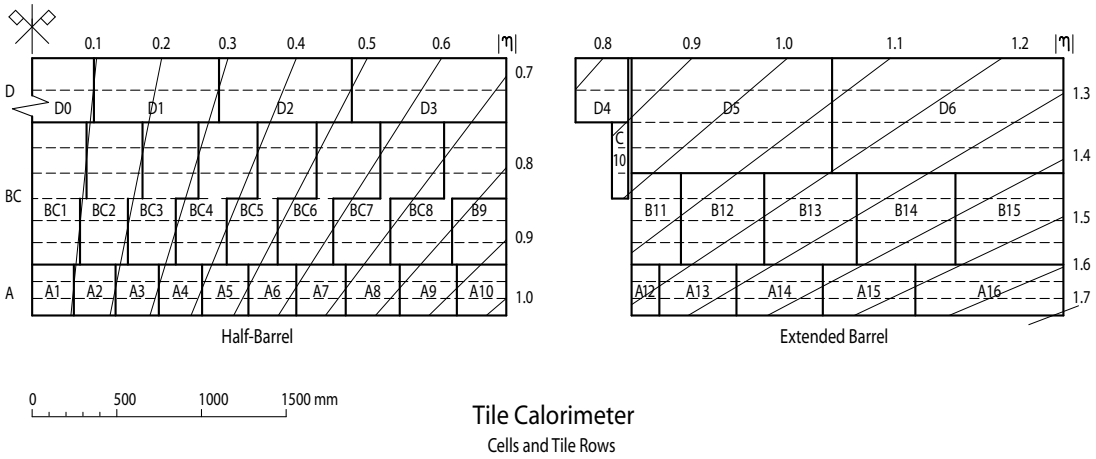

Figure 2.2: Tile Calorimeter cells and rows in the RZ plane.

region and are used for sampling the hadronic showers. The crack scintillators (E3 and E4) are located in the $1.2 < |\eta| < 1.6$ region and are used for sampling the electromagnetic showers. The MBTS, located in the $2.1 < |\eta| < 3.8$ region, are useful for the identification of beam background and triggering in the (early) collisions phase. Each Tile Calorimeter partition is divided in 64 modules – ϕ segmentation. Each module is divided in cells, each one read-out by a pair of photomultipliers. In total the Tile Calorimeter has 9856 channels, corresponding to 4672 cells, of which 512 channels are used to readout the gap, crack and MBT scintillators mounted along the inner face of the EB modules. The division in cells follows a projective distribution, illustrated in Figure 2.2 [11]. The cells define three radial samplings that are identified by the letters A, B/C and D. The A and B/C cells are characterized by a segmentation in ϕ and η of

$$\Delta\phi \times \Delta\eta = 0.1 \times 0.1 \tag{2.1}$$

and for the D cells of

$$\Delta\phi \times \Delta\eta = 0.1 \times 0.2\,. \tag{2.2}$$

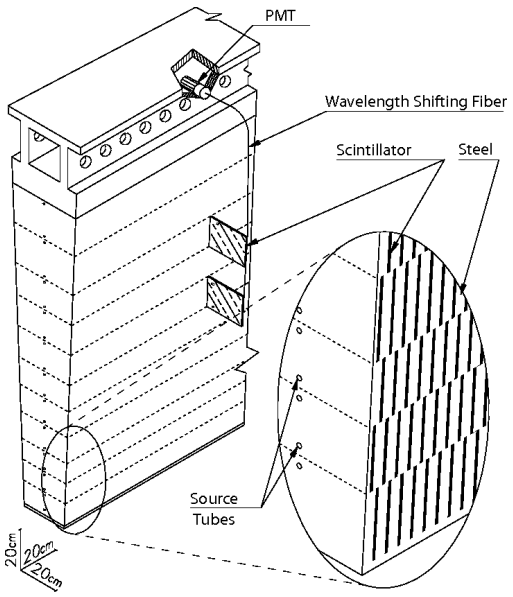

Figure 2.3: Tile Calorimeter module structure: sampling calorimeter with a steel matrix where scintillating plastic tiles are embedded. The signal produced in each scintillating tile by ionizing particles is double-readout two photomultipliers. The signal is carried to the PMTs by WLS optical fibers.

2.1.2 Readout principle and front-end electronics

The ionizing particles crossing the detector volume lose energy and produce a light signal proportional to the energy deposited in the scintillating tiles. The light is transported by Wave Length Shifting (WLS) fibers to the photomultipliers (PMTs). The detector is characterized by a double readout with two PMTs reading the same unit volume – a cell. Due to the cell segmentation described above 23 different WLS fiber lengths are necessary to collect the signal from the different cells that are located at different radial distances from the readout PMTs [13] [12]. A light mixer is placed in front of each PMT window to produce an uniform light distribution. In Figure 2.3 a scheme of a Tile Calorimeter module is shown.

The PMTs collect the optical signal coming from the Tile Calorimeter cells to produce an analog electronic signal. The signal is shaped and amplified in the 3-in-1 card and then distributed by its four signal outputs. An analog integration output is connected one by one to a slow ADC integrator card used for calibration purposes and minimum bias measurement. A summing circuit called adder receives outputs from five front-end 3-in-1 cards and sends

the analog sum to the L1 trigger processor. The remaining two are dedicated for the fast signal digitization with a high gain (HG) output, for the very low energy deposits such as the ones produced by muons, that typically leave about 2 GeV in Tile Calorimeter [15], and with a low gain (LG) output for the larger energy deposit such as the ones resulting from jets that, in a single cell, can reach energies of the order of the TeV. Each digitizer is composed of two 12-bit Analogue-Digital converters (ADC), one for LG and the other for HG, a Timing Trigger and Control receiver chip (TTCrx) and two data management unit (TileDMUs). Each digitizer can receive and digitize the signal from up to six PMTs. In the LB there are 8 digitizers and in EBs there are 6 digitizers.

2.1.3 Tile Calorimeter data acquisition concept

The PMT signals are always digitized, but their reconstruction depends on the arrival of a L1 accept signal. The digitization is done in the front-end-electronics (FEE) of the calorimeter and the decision to accept the event comes from the L1 trigger system based on fast signals from the muon spectrometer and calorimeters, including the analog sums provided by the Tile Calorimeter. A Timing, Trigger and Control system (TTC) [16] is in charge of the detector synchronization and is responsible for the distribution to the front-end electronics of fast signals such as the 40MHz system clock and the L1 trigger accept (L1A), that are the most relevant for the present discussion. These signals reach the TTCrx through optical fibers to be converted into electronic signals and distributed. Within the signals distributed by the TTCrx to the ADCs and TileDMUs are two clock signals:

- The 40MHz system clock that is distributed to the TileDMUs.
- A clock signal (*clock40des2*), synchronous with the system clock, with adjustable delay in units of 0.104 ns up to 25 ns, is distributed to the Tile Calorimeter ADCs.

The *clock40des2* clock is used to drive the sampling of the analogue signal in the digitizers every 25 ns. The different 25 ns samples are sent to the TileDMUs units and stored in a pipeline memory for up to 6400 ns waiting for the arrival of a L1A produced by the trigger processor. The TTCrx distributes this signal to the TileDMUs that gives a command to allow the readout

of seven consecutive 25 ns samples that are sent to the RODs for reconstruction. If necessary the TileDMUs can be programed to delay the readout in units of 25 ns i.e. define from which sample should the readout start.

2.1.4 Signal reconstruction in the RODs

The seven consecutive 25 ns samples are sent to the RODs where the amplitude and time of the signal from a PMT are reconstructed using an optimal filter (OF) algorithm [17]. The algorithm takes the weighted sum of the seven samples for which OF weights for amplitude a_i and time b_i must be calculated:

$$A_j = \sum_{i=1}^{n=7} a_i S_{ij}$$

$$A_j \tau_j = \sum_{i=1}^{n=7} b_i S_{ij}$$

where

A_j Pulse amplitude proportional to the energy measured by PMT j.

τ_j Difference between the peak of the reconstructed signal and the 4^{th} sample start. This phase is also called as the time of PMT j.

S_{ij} Amplitude of the physics signal of PMT j in sample i.

a_i and b_i Optimal filter coefficients.

A value of $\tau_j < 0$ ($\tau_j > 0$) indicates that the signal is early (late) or the trigger accept signal is late (early). The OF weights, also called OF coefficients, depend on the phase τ_j of a channel and are calculated to reconstruct the digitized pulse while minimizing the impact of noise.

It has been verified that in order to achieve a measurement of the energy with a precision better than 2% the accuracy of the channel time must be better than 5 ns [17]. It is possible to correct time offsets of a PMT signal and respectively improve the amplitude reconstruction applying an iterative procedure. However during the LHC operation the time available for the reconstruction of an event is limited. The number of iterations for online processing are

set to only one and a prior knowledge of the phase τ_j of a PMT channel is required. This operational constraint implies that time calibration is mandatory in order to achieve the best performance of the L2 trigger. Offline corrections to the online reconstructed energy, resulting from mis-calibrations in time, are possible for channels in which $|\tau_j| < 10$ ns with a minimal $< 1\%$ degradation of the energy measurement precision.

2.1.5 Fit method

The signal reconstruction method briefly described in the previous section is the currently used for the LHC operation. Until the installation of the RODs the signal was reconstructed using an alternative algorithm designated as the Fit Method. It was developed during the testbeam and used until the installation of the RODs in the reconstruction of the Tile Calorimeter signal in the ATLAS experimental cavern. Presently, it is used for the reconstruction of the signal from the charge injection calibration system.

The Fit Method uses the knowledge of the pulse shape to provide an energy measurement and obtain a measurement of the time of the energy deposition. For each channel, given a normalized pulse shape $g(t)$, a fit is performed to the function

$$f(t) = Ag(\,t\,-\,\tau\,)\,+\,c$$

to three parameters: amplitude A, phase τ and pedestal. A comparison with testbeam data of the Optimal Filter and Fit method has shown that they are equivalent. However, the Fit Method is not suited for fast online processing.

2.1.6 Noise description

It was observed that the calorimeter cell clustering algorithms were measuring an excessive number of clusters per event in the Tile Calorimeter. After a dedicated investigation it was found that a wrong pedestal description was being applied. In Figure 2.4 the significance (E/σ) for random triggers is compared for a single gaussian description and a double gaussian description. In black is shown the ideal model for a gaussian noise like response. It is seen

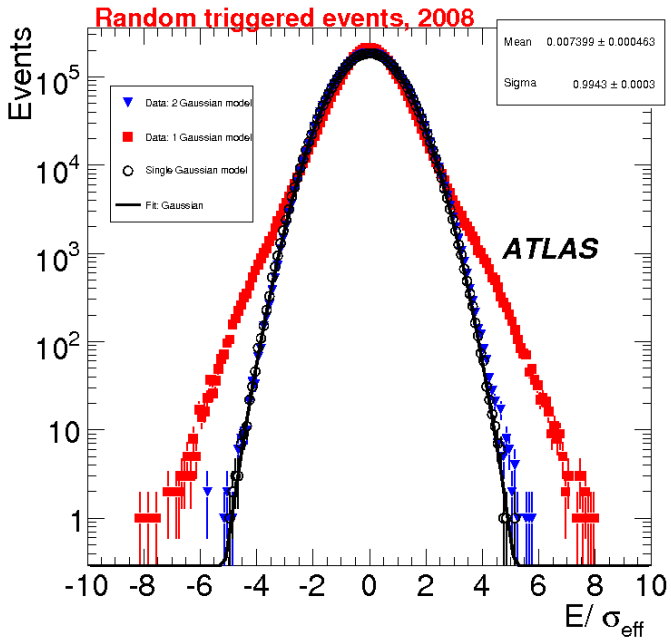

Figure 2.4: Significance of random triggered events in the tile calorimeter cells. A single gaussian description of noise □ is compared with a double gaussian description △ [18].

that the single gaussian response fails on the agreement with the model in particular in the tails. Considering now the noise description as defined by an effective sigma that combines the information of the two convoluted gaussian it is seen that the results fit well the expected modeled response. Concluding, the tile calorimeter pedestal is described using a double gaussian distribution [18].

In Figure 2.5 [19] the noise measured during a physics run but using a dedicated stream designated RNDM (data from a random trigger). The RMS for each Tile Calorimeter module (a slice in ϕ) shows that the electronic noise is below 50 MeV for all partitions. Each entry for each one of the four plots, corresponds to the average response over all the operating channels of a module.

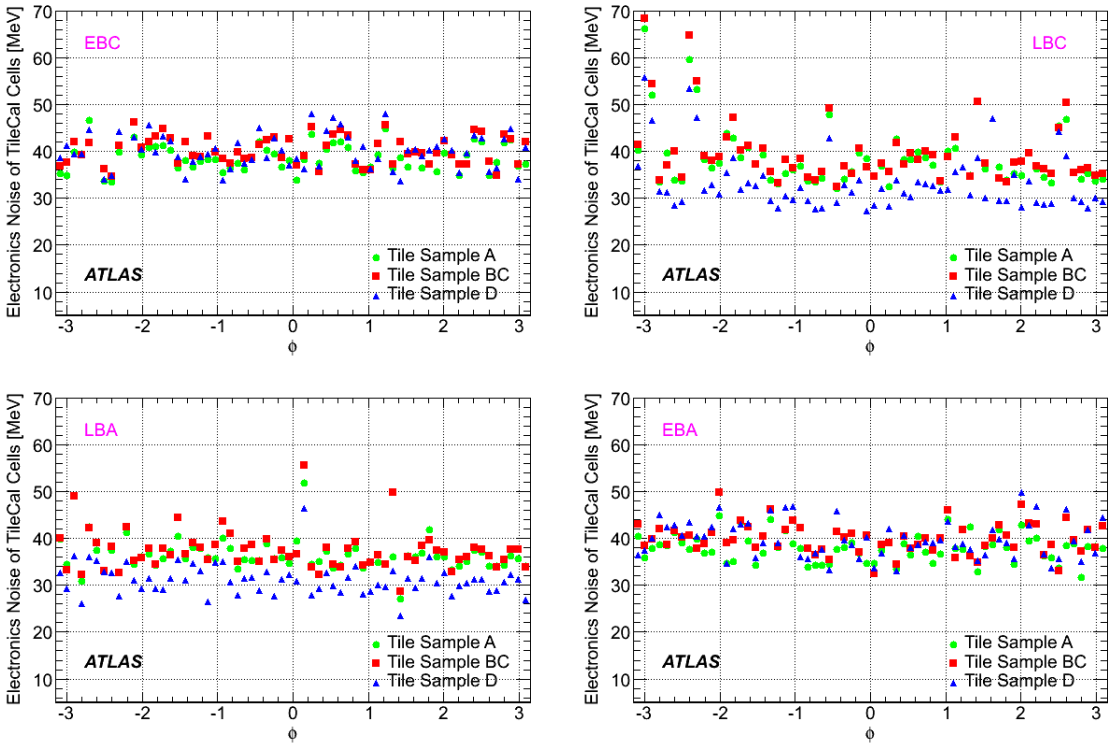

Figure 2.5: The electronic noise in Tile Calorimeter modules measured using the RNDM stream during a cosmic ray muon on September 2008 [19].

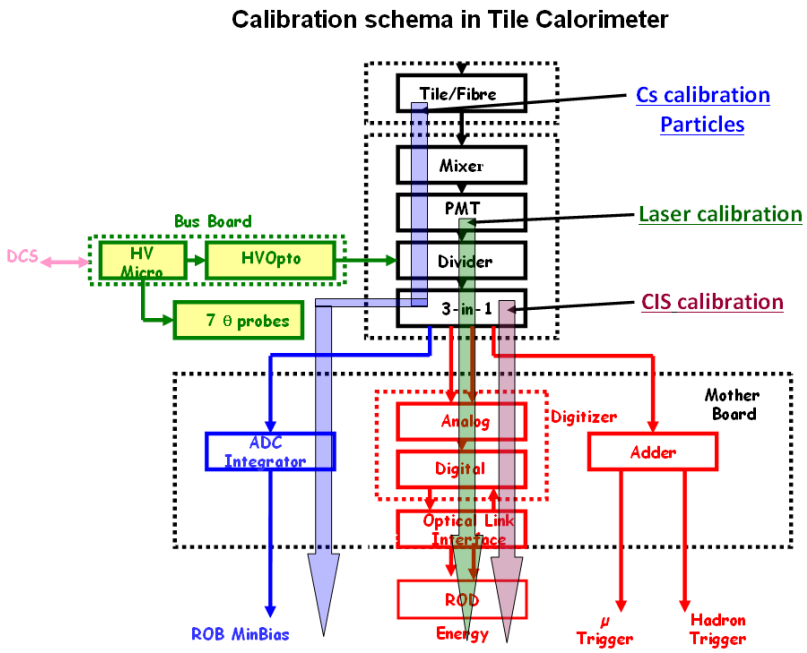

Figure 2.6: The calibration systems of the tile calorimeter and their interface to the readout system from scintillating tiles to front-end electronics.

2.2 Calibration and monitoring systems

The Tile Calorimeter calibration and monitoring is achieved using four dedicated systems: the Charge Injection System (CIS), the Integrator, the Laser System and the Cesium System. During its operation the detector modules are monitored to learn about its status and evaluate if it is necessary any update on the calibration constants on the database or if any channel is not working properly in which case it can be masked. In Figure 2.6 the four systems are depicted as a part of the read-out scheme of the Tile Calorimeter.

The calibration systems are used to provide the different terms on the following equation:

$$E_{channel} = A \cdot C_{ADC \to pC} \cdot C_{pC \to GeV} \cdot C_{Cs} \cdot C_{laser}$$

where

$E_{channel}$ The energy in GeV.

A signal amplitude in ADC counts.

$\mathbf{C_{ADC \to pC}}$ conversion factor of ADC channel to charge in pC (measured by the CIS).

$\mathbf{C_{pC \to GeV}}$ conversion factor from charge (pC) to energy (GeV) that was established in testbeam for 12% of modules using beams of high energy electrons (more details given ahead).

$\mathbf{C_{Cs}}$ is a factor that corrects for residual non-uniformities after the gain equalization (measured with the Cesium system).

$\mathbf{C_{laser}}$ is a factor used to correct non-linearities of the PMT response (measured with the laser system).

Figure 2.6 also shows, on the center left, the Detector Control System (DCS) [20]. This is the slow control tool of ATLAS that has a branch fully dedicated to the Tile Calorimeter monitoring of the front end electronics (FEE) low voltage, the photomultipliers (PMT) high voltage and the temperature in several points along the Tile Calorimeter FEE.

2.2.1 Charge Injection System

A known charge signal with a systematic uncertainty of ± 0.7 % is injected in each digital channel of the FEE. The injected signal reproduces approximately the photomultiplier output signal and is used to calibrate and monitor the digital outputs, Low Gain (LG) and High Gain (HG), ADC counts to pC conversion factors and measure their linearity. The CIS system is planned to operate from a daily to a weekly basis during the LHC operation.

In Figure 2.7 shows the measurements of the ADC counts/pC response for the two outputs prior to any correction. Both LG and HG show already a resolution $\sigma/mean$ of 1.5%.

The stability in time of these two outputs was monitored and in Figure 2.8 measurements between August 2008 and October 2009 are presented. In each time trend can be depicted the results for a single channel and for the mean over the 19 595 ADC channels. A stability for the individual channel of 0.07% is measured for HG and of 0.05% for LG. The mean ADC channels stability is of the order of 0.03% for HG and 0.04% for LG.

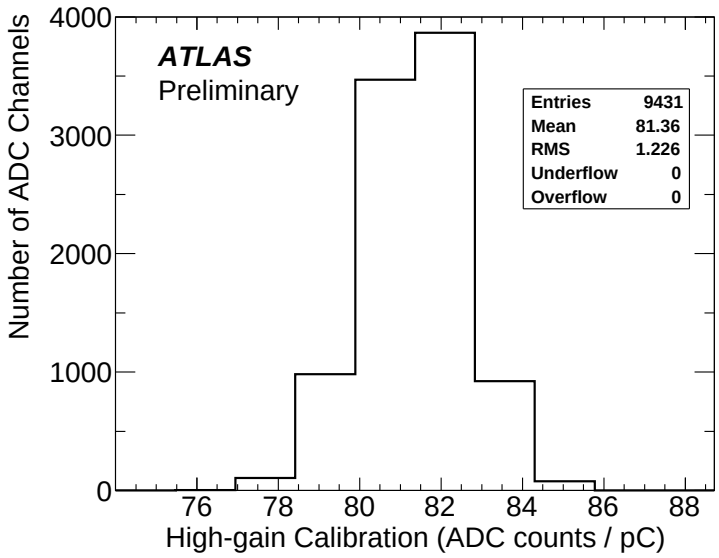

(a) high gain

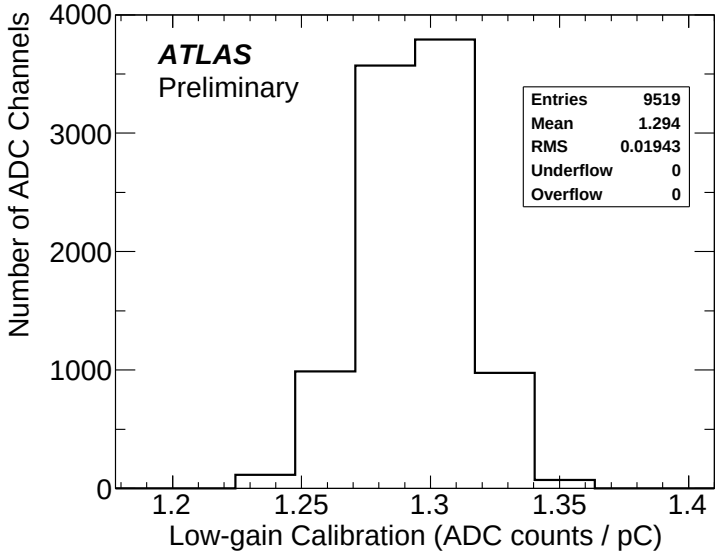

(b) low gain

Figure 2.7: Channel-to-channel variation of the high gain (a) and low gain (b) readout calibration constants $C_{ADC \to pC}$ prior to any correction [18].

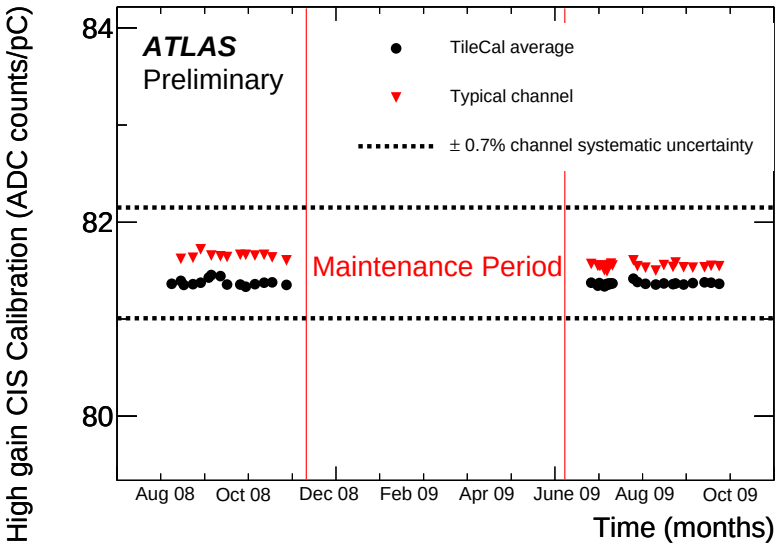

(a) high gain

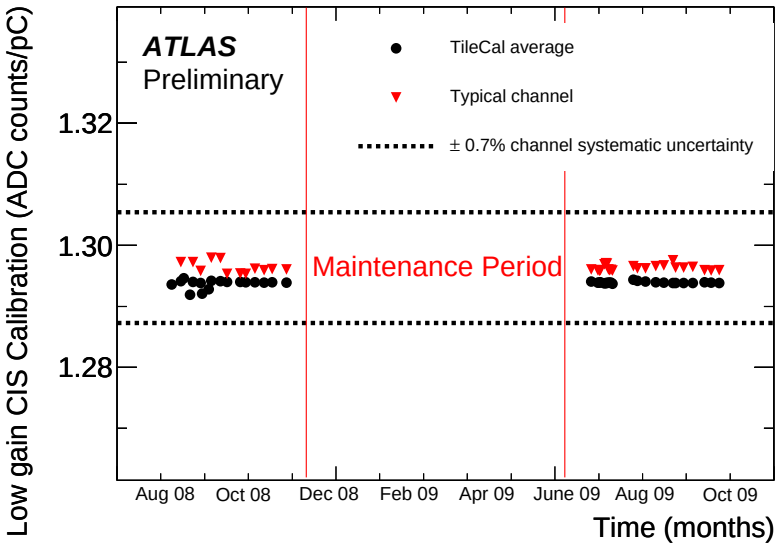

(b) low gain

Figure 2.8: Time stability of the average high gain (top) and low gain (bottom) readout calibration constants from August 2008 to October 2009, for 19,595 ADC channels [18].

2.2.2 Laser System

The principle of operation of the laser system is to inject a common light signal to all PMTs that will produce a response similar to the one produced by the ionizing particles in the scintillating tiles. Since the accuracy of the injected pulse is better than 1% the results from monitoring the reconstructed signal, during a period of time and for different intensities, are a measurement of the photomultipliers stability and linearity with a very good precision. The main role of the laser system is to measure the stability and linearity of the PMTs and associated electronics [21].

In Figure 2.9, the relative gain variation evaluated for a period of 50 days is presented for both output gains. Using a relative quantity allows to cancel out the systematic errors associated with the measurement (stability of light intensity), and obtain an exact evaluation of the gain fluctuations. For the low gain output 14 channels are out of the 1% target range, which corresponds to 0.14% of the total number of PMTs. The high gain output has 57 channels in these conditions corresponding this to 0.58% of the total number of PMTs. The σ is from a gaussian fit applied to the distributions and is in agreement with the intrinsic resolution of the laser system.

Another application of the laser system is to monitor the time response of the Tile Calorimeter channels and produce calibration constants in order to have all channels equalized in time. This procedure requires the usage of a high amplitude pulse in order to take advantage of the higher time resolution but at the same time the amplitude should avoid saturation that tends to distort the signal shape and deteriorate the time response [29].

2.2.3 Cesium System

The Cesium system consist of a movable radiactive source that travels across all the calorimeter cells (Figure 2.10). The response to this source is sensitive to the Tile Calorimeter structure and was used previous to the commissioning to test the optical instrumentation of the modules [25]. The integrated signal over a cell is used to set and monitor the electromagnetic energy scale (EM scale) for all cells. The EM scale was established in testbeam using high energy electrons

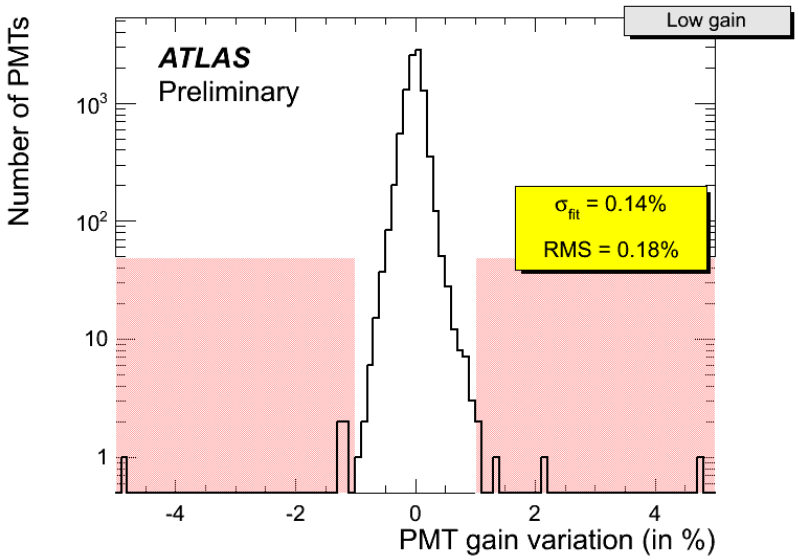

(a) low gain

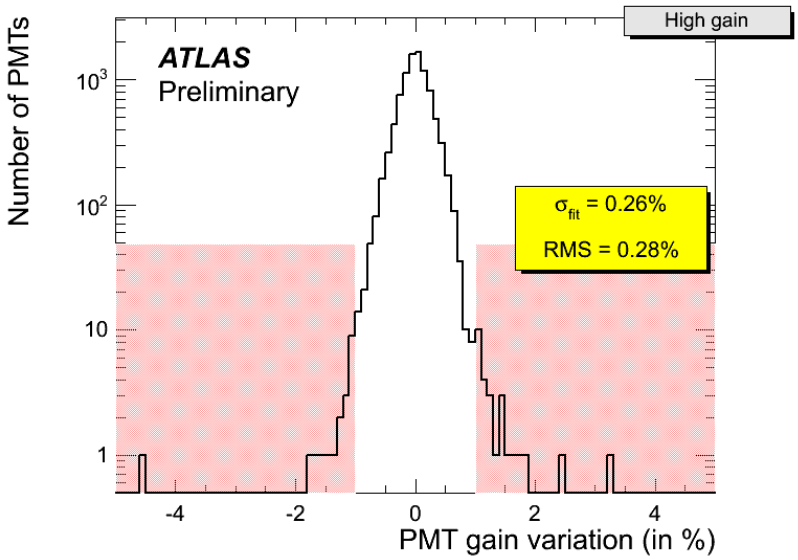

(b) high gain

Figure 2.9: Relative gain variation (to a reference measurement) for the tile calorimeter photomultipliers during a period of 50 days. Each entry in the histogram is a photomultiplier. Shaded areas correspond to relative gains above 1% [18].

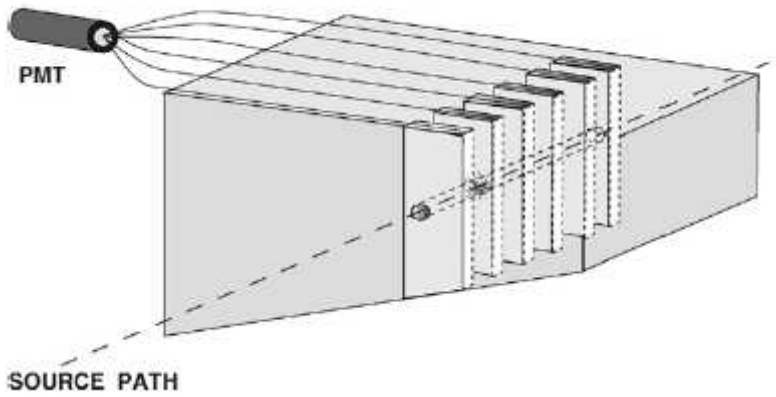

Figure 2.10: Cesium system working principle.

impiging in the calorimeter at 20° where cell equalization of modules was done using the cesium system and later confirmed using high energy muons [26].

The signal measured by the Tile Calorimeter channels of the cesium radioactive source should fall according to its life-time. The expected performance is represented in Figure 2.11(a) by three solid lines that represent the three radioactive cesium sources used for the three Tile Calorimeter cylinders. The points are data average and RMS per partition, normalized to the activity of the cesium source in barrel cylinder in July 2008. The RMS was measured to be better than 0.3%.

From the cesium results it is observed that:

- The Tile Calorimeter response depends on the magnetic field status. If it is ON an increase is observed. In the figure these data points have a MF sign attached.

- The data points are not following the expected decay rate of the cesium sources. There are two points which are set exactly on the cesium expected performance line. These resulted from equalizations at the beginning of these series of monitoring measurements and also after the maintenance period.

In Figure 2.11(b) the deviation of the measured values from the expected values are plotted against time. It can be seen that the effect of the magnetic field is stronger in the barrel

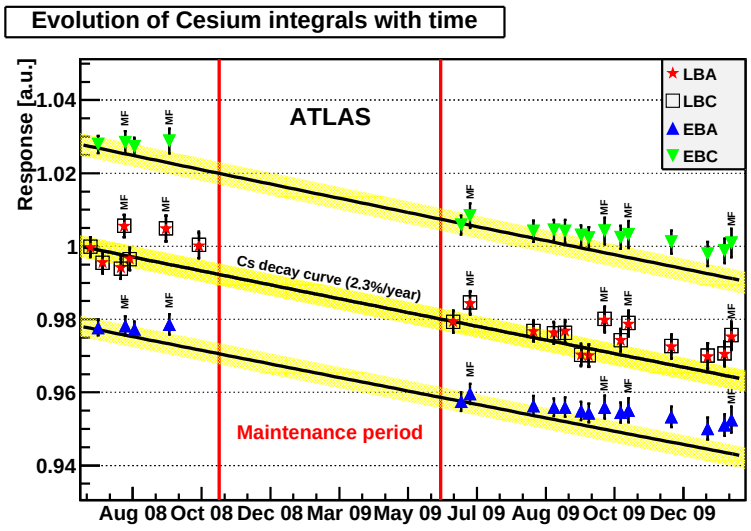

(a) Time evolution of EM scale

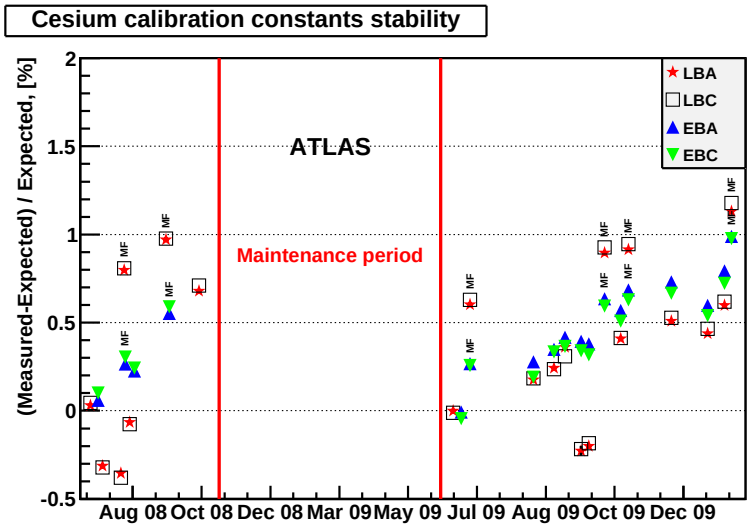

(b) Absolute updrift on the EM scale from the Cs system

Figure 2.11: Cesium system measurements in the ATLAS experimental cavern. (a) The solid lines are the expected decay curves for the cesium sources (one for each cylinder). The experimental points are from Cesium data taken with the magnetic field off and on (with MF close to data points). (b) Normalized response where the up-drift of the Tile Calorimeter absolute value is measured [18].

partitions. An updrift of the order of 1% for the EM scale is measured between July 2009 and December 2009.

The effect of the magnetic field on the response of the calorimeter is detailed in Figure 2.12. It is observed that the effect is much larger in the LB region $|\eta| < 1$ where an increse of the order if 0.6-0.7% is measured for the distribution in η (Figure 2.12(a)). For the response in ϕ (Figure 2.12(b)) the results are uniform and an increase of the order 0.6-0.7% is seen for all ϕ slices.

2.2.4 Integrator

The integrator is a component of the FEE of the Tile Calorimeter and it is used by the Cesium calibration for the integration of the light signal produced in the scintillating tiles. During the LHC collisions and data taking its usage is planned to monitor the calorimeter channels over several bunch crossings.

The calibration of the integrator is done also by injecting a known charge pulse using the CIS system. Figure 2.13(a) shows the distribution of the integrator gains of all the Tile Calorimeter channels. The results refer to the gain used by the cesium system. A mean value of 28.81 MΩ with a RMS of about 1% is measured. The left tail of the distribution results from a 2% lower response in 16% of the Tile Calorimeter integrator ADC cards. From Figure 2.13(b) the relative variation of the integrator gain measured during 2 years of measurements shows a stability of 0.01%. The error bars represent the stability of individual channels that is better than 0.01%. In Figure 2.13(c) is presented the measurement of integrator noise. An average of 1 ADC count is measured, and for 99% of the Tile Calorimeter channels the noise level is below 2 ADC counts. Typically the cesium system signal is about 2000 ADC counts which represents a very good separation between signal and noise.

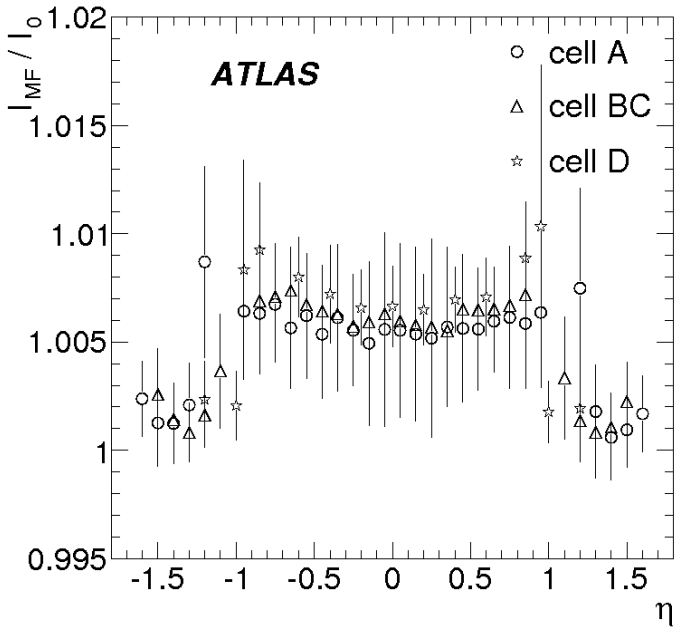

(a) I_M/I_0 vs η

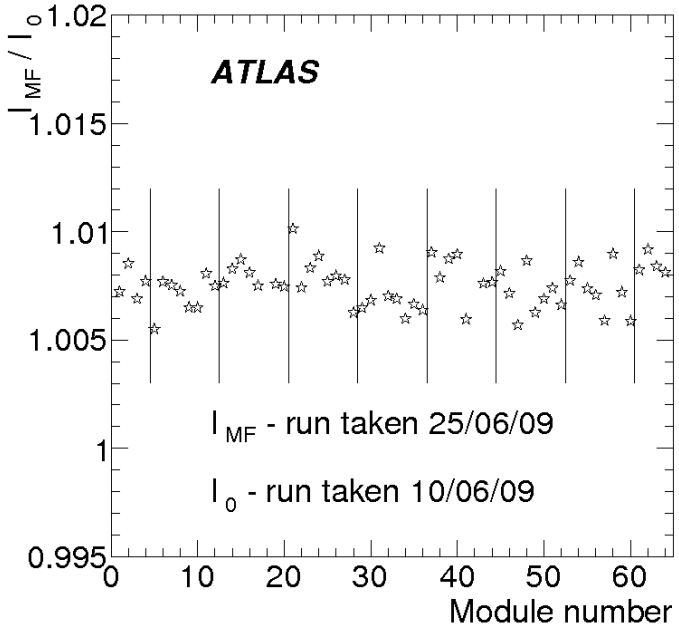

(b) I_M/I_0 vs ϕ

Figure 2.12: The Tile Calorimeter up-drift due to the presence of the ATLAS magnetic field. The ratio between the integrated signal with magnetic field I_M and integrated signal without magnetic field I_0 in η and ϕ [18].

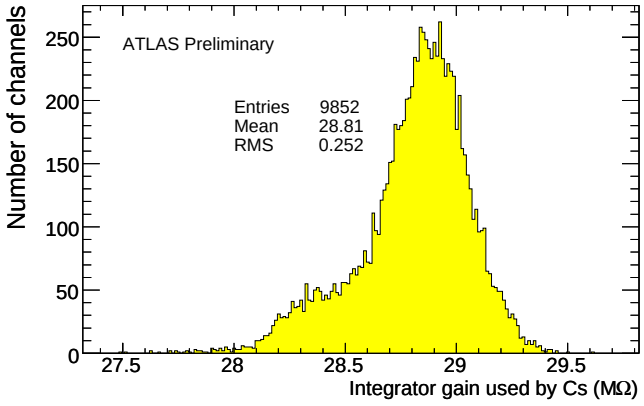

(a) Gain

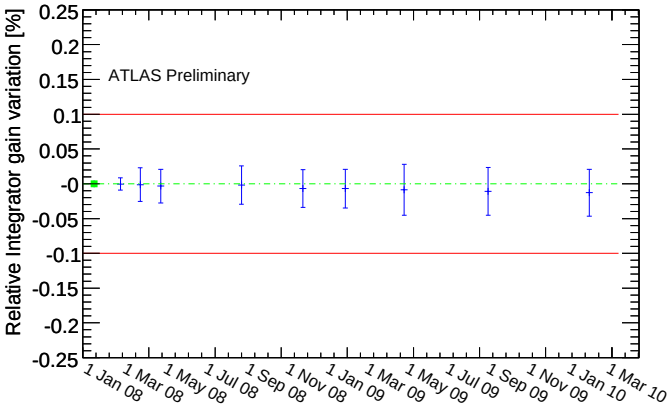

(b) Gain stability

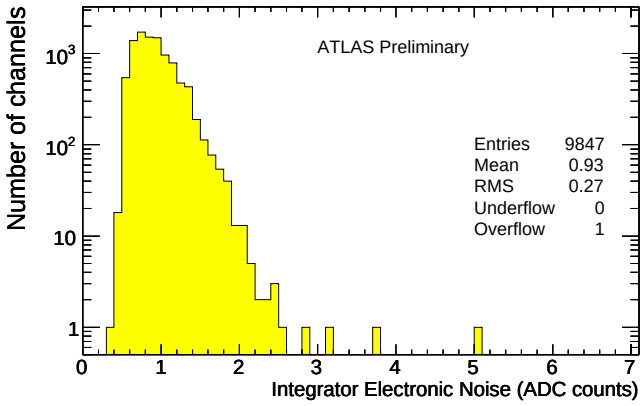

(c) Electronic noise of the integrator

Figure 2.13: Integrator response: (a) Gain stability (b) Stability in time during approximately 2 years of monitoring relative to January 2008 (c) Electronic noise. The measurements used 95.3% of the Tile Calorimeter channels [18].

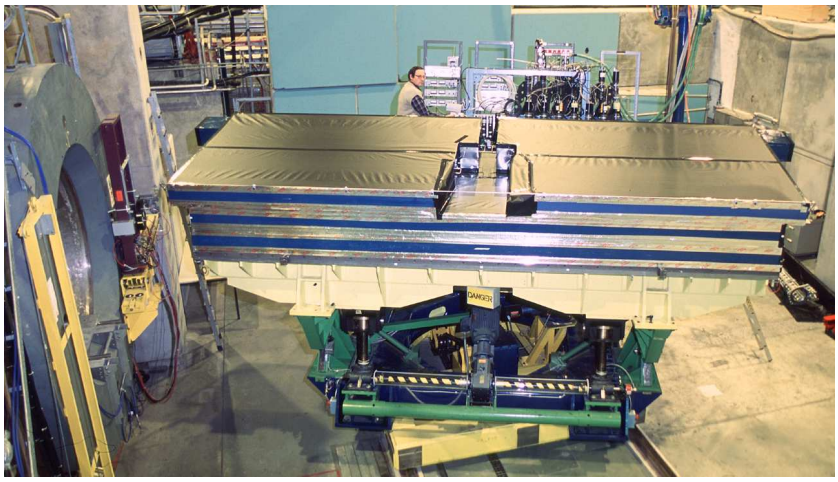

Figure 2.14: The Tile Calorimeter setup during the 2000 to 2003 standalone testbeam.

2.3 Tile calorimeter performance from testbeam

2.3.1 Experimental setup

The standalone testbeam dedicated to the calibration of production modules was done between the year 2000 up to the year 2003. In these setup four modules were put to test for each run period. The reference module named Module 0 (a long barrel module), a long barrel module and two extended barrel from the production modules. In these tests high energy particles were used to investigate the performance of the detector using elelctrons, pions and muons. The particle beams impact the Tile Calorimeter modules with different incident energies and angles. In Figure 2.14 a photo of the setup is depicted. In the standalone testbeam about 12% of the whole Tile Calorimeter were calibrated and characterized and the results between modules have shown agreements of the order of 1%. In the next section a selection of the main results of these performance studies are summarized.

2.3.2 Performance

electrons

Electrons were the main instrument to set the electromagnetic energy scale (EM scale) of the Tile Calorimeter cells. This was done using high energy beams of electrons with an incidence

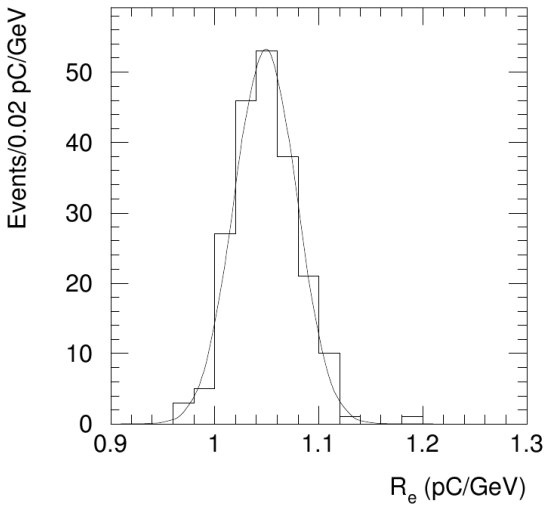

Figure 2.15: Electromagnetic energy scale of the Tile Calorimeter for electrons measured during testbeam. The cell response of electrons entering the calorimeter modules exposed to the beam at incidence angle of 20°, normalized to beam energy, with one entry for each A-cell measured. The plot contains data at various energies ranging from 20 to 180 GeV [26].

angle of 20° and the beam energy ranging from 20 GeV to 180 GeV. The energy response for electrons is summarized in Figure 2.15. The entries on the plot correspond to measurements done in cells of the first radial layer (A-Cells). The mean value 1.050±0.003 pC/GeV defines the Tile Calorimeter EM scale factor. The RMS spread of 2.4±0.1% is due to local variations in individual tile and tile/fiber responses which was confirmed by dedicated MC studies.

In order to transport the EM scale to the other cells in a module, muon beams and electron beams using different incindence angles were used. These measurements are combined with the cesium systems measurements in order to equalize the cells in a module, and also as a preparation for the global equaliazation of the whole Tile Calorimeter in the experimental cavern.

muons

Muons were used to measure the light yield of the Tile Calorimeter cells [23]. The results have shown that the light yild within layers was uniform. Between radial layers the results showed differences of the order of 20% resulting from using in the Tile Calorimeter polystyrene

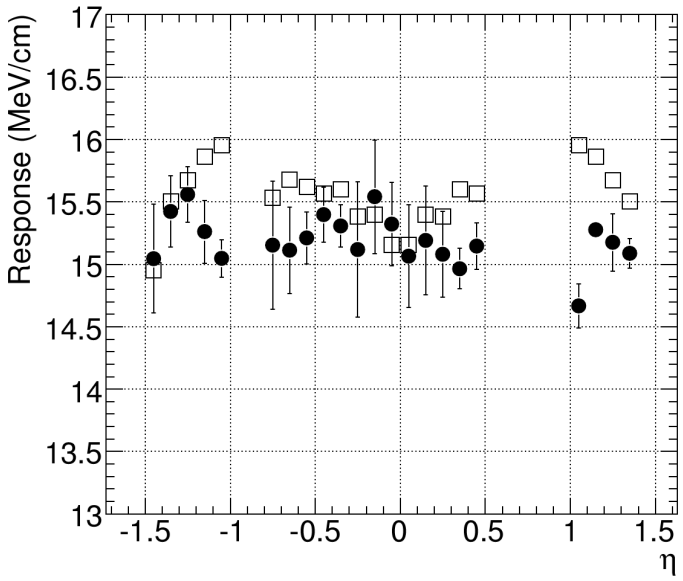

Figure 2.16: Uniformity in η of 180 GeV muons in MeV/cm. The experimental data are the filled circles • and Monte-Carlo simulation results are the open squares □ [26].

coming from two different producers. These differences have to be compensated by adjusting the photomultipliers high voltage in order to have an equalized energy scale in the whole calorimeter. A reference value of $N_{p.e.} = 70\ GeV^{-1}$ [26] is the reference value used in simulations and data reconstruction.

Muons were also used to measure the uniformity of the response of the detector cells to electromagnetic radiation. The muons fit well this purpose since they cross the whole calorimeter, leaving a signal that in good aproximation is proportional to the crossed path length. Figure 2.16 shows the uniformity in η of the muon energy divided by the crossed path lenght for 180 GeV electrons using a 2.5% event truncation on the high energy tail; the muon singnal is corrected by using the $e/\mu = 0.91$ ratio [26].

In Figure 2.17 an example of the signal and noise separation is presented for a beam incidence along $\eta = 0.35$ in the whole tower and in the D radial layer.

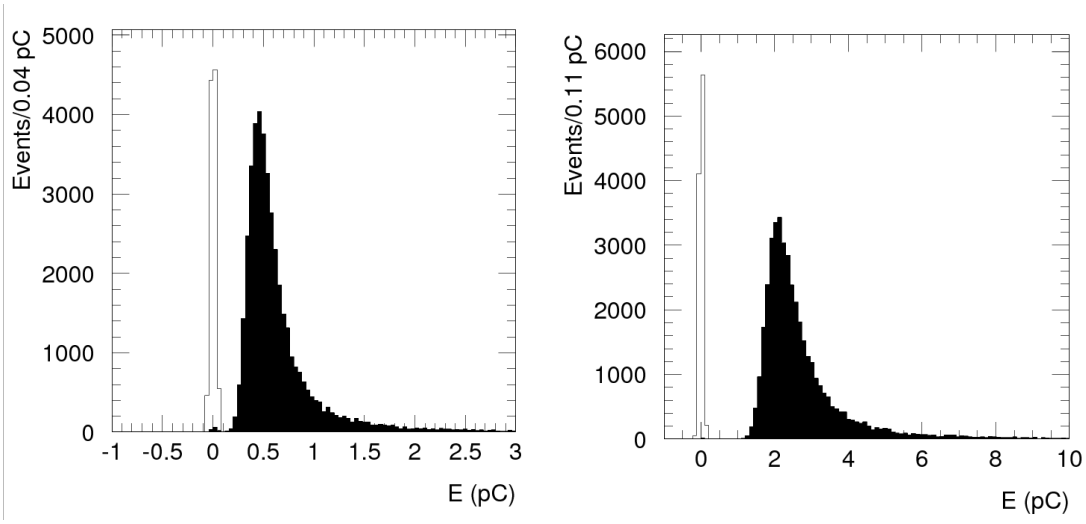

(a) D cell (b) Tower

Figure 2.17: Separation of signal and electronic noise for 180 GeV muons entering the calorimeter at $\eta = 0.35$ [26].

pions

In the standalone setup pions will set an upper limit to the energy resolution to hadrons and jets and also measure the linearity of the detector response to hadrons. The Tile Calorimeter is a non compensated detector, meaning that the response to pions is shifted from the one of electrons by a factor π/e. This is a ratio that is expected to rise slowly with pion energy.

The results for energy resolution with pion beams are summarized in Figure 2.18. These are results from pions impinging on the calorimeter at $|\eta| = 0.35$ as a function of the beam energy. The measured energy resolution is worse than the one expected and designed response for the full ATLAS detector. It should be added that in the ATLAS configuration the total calorimeter (Electromagnetic LAr + Tile calorimeter) depth is larger by about 30% and the contribution of longitudinal leakage to the energy resolution degradation is smaller. The expected constant term for jet energy resolution in ATLAS is typically 2.6%.

Figure 2.19 presents the linearity for pion beams impinging the detector for $|\eta| = 0.35$. The measurements were taken with many calorimeter modules and the response of each is normalized to the mean response at the common energy of 180 GeV. Open squares represent Geant 4.8.3 Monte Carlo simulations, with QGSP and Bertini intranuclear cascade

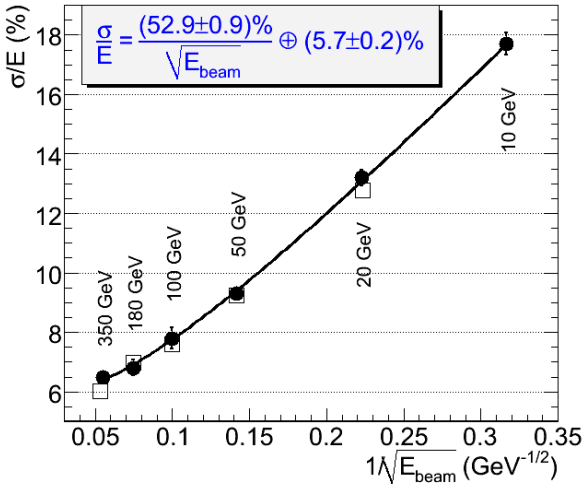

Figure 2.18: The Tile Calorimeter standalone energy resolution for pions impinging on the calorimeter at $|\eta| = 0.35$ (7.9λ), as a function of the beam energy. MC simulation results (Geant 4.8.3 QGSP+Bertini models) shown with open squares and full circles data [26].

models. The plot on the right shows the experimental data, corrected for longitudinal and transverse energy leakage, as derived from data taken in the 90° configuration and from the Geant4 MC simulation. The energy dependence is due to calorimeter non-compensation; the displayed fit uses Groom's parametrization of the non-EM component of hadronic showers with $F_h = (\frac{E_{beam}}{E_0})^{m-1}$ which represents the non-electromagnetic energy component of the showers produced by the incident pions; E_0 is the energy at which multiple pion production becomes significant; and m is an empirical parameter dependent of the calorimeter characteristics. From this analysis measurements of the $\frac{e}{h}$ ($\frac{e}{h} = 1.33 \pm 0.06 \pm 0.02$) [26] and m ($m = 0.85 \pm \pm 0.03 \pm 0.01$) [26] factors are obtained.

2.4 Performance of Tile Calorimeter in the 2004 combined testbeam

After the standalone testbeam period and prior to the installation in the experimental cavern the combioned performance of the different subsytems of the ATLAS detector was studied in a combined testbeam. In 2004 a fully instrumented slice of the ATLAS detector ($\simeq \frac{1}{16}$ of the

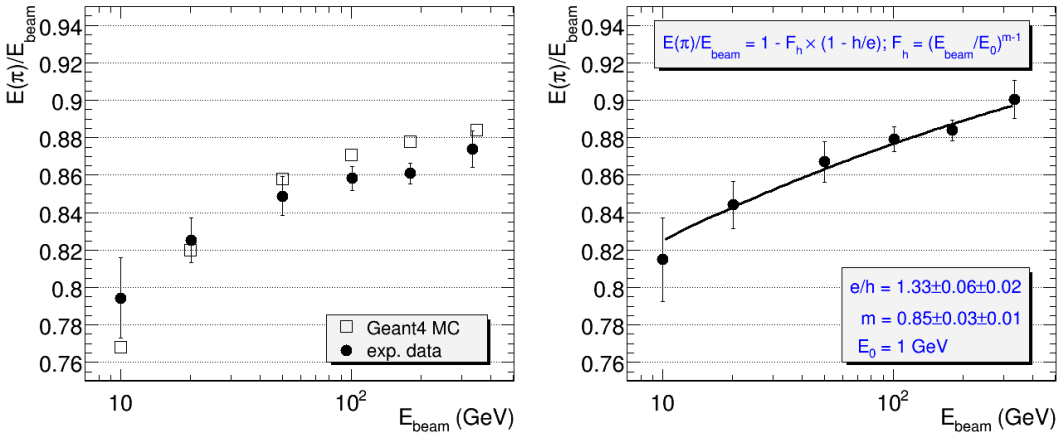

Figure 2.19: Normalized energy response plotted against the pion energy impinging the calorimeter for $|\eta| = 0.35$. Open squares represent Geant 4.8.3 Monte Carlo simulations, with QGSP and Bertini intranuclear cascade models and full circles data. In the figure on the RIGHT corrections for longitudinal and transverse leakage are introduced [26].

detector) was exposed to particle beams coming from the SPS (Super Proton Synchrotron). The combined test-beam (CTB) was accomplished in the H8 hall at CERN during several data taking periods. The sub-detectors configuration and Data Acquisition System were close to the ATLAS final configuration.

2.4.1 Experimental Setup

Beams of pions, protons and muons were produced with several energies: energies from 1 to 9 GeV called the very low-energy (VLE), and from 10 to 250 GeV, called high-energy (HE). The combined testbeam setup ((Figure 2.20) consisted on a full barrel slice of the ATLAS detector with three main systems: the inner detector from which only the TRT was fully operational, and even so for a small period of time, and the two central calorimeters, the electromagnetic (LAr) and the hadronic (Tile Calorimeter). The particle beams, after passing through the detectors that monitor the beam position and identify the particle type, first reach the Pixel and SCT modules and then continue through the TRT, calorimeters and finally the particles hit the muon chambers. Also a LVL1 trigger and DAQ system were used. The LAr and Tile Calorimeter calorimeters were on top of a movable table. This allowed the orientation of the

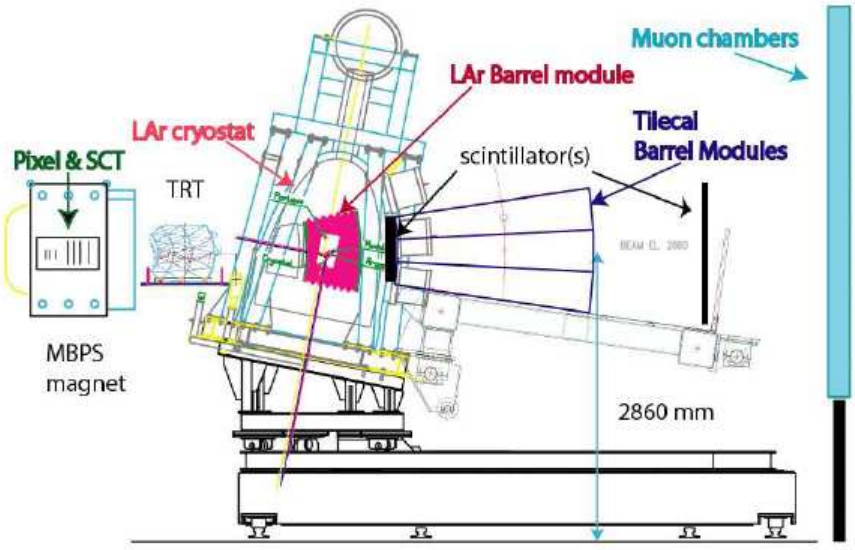

Figure 2.20: Lateral view of the sub-detectors used in the 2004 combined testbeam.

modules in a way that beam particles that enter the calorimeters are projective in pseudo-rapidity, like in the ATLAS experiment. Several components of the muon spectrometer were also present. More details of each detector can be found in [1]. The electromagnetic calorimeter was specifically built for the combined testbeam. One module of the Liquid Argon Calorimeter (LAr) was placed inside an aluminium cryostat (with 0.1 interaction lengths thickness) filled with Argon gas. The hadronic calorimeter was composed of three production barrel modules, positioned 30 cm behind the LAr calorimeter (in the ATLAS final setup this distance is of 25 cm).

2.4.2 Performance of the combined calorimeters

From the hadronic point of view, the most important results achieved from the CTB are the pion energy performance results and their comparison with the MC simulations. The following results refer to a single data taking period when all sub-detectors were operational. These results include data from pions with energies between 2 and 180 GeV. The measured mean energy and resolution for data and Monte-Carlo are shown in Figure 2.21 for $\eta = 0.45$. From these results it is seen that data is described by the Monte-Carlo within 5% in the VLE

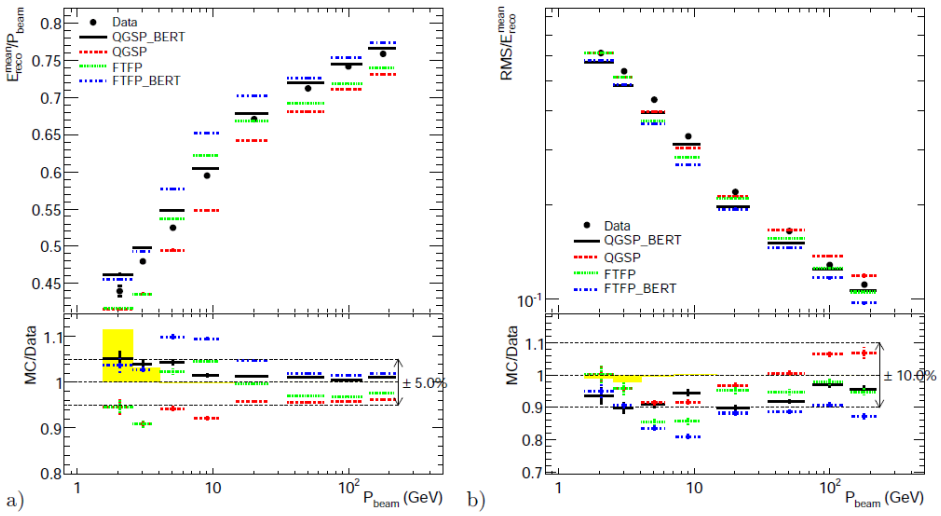

Figure 2.21: Mean energy (a) and resolution (b) for pions at beam momenta from 2 to 180 GeV are shown. Data is represented as closed points and Monte Carlo simulations as lines. Only statistical uncertainties are shown. The light band represents the uncertainty due to the cut to remove muons from pion decays.

range and within 1% for higher energies. However, the uncertainty for 2 GeV and 3 GeV due to muon contamination in the beam is large. As for the resolution it presents values from 60% at 2 GeV and about 10% at 180 GeV which are in accordance with the previous results present for the stand alone tests [27].

3 Tile Calorimeter performance and ATLAS/LHC physics

The work described in this thesis is centered on the performance of the Tile Calorimeter with cosmic ray muons. These were the only high energy particle available for a long period of time before the LHC start-up. With the start of the LHC collisions era on November 2009, it is now time for the Tile Calorimeter to face new challenges. In this chapter is presented a short overview on some channels and physical quantities of the ATLAS/LHC physics program on which the Tile Calorimeter performance plays a relevant role.

3.1 Main requirements of the Tile Calorimeter

The main functions of the Tile Calorimeter are to contribute to the energy reconstruction of jets and to provide a good measurement of the missing transverse energy. These are physical quantities that are necessary for the achievement of the main LHC physics goals. Both of them contribute to measurements in fundamental physics channels, such as the leptonic decays of the W boson where the neutrino reconstruction needs a good understanding and precision on the missing transverse energy in ATLAS or for the top mass measurement where the jet energy scale is required to be known at 1% level [10]. These quantities are also of striking importance for the discovery of new physics and in particular for the searches towards Super-Symmetric (SUSY) models where jets and the missing transverse energy are considered to be the most sensitive physical quantities.

Geometry and radiation hardness In order to resolve the physics events over a background due to pile-up and underlying event of ~21 minimum bias events per bunch crossing at nominal luminosity a fast detector with a fine granularity is required. A good hermeticity is crucial for a good performance however from construction it is known that there are:

- Cracks in the detector: there are two gaps of approximately 1 meter necessary for the passage of services for the innermost detectors i.e. the Liquid Argon calorimeter and the Inner Detector.

- Dead material: the services, the cryostat and other structural parts will compromise the uniformity of the detector.

that must be compensated. First these effects are partially compensated by the inclusion of scintillators to sample the hadronic jets (crack scintillators) and electromagnetic jets (gap scintillators).

Due to the high luminosity the detector should also have a high radiation resistance to go through, in order to tolerate a dose of XXX during the expected 10 years of operation.

Resolution and linearity The Tile Calorimeter must have a good performance in a very wide dynamic range from a few GeV, like the typical signal deposited by muons, up to several TeV from the most energetic hadronic jets. The ATLAS/LHC overall physics performance, combining the signal from all the calorimeters, requires an intrinsic resolution for jets of:

$$\frac{\Delta E}{E} = \frac{50\%}{\sqrt{E}} \oplus 3\% \qquad for\ |\eta| < 3$$

with a segmentation of $\Delta\eta \times \Delta\phi = 0.1 \times 0.1$. Testbeam measurements with high energy pions have shown very promising results for the Tile Calorimeter. The measured energy resolution for pions was [26],

$$\frac{\Delta E}{E} = \frac{(52.9 \pm 0.9)\%}{\sqrt{E_{beam}}} \oplus (5.7 \pm 0.2)\%$$

but it should be taken in consideration that this is the Tile Calorimeter standalone performance. When combining the Tile Calorimeter with the LAr calorimeter the performance is expected to

be better. It is also fundamental a linearity better that 1% in the range of energies of operation. More details are presented later in the Section 2.3 dedicated to testbeam results. For both of these two quantities it is crucial to set the detector to the correct energy scale and guarantee its uniformity.

Timing The timing of the detector is crucial for its operation, to achieve the main goals in Standard Model precision measurements and discoveries, for the search of new physics and on the trigger performance. In order to obtain the best precision on the energy and momentum reconstruction and to be efficiently used within the ATLAS trigger all detectors must be internally synchronized and also externally synchronized to the LHC clock. From the point of view of the Tile Calorimeter this means that almost 10000 channels must be synchronized to achieve the required performance.

In this thesis the Tile Calorimeter energy scale and synchronization are addressed in detail.

3.1.1 Energy scale

The energy scale of the Tile Calorimeter is primarily adjusted to reach the electromagnetic energy scale (EM scale) set at testbeam and equalized across all channels using the cesium system (vd. Section 2.2.3) to adjust the photomultipliers high voltage. This has been cross-checked using cosmic ray muons and results are presented in Section 5.7.

Non-uniformities in the electromagnetic energy scale of the calorimeter are also reflected in the jet energy scale. During the LHC operation the EM scale must be monitored using the Cesium system (Cf. Section 2.2.3) but this could also be done either using particles coming from the interaction point or cosmic ray muons. The work and analysis done to monitor the energy scale with cosmic ray muons can be extended to the isolated muons produced in the proton collisions.

Another aspect of the energy scale is that the main objects measured in a calorimeter are

jets and an energy scale for jets must be established. The Tile Calorimeter is a non-compensated calorimeter which means that:

$$\frac{e}{h} > 1$$

i.e. the response to hadrons is smaller than the response to electrons. The energy scale for jets must include correction due to the non-compensation besides the corrections for dead material, cracks, differences in energy loss of particles. This is done using a set of calibration weights that can be calculated using two methodologies: the Local Energy Calibration [28] or the Global Energy Calibration [10].

3.1.2 Tile Calorimeter Synchronization

The Tile Calorimeter channels synchronization was achieved using the laser system [29], cosmic ray muons (work reported in Chapter 6) and muons from single beam data [30] and follows three stages: intra-module, inter-module and inter-partition synchronization. For the synchronization with LHC it is still necessary to correct for the different distances of the calorimeter cells to the interaction point (IP). This is done prior to the data taking by setting all channels to 0 ns for particles travelling with the speed of light and coming from the interaction point. For example muons with an energy of 300 MeV is already $0.9 \times c$.

Time has a direct effect on the energy reconstruction of the physics signal that is done in the Tile Calorimeter. Due to the operation requirements the optimal filter algorithm, is only able to make one iteration for the energy reconstruction of the calorimeter signal. In addition, the optimal filter needs a set of coefficients that depend on the time offsets of each channel relatively to the reference value. So these time offsets must be known in order to have the best precision in the energy measurement, to achieve the required precision in the jet energy scale, and a synchronization is important for the trigger operation but also for the detection of particles for which the most evident signal is a delayed response like the stable massive particles which are the subject of Section 3.2.4.

In Figure 3.1(a) the online precision of the optimal filter $\frac{E_{online}-E_{offline}}{E_{offline}}$ is plotted against the channel time using data from collisions with $\sqrt{s} = 900\ GeV$. In the plotted data are shown

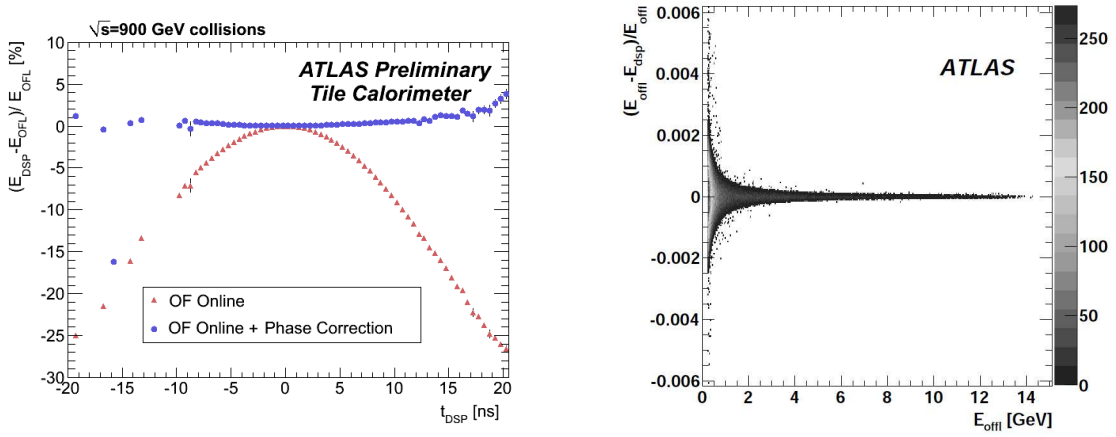

(a) Online energy reconstruction versus channel time

(b) Online reconstruction precision at the DSPs: $E_{offline} - E_{online}/E_{offline}$

Figure 3.1: Precision of the online reconstruction with the optimal filter algorithm [18].

the online reconstruction with the optimal filter, the filled triangle (▲), and for the online reconstruction including a phase correction, the filled circle (●). It is seen that the OF precision is degraded as the time offset increases, however up to an offset of 10 ns a precision of 1% can still be obtained. The online measurement also has a limited numerical precision. This is shown in Figure 3.1(b) where the energy calculated online and offline without iterations are compared for a charge injection run. This quantity increases considerably as the energy decreases but the maximum shift it is of the order of 0.6 %. The online reconstruction done at the DSP on the RODs has already a very good precision.

3.2 Contribution to Physics studies

3.2.1 Rejection of non-collision backgrounds and jet selection

Event selection in the LHC means to make sure that the data that are analysed come from a proton-proton inelastic collision. The main backgrounds are the collisions of protons with the residual beam gas, muons and pions travelling in the beam halo as well as cosmic ray muons. One of the used quantities during 2010 to discriminate between collisions and other type of events is the agreement in time of the MBTS (read out in FEE of the Tile Calorimeter) and LAr

calorimeter. As already detailed in the ATLAS detector description in Chapter 1.2 the MBTS are two sets of scintillators symmetrically assembled relatively to the interaction point (IP). Particles from the IP should be within some coincidence window contrary to other particles for which a large time difference is expected. For the LAr calorimeter an average over the time of all cells is considered. In studies performed in 2010, for cleaning missing transverse energy and jets events [10], time requirements for the difference in time between the A side and the C side, $|\Delta t_{LArEC}| < 5\ ns$ and $|\Delta t_{MBTS}| < 10\ ns$ are used to reject the background. This time selection is applied in addition to the identification of a primary vertex. All combined, a level of less 0.01% of beam background is found in the data samples.

For the jet selection a loose jet time cut is applied. Jets are required to have an energy-square-weighted cell time to be within two beam bunch crossings i.e.

$$|t_{jet}| = |\frac{1}{\sum_{jetcells} E_j^2} \sum_{jetcells} \frac{t_j E_j^2}{|} > 50\ ns$$

However the $|t_{jet}|$ cut is only applied after the rejection of fake jets produced by noise bursts in the LAr calorimeter. The result after this quality cuts is in Figure 3.2, with the jet time measured for all the jet candidates. Only one event appears out of the time window presented above being most part of the events within one bunch crossing (25 ns).

3.2.2 Fake missing E_T

In the LHC the p-p collisions are now working with a center of mass energy of 7 TeV. Since protons are not elementary particles, the interactions will occur between its constituents or partons: gluons and quarks. The effective center of mass energy is distributed among the different partons. The resulting events are produced with an wide array of energies and momentum. Since the protons, and so the quarks and gluons, do not have a transverse component the conservation of momentum in the transverse plane for the inelastic collisions is used. The conservation of the momentum in the transverse plane means that all the produced particles are collected, with their energy and/or momentum measured including the necessary corrections due to dead material, cracks and still muons that escape the detector

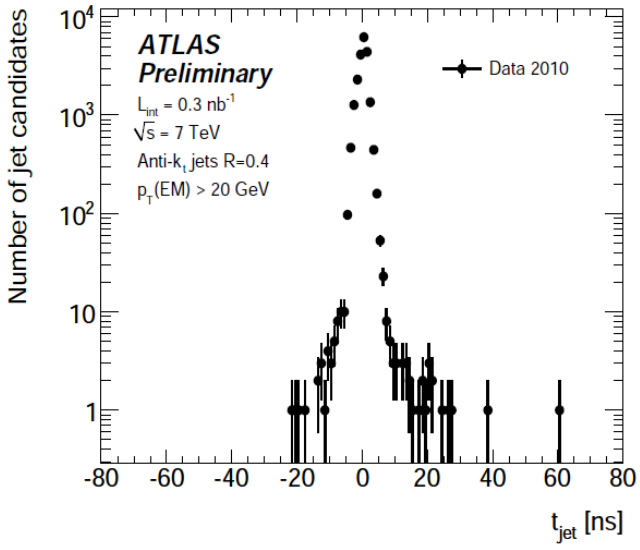

Figure 3.2: Jet time after rejection of fake jets due to noise burst in LAr calorimeter.

volume, then the components of the missing energy in the transverse plane must be canceled:

$$\sum_{allparticles} p_T = 0$$

There are many events for which particles that do not interact with any of the detecting systems are produced. This is the case of the decays of the charged electroweak bosons $W^{\pm}$ in their leptonic channel decay to a lepton and a neutrino. In this case there will be a $E^{miss}_{x(y)} \neq 0$. The missing transverse energy must be measured with a good precision to achieve the Monte-Carlo simulations predictions for these kind of channels. There are other channels for which the missing energy is of the most importance such as any channel in Super-Symmetric models that are expected to have a large missing energy.

In ATLAS the missing transverse energy [10] is calculate by the sum of several terms,

$$E^{miss}_{x(y)} = E^{miss,calo}_{x(y)} + E^{miss,cryo}_{x(y)} + E^{miss,\mu}_{x(y)}$$

where $E^{miss,calo}_{x(y)}$ are the energy measurements in the calorimeters, $E^{miss,cryo}_{x(y)}$ the corrections due to the cryostat and $E^{miss,\mu}_{x(y)}$ the contribution from the muons flying out to the muon chambers.

The missing transverse energy is then defined for each coordinate in the plane xy:

$$E_x^{miss,calo} = -\sum_{i=1}^{N_{cell}} E_i sin\theta_i cos\phi_i$$

$$E_y^{miss,calo} = -\sum_{i=1}^{N_{cell}} E_i sin\theta_i sin\phi_i$$

resulting in

$$E_T^{miss,calo} = \sqrt{(E_x^{miss,calo})^2 + (E_y^{miss,calo})^2}$$

The contribution of muons is given by

$$E_{x(y)}^{miss,\mu} = -\sum_{selectedmuons} E_{x(y)}^{\mu}$$

and its application depends if the muon is isolated or not. The main objective is to avoid a double account of the muon contribution. For an isolated muon when calculating the calorimeter $E_T^{miss,calo}$ the cell crossed by the muon is not included and only the combined muon is included. The combined muon combines the signal from the muons spectrometer, the inner detector and the calorimeters for energy loss corrections. If the muon is not isolated then the combined measurement minus the parametrized energy loss is

For the energy losses in the cryostat a correction must be included given by:

$$E_{x(y)}^{miss,cryo} = -\sum_{jets} E_{x(y)}^{jet,cryo}$$

with,

$$E_x^{jet,cryo} = w^{cryo} \sqrt{E_{EM3}^{jet} \times E_{HAD1}^{jet}} \cdot \frac{cos\phi_{jet}}{cosh\eta_{jet}}$$

$$E_y^{jet,cryo} = w^{cryo} \sqrt{E_{EM3}^{jet} \times E_{HAD1}^{jet}} \cdot \frac{sin\phi_{jet}}{cosh\eta_{jet}}$$

where w^{cryo} is a calibration factor, E_{EM3} and E_{HAD1} are the energies in jets deposited on the third layer of the electromagnetic calorimeter and in the first layer of the hadronic calorimeter.

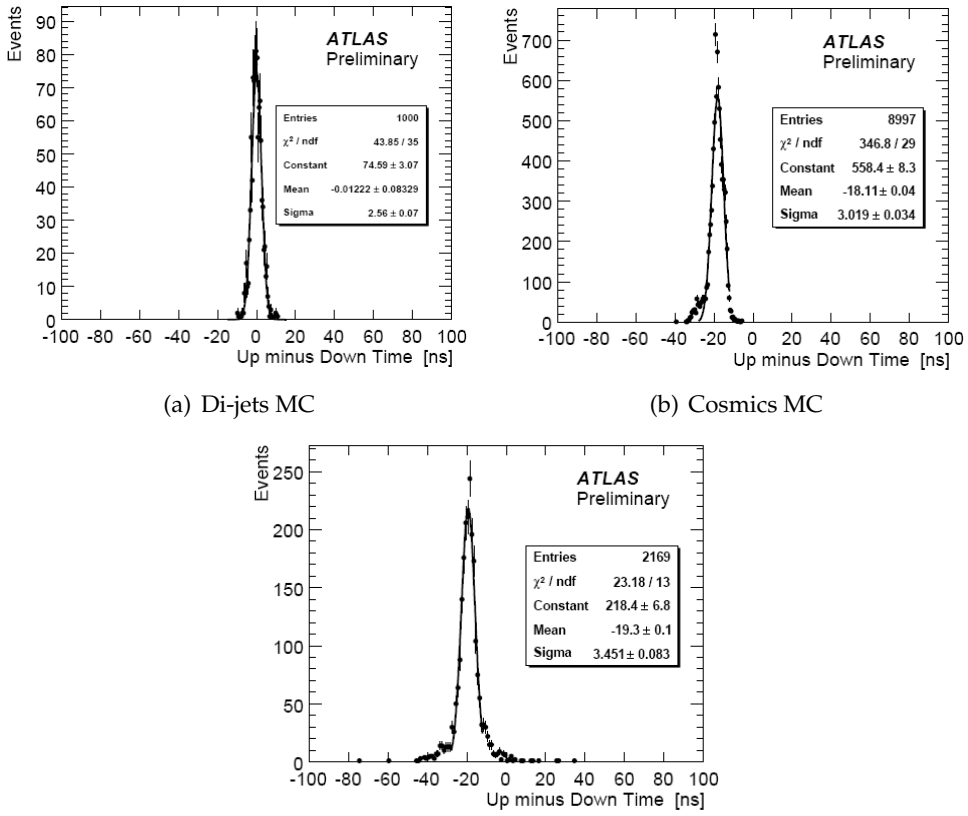

(a) Di-jets MC

(b) Cosmics MC

(c) Cosmics Data

Figure 3.3: Difference between the cell time of modules on the top ($y > 0$) and modules on the bottom ($y < 0$) for (a) di-jets MC (b) cosmics MC and (c) cosmics data [31].

Within an event a large quantity of effects can damage an energy measurement and so the missing energy calculation: dead channels, noisy channels, energy deposits from particles not originating in the interaction point.

The last one could result for example from cosmic ray muons, halo muons, cavern backgrounds etc. Measurements not coming from the interaction point will have a time pattern within the detector different from the ones coming from the interaction point. For this reason the time associated with this measurement can be rejected using the time variable.

Cosmic muons were used for a long period in the commissioning of the ATLAS detector. The cosmic ray muons reaching the ATLAS detector are characterized by a trajectory with a well defined direction. The muon will enter the top of the detector and having enough energy

will come out at its bottom. The time in the ATLAS detector is synchronized for particles coming from the ATLAS interaction point which means that the time difference between the particles is close to zero such as for the di-jets of Figure 3.3(a). Cosmic ray muons will however have a time difference not equal to zero but related to the time of flight between the hits in the different parts of the detector. In Figure 3.3(b) and Figure 3.3(c) are presented the results for the time difference in cosmic ray muons Monte-Carlo and data measured in the Tile Calorimeter. An averaged difference of 20 ns is measured that corresponds to the time of flight of the relativistic muons crossing the calorimeter. This characteristic can be used to reject this event.

3.2.3 Lepton isolation in $H \rightarrow ZZ^{(*)} \rightarrow 4l$

The Higgs boson discovery and the measurement of its properties is the main goal of the LHC experiments. The Higgs boson decay to four leptons (electrons and muons) $H \rightarrow ZZ^{(*)} \rightarrow 4l$ is the cleanest signature for the discovery of the Higgs boson. The most relevant backgrounds are the irreducible $ZZ \rightarrow 4l$, the $Zb\bar{b} \rightarrow 4l$ and the $t\bar{t} \rightarrow 4l$. Their importance depend on the Higgs mass. The limits to the Higgs boson mass (M_H) comes from:

- Direct searches:
  - In the e^+e^- collider LEP a lower bound of $M_H > 114.4\ GeV$[9] is set.
  - In $p\bar{p}$ collider TEVATRON a produced an exclusion for masses in the range $163\ GeV < M_H < 166\ GeV$ with a 95% confidence level, but new results from this year already exclude a wider mass region from 158 GeV to 175 GeV. [8].
- Indirect searches at LEP [4]
  - Using high precision electroweak data, sensitive to loop corrections, constrain the Higgs mass to $M_H < 157 GeV$ with a 95% confidence level limit.

For Higgs boson masses between 120-150 GeV one of the Z bosons is produced off-shell resulting in leptons with low transverse momentum. In this region the backgrounds from the heavy quarks (t,b) decays to leptons will be dominant. The hadronic channels have huge

cross sections (Table 3.3), more than 10 times the value for Higgs boson channel (Table 3.2). It is expected that the leptons in Z bosons decays are more isolated than the leptons produced in the heavy quarks decays [1], and for this reason lepton isolation with the calorimeter is important to discriminate between the events.

Expected performance of ATLAS with $H \rightarrow ZZ \rightarrow 4l$

In this section a brief look of the expected performance of the ATLAS detector for the Higgs boson decay to four leptons channel is presented. The focus is on the isolation of muons in the calorimeter, however results for electrons as well as for tracking are presented for comparison and completeness. These results refer to p-p collision at $\sqrt{s} = 14\ TeV$ [10].

For the muon isolation both calorimeter and track criteria are defined. The calorimeter isolation is defined as the sum of the transverse energy deposited inside a cone with a radius $\Delta R = \sqrt{\Delta\eta^2 + \Delta\phi^2}$ around the muon and subtracting the muon energy loss from a cone with $\Delta R = 0.05$ (isolation cone). The isolation cone energy of the least isolated muons is used as discriminant. The track isolation follows a similar procedure. Muons must satisfy the track isolation cut:

$$\frac{\sum_{\Delta R<0.2-muon} p_T}{p_T^{muon}} < 0.15$$

and the calorimeter isolation cut:

$$\frac{\sum_{\Delta R<0.2-muon} E_T}{E_T^{muon}} < 0.23\ .$$

An electron is isolated in the calorimeter if contained in a cone of $\Delta R = 0.2$. Electron track isolation is the same used for muons requiring still one hit in the b-layer to reject the electrons resulting from conversion of bremsstrahlung photons. Electrons must satisfy the track isolation cut defined by:

$$\frac{\sum_{\Delta R<0.2-electron} p_T}{p_T^{electron}} < 0.15$$

[1] Besides the leptons from **b** and **c** quarks come from secondary vertexes and not the interaction point

Event Preselection
Four leptons (Loose Electrons or muons) with $p_T > 7$ GeV and $\|\eta\| < 2.5$ and at least two with $p_T > 20$ GeV

Event Selection	
Kinematic Cuts	– Lepton quality: 2 pairs of same lepton flavour with opposite charges. – Electrons must be Medium Electrons satisfying the CaloIso criterion. – For H masses of 200 GeV and higher, four Loose Electrons are required instead. – Z, Z^* and Higgs boson reconstruction require a single quadruplet with: $\|m_{ll1} - m_Z\| < \Delta m_{12} GeV$ $m_{ll2} > m_{34}$.
Isolation and Vertexing cuts	– Muon Calorimeter isolation: $\sum E_T/E_T < 0.23$. – Lepton Inner detector track isolation: $\sum p_T/p_T < 0.15$. – Cut on maximum lepton impact parameter: $d_0/\sigma_{d_0} < 3.5$ for muons $d_0/\sigma_{d_0} < 6.0$ for electrons.

Table 3.1: Selection cuts for the Higgs boson decay to four leptons. The m_{12} defines a mass window for the first pair of leptons match with the Z boson nominal mass. The m_{34} is the minimum mass required for the second Z boson for Higgs boson masses up to 200 GeV. For higher Higgs boson masses an equivalent mass window for the second lepton pair is applied [10].

The lepton selection works in three stages. In the first stage all leptons within $|\eta| < 2.5$ and $E_T > 5\ GeV$ for electrons and $p_T > 5\ GeV$ for muons are selected. Then the second stage is the preselection described in Table 3.1. The third stage is the event selection which is divided in Kinematic and Isolation and Vertexing cuts. So isolation only is applied in a very late stage of the event selection.

In Table 3.4 is presented the fraction of events from the signal that pass each selection

Process	$\sigma_{LO} \cdot BR$ [fb]	$\sigma_{NLO} \cdot BR$ [fb]
$H[120] \to 4l$	1.68	2.81
$H[130] \to 4l$	3.76	6.25
$H[140] \to 4l$	5.81	9.72
$H[150] \to 4l$	6.37	10.56

Table 3.2: Higgs boson to four leptons decay leading order and next to leading order cross sections for different Higgs boson masses ($l = e, \mu$) [10].

Process	$\sigma \cdot BR$ [fb]	Corrections [fb]
$q\bar{q} \to ZZ \to 4l$	158.8	+47.64
$gg \to Zb\bar{b} \to 2lb\bar{b}$	52030	+8640 ($q\bar{q} \to Zb\bar{b}$)
$gg \to Zb\bar{b} \to 2lb\bar{b}$	52030	+8640 ($q\bar{q} \to Zb\bar{b}$)
$gg, q\bar{q} \to t\bar{t}$	833000	—
$q\bar{q} \to WZ$	26500	—
$q\bar{q} \to Zinclusive$	1.5×10^6	—

Table 3.3: Backgrounds to the Higgs to four leptons decay cross sections. Corrections are introduced as a compensation for diagrams not included in used generators [10].

Selection cut	Selection step	Higgs		
		$4e$	4μ	$2e2\mu$
Trigger selection	1	94.7	95.3	95.7
Lepton preselection	2	57.0	73.8	66.8
Lepton quality and pT	3	24.7	60.5	39.7
Z's mass cuts	4	17.1	42.9	27.6
Calo Isolation	5	17.1	39.5	25.4
Tracker Isolation	6	16.5	38.1	24.7
IP cut	7	15.1	36.5	23.2
H Mass cut	8	12.5 ± 0.3	31.4 ± 0.5	19.2 ± 0.4

Table 3.4: Fraction of signal events (%) for each selection cut and for a Higgs mass of 130 GeV [10].

Selection		ZZ			$Zb\bar{b}$	
step	$4e$	4μ	$2e2\mu$	$4e$	4μ	$2e2\mu$
1	96.6	96.6	96.6	91.4	91.4	91.4
2	13.8	17.6	31.4	2.6	9.4	12.0
3	7.3	16.0	21.9	$1.1 \cdot 10^{-1}$	2.1	1.7
4	6.9	14.8	20.2	$4.7 \cdot 10^{-2}$	1.1	$8.4 \cdot 10^{-1}$
5	6.9	13.9	19.5	$4.7 \cdot 10^{-2}$	$8.5 \cdot 10^{-2}$	$1.2 \cdot 10^{-1}$
6	6.8	13.6	19.2	$1.3 \cdot 10^{-2}$	$3.3 \cdot 10^{-2}$	$4.4 \cdot 10^{-2}$
7	6.2	13.0	17.8	$5.6 \cdot 10^{-3}$	$1.1 \cdot 10^{-2}$	$1.8 \cdot 10^{-2}$
8	$5.2 \cdot 10^{-2}$	$11.3 \cdot 10^{-2}$	$12.0 \cdot 10^{-2}$	$5.2 \cdot 10^{-2}$	$11.3 \cdot 10^{-2}$	$12.0 \cdot 10^{-2}$

Selection	$t\bar{t}$		
step	$4e$	4μ	$2e2\mu$
1	75.1	75.1	75.1
2	1.0	4.7	10.1
3	$6.8 \cdot 10^{-3}$	$7.3 \cdot 10^{-1}$	$5.8 \cdot 10^{-1}$
4	$1.6 \cdot 10^{-3}$	$2.0 \cdot 10^{-1}$	$1.0 \cdot 10^{-1}$
5	$1.6 \cdot 10^{-3}$	$1.6 \cdot 10^{-3}$	$5.4 \cdot 10^{-3}$
6	$2.6 \cdot 10^{-4}$	$2.5 \cdot 10^{-4}$	$1.0 \cdot 10^{-3}$
7	$2.6 \cdot 10^{-4}$	$< 6 \cdot 10^{-4}$	$2.6 \cdot 10^{-4}$
8	$< 6 \cdot 10^{-4}$	$< 6 \cdot 10^{-4}$	$< 6 \cdot 10^{-4}$

Table 3.5: Fraction of events (%) for backgrounds processes for each selection cuts and for a Higgs mass of 130 GeV [10].

cut for a Higgs boson mass of 130 GeV. The most promising channels for a measurement are the ones in which muons participate, which have overall higher efficiencies, of about 30% for the 4μ channel and 20% for the $2e2\mu$ channel. However these are also the ones where the calorimeter isolation contributes to decrease the efficiency of the measurement in about 3%. For the $4e$ channel the calorimeter isolation has no effect.

Table 3.5 presents the efficiency for the rejection of the three main backgrounds refered in the beginning of this section. As before the calorimeter isolation does not play a role in the decays to electrons. However for muons the effect can be considerably large and of about 2 orders of magnitude. The rejection efficiency is larger if the 4 leptons are muons.

3.2.4 Stable massive particles

The LHC is producing collisions with a center of mass energy higher than any other accelerator and expectations are on the new physics that can appear from this scenario. There are several physics models that go beyond the standard model and are very well motivated giving

response to some of the open questions appearing within the Standard Model. Some of these questions are:

- What is(are) the source(s) of dark matter ? In here the R-parity conservation is the main requirement. In SuSy models are permited couplings where there is no conservation of the leptonic or baryonic numbers and for that reason a quantity defined as

$$R = -1^{2j+3B+l}$$

  with j the spin, B the baryonic number abd l the leptonic number. R is -1 for SuSy decays, but 1 for Standard Model decays. So imposing R-parity conservation implies that the least super symmetric particle will not decay or interact with the standard model particles and for that reason can be a candidate for dark matter.

- Why does the electroweak scale (100 GeV) is so below the unification scale ($\sim 10^{18}$ GeV) where all forces should be unified - Hierarchy problem ? The question is not only the gap in energy scales it is also a problem with the calculations of high order terms e.g. the Higgs boson mass, where the unification scale enters and can extreemly shift the theorethical predictions.

- Are there only three generations of elementary particles ? Or other way to write the same question is: Why three? The LEP results have showed that at the EW scale there are only three leptonic families. The LHC is going to look at very high energies where other particles, and resonances can appear. Wether the leptonic and quark families will also be enlarged with this increase in energy is something that cannot be predicted.

One of the implications of these models is the appearance of several new particles and in particular stable massive particles [33] (SMPs) that can be directly detected within the LHC experiments. A much broader definition is used to describe these particles saying that they are very heavy particles (hundreds of GeV) that will not decay during their trajectory within the detector volume and will be detected by their strong and electromagnetic interactions with matter. Taking in account their large mass Having a very large mass of the order of

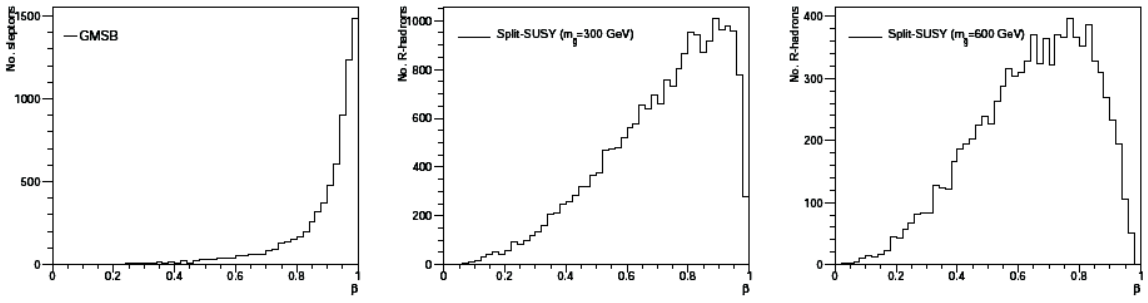

Figure 3.4: Velocities (β) for different predicted SMPs in Super-Symmetric models.

hundreds of GeV and the production spectra of momenta, these particles can be identified by their main characteristic that is having a speed below the speed of light. For this the timing of the detector is crucial. This is also a very important aspect that turns the search of stable massive particles to be model independent. In Figure 3.4 the expected velocities for particles in SuSy models are presented. Many of these particles are also characterized by producing in the detector a signal similar to the one observed for high energy muons and here the response to muons and energy scale are the important terms. Summarizing a clear understanding of the detectors response with muons as well as of the detector timing characteristics are important for the detection of these particles.

Detection of stable massive particles

The expected SMPs are of three general types:

Type I : Charged particles that can leave signals in the inner trackers, calorimeters and outer trackers;

Type II : Neutral particles that are converted to charged particles when interacting in the calorimeters and still be seen by the muon spectrometer;

Type III : Neutral particles that would only produce a signal in the calorimeters;

The most striking characteristic of SMPs is that they travel at velocities slower than the speed of light $\beta = \frac{v}{c} < 1$. To measure its properties the ATLAS detector must combine the information of different subsystems. In order to have a mass measurement the velocity and

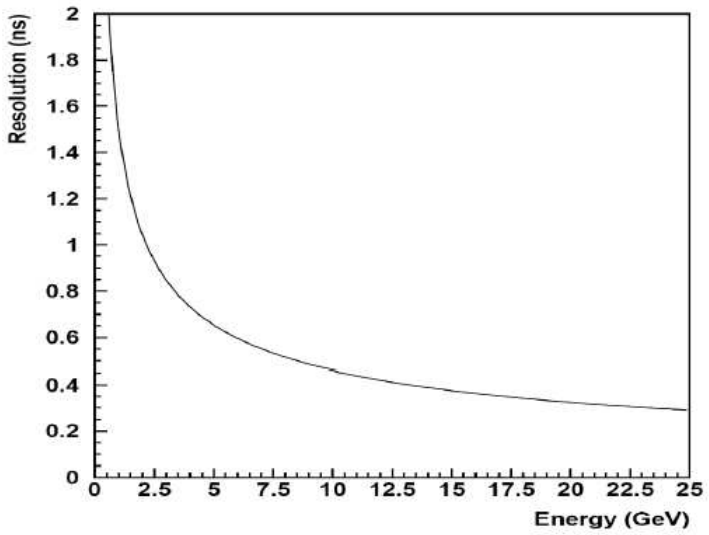

Figure 3.5: Timing resolution from testbeam data for cell A-6.

momentum of the particle must be obtained. The velocity measurement relies in a time delay measurement. The momentum measurement relies in having a charged particle that produces a signal in the tracking systems. So for a particle of Type III the measurement of mass is not possible and only a lower bound can be established.

The efficiency to detect this kind of particles will depend on their velocity β and on the η region. For the same velocity the equivalent time of flight increases with the value of η and consequently the easier will be to distinguish a SMP from events with particles with $\beta \simeq 1$. In testbeam it was measured that the precision of the time measurement in a channel depends on the energy deposited. For energies above 1.5 GeV a time resolution better that 1.2 ns is obtained in a Tile Calorimeter single cell (A-6 that has an $\eta = 0.55$) [32] as shown in Figure 3.5.

Measuring the mass of a stable massive particle

The following discussion is perfectly general. However some comments will be set around the Tile Calorimeter but that could be extended to any other sub-detectors of ATLAS. The reconstructed time t_{reco}, the time measured by the reconstruction algorithm, of a particle

produced in the interaction point can be represented by the following expression [35]

$$t_{reco} = t_{true} - \frac{d_{cell}}{c}$$

where

c is the speed of light

d_{cell} distance between the center of the cell and the interaction point

t_{true} is the time a particle took to travel from the interaction point to a cell

Particles travelling close to the speed of light will have an average reconstructed time $t_{reco} \sim 0$ ns and with a width that combines the precision of the time measurement and the cell dimensions. For example in the Tile Calorimeter the D cells of the long barrel are very large and bigger errors in the time of an event are expected in comparison to the A cells. For particles travelling slower than the speed of light will have an average time $t_{reco} > 0$ ns.

From the definition of the particle speed β_{cell} combined with the previous relation between t_{true} and t_{reco} it is obtained the velocity of the particle reaching a cell:

$$\beta_{cell} = \frac{v}{c} = \frac{d_{cell}}{t_{true} \cdot c} = \frac{d_{cell}}{t_{reco} \cdot c + d_{cell}}$$

For $t_{reco} = 0$ the value $\beta_{cell} = 1$ is obtained as required.

To obtain the particle mass the particle momentum must be measured. From relativistic kinematics a simple relation is established between the particle mass m, the momentum p and its velocity β:

$$\gamma \cdot \beta \cdot m = p$$

where

$$\gamma = \frac{1}{\sqrt{1-\beta^2}} \,.$$

Collider	Bunch crossing
LEP	25 μs
HERA	96 ns
TEVATRON	396 ns
LHC	25 ns

Table 3.6: Bunch crossing times for some colliders.

The mass results from the combination of the speed and momentum measurement

$$m = p \cdot \frac{\sqrt{1-\beta^2}}{\beta}$$

The energy loss in the calorimeter can be used to isolate these particles and also to contribute to the momentum measurement in the muon spectrometer. The uncertanty of the measurement considering only the direct contributions of time-of-flight (or velocity) and the momentum is given by:

$$\left(\frac{\Delta m}{m}\right)^2 = \left(\frac{\Delta p}{p}\right)^2 + \left(\gamma^2 \frac{\Delta \beta}{\beta}\right)^2$$

noticing also that velocity and time-of-flight uncertanties have the same value since the former is calculated using the latter:

$$\frac{\Delta \beta}{\beta} = \frac{\Delta t}{t}$$

Not considering the momentum contribution, for a typical timing resolution of 1 ns and considering particles with a velocity range $0.2 < \beta < 0.8$, traveling over a distance of approximately 3 m the mass uncertainty varies between 2% and 23%.

SMPs at the LHC

The LHC will allow the searches for SMPs to masses up to several TeV which is an increase of one order of magnitude higher relatively to earlier colliders. In the LHC the time between collisions is of 25 ns, which poses limitations to the measurement of slow moving particles within the bunch crossing time. In Table 3.6 a comparison is made between the LHC bunch crossing and the one from other colliders. The short bunch crossing implies that the SMPs must be triggered or detected within a 25 ns window. Later arrival would imply triggering

or detection in the next time window and possibly mixed up with another event. In the LHC operation between bunches with protons are also planned empty bunches. In these event sobreposition is not an issue, but event information loss is e.g. the calorimeter and track measurements stay in the last bunch and the the muon spectrometer measurements triggers the event in the current bunch.

The muon spectrometer is the natural detector for the triggering and characterization of the SMPs. They have a good time resolution, measure the momentum and charge of the SMPs.

In ATLAS the muon spectrometer extends up to 10 m and to reconstruct the track of SMP within the time window of 25 ns limits the the velocity of the particle to $\beta \geq 0.5$. There are other factors that can also degrade the signal for a SMP like the sampling time and the reconstruction software that are tuned for particels traveling at the speed of light.

Calorimeters can still play an important role in their characterization distingushing between hadronic and leptonic SMPs, provide additonal dE/dx information as well as aditional time information. Specif triggers based on the visble energy, or jet multiplicities may also be used to select events. It should also be added that for Type III SMPs the calorimeters might be the unique detecion device.

There is already within the second level trigger a selection tool [34] to produce a preliminary selection of heavy long lived particles, using the Resistive Plate Chambers (RPC) in the barrel of the muon spectrometer. Event filter algorithms the final stage for selection of events were being developed and are already included in the data taking.

4 Commissioning of the Tile Calorimeter

The Tile Calorimeter was the first detector to take data in the ATLAS pit. This was in 2005 when the first cosmic ray muons were measured by the Tile Calorimeter. Since then and until the LHC start-up of the p-o collisions in 2009, the Tile Calorimeter was using its calibration tools and physics data from cosmic muons and single beam (October 2008 and November 2009) to prepare for collisions. Later, when the other sub-systems started with their installation in the ATLAS pit, dedicated periods, called 'Milestone Weeks', worked as integration periods during standard physics runs, using a common trigger and with the full data acquisition architecture of the ATLAS detector. These integration weeks were fundamental to have a full working chain of the detector, DAQ, data processing and analysis and to achieve the widely announced results for the 1970's mesons (π^o, ρ, J/ψ, etc.) now measured in a detector of the LHC era. In this chapter an overview of this period is given, but centered on the Tile Calorimeter, and in the next two chapters dedicated studies on the energy scale, uniformity (Chapter 5) and timing (Chapter 6) of the Tile Calorimeter using cosmic ray muons are presented.

4.1 Installation in the pit and detection of first cosmic ray muons

The assembly of the Tile Calorimeter has started long before lowering the first modules into the ATLAS pit. Two of the three cylinders, the barrel and one extended barrel, were fully assembled on the surface to prepare for the final assembly in the ATLAS pit. These preparations consisted in: test and certification of tools and support, deformation measurements, confirmation of shims [1] dimensions, load tests such as of the LAr

[1] Shims are small metallic plates that are positioned between modules and are necessary to obtain the final cylindrical configuration.

electromagnetic calorimeter weight. The milestones of these pre-assembly tests on the surface are listed on Table 4.1. The pre-assembly was fundamental to have a fast and smooth assembly

	Assembly		Disassembling
	Start	End	End
EBC	11 Nov. 2002	14 Apr. 2003	12 Jun. 2003
LB	7 Jul. 2003	30 Oct. 2003	12 Feb. 2004

Table 4.1: Milestones of the Tile Calorimeter pre-assembly tests on the surface.

of the Tile Calorimeter cylinders in the ATLAS pit. Later, after the start of the assembly in the ATLAS pit of the long barrel, the EBA cylinder was pre-assembled on the surface but only up to 24 modules which was enough to make a final LAr load test.

On February 4^{th}, 2004 the first fully instrumented modules (i.e., with optics and all the certified front-end electronics inserted inside each module) are lowered into the pit. The start of the central barrel (LBA and LBC) assembly was determined by lowering, over a cradle, 8 pre-assembled modules on March 1st, 2004. Figure 4.1 the first 8 modules over the cradle already in the pit of ATLAS cavern waiting for the start of the final assembly.

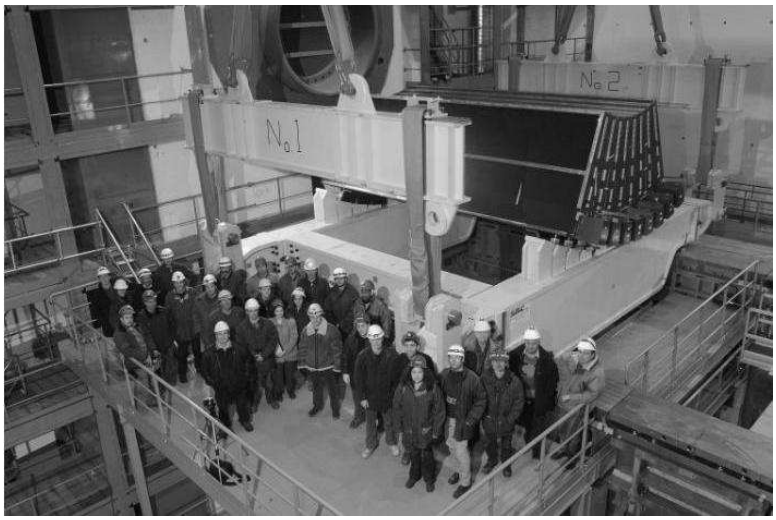

Figure 4.1: The start of the assembly in the ATLAS cavern on March 1st, 2004. The first 8 modules, pre-assembled on the surface, on a cradle.

The assembly of the three cylinders in the ATLAS pit took place between 2004 and 2006 as summarized in Table 4.2.

	End of assembly
Central Barrel	December 2004
Extended Barrel C	February 2006
Extended Barrel A	May 2006

Table 4.2: Milestones of the Tile Calorimeter assembly in the ATLAS cavern.

During the commissioning, services installation such as the cabling necessary to power the detectors, transport the signal from detectors to the trigger systems and to the racks where the read-out-drivers are installed and the online signal reconstruction is done as well as the installation of the different cooling systems needed for the detectors operation. Different tests were done to the different installed services such as:

- Measure the conductivity of the HV power supply cabling to guarantee there was no broken or damaged cables.
- Measure the the light loss in the readout and trigger optical fibers (Section 4.3).
- Flux tests of the cooling systems, leakages detection etc.

In the early stage of the commissioning, during the installation of the sub-systems, the already functional parts of the detector were on operation, following their necessities and assemblage progression, mostly in a standalone mode using their specific tools to evaluate the status of the newly assembled elements. For the Tile Calorimeter the monitoring and calibration tools, CIS, Laser and Cesium, described in the previous chapter were used for this purpose.

On June 21st, 2005 at 18h30 the first cosmic muon was recorded by the ATLAS barrel Tile Calorimeter. In Figure 4.2 the event display of this important achievement is presented. This was the start-up of the commissioning phase with cosmic ray muons. At that time a standalone trigger had to be developed that used the Tile Calorimeter level 1 trigger towers to select events. Due to its success, it was used until the end of the commissioning with cosmic muons. A detailed description of this trigger system is given in Section 4.2. Finally at the end of 2006 the first run combining sub-systems in the ATLAS cavern took place with the Tile Calorimeter and the Liquid Argon electromagnetic calorimeter. Following this first

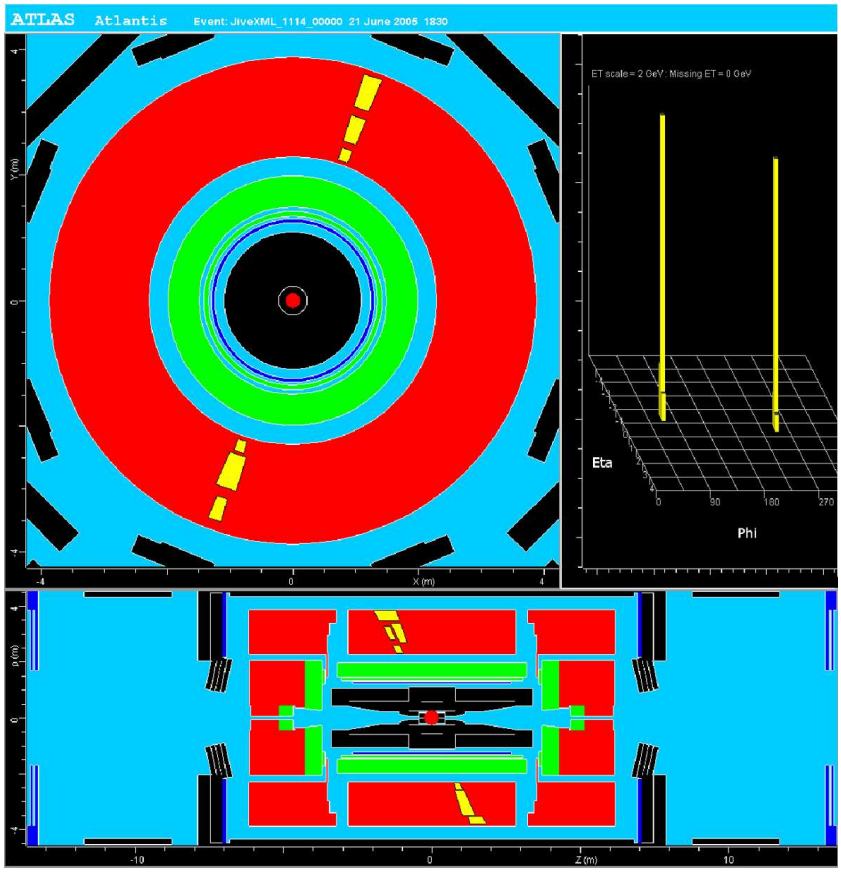

Figure 4.2: A cosmic ray muon recorded by the ATLAS barrel Tile Calorimeter at 18:30, on 21 June 2005 [36].

M1	December 2006
M2	February 2007
M3	June 2007
M4	August 2007
M5	November 2007
M6	February 2008
M7	May 2008

Table 4.3: Commissioning integration weeks ("Milestone Weeks") in ATLAS

achievement several integration periods took place as more and more systems were being included in the data taking. These were called the "Milestone Weeks". Having the different systems combined enabled the collection of cosmic ray muons data using different trigger sources, getting closer and closer to the ATLAS final trigger configuration, perform timing and trigger calibrations, train shifters and develop several online monitoring tools. At this period in time the whole ATLAS was preparing for the beam arrival.

The beam arrived in the LHC on the September 10th, 2008. The LHC machine team fully commissioned the 7 out of 8 sectors to operate at 5 TeV; the remaining sector was only commissioned up to 4 TeV. Just after, on September 19th, 2008 the unexpected (the unwanted) occurred. The last sector started to be commissioned to 5 TeV. Suddenly in this sector a magnetic field quenching was detected that resulted in a helium leakage into the insulation vacuum of the cryostat that later was released to the tunnel. The very fast and out of control pressure increase lead to the damages in several sub-sectors [37].

Before the accident the LHC was still able to provide to the different detectors (ATLAS, CMS, LHCb, ALICE) data taking periods in an operation mode called single beam (detailed in Section 4.5). Following the forced stop of the LHC operation, as the accelerator went for one year of repairs and commissioning, but the activities of the detectors on the pit continued and the detectors also took the opportunity to advance with repairs postponed due the LHC start-up. In the fall of 2009 the LHC was again ready for operation and after having a single beam circulating in both directions and providing again data from single beam to the detectors the first collisions of two proton bunches took place in November 2009. The first collisions were at the nominal energy of the beams injected in the LHC 450 GeV i.e. with a center of

mass collision energy of 900 GeV. The collision center of mass energy has been increased until stabilizing on $\sqrt{s} = 7\ TeV$ in March 2010.

4.2 A dedicated trigger for cosmic muons

The Tile Calorimeter was the first detector to take data from cosmic ray muons in the ATLAS pit. In order to properly do it, it was necessary to have a system to trigger the detector at the passage of muons arriving to the ATLAS cavern. Since both the muon spectrometer and the level 1 trigger of ATLAS were not ready to take data in the early phase of the commissioning (2005-2006) a dedicated system was needed. The first cosmic ray muons results mentioned in the previous section were obtained using this standalone trigger.

The following features made the Tile Calorimeter a good source for the cosmic ray muons trigger:

- A large coverage in $|\eta| < 1.7$ and a full coverage in ϕ;
- A large signal to noise ratio measured in testbeam for 180 GeV muons: $S/N \sim 40$;
- Dedicated outputs useful for trigger purposes. A **tower output**, using 5 Tile Calorimeter channels, to be connected to the level 1 trigger, and a **muon output**, using the two channels of D cell, that could be used for this purpose.

As previously mentioned a tower combines the information from the three radial layers of the Tile Calorimeter in slices of $\eta \times \phi = 0.1 \times 0.1$. A dedicated trigger board was developed within the Tile Calorimeter collaboration by the Chicago University Group [38]. Without being possible to have the detector volume fully covered due to lack of input channels on the trigger board the ultimate goal was set to have a coverage on the most vertical 12 modules (each readout by a super-drawer). For such a configuration, 8 trigger boards were needed, distributed as illustrated in Figure 4.3 [2]. To each partition two trigger boards are connected, one for the top modules ($y > 0$ and module #11 to #22) and the other for the bottom modules

[2] In the beginning of the commissioning only 2 trigger boards were available, which limited the number of modules to be used in the trigger. More were produced to achieve the projected coverage.

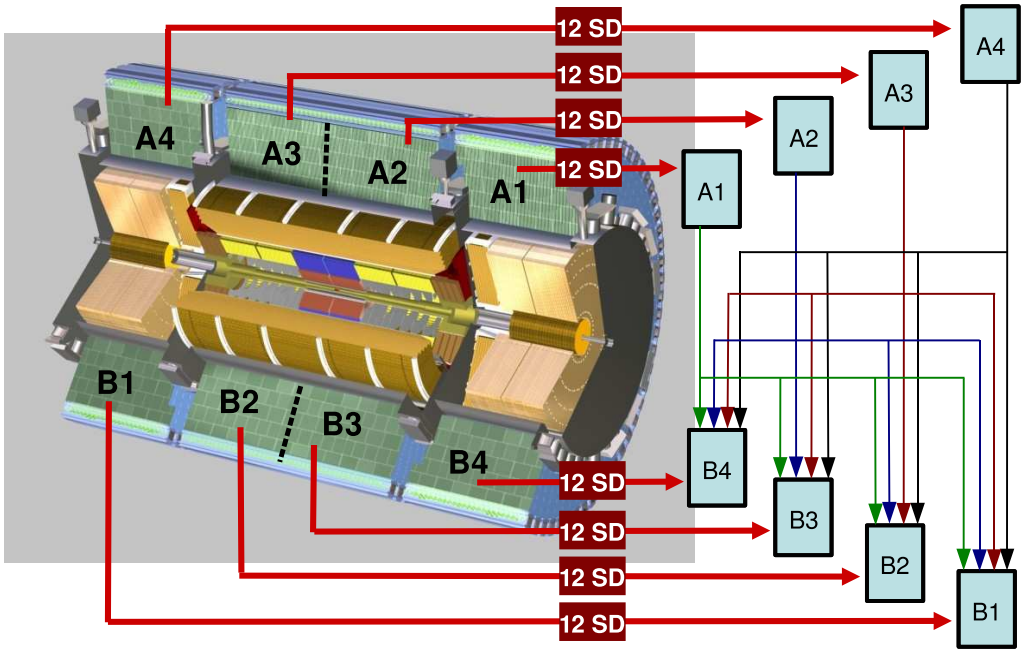

Figure 4.3: The Tile Calorimeter standalone cosmic ray muons trigger setup: coincidence between top and bottom modules.

($y > 0$ and module #43 to #54). Since each trigger board has 96 channels, only 8 towers could be used from each Tile Calorimeter module: for the long barrel towers in $|\eta| = [0.0, 0.8]$ (all towers but one) and for the extended barrel towers in $|\eta| = [1.0, 1.7]$ (all towers). A very low noise differential amplifier with limited bandwidth and a fast discriminator with programmable threshold are used for each analog signal input on the coincidence board. Varying the discriminator threshold it is possible to mask noisy towers.

The trigger boards usage was tested for different configurations:

- A single tower in any of the Tile Calorimeter modules.

- A pair of towers with one tower triggered in the top region of the detector ($y > 0$) and the other tower in the bottom region of the detector ($y < 0$).

- A pair of towers set back-to-back i.e. $\eta_{top} = -\eta_{bottom}$ and $\Delta\phi = \phi_{top} - \phi_{bottom} = \pi$.

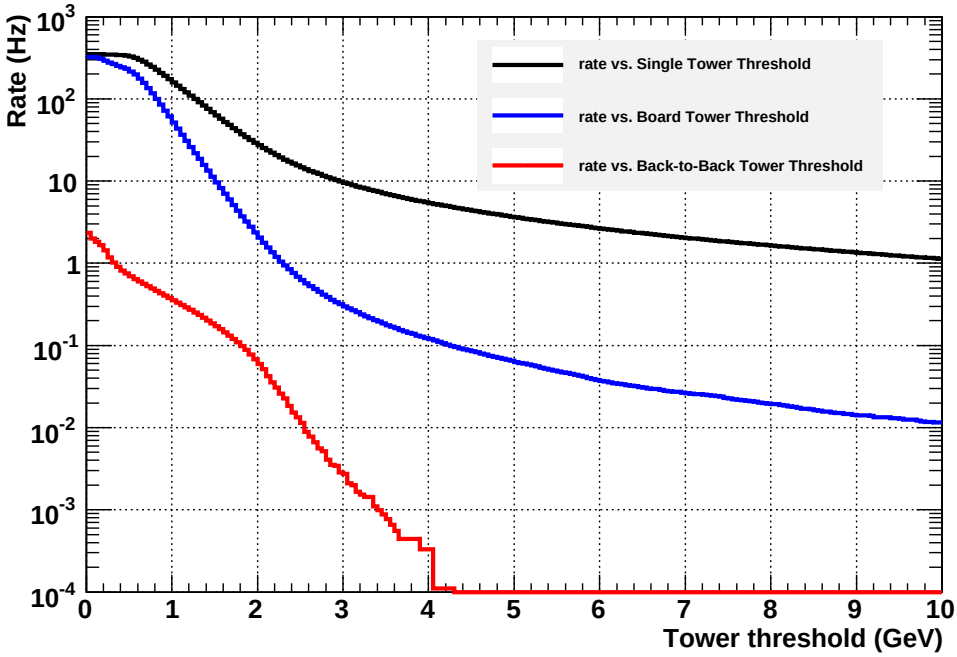

Figure 4.4: Expected trigger rates from Monte-Carlo for the Tile Calorimeter standalone trigger.

The expected trigger rates for these three cases obtained from Geant 4 Monte-Carlo simulation for the long barrel and using all modules can be seen in Figure 4.4. From the analysis of the results of this simulation it was decided to use the second option listed above. The single tower was too sensitive to noise and the one requesting for a back-to-back event was very limited by statistics. As the detector construction and operation was progressing it was necessary to connect the tower output to the level 1 trigger and the muon trigger output – only using cells from the third radial layers (D cells) – was used instead (2007). Later when all the issues with the muon spectrometer operational and the level 1 trigger performance were optimized (2008) the analysis used mostly cosmic ray muons triggered with the muon spectrometer.

4.3 Certification of trigger and readout optical fibers

The timing, trigger and control (TTC) signals and the digitized data are transported between the front-end electronics (FEE) and the RODs in optical fibers. These are multi-mode optical

fibers with a core diameter of 50μm and a cladding diameter of 125μm. The fibers are called either TTC fibers or ROD fibers depending on their usage. The TTC fibers transport different types of signals: trigger signals (ATLAS level 1 accept signal, test and calibration triggers), timing signals (bunch crossing signals, LHC clock, and synchronization signals, such as bunch crossing reset and event counter reset) and commands from the central trigger processor and/or sub-detector electronics. The physics data transport is made using the ROD fibers. Upon reception of the level 1 accept signal the digitized signal in the Tile Calorimeter front-end electronics is transported to the back-end electronics. The ROD is the main component of the back-end electronics. It processes the digitized data in real time and sends information about the energy, timing and a quality factor to the second level trigger.

For the certification of the readout and trigger optical fibers (ROD and TTC fibers) [39] the following equipment was used:

- Optical power meters to measure the attenuation of the signal between the approximately 100 m that separated the FEE and the instrumentation racks.
- An optical time domain reflectometer (OTDR) to locate with the precision of a few centimeters any break or splice loss and measure the length of the optical fibers.

For the attenuation measurement the requirements [39] for losses in the light output level should be for the TTC fibers better than 3 db and for ROD fibers better than 7 db. The attenuation results showed that for both 850 nm and 1300 nm pulses the average attenuation

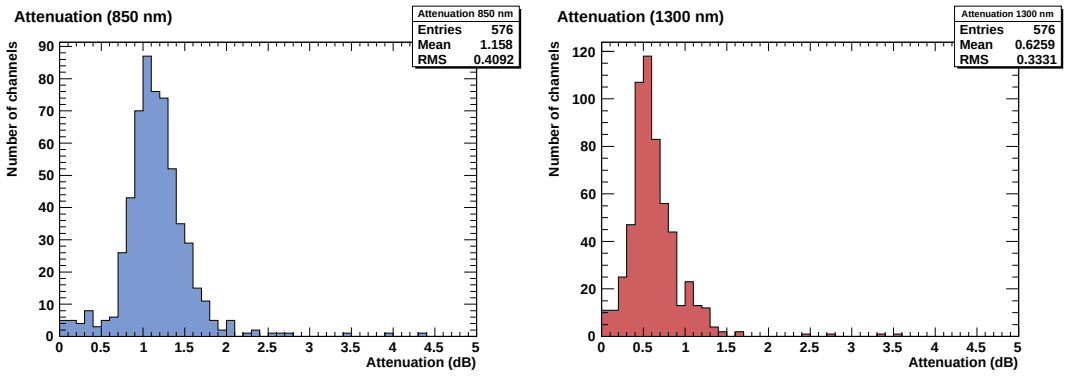

Figure 4.5: ROD and TTC optical fibers attenuation results for two different wavelengths.

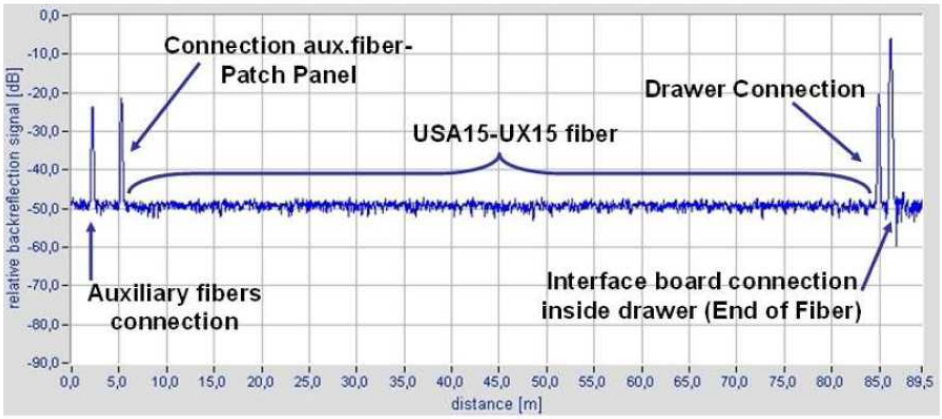

Figure 4.6: Response from a good optical fiber seen by the OTDR.

.

fulfilled the requirements as shown by the two histograms in Figure 4.5, where all the fibers showing attenuation below the 3 db requirement.

The OTDR injects a high intensity laser pulse in the optical fiber and measures the reflected light in function of time. The reflected light has two sources: Rayleigh scattering and Fresnel reflections. In Figure 4.6 the result of the measurements with the OTDR of a good fiber is seen. A baseline coming from Rayleigh scattering along the optical fiber body is seen between the patch panel and connection on the Tile Calorimeter drawer. The different peaks result from Fresnel reflections and are expected, representing specific points along the optical fiber path which are detailed in the figure. These are related with the measurement (the first peak on the left due to the auxiliary fiber used in the measurement) and the setup (from left to right: 2^{nd} peak, the patch panel, 3^{rd} peak, drawer connection and 4^{th} peak, the interface board connection inside the drawer or the fiber end). Fiber breaking, excessive bending or bad connections will produce additional Fresnel peaks. These are exemplified in Figure 4.7. In Figure 4.7(a) is show the result of a bad splicing that results in the appearance of an additional Fresnel peak. The procedure is to make a verification of the splicing and correcting it. In Figure 4.7(b) is illustrated the effect of accumulated dirt in the patch panel connector. Usually cleaning the connector with compressed air would restore the performance of those fibers. The OTDR measurements showed that the optical fibers lengths were between 60 m and more that 100 m. These were observed both for the TTC fibers and the ROD fibers. In Figure 4.8

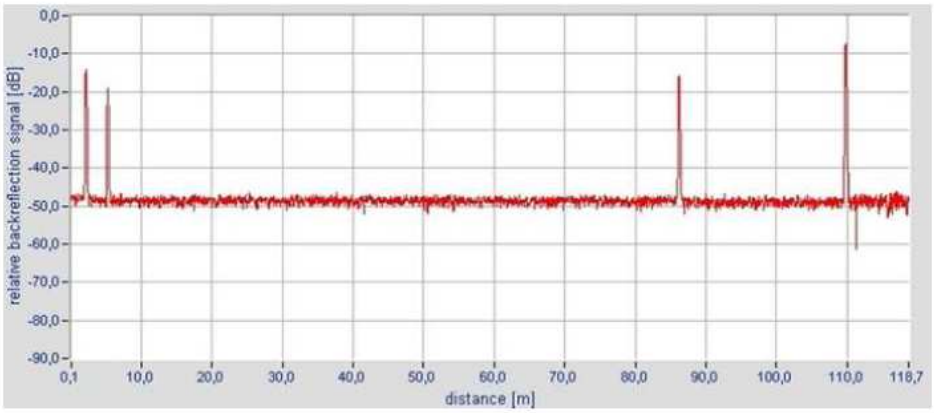

(a) A high peak appears 25 meters before the end of the drawer.

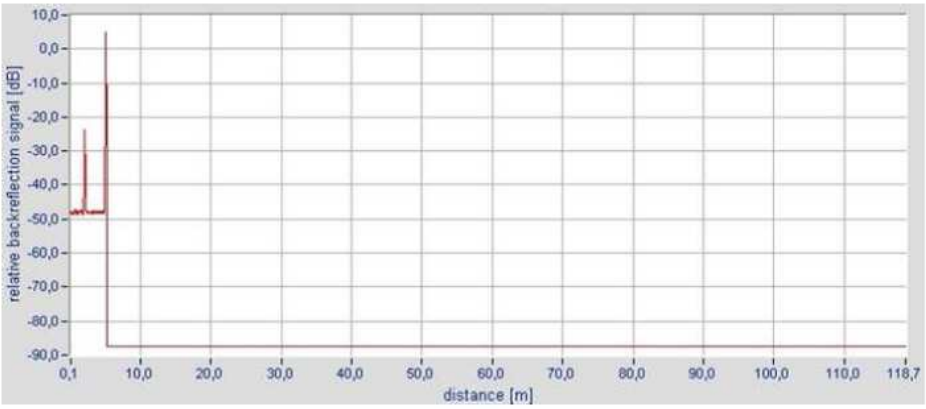

(b) Dirt in the patch panel connector.

Figure 4.7: Typical problems found in optical fibers during the OTDR tests.

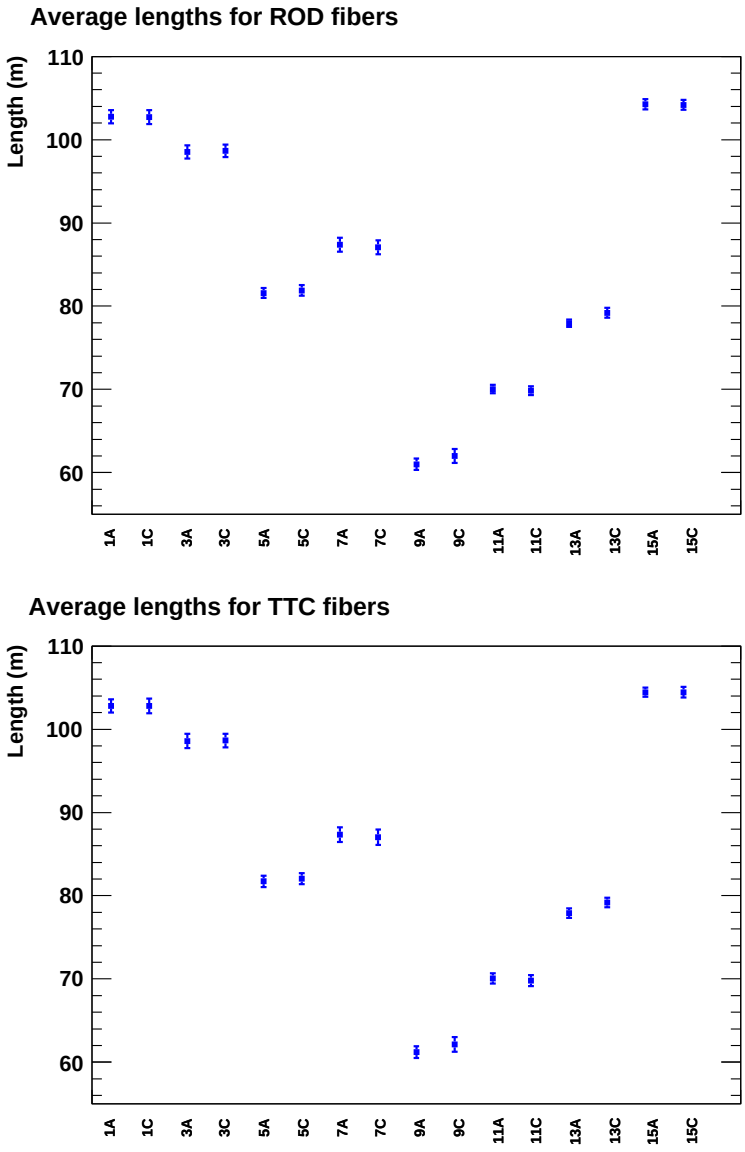

Figure 4.8: ROD and TTC optical fibers length results.

these results are summarized. The label in the x-axis refers to sectors in the Tile Calorimeter cylinder existing 8 modules/sector. The data points in the figure is the average over the 8 barrel modules and their RMS. On the figure on the left are the average fibers lengths for the ROD fibers and on the right the average fiber lengths for the TTC fibers. The results show that both ROD and TTC fibers have a same pattern for the fiber lengths distribution which is expected since for each sector both sets of fibers are routed together.

4.4 Contribution of cosmic ray data to the certification of the Tile Calorimeter operations

In addition to the different calibration and monitoring runs of the Tile Calorimeter, using the tools described in Chapter 2.2, the cosmic ray muons data taking was also useful for the detector's certification. A description over the most relevant quantities explored in a fast analysis is now presented. In the early commissioning this was done offline since no online monitoring tools were available or working in an user friendly manner. After a long debugging, as the monitoring tools improved, this type of quality checking was included in the data quality shifts check list, also made online, to provide to the people in the hardware side hints for planning the necessary hardware repairs.

Rates of cosmic muons The event rate is the first quantity that can be used to evaluate the quality of a run. A too large deviation from what is expected by the Monte Carlo (Figure 4.4) can be the first clue on hardware problems either in the setup (trigger thresholds) or on the detector itself (noisy or dead channels).

Trigger towers distributions When using the Tile Calorimeter standalone trigger the distribution of the trigger towers coincidences was available and it was useful to identify noisy or dead trigger towers (TT). It would only give information on the trigger operation and not on the detector performance for which a more detailed analysis was necessary. The concern was to identify the dead and noisy trigger channels. A TT with an unexpected low count rate could be due to:

- A too high threshold being set for that channel;
- A hardware problem for that calorimeter tower;

and a TT with an unexpected high rate due to:

- A very low threshold increasing the contribution due to noise;
- The right threshold but a tower with an atypical noise;

The final decision would result from checking the detector response in energy and a decision to mask or to change the threshold would be decided. In Figure 4.9 it is presented experimental results for such a distribution for a setup with 8 modules on the top and 8 modules on the bottom. Each entry is a coincidence between a tower top and a tower bottom and for each module 8 bins are used to identify each one of their 8 towers. The 16 bins with very few or no entries correspond to module #16 that tripped off during the run and module #18 that was not included in the data taking.

Energy distribution The expected energy distribution for cosmic muons is well established for the Tile Calorimeter. A large experience from testbeam along the years [26] showed that the expected energy distributions from muons crossing the full height of a Tile Calorimeter module should peak around 2 GeV. Due to the trigger configuration, and in particular with the standalone trigger used in the early commissioning, a signal is required in both top ($y > 0$) and bottom ($y < 0$) parts of the Tile Calorimeter. In Figure 4.10 this result is presented for the top and bottom parts of the detector. The muons reaching the bottom parts have already lost some of the energy in the top part and this explains the shorter high energy tail observed in the energy collected over the modules on the bottom. During the early commissioning, when using the standalone trigger, the synchronization between the top and bottom regions was sometimes poor resulting in runs with no energy deposits either in the top or bottom parts or even in both of them. So the verification of the total signal both in top and on the bottom was also a diagnostic tool on the synchronization of the Tile Calorimeter and the trigger.

Distribution of events in ϕ vs η The distribution of events in ϕ and η is also useful to detect

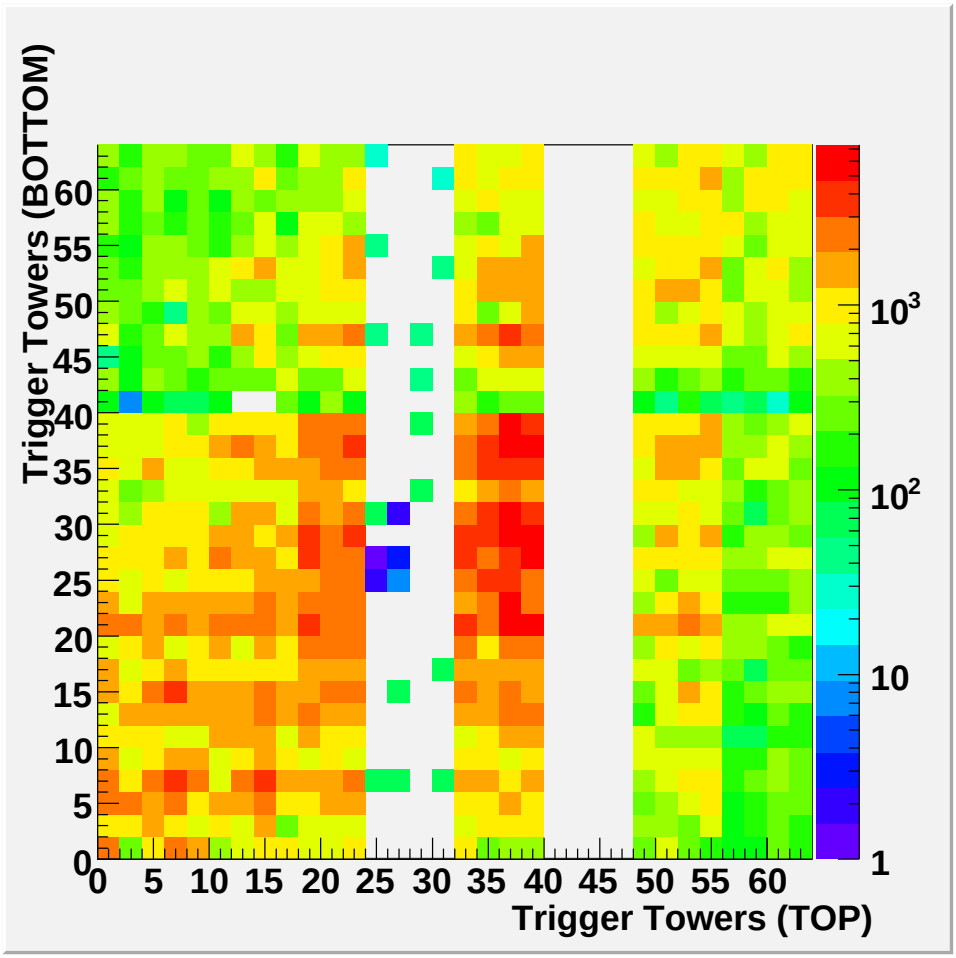

Figure 4.9: The distributions of triggers from the trigger board output in early commissioning (2006): 8 modules TOP in the C side and 8 modules BOTTOM in the A side

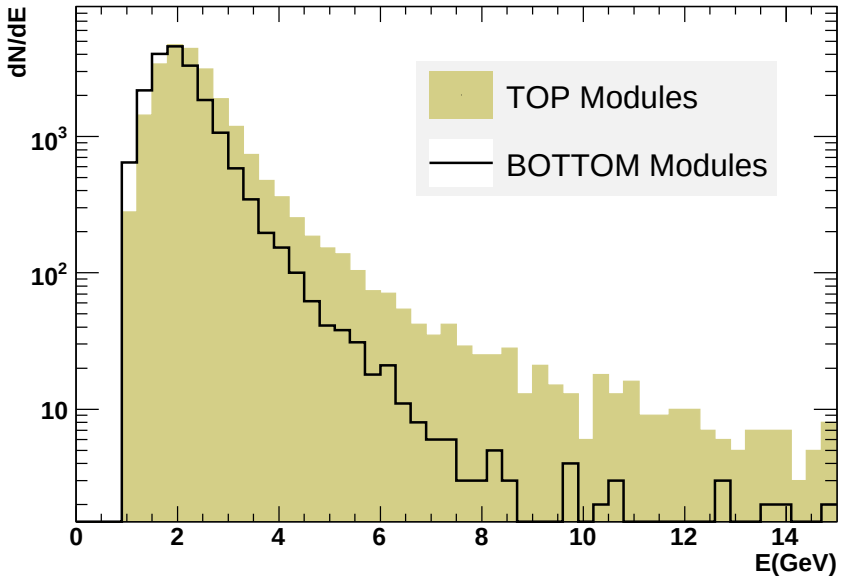

Figure 4.10: Tower of maximum energy: TOP and BOTTOM modules.

noisy and dead regions of the detector. In Figure 4.11 and Figure 4.12 two examples for this kind of distributions are presented for the Tile Calorimeter. Each figure corresponds to two different periods of the commissioning with cosmics muons where it is visible the evolution of the experimental setup.In these two plots the colors or z-axis shows the occupancy of each $[\eta, \phi]$ bin.

Figure 4.11 shows the Tile Calorimeter operating regions during the M4 integration week where the EBC partition was not being used and only the bottom part of the LBC was being included in the data taking. The distance between the EBA and LBA (or the EBA end in η) shows that the EBA was not in its final position since instrumentation and repairs on the front-end electronics were still being made. This works also as a crosscheck on the reconstruction software. From these type of plots it is possible to verify if the correct geometry was the one used in the reconstruction.

In Figure 4.12 it is presented another configuration later in the commissioning during the M7 where the EBA was not being used. The EBC is now included in the data taking and it can be seen that the EBC is in its final position. These plots still use data collected

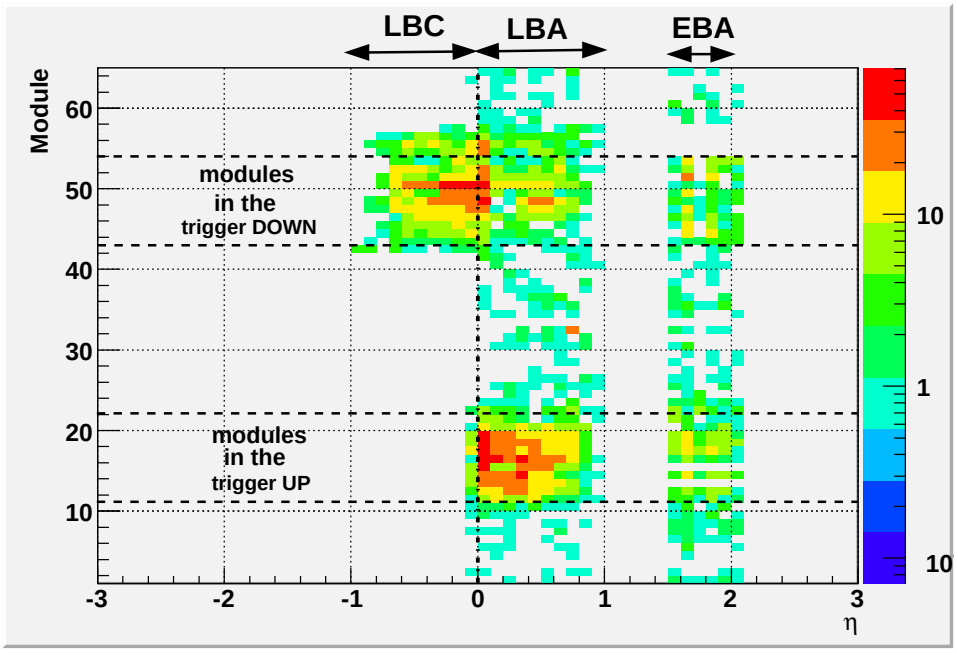

Figure 4.11: The distribution of the TileCal towers above a 1 GeV tower threshold (300 MeV cell threshold) probing on all the connected modules during the M4 integration week.

with the Tile Calorimeter standalone trigger. This explains the preferred regions in the distribution of the events with hot regions around the regions in ϕ that are connected to the trigger boards. There is also an asymmetry between the C side ($\eta < 0$) and the A side ($\eta > 0$) that can be explained by the expected asymmetry of the muons distribution due to the large shafts that exist in the ATLAS pit. In a quality check the concern is on the $[\eta,\phi]$ bins for which an excess of events relative to the first neighbours is evident and that are not understood as resulting from a specific trigger configuration.

Another option would be to have the integral of the energy for each one of these histogram bins as exemplified for two modules in Figure 4.13. The figure shows that the charge integral is typically smaller for module 15. This could be explained also due to the trigger configuration or the necessity of a larger threshold for the towers of that module. However there is a pair of channels in which the response of module 15 is higher, being two times higher in one channel. This could also be the evidence of a problem in those channels that requires a more dedicated analysis.

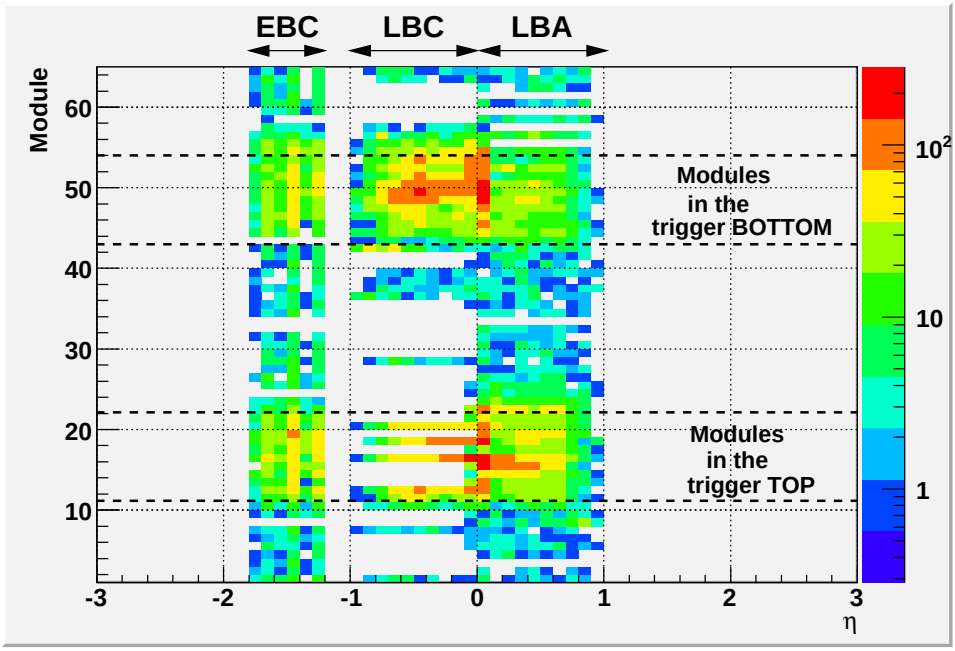

Figure 4.12: The distribution of the TileCal towers above a 1 GeV tower threshold (300 MeV cell threshold) probing on all the connected modules during the M7 integration week.

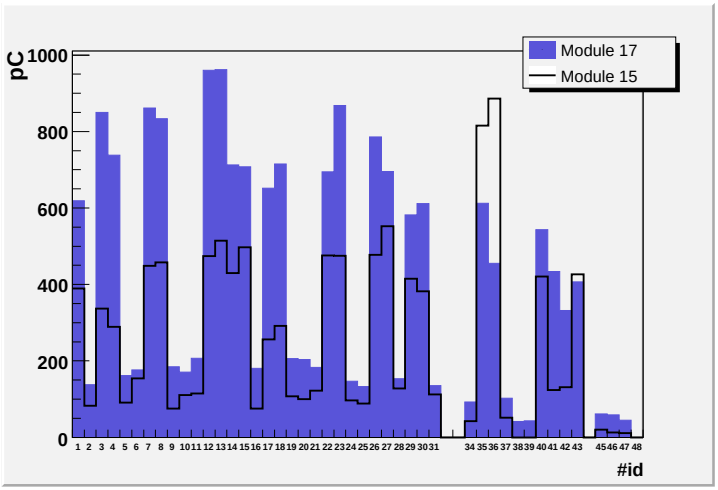

Figure 4.13: Charge integrals for the channels of two Tile Calorimeter modules: module 17 and module 15.

PMT charge response - ADC Samples The digitized samples of the Tile Calorimeter photomultipliers signals were also available in the data files. For each photomultiplier there would be 9 samples, each one with 25 ns width. For each sample an amplitude in ADC

counts is stored. This sampled signal is used to measure the energy, the phase relatively to a trigger and the value of the pedestal for each PMT. The distribution of these samples (Figure 4.14) should have as basic features:

- A symmetric distribution that is fully contained in the time interval with a well defined peak;
- The distribution maximum should be set on samples 4-5 if the channel is well synchronized with the trigger;
- The 2^{nd} and 8^{th} samples should have approximately the same amplitude;

If the above conditions are not observed for a considerable number of trigger channels the run should be rejected, since in that case the only stored information are random triggers coming from noise. In Figure 4.14 it is shown a case where a bottom module (LBA48) is delayed relatively to a top module (LBC17).

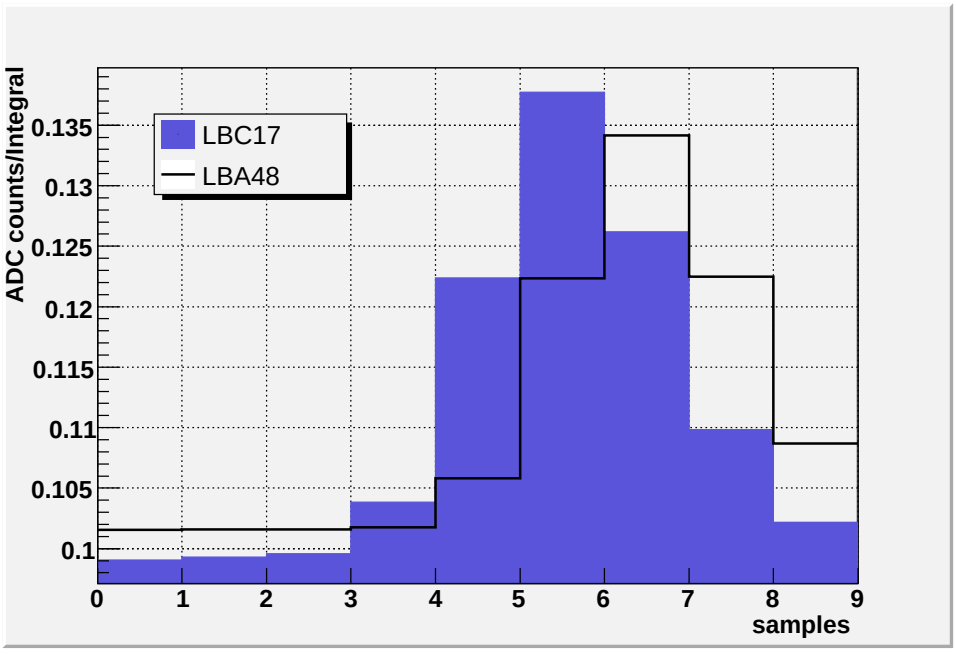

Figure 4.14: Digitized signal samples distributions: a symmetric distribution with a peak in sample 5 for LBC17 and in sample 6 for LBA48

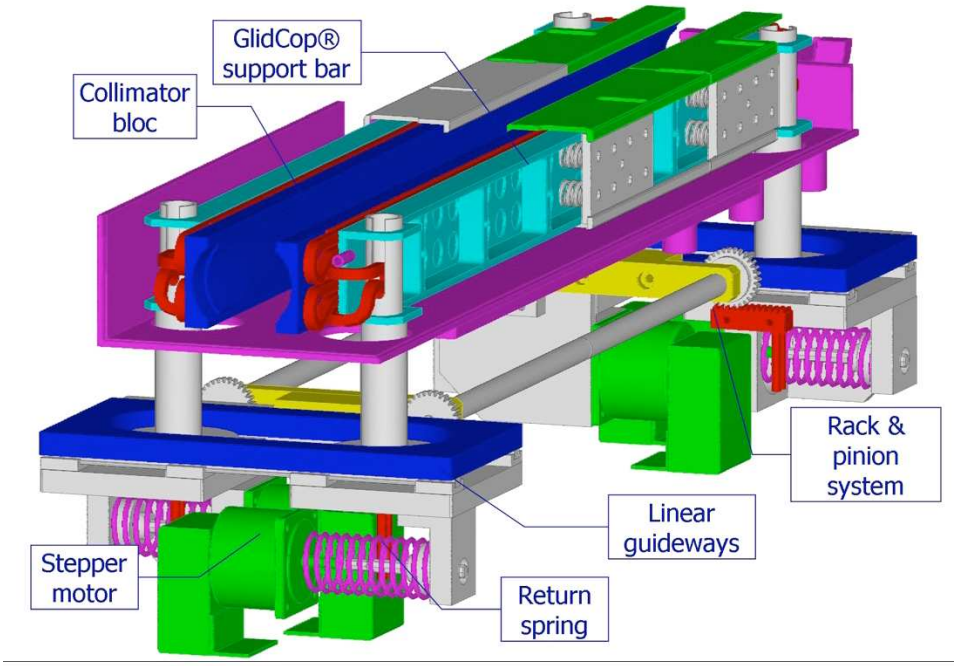

Figure 4.15: The technical drawing of the collimator of the LHC accelerator.

4.5 Single beam

Before the collisions start-up there are periods of time when each LHC beam circulates around the accelerator ring. For the first injections the beam is circulating at its nominal injection energy of 450 GeV. Beam 1 (2) is used for a beam circulating clockwise (anti-clockwise) which in ATLAS means that it goes from positive (negative) to negative (positive) z. These accelerator tests were also used in benefit of the different LHC detectors and this operation mode is referred as Single Beam data acquisition period. Results with Single Beam are presented in Chapter 6.

The Single Beam data was of two types: splash events and scraping events. The names derive from the manner these events are produced. A common element for these two types of events are the tertiary collimator located 140 m from the interaction point (IP) and the beam pick-up (BPTX) system, part of one of the beam monitors, that is located 175 m from the IP and is used as trigger and reject efficiently the cosmic ray muons. In Figure 4.15 can be depicted details of the collimator in a technical drawing. The tertiary collimator made of

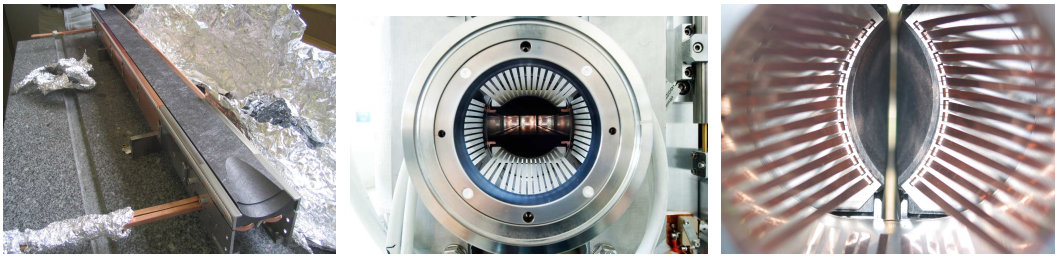

(a) Collimator jaw (b) Open collimator (c) Closed collimator

Figure 4.16: Details of the collimator's (a) One of the collimator jaws used in the secondary collimator that has the same dimensions but it is made of carbon (b) The collimator is opened (c) The collimator is closed.

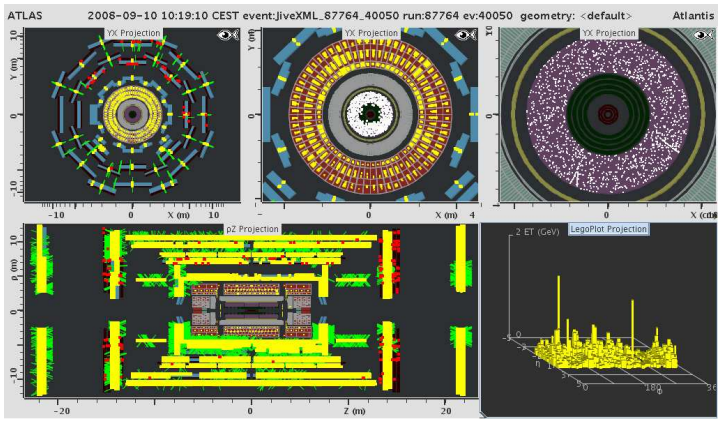

Figure 4.17: A event display of a splash event in the ATLAS detector. Each splash event could reach up to a few TeV of deposited energy.

copper (Cu) with an inlay of tungsten (W) are 1 m long and are located before the interaction points for protection of the triple superconducting magnets. In Figure 4.16 details of the collimator are presented. On the left one of the jaws before the collimator's assembly, in the center the collimator is open with the two jaws being apart from one another and on the right after sliding in the jaws and closing the collimator. For splash events the collimator is closed and the protons collisions produce millions of high energy particles that reach the ATLAS detector. The scrapping events are produced by defocusing the beam resulting then that the outermost protons will collide with the collimator jaws producing a relatively small number of particles. The particles reaching the calorimeter are mostly muons from the decay of pions.

In Figure 4.17 the event display of a reconstructed splash event can be depicted. The different views show that all the subsystems were collecting data in 2008. These events are

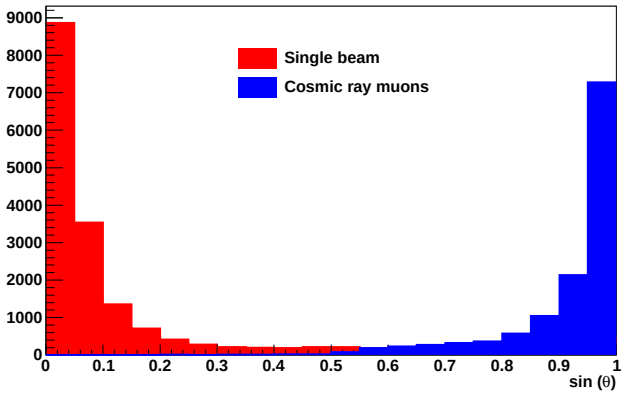

Figure 4.18: Comparing the trajectories of muons in Single Beam data and cosmic ray muons data.

clearly coming from a different position that the cosmic ray muons come. This is clear if the sinus of the angle relatively to the z axis of the muons trajectory is calculated. In Figure 4.18 a comparison is made between muons produced in the Single Beam runs and the cosmic ray muons runs. Two peaks can be distinguished: one close to 0 which correspond to the trajectories closer to the horizontal and another close to 1 which corresponds to trajectories close to the vertical. These correspond respectively to Single Beam and cosmic ray muons data. The muon track parameter was calculated using the TileMuonFitter algorithm which will have a dedicated section in the next chapter.

5 Certification of the energy scale with cosmic ray muons

5.1 Cosmic ray muons

The commissioning of the ATLAS detector made extensive use of the ionizing particles resulting from the interaction of cosmic rays in the earth's atmosphere. Figure 5.1 [3] shows the variation of the flux of particles originating in cosmic rays with the atmospheric depth. As the atmospheric depth increases the flux of muons and neutrinos is approximately constant or slowly decreasing but for all other particles types such as protons and electrons, the flux decreases by several orders of magnitude. These muons (and neutrinos) are produced from the decay of charged pions ($\pi^{\pm}$) and are the only particles that will reach the surface with a rate high enough in order to be used in the commissioning of the LHC detectors.

Figure 5.1 also shows that the muons start to appear at an altitude of about 15-17 km. During their path they lose around 2 GeV by ionization before reaching the surface of the earth. In Figure 5.2 [3] the distribution of the muons momentum (p_{μ}) at the earth surface is depicted. The line represents the modeled curve for vertical muons ($\Theta = 0^{o}$) reaching the earth surface and the different symbols refer to different sources of experimental data; the shifted distribution represents the same distribution but now for an angle $\Theta = 70^{o}$. The shift on in the muon p_{μ} spectra is due to two factors: the low energy muons will decay before reaching the surface reducing the lower account of muons with low momentum; at 70^{o} the path travelled is longer so there will be more pions with higher energies that decay before reaching the earth's surface. The ATLAS detector is installed in a experimental cavern 100 m underground. A

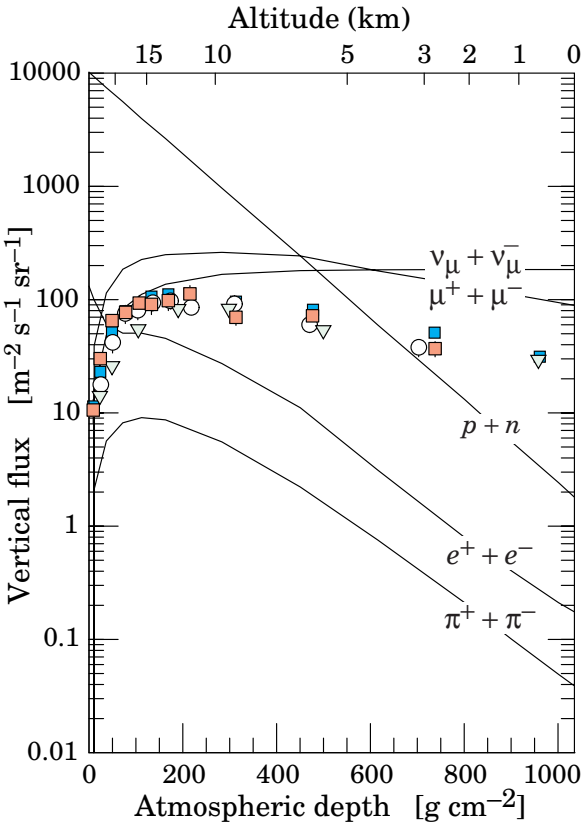

Figure 5.1: Vertical flux of particles with energy above ¿ 1 GeV in the atmosphere. The lines are estimated values and the points are experimental results from negative muons with $E > 1\ GeV$ [3].

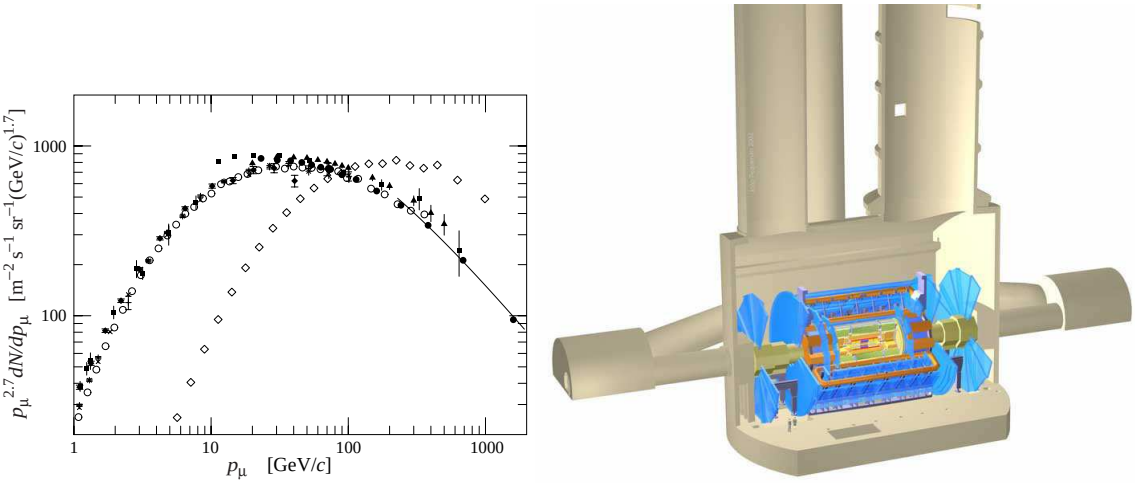

Figure 5.2: Distribution of muons at the earth surface [3] (left) and the ATLAS detector in the experimental cavern (right).

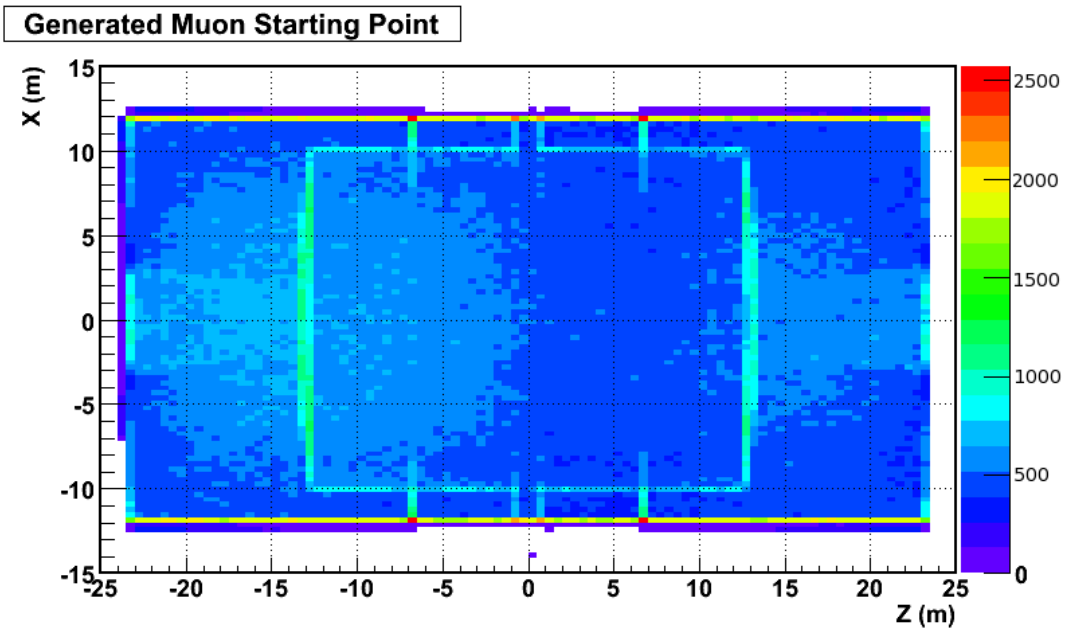

Figure 5.3: The ATLAS cavern muon-ray plate. The circular regions with higher statistics represents the ATLAS experimental caver shafts.

free path between the surface and the ATLAS detector is available through two large shafts that were necessary for the detector installation. In Figure 5.3 the cavern muon-ray diagnostic where the shafts are clearly identified by the two circular regions with larger statistics. In addition there are the geometric constraints due to the pit walls. So the cosmic ray muons flux distribution over the ATLAS detector will be drastically different from what is seen on the surface. There will be preferred regions simply due the loss of muons along their traveling along the rock which is of greater importance for low momentum muons that are the most abundant.

The energy loss of muons in matter is described by Figure 5.5 [3]. This is the response for muons going across copper. For steel the response is not very different since the $dE/dx \propto Z/A$ and the relative ratio of Z/A between the two metals is on the order of 2%. Even if we consider that the tile calorimeter is a mixing of iron with 5.5% polystyrene, the effect of the latter should be small due to a density six times smaller than iron (steel). Comparing Figures 5.5 and Figure 5.2 it is seen that for most cases the cosmic ray muons spectra is on the right of the ionization minimum but still in a region where the dominant effects are the energy loss

due to ionization. From Figure 5.5 the two contributions are equal for $E = E_{\mu c}$ and above this value radiative effects increase considerably as the muon momentum increases. This guides us to the contents of the next section where a description of the Tile Calorimeter muon energy response is made.

5.2 Description of the energy response from cosmic ray muons

Muons have been studied using the tile calorimeter geometry for a long period of time since the first beam tests back in 1995 [24] an through the testbeam calibration period 2000-2003 [26] and in the last combined testbeam in 2004. The usual scenario was to have a well known source of muons with a controlled flux, and pre-defined energy. This was during testbeam where mono-energetic high energy muon beams were used to study the tile calorimeter response. Typically the used energy was 180 GeV although studies using lower energy muons were also made. Cosmic ray muons have a large momentum spectra from a few GeV to hundreds of GeV.

The muon spectra in the Tile Calorimeter 5.4 is characterized by having a well defined peak that is referred as the most probable value (MOP). To the left of the peak a low energy gaussian tail that characterizes the ionization energy losses and to the right of the peak a Landau tail which characterizes the radiative energy losses of the muon interactions.

The main factor determining the energy response of muons in a calorimeter is the crossed path length. The measurement of a dE/dx in MeV/mm eliminates the dependency on detector and trigger coverage geometry. It also allows the comparison with Monte-Carlo more straight forward. This justifies that one of the main outcomes of ultimate version of the TileMuonFitter algorithm has in the output the calculation of the crossed path length.

5.3 Datasets

Unless mentioned the presented results used data from cosmic ray muons taken during 2008 with all ATLAS sub-systems operational. The used data is as follows:

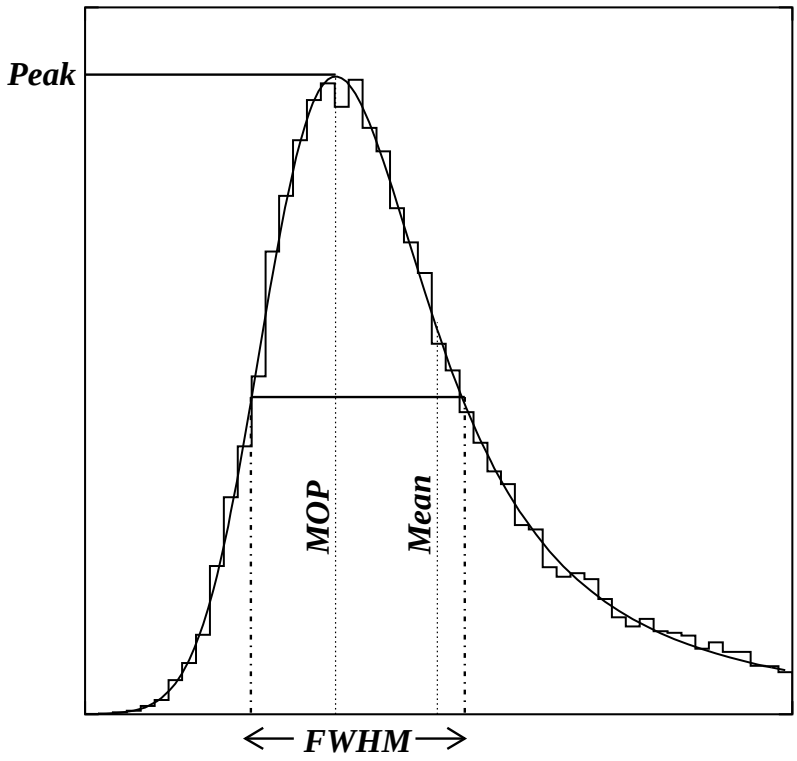

Figure 5.4: Typical shape of the muon spectra crossing the Tile Calorimeter detector. The usual quantities used to characterize the muon response are indicated.

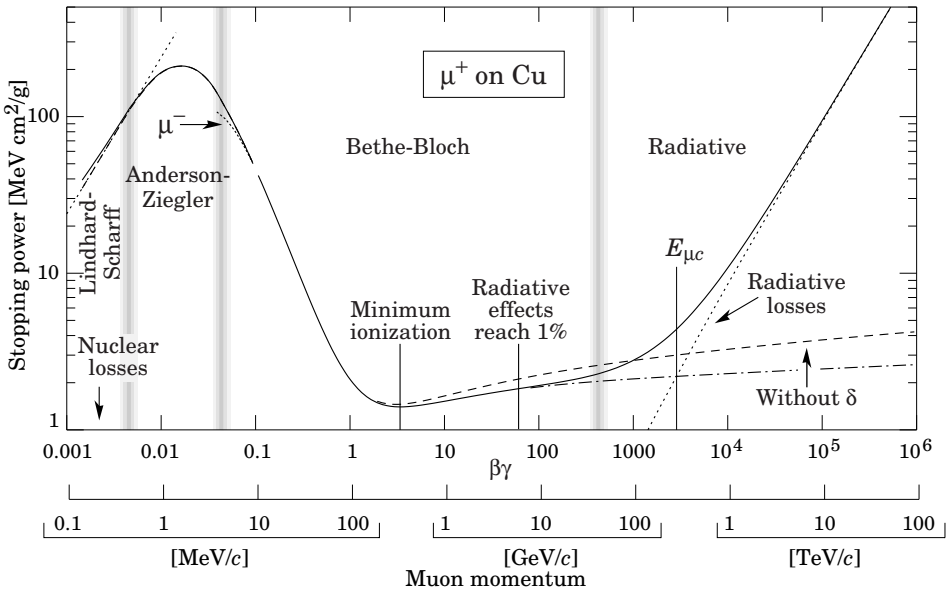

Figure 5.5: Energy loss by muons in copper [3].

- ID-COMM Events triggered by the Resistive Proportional Chambers (RPCs) of the Muon Spectrometer and requiring one track reconstructed in the Inner Detector (ID). The run numbers are 91885 (116974 events) , 91888 (84717 events), 91890 (124873 events), 91891 (108925 events) and 91900 (165913 events). The re-reconstruction is from November 2009 reprocessement with the latest cesium corrections. In the text this comes referred as: ID-COMM data stream

- CosmicDownwardMuons Events triggered by the RPCs. This is the very long run 91387 and for the energy analysis only 329251 events have been re-reconstructed. For simplicity this will be called as: RPC data stream

- MC A Monte Carlo (MC) was produced using the ATLAS geometry reconstruction version 7.0.0 of May 2009. In the simulation both solenoid and toroid were active. This MC produce 787732 events from run number 108867. The simulated events had the TRT as the selection volume.

5.4 The Tile Muon Fitter algorithm

As already mentioned, when the commissioning of the ATLAS detector started not all systems including the tracking and triggering systems were operational and the Tile Calorimeter had to operate in physics runs as standalone (2005-2006). So, it was necessary to develop specific tools for the analysis of the cosmic ray muons events, hardware tools such as the standalone trigger boards described in the previous chapter, as well as software tools. One of these software tools is the Tile Muon Fitter (TMF) [42] algorithm.

When crossing the calorimeter the typical cosmic ray muons, with energies from a few GeV up to the order of hundreds of GeV, will lose energy mainly through ionization and will not be stopped within the calorimeter volume. So these muons are well identified in the Tile Calorimeter by their energy deposits and by a well defined crossed path. The TMF algorithm identifies the cells with energy deposits resulting from the passage of the cosmic muons and these cells are used to define the cosmic muon track in the following sequence:

- Identification cells with a measured energy above 250 MeV (approximately 4 times the noise RMS) both on the top ($y > 0$) part and the bottom part ($y < 0$) of the calorimeter.
- Combine the cells in the top and bottom region to find a track, obtain the track parameters.
- Calculate the crossed path length per radial layer, module and partition (but not per cell). For the track definition the geometric center of the Tile Calorimeter cell is used and latter a linear fit is applied.
- Identification and collection of all the cells within a minimum distance of the track. The distances used were respectively for the A, BC and D cells: 300, 375 and 860 mm in the Long Barrel and 750, 750 and 1700 mm in the Extended Barrel.

Due to the large size of the tile calorimeter cells it is possible to neglect the effect of the magnetic field in the trajectory of the cosmic ray muon so TMF considers that the muon goes across the detector volume following a straight path. Typical tracks reconstructed by the Tile Muon Fitter algorithm are shown in Figure 5.6 and Figure 5.7.

Two track finding algorithms were developed: a first one based on a χ^2 minimization of the orthogonal distances of the cells (using the position of the cell center) to the track, using Minuit; a second method, based on the Hough Transform, proved to be more robust with respect to noise rejection, and able to handle multiple tracks (as shown in Figure 5.6 and Figure 5.7), so it became the default method. Unless otherwise specified, all TMF results shown use the Hough Transform method.

Hough transform

The Hough Transform[43] (HT) is a well known technique aiming at detecting data tracks a noisy environment and/or with missing information. The TMF algorithm uses the Hough Transform on the detection of the Tile Calorimeter cells that can be associated to the same track of the cosmic ray muon. Due to the low signal-to-noise ratio of muon interaction, this approach has proved to be highly efficient in the commissioning phase of ATLAS using cosmic

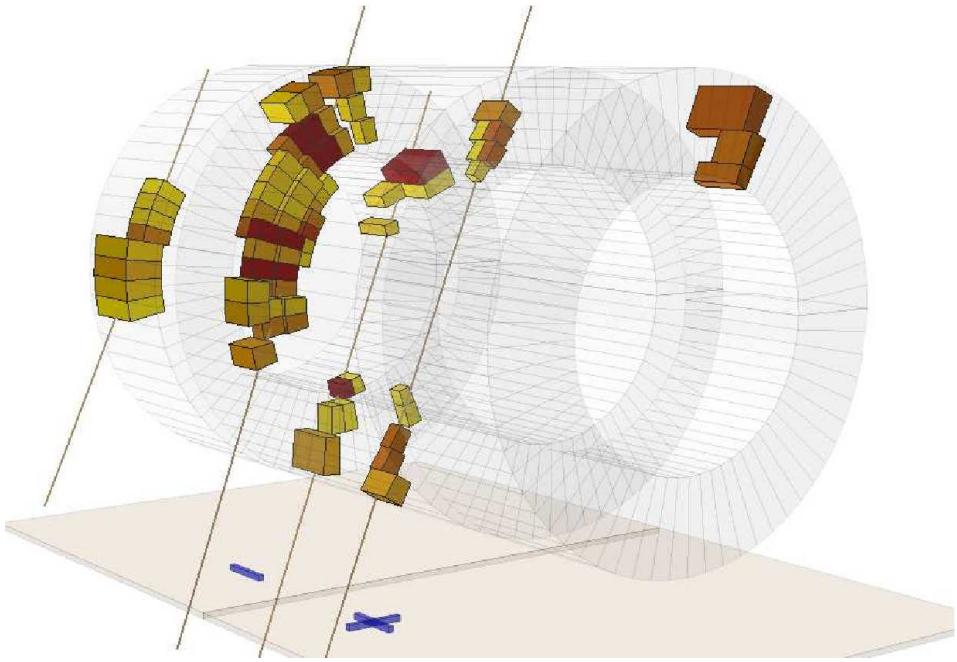

Figure 5.6: Tracks detected in a cosmic event.

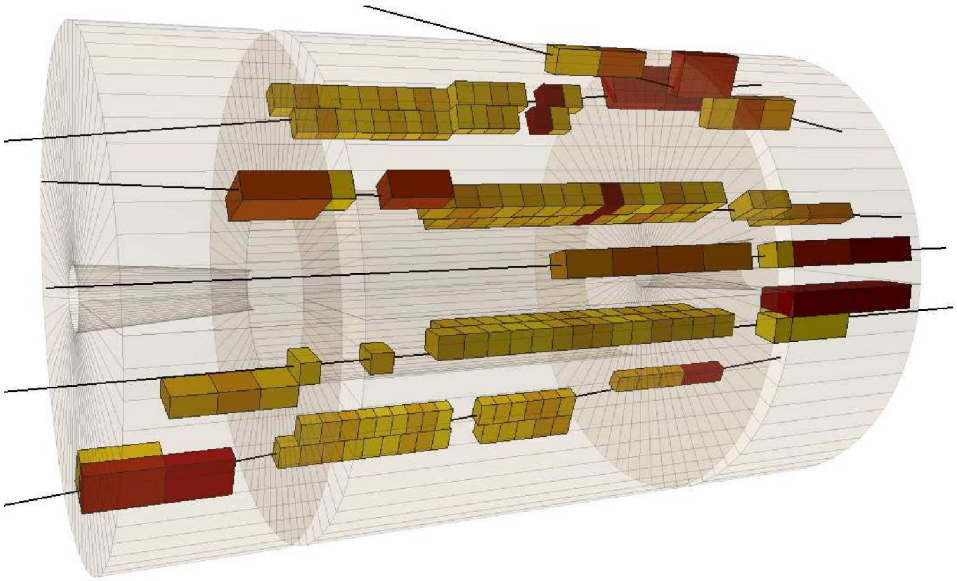

Figure 5.7: Tracks detected in a single-beam data event.

rays, over performing the initial method based on least-squares fitting.

Before proceeding the concept of the HT is presented. For this purpose a simpler problem, the one of a straight-line in a two dimensional space x,y (coordinates space) is chosen. In a plane two parameters are necessary to parametrize a straight-line. The idea of the HT is to build a parameter space where to each straight-line in the coordinates space, a unique point in the parameter space is associated.

Let us consider the following parametrization,

$$y = m \times x + b \, .$$

In this case the used parameters are the slope m and the y-axis interception b uniquely identify a straight-line. However these are unbounded parameters and for vertical or close to the vertical trajectories ($b, m \to \infty$), problems may occur. An alternative parametrization [44] is the following

$$\rho = x \cos\theta + y \sin\theta \tag{5.1}$$

where the parameters that identify the points along this line are the angle θ measured relatively to the positive x-axis and the algebraic distance ρ from the origin. If $\rho > 0$ and θ is an angle within $[0., 2. \cdot \pi[$ a unique pair of parameters will identify a line. The relation between the coordinate space (x,y) with the parameter space (ρ,θ) can be summarized as follows:

- A point in the coordinate space corresponds to a sinusoidal curve in the parameter space.
- A point in the parameter space corresponds to a straight line in the coordinate space.
- Points on the same line in the coordinate system will correspond to curves that go through a same point (ρ,θ) in the parameter space.
- A point or points lying on the same curve in the parameter space correspond to lines through the same point in the coordinates plane.

Following this procedure a scan over all the data points in the coordinate space is made,

to calculate the corresponding parameters in the parameter space. The parameter space is divided in small bins of ρ and θ and the results of the scan are used to fill these bins. A straight-line will be identified by a pair (ρ_0,θ_0) to which corresponds the equation

$$\rho_0 = x\cos\theta_0 + y\sin\theta_0$$

and every pair (x,y) verifying this equation will be located on the same straight-line.

The HT approach as presented above has however an extensive computational cost since the parameter space requires a fine-grained quantization in most applications. Some variations of the standard HT method have been proposed in order to reduce the computational cost. Among them, a combination of the Local Hough Transform (LHT) [45] and the Adaptive Hough Transform (AHT) [46] is used in the TMF algorithm.

In order to implement a cosmic ray track detection in TileCal HT-based, some previous steps should be executed in order to extend the above methodology to a 3-dimensional space. The whole procedure is listed bellow:

1. Project the corresponding cell center point onto two orthogonal planes: XY and ZY.
2. Find the target straight-line track on each plane using the HT method.
3. Merge the 2 lines in a 3-D track.

The HT algorithm used was the LHT with two AHT iterations. The first iteration seeks for the peak position in the parameter space, looking for the highest accumulator bin. The second iteration computes the mean value for ρ and θ, looking only around the peak position found by the first iteration. Those mean values are the most probable straight-line parameters in the data space. The energy to each calorimeter cell is used as a weighting factor for the accumulator increment, allowing a fine tuning of the reconstructed track.

Tile Muon Fitter output

The main output of the TMF are the track parameters of the muon that goes across the Tile Calorimeter volume. Each track is defined using two angles, the ϕ and θ of the spherical

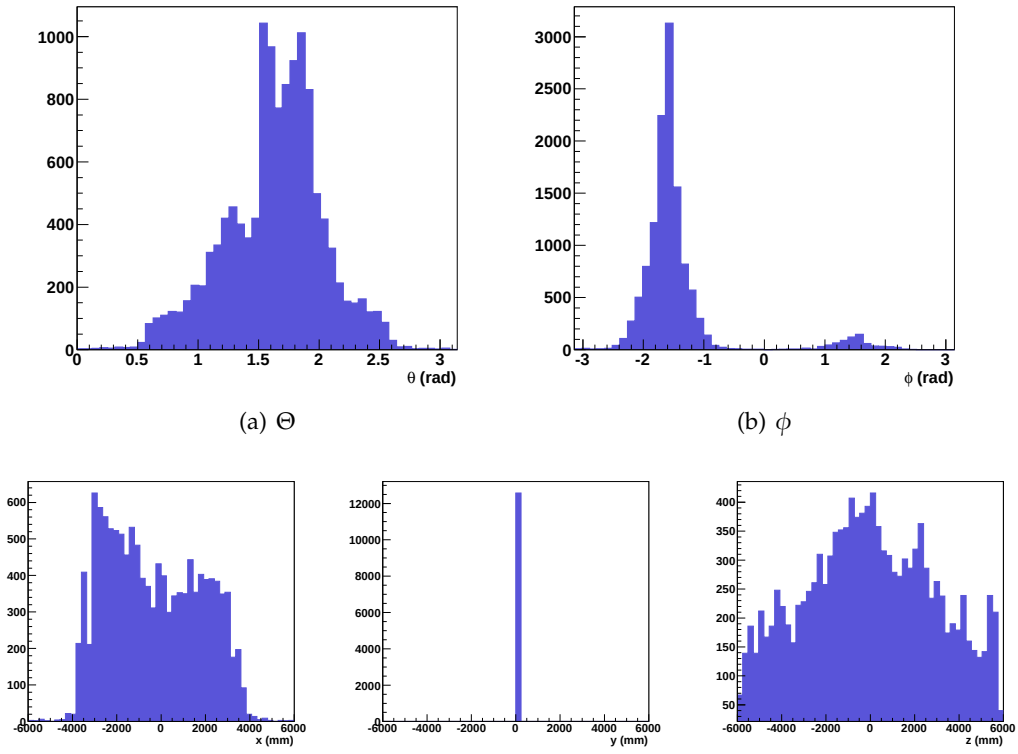

(a) Θ (b) ϕ

(c) X (d) Y (e) Z

Figure 5.8: The parameters of the track calculated using the TMF algorithm: a direction given by the angles θ and ϕ and a point given by the intersection of the track with the plane $y = 0$.

coordinates, and one point, defined as the intersection with the XZ plane for y=0 (X0Z). These variables are presented in Figure 5.8 and Figure 5.9. As expected the results show a predominance of events with directions close to vertical. The x and z distributions are more uniform, showing that the whole Tile Calorimeter is populated with cosmic muons energy deposits.

In addition the Tile Calorimeter cell time measurements are used to calculate a TMF event time. The point at which the muon track crosses the horizontal plane X0Z is taken as a reference. For each selected cell, the time-of-flight (ToF) is added (or subtracted) to the measured cell time. The ToF is calculated considering the muons travelling at the speed of light, from the y=0 point to the point in the track closest to the cell center, if the cell is on the top (bottom) part of the detector. The y=0 time is then calculated as the energy-weighted

average of the cell's time.

The intersections of the reconstructed track with the detector volume are also calculated within TMF. This crossed path length is calculated within a partition (p), within a module (m) and within a layer (l). It does not detail which and how many cells have been crossed by the cosmic ray muon. The quantity defined per each (l,m,p) combination is designated as a segment.

The TMF still collects the cells used by the HT fit as well as all the cells within a region of interest around the track. This region of interest is defined as described above by using a set of maximum distances from the track to the cell center. The energy summed over the two channels of a cell, the average time of a cell, the time difference between the two channels of a cell, the cell coordinates (X,Y,Z) and (η, ϕ) are saved and delivered for each cell by the TMF algorithm.

Tile Muon Fitter precision

The TMF precision was evaluated using Monte-Carlo simulation and by comparing per-event the track parameters with the generated track parameters also referred as the Monte-Carlo truth data. The results obtained for the two angles θ and ϕ that define the track are presented in Figure 5.10. The precision obtained for both angles is of 1.6°. For the coordinates in X0Z plane the same exercise was carried out and the results are presented in Figure 5.11. The width of both histograms corresponding to the coordinates X and Z is of the order of 200 mm. The precision is poor but it is something expected due to the large cell sizes. In fact the 200 mm value correspond approximately to the width of a A cell in the Long Barrel partition that is the best possible precision that can be achieved with an algorithm with the characteristics of the TMF.

The error in the path length determination caused by a 1.6° error in for θ and ϕ can be conservatively estimated as 2.4%, by considering a track crossing the outer edge of the long barre D3 cell.

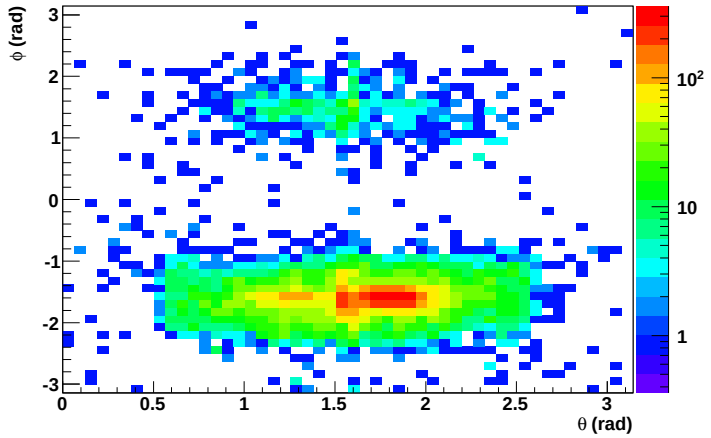

(a) Θ vs ϕ

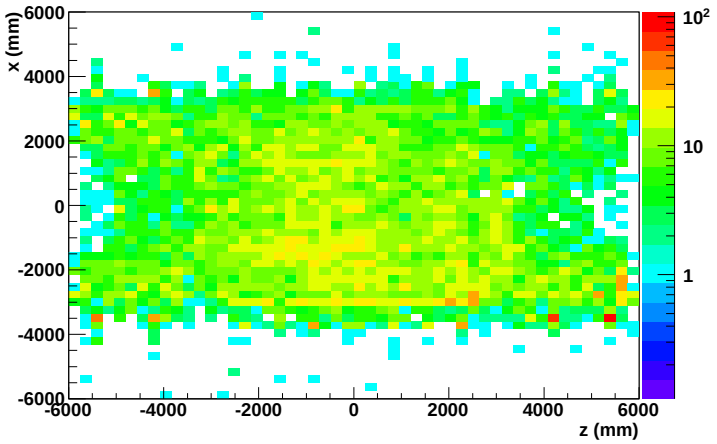

(b) X vs Z

Figure 5.9: The definition of a track by the tile muon fitter algorithm is based in 2 angles (a) and in the coordinates in the plane XZ for y=0 (b).

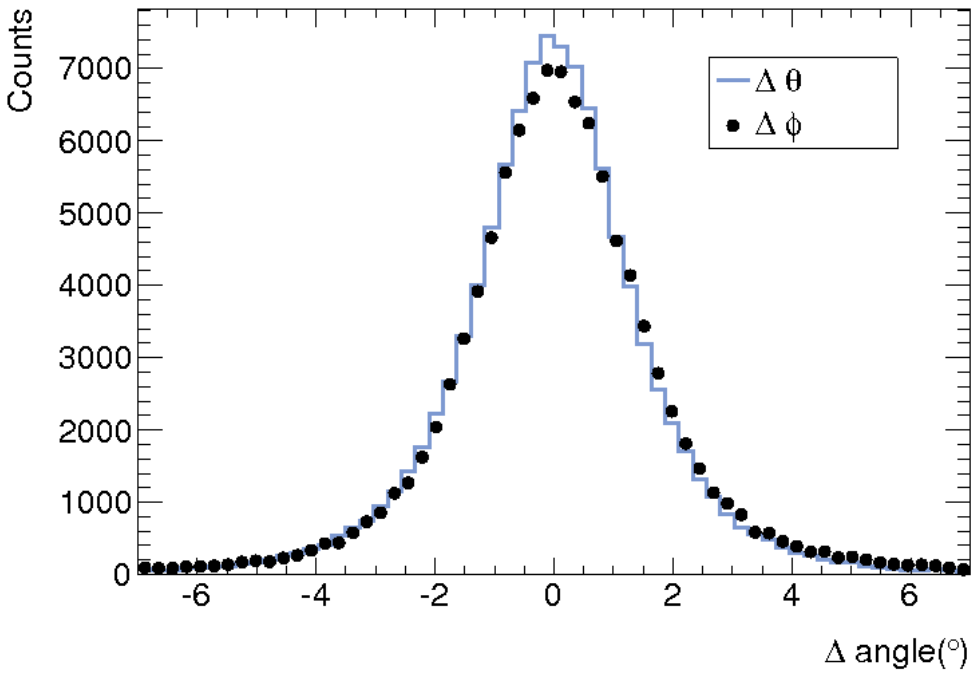

Figure 5.10: Angular precision for the zenith angle θ and azimuth angle ϕ. The histograms entries are per-event differences between the reconstructed and the generated angles.

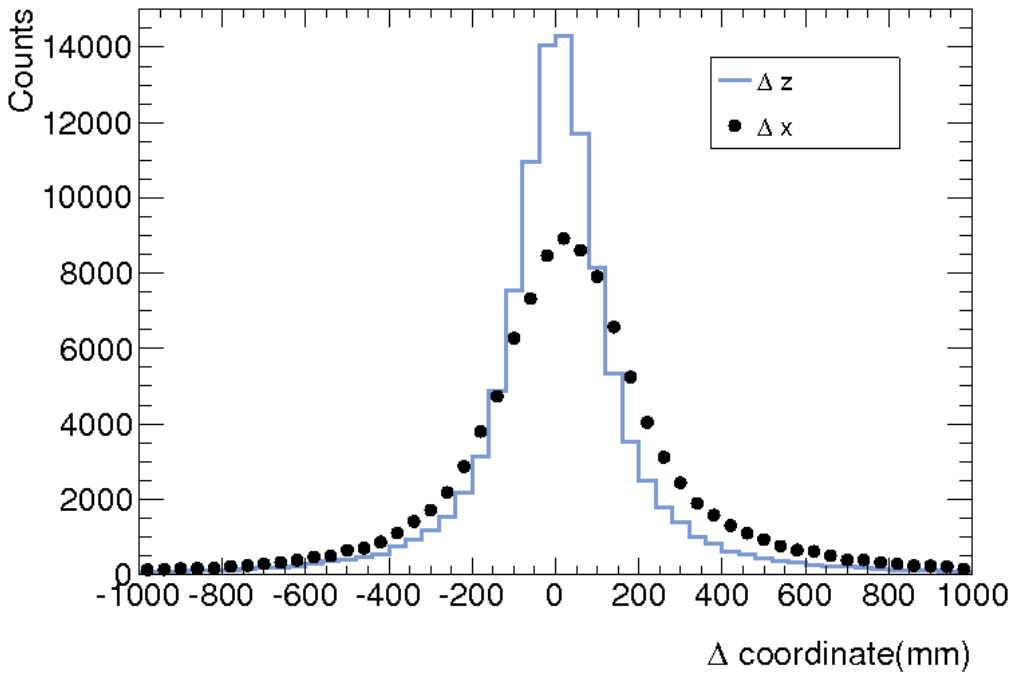

Figure 5.11: Position precision in the X and Z-coordinate respectively, both at the horizontal plane ($Y = 0$) crossing. The histograms entries are per-event differences between the reconstructed and the generated angles.

5.5 Energy imbalance of calorimeter modules with early commissioning data

A first approach to check the performance of the Tile Calorimeter energy scale was done by measuring the imbalance of the measured energy of the two photomultipliers that read-out a cell. This was done very early in the commissioning (2006 data) where very few Tile Calorimeter modules were being used in data taking. For this preliminary analysis only 8 modules on the top ($y > 0$) and 8 modules on the bottom ($y < 0$) were available. In the list of connected modules, two of them were used during the testbeam and calibrated using the tools described in Section 2.2. For the remaining modules the photomultipliers have been simply set to the nominal gain of 10^5.

The quantity used in this analysis is obtained for each tile calorimeter cell:

$$A_E = \frac{E_j^k - E_i^k}{E_j^k + E_i^k}$$

where E_j^k and E_i^k are the energy measured in each one of the two photomultipliers i and j of a cell k. The double read-out of the Tile Calorimeter has the main purpose of producing a signal that is independent of the region of the cell where the energy is deposited. This quantity can be used to measure the uniformity of a cell response within a module, and of a module relatively to the others by combining the different cell measurements.

If the two channels that read-out a cell are equalized then it is expected that, if a large statistics is accumulated, in average the energy difference should be approximately zero and the same for A_E. If this is not the case, a shift from zero is expected that should be related to the mis-calibration of the channels in a cell.

Cosmic ray muons were used in this study although they may not be the most adequate source of data for this type of studies since there is no direct and experimental control over the distribution of these particles. However it is expected that after some time the distribution of events will cover the cell volume precisely due to the randomness of the trajectories of the cosmic ray muons. In this case the above quantity can still be used for the described

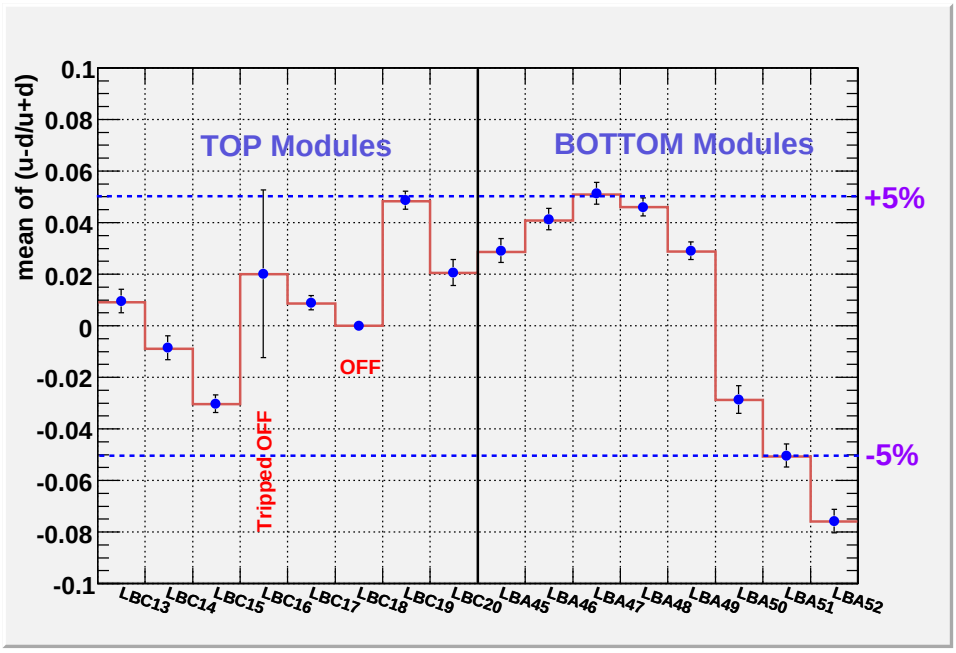

Figure 5.12: Average imbalance $< A_E >$ in TileCal modules as a cross-check on energy calibration

purpose. This was done with 2006 data and a summary of the results is shown in Figure 5.12. It is observed that the calibrated modules (LBC 14 and LBC 17) have an $< A_E > \simeq 1\%$ and globally $< A_E >$ is below 5%. Since the non-calibrated modules channels/PMT's were set to the nominal gain it can be concluded that the fluctuations in the optical chain must be below 5%.

5.6 Signal to noise separation

A quantity that characterizes the response of a detector is the capacity to distinguish signal from the electronics noise (pedestal). The tile calorimeter cell performance is driven towards the measurement of high energetic particles included inside the hadronic jets produced in the LHC collisions. However it is also to note that the detector has a good performance even for particles, like muons, which leave a relative small energy deposit along their path inside the calorimeter. This is also the case of a class of particles predicted in models beyond the standard model, such as the stable massive particles (see Section 3.2.4) that also have a relatively small

		Peak	FWHM	σ_{left}	σ_{right}
A+BC+D		4.21 ± 0.02	3.01 ± 0.02	1.13	1.43
	TOP	2.16 ± 0.01	2.07 ± 0.01	0.84	0.92
	BOT	2.22 ± 0.01	2.15 ± 0.02	0.86	0.96
A Cells		0.76 ± 0.01	1.04 ± 0.01	0.41	0.48
	TOP	0.41 ± 0.00	0.63 ± 0.00	0.25	0.28
	BOT	0.40 ± 0.00	0.65 ± 0.00	0.25	0.30
BC Cells		2.04 ± 0.01	1.90 ± 0.01	0.74	0.87
	TOP	1.05 ± 0.01	1.19 ± 0.01	0.48	0.53
	BOT	1.05 ± 0.01	1.22 ± 0.01	0.48	0.56
D Cells		1.18 ± 0.01	1.26 ± 0.01	0.50	0.58
	TOP	0.64 ± 0.00	0.84 ± 0.01	0.33	0.38
	BOT	0.61 ± 0.00	0.83 ± 0.01	0.33	0.37

Table 5.1: The results from a fit with a gauss and landau convoluted function for the module response (A+BC+D) and for each radial layer (RPC data stream).

energy deposit on the calorimeter.

The separation of noise and signal for the cosmic ray muons in each radial layer of the calorimeter has been investigated. In Table 5.1 the results from fits to the cosmic muon rays tracks distributions are presented. A complete description of the detector response to muons is obtained using the result from a convolution of a gaussian and a Landau distributions [40]. The columns of this table give the peak value which is also referred as the most probable value (MOP), the full width at half maximum (FWHM), the σ_{left} that is the width of the gaussian tail (low energy) and the σ_{right} which characterizes the width of the landau tail (high energy). The distributions were produced taking in account the following procedure:

- Events were selected by the TMF algorithm;

- These events use cells whose energy is above 60 MeV:

$$E = E_1 + E_2 > 60\ MeV$$

;

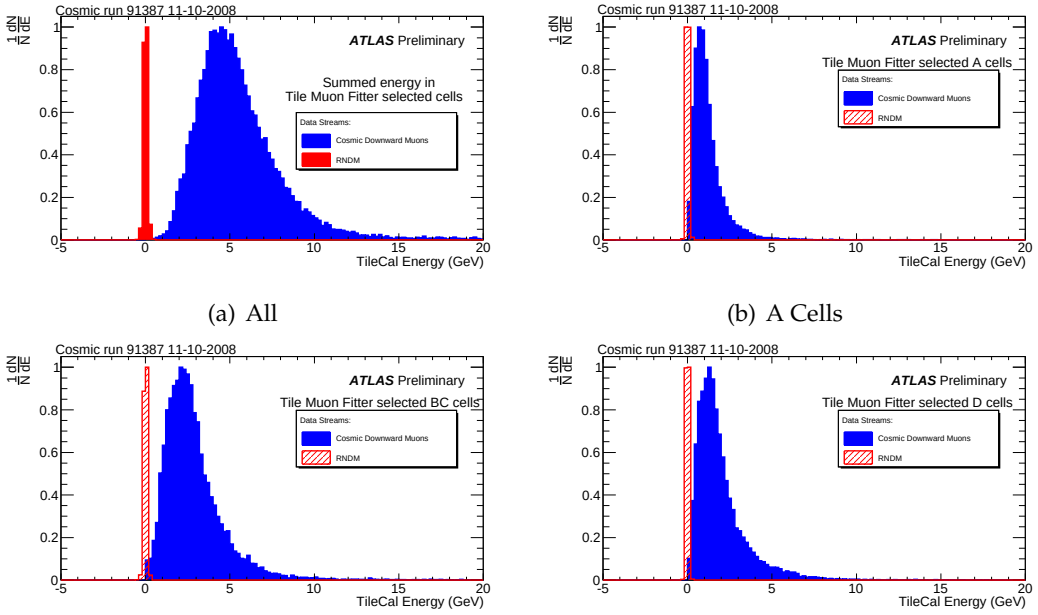

(a) All (b) A Cells

(c) BC Cells (d) D Cells

Figure 5.13: Signal and noise separation considering all possible trajectories for the cosmic ray muons. Data and pedestal include exactly the same cells per event. The RNDM stream was used for pedestal and RPC data stream was used for data.

- These events use cells with a time difference between photomultipliers below 6 ns:

$$T_{diff} = \frac{T_1 - T_2}{2} < 6\ ns$$

This was obtained using the RPC data stream. In addition to all the different physics stream there is one that collects the detectors response relative to random triggers that for each tile calorimeter cell will give the distribution for the electronic noise (pedestal). For the pedestal distribution and for each event only cells with a measured physic signal in the physics stream are used in this measurement.

The signal to noise (S/N) separation results are summarized in Table 5.2. The top modules and the bottom modules show comparable values $S/N = 19$ for the the combination of the three radial layers and 5.9, 13.9 and 9.4 for A, BC and D cells respectively. Summing the contributions of the top and bottom modules the S/N increases to 25 for the combination of

	ALL			TOP			BOT		
	Peak (GeV)	σ_{noise} (MeV)	S/N	Peak (GeV)	σ_{noise} (MeV)	S/N	Peak (GeV)	σ_{noise} (MeV)	S/N
A+BC+D	4.21	166	25.4	2.16	115	18.9	2.22	117	19.0
A Cells	0.76	86.7	8.78	0.41	68.6	5.96	0.40	67.0	5.92
BC Cells	2.04	105	19.5	1.05	76	13.9	1.05	77.7	13.6
D Cells	1.18	89.2	13.2	0.64	68.5	9.4	0.61	68.3	8.96

Table 5.2: The signal to noise ratio (S/N) for the average module response and for each radial layer (RPC data stream).

the three layers and 8.8, 19.5 and 13.2 for the A, BC and D cells respectively.

If a more stringent selection is done, requiring only muons that cross within a small slice in η the obtained S/N gets closer to the value measured in testbeam for mono-energetic muons. In Figure 5.14 [18] the muon selected for $0.3 < \eta < 0.4$ are plotted for data and Monte-Carlo. The entries are energy deposits per module so top and bottom parts are included in the plot as separate contributions. A good agreement is seen between data and Monte-Carlo. The pedestal distribution only includes per event, as before, the cells crossed by the muons and passing the selection cuts. The S/N separation is larger and if for the D cell $S/N = 16$ and for the whole module $S/N = 29$. Taking in account the typical momentum spectra of the cosmic ray muons (muon with tens of GeV) the ratio is smaller that the one measured in testbeam using 180 GeV muons. This is expected by the Beth-Bloch energy distribution showed earlier. Since the signal and noise are well separated these S/N is considered as a good performance result.

5.7 Energy scale and ϕ uniformity

This section is divided in three parts. First the selection cuts are presented since these are common to the two developed analyses. In a second section the energy scale of the Tile Calorimeter is evaluated using cosmic ray muons and after the results for the uniformity in ϕ are presented [41]. For the two results a comparison with earlier results submitted for publication on the Tile Calorimeter readiness paper [18] is made.

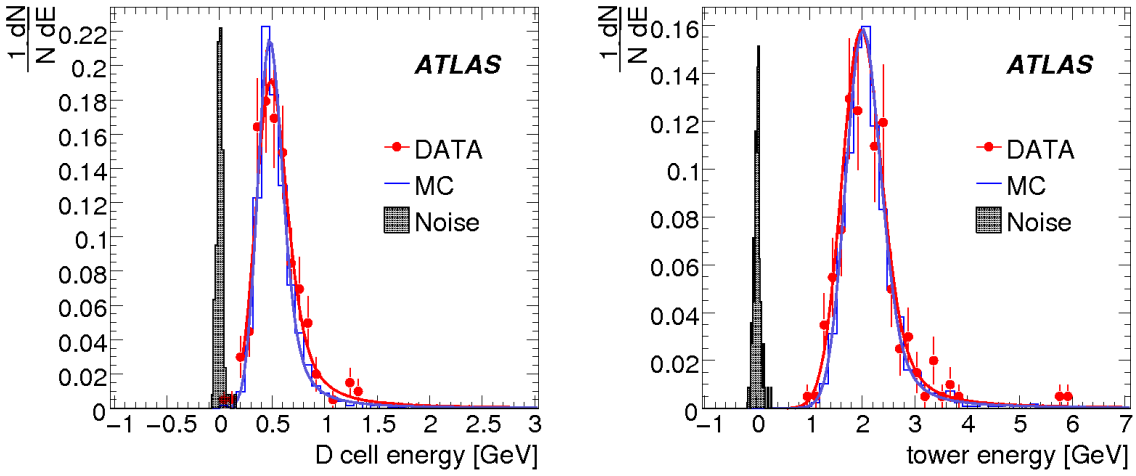

(a) D cells (b) Total

Figure 5.14: Energy muon for projective muons selected in $0.3 < \eta < 0.4$. The pedestal distribution uses per event the same selected cells as the ones used for data. The ID-COMM data stream is used for data and RNDM stream used for the pedestal.

5.7.1 Selection cuts

The TMF algorithm will collect all the cells that are close to the reconstructed track as already described in Section 5.4. Even these cells may have problems that require their measurements to be rejected within a event. There are also features related to the geometry of the detector, triggered events and the quantity used for this certification that require an evaluation to decide if a measurement is or is not suitable to be used for the present analysis. In what follows, a detailed discussion of the selection cuts needed for this analysis is presented and a justification is presented.

Cell selection

After defining the track parameters, the TileMuonFitter algorithm collects all the cells within a radial distance from the track. This radial distance depends on the radial layer. There is no quality factor that is imposed for the selection of these cells. This is done in the analysis by selecting cells using a energy threshold and a time correlation.

Length Cuts (mm)		Layers		
DATASET	Partition	A	BC	D
ID-COMM	LB	310	855	390
	EB	310	550	700
RPC	LB	221.3	249.5	332.0
	EB			302.6

Table 5.3: Crossed path length cut values.

Energy threshold

The applied energy threshold is used to reject cells that are compatible with noise. All cells with an energy below 60 MeV are not considered when the energy per layer or the total energy is calculated.

Time difference between cell photomultipliers

The time difference between the two photomultipliers of a cell represents a correlation of the two channels that are measuring the same cell. For physics signals the time measured in each photomultiplier should be similar. This is not the case for electronic noise events where each photomultiplier will have a random time associated to the energy measurement or equivalently the two photomultipliers are not in coincidence [31].

Crossed path length threshold

During the analysis it was verified that the crossed path length calculation often provided very small segments associated to large energy deposits, which results in very large values of $\frac{dE}{dx}$. For this reason these very small segments are rejected and selection cuts has the ones presented in Table 5.3 are used.

Angular threshold: $|90° - \Theta_{TMF}|$

The periodic structure of the calorimeter results in large sampling fraction fluctuations that depend on the angle with which the muons cross the calorimeter. The angle defined as $|90° - \theta_{TMF}|$, where θ_{TMF} is the usual spherical coordinate measured relatively to the z-axis,

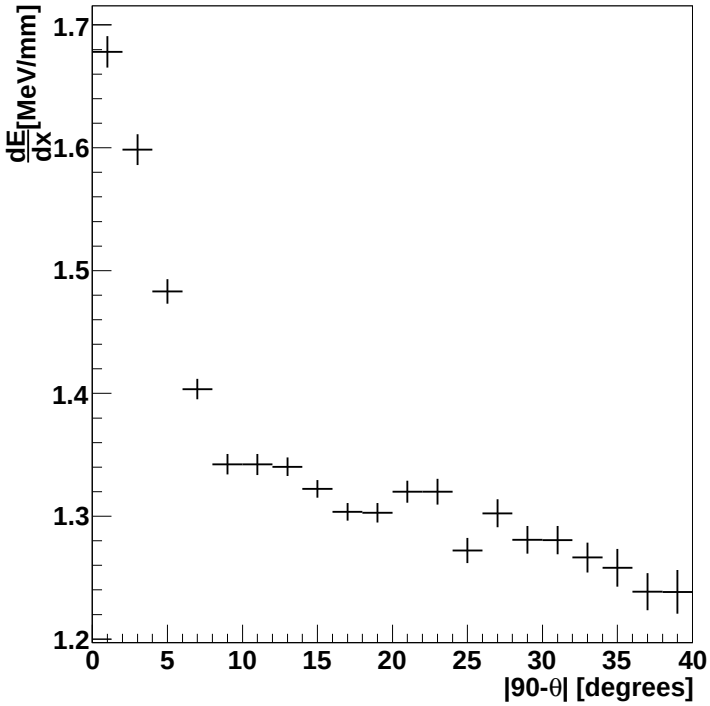

Figure 5.15: The effect of sampling fraction with the variation of the θ_{TMF}. The data points on the left for small values of $|90 - \theta_{TMF}|$

that is small and close to zero for muon travelling with trajectories parallel to the xy-planes. In Figure 5.15 the effect of the sampling fraction in the path of the cosmic ray muon is very large for $|90° - \Theta_{TMF}| < 8°$ which is used to select the trajectories of the muons.

Momentum measured by the Muon Spectrometer

The cosmic ray muons have a momentum distribution that spans over a large interval as seen by the histogram in Figure 5.16. However it is known that the muon energy loss depends strongly on the momentum of the muon. So to minimize the fluctuations that could occur due the usage of a so large momentum interval a selection is made requiring the muons to have $10\ Gev/c < p_\mu < 30\ Gev/c$.

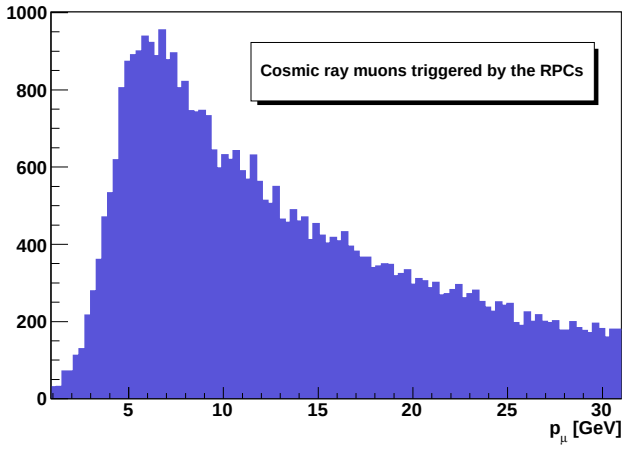

Figure 5.16: Cosmic ray muons triggered by the RPCs and momentum measured by the muon spectrometer.

x_{TMF} and z_{TMF}

The x_{TMF} and z_{TMF} are the coordinates of the muon track in the horizontal plane y=0 as provided by the TileMuonFitter algorithm. These variables ca be used to reject wrongly reconstructed tracks due to noise that fall out of the inner detector volume, for ID-COMM stream, or out of the Tile Calorimeter volume, for the RPC data stream.

Truncation

The truncation of 1% of the high values of dE/dx (Figure 5.17) is used to eliminate the fluctuations resulting from the muon radiative contribution to the high energy tail.

5.7.2 EM energy scale from cosmic ray muons

The EM energy scale has been transported to the ATLAS cavern for all the Tile Calorimeter cells using the cesium calibration system (Section 2.2.3). The goal of this analysis is to validate This calibration and its uniformity using the signals from cosmic ray muons. To achieve this it is required a high statistics so that the limit to the measurement results mainly from systematic errors. The quantity used for this purpose is the dE/dx (in MeV/mm) using the selection cuts described in the previous section. This quantity is calculated per radial layer

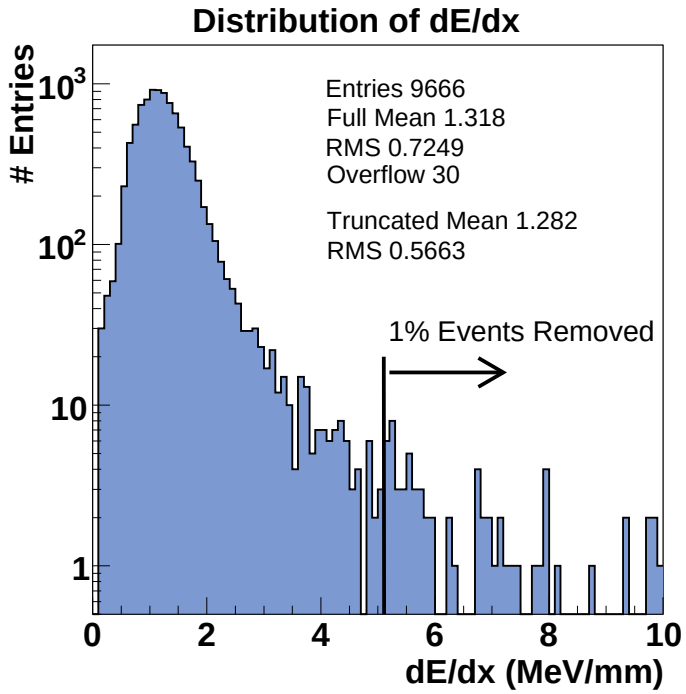

Figure 5.17: Distribution of energy loss (dE/dx) showing the region eliminated with a 1% truncation on the high energy tail.

using the segments that are the output of the TileMuonFitter. The segments are as already mentioned defined per partition, module and radial layer. In the present study the dE/dx is calculated per radial layer and for partition type: LB and EB. First a discussion over the systematic errors is presented and later the results are summarized.

Systematic errors

The contributions to the systematic errors are the following:

- One of the source of systematic errors is the definition of the selection cuts. A variation around the nominal values presented in the above section gives the sensitivity of the calorimeter to the measurement of the dE/dx to the cut definition. The sensitivity is the systematic error associated to this cut. This is applied for the energy, time difference, angular selection, z_{TMF} and x_{TMF} and truncation. A positive shift (nominal + ϵ) and a negative shift (nominal - ϵ) are applied to this variables to give the upper error limit

and a lower error limit and after half of the difference between this two variations is the systematic error for these contributions.

- For momentum and path a set of intervals within the existing data are used. For the momentum five intervals of 4 GeV/c are used. All these intervals have enough statistics so that systematic effects will be the dominant error. For the path five intervals with different width but equal statistics were chosen, since an approach with the same width bins would lead to several intervals limited by statistics, which would over estimate the contribution of this quantity to the systematic error. Half of the maximum difference between the bins is used to calculate the systematic error.

- The results presented refer to the radial layers on the bottom part of the cylinders, which results in another systematic contribution as the difference between the Top ($y > 0$) and the Bottom ($y < 0$). Half of the difference between the measurement on the two regions of the cylinder is used as the systematic error.

- Since the total data corresponds to measurements from 5 different runs the differences between these runs will also be a contribution to the systematic error. It should be added that these runs were taken within a relative small interval of time in the end of 2008. Half of the maximum difference between masurements is used to calculate the error.

- The global EM scale factor contribution encloses:

  – The systematics from the different calibration systems (Cesium, CIS, Laser and Integrator), the hysteresis effect of the magnetic field, the uncertainty of the radial depth length and the uncertainty of the EM scale from testbeam. Combining these contributions in quadrature a value of 0.7% is obtained.

  – The cesium calibration was made with the magnetic field off but cosmic ray muons data has been collected with the magnetic field on. In addition the up-drift measured by the cesium system must also be considered as a contribution to the final systematic errors. These two effects result in a value of -1% for the LB partitions and -0.6% for the EB partitions.

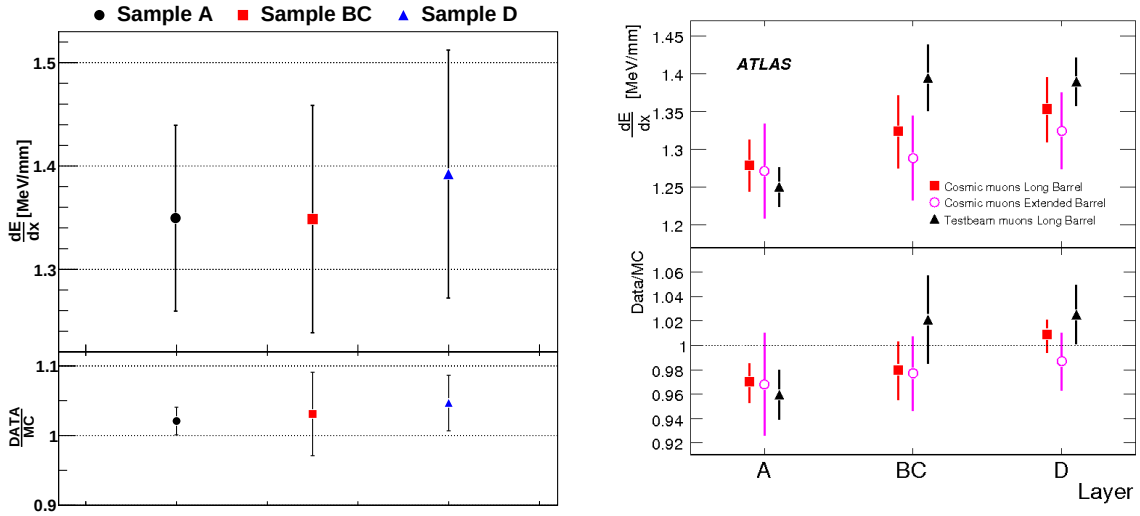

(a) TMF (b) IDtrack

Figure 5.18: Energy loss per radial layer using (a)the TMF for track reconstruction. The error bars are the systematics errors from Table 5.4 and (b) the IDtrack [18].

The results are summarized in Table 5.4 for the runs in the ID-COMM stream. For these runs there was a corresponding Monte-Carlo simulation and the systematics are also calculated for the simulated data. For last the same is done for the data and Monte-Carlo ratio. In Table 5.5 the systematic errors for a run in the RPC data stream are presented. The combination of the different errors is made by making the quadratic sum of the different contributions and no correlations are taken into account. However this is a conservative approach that results in an overestimation of the errors.

Results

The energy loss per radial layer results are summarized in Table 5.6 and Table 5.7. The values are the 1% truncated average of the dE/dx distribution. The errors are the systematic errors calculated as explained in the above section.

In Table 5.6 are presented the results for the ID-COMM stream. This is the same cosmic ray muons data used in the readiness paper [18] using a method referenced as ID-track that requires cosmic ray muons with a reconstructed track by the inner detector. So a direct comparison is possible between the two methodologies. In Figure 5.18(a) the main results are

		Long Barrel			Extended Barrel		
		A	BC	D	A	BC	D
TOP/BOTTOM	Data	± 0.000	± 0.005	± 0.013	± 0.016	± 0.010	± 0.008
	MC	± 0.016	± 0.009	± 0.023	± 0.026	± 0.010	± 0.004
	Data/MC	± 0.012	± 0.011	± 0.007	± 0.007	± 0.016	± 0.003
Z	Data	± 0.000	± 0.000	± 0.000	± 0.002	± 0.003	± 0.002
	MC	± 0.001	± 0.007	± 0.015	± 0.002	± 0.007	± 0.006
	Data/MC	± 0.001	± 0.006	± 0.012	± 0.003	± 0.007	± 0.006
X	Data	± 0.001	± 0.001	± 0.000	± 0.001	± 0.000	± 0.000
	MC	± 0.002	± 0.007	± 0.015	± 0.003	± 0.007	± 0.006
	Data/MC	± 0.001	± 0.006	± 0.012	± 0.001	± 0.006	± 0.005
Truncation	Data	± 0.066	± 0.047	± 0.054	± 0.070	± 0.045	± 0.048
	MC	± 0.051	± 0.032	± 0.041	± 0.048	± 0.039	± 0.037
	Data/MC	± 0.010	± 0.011	± 0.018	± 0.017	± 0.006	± 0.012
Time diff.	Data	± 0.002	± 0.007	± 0.002	± 0.018	± 0.015	± 0.006
	MC	± 0.006	± 0.010	± 0.016	± 0.008	± 0.011	± 0.008
	Data/MC	± 0.003	± 0.006	± 0.012	± 0.007	± 0.009	± 0.005
Energy	Data	± 0.013	± 0.004	± 0.029	± 0.048	± 0.028	± 0.035
	MC	± 0.025	± 0.011	± 0.040	± 0.110	± 0.039	± 0.057
	Data/MC	± 0.009	± 0.006	± 0.012	± 0.040	± 0.012	± 0.016
Theta	Data	± 0.003	± 0.002	± 0.000	± 0.000	± 0.000	± 0.000
	MC	± 0.005	± 0.008	± 0.016	± 0.002	± 0.007	± 0.006
	Data/MC	± 0.002	± 0.006	± 0.013	± 0.003	± 0.006	± 0.006
Path	Data	± 0.054	± 0.015	± 0.020	± 0.016	± 0.007	± 0.075
	MC	± 0.058	± 0.035	± 0.031	± 0.036	± 0.007	± 0.039
	Data/MC	± 0.009	± 0.039	± 0.018	± 0.028	± 0.028	± 0.051
Momentum	Data	± 0.015	± 0.104	± 0.095	± 0.031	± 0.093	± 0.042
	MC	± 0.017	± 0.073	± 0.068	± 0.023	± 0.062	± 0.059
	Data/MC	± 0.004	± 0.024	± 0.016	± 0.014	± 0.051	± 0.036
5 runs	Data	± 0.008	± 0.011	± 0.012	± 0.024	± 0.028	± 0.024
	MC	—	—	—	—	—	—
	Data/MC	± 0.006	± 0.009	± 0.009	± 0.018	± 0.021	± 0.018
Global EM scale factor	Data	+0.005 -0.013	+0.005 -0.013	+0.005 -0.014	+0.000 -0.008	+0.000 -0.008	+0.000 -0.008
	MC	—	—	—	—	—	—
	Data/MC ratio	+0.004 -0.010	+0.004 -0.010	+0.004 -0.010	+0.000 -0.006	+0.000 -0.006	+0.000 -0.006
TOTAL	Data	+0.088 -0.089	± 0.117	+0.116 -0.117	± 0.098	± 0.012	± 0.107
	MC	± 0.084	± 0.090	± 0.102	± 0.130	± 0.085	± 0.098
	Data/MC ratio	+0.022 -0.024	± 0.052	+0.043 -0.044	± 0.058	+0.066 -0.067	± 0.096

Table 5.4: Systematic error for the energy loss measurement using data from the ID-COMM physics stream. The total error is the quadratic sum of the different contributions. The Global EM scale factor is the one included in the Tile Calorimeter readiness paper for collisions [18]

	Long Barrel			Extended Barrel		
	A	BC	D	A	BC	D
TOP/BOTTOM	± 0.035	± 0.018	± 0.020	± 0.008	± 0.020	± 0.014
Z	± 0.000	± 0.000	± 0.000	± 0.000	± 0.000	± 0.000
X	± 0.000	± 0.000	± 0.000	± 0.000	± 0.000	± 0.000
Truncation	± 0.053	± 0.039	± 0.046	± 0.082	± 0.053	± 0.040
Time diff.	± 0.004	± 0.006	± 0.004	± 0.006	± 0.006	± 0.003
Energy	± 0.001	± 0.005	± 0.023	± 0.046	± 0.020	± 0.037
Theta	± 0.005	± 0.003	± 0.005	± 0.008	± 0.006	± 0.002
Path	± 0.067	± 0.062	± 0.058	± 0.088	± 0.020	± 0.127
Momentum	± 0.013	± 0.054	± 0.035	± 0.029	± 0.042	± 0.055
Global EM scale factor	+0.005 -0.013	+0.005 -0.013	+0.005 -0.014	+0.000 -0.008	+0.000 -0.008	+0.000 -0.008
TOTAL	+ 0.094 - 0.095	+ 0.094 - 0.094	+ 0.088 - 0.088	+ 0.133 - 0.133	+0.076 -0.077	+ 0.150 - 0.150

Table 5.5: Systematic error for the energy loss measurement using data from the RPC data stream. The total error is the quadratic sum of the different contributions. The Global EM scale factor is the one included in the Tile Calorimeter readiness paper for collisions [18]

Radial layer		A	BC	D
ID-COMM,LB	Data	1.35 ± 0.09	1.35 ± 0.12	1.39 ± 0.12
	MC	1.32 ± 0.08	1.31 ± 0.09	1.33 ± 0.10
	Data/MC	1.02 ± 0.02	1.03 ± 0.05	1.05 ± 0.04
ID-COMM,EB	Data	1.29 ± 0.10	1.31 ± 0.11	1.31 ± 0.11
	MC	1.33 ± 0.13	1.30 ± 0.09	1.32 ± 0.10
	Data/MC	0.97 ± 0.06	1.01 ± 0.07	0.99 ± 0.10
TB, LB	Data	1.25 ± 0.03	1.39 ± 0.04	1.39 ± 0.03
	MC	1.30 ± 0.02	1.30 ± 0.03	1.36 ± 0.02
	Data/MC	0.96 ± 0.02	1.02 ± 0.04	1.02 ± 0.02
Double ratio ID-COMM		1.06 ± 0.03	1.01 ± 0.07	1.03 ± 0.05

Table 5.6: Energy loss 1% truncated mean [MeV/mm] for ID-COMM. The errors are systematic uncertainties from Table 5.4. Results from 2000-2003 testbeam for 11-20 GeV/c muon spectra. The double ratio divided Data/MC from cosmics with Data/MC from testbeam (Eq. 5.2).

summarized. From the table it is shown that for the LB the energy loss is equal for the A and BC layer, and higher by 0.04 MeV/mm for the D layer. For the Monte Carlo all three radial layers have an equal performance and the results from the ratio of data and Monte Carlo show that the agreement is better that 3% for the A and BC layer but larger for the D layer with a value of 5%. The systematics are typically of the order of 0.10 MeV/mm. For the EB the results of the energy loss per radial layer are measured to be smaller, with the radial layer A smaller in 0.03 MeV/mm that the other two layers. The Monte-Carlo agreement is 3% for the A layer and 1% for the BC and D layer. The order of magnitude of the systematics is the same. This leads to a conclusion that within the measured systematic errors the response for data is well reproduced by the Monte-Carlo.

From the ID-track analysis (Figure 5.18(b)) a difference between radial layer A and D of the order of 5% is measured for EB and LB partition. In the TMF analysis a smaller difference of only 3% is measured, however the systematic errors are twice the ones in the ID-track and these two results can be considered compatible.

The results from cosmic ray muons are also compared with the testbeam measurements with muons produced in the decay of 20 GeV pions. The muons had a spectra of 11-20 Gev/c and peaking at 17 GeV/c coming from the decay of 20 GeV pions. To compare the two experimental quantities their will be systematics associated with the setup and used spectra. As expressed in the table a double ratio is calculated,

$$Double\ ratio\ =\ \frac{\left(\frac{dE}{dx}\right)^{data}_{cosmics}}{\left(\frac{dE}{dx}\right)^{MC}_{cosmics}} \times \frac{\left(\frac{dE}{dx}\right)^{MC}_{testbeam}}{\left(\frac{dE}{dx}\right)^{data}_{testbeam}} \tag{5.2}$$

This quantity checks if the energy scale transport from the testbeam was done successfully. The results show that the energy scale in the Tile Calorimeter installed in the experimental cavern and the modules measured in testbeam the agreement is better than 6%.

In Table 5.7 are the results per layer using the RPC data stream. The agreement of the two data streams is of the order of 1% for the three radial layers of the LB partition. The systematic errors are larger being now of the order of 0.14 MeV/mm. For the EB the disagreement between

Radial layer	A	BC	D
RPC, LB	1.33 ± 0.09	1.34 ± 0.09	1.38 ± 0.09
RPC, EB	1.43 ± 0.13	1.39 ± 0.08	1.42 ± 0.15
ID/RPC, LB	1.01 ± 0.14	1.01 ± 0.16	1.01 ± 0.16
ID/RPC, EB	0.90 ± 0.18	0.94 ± 0.15	0.92 ± 0.20

Table 5.7: Truncated mean and the systematic uncertainties [MeV/mm] for RPC data stream.

the two streams is larger, of the order of 10% for the A layer, 6% for the BC layer and 8% for the D layer. However in the EB results the difference between layers is still small and of the order of 4%.

Concluding, the TMF method has systematic errors that typically duplicate the ones for ID-track. However and even so the overall results confirm that the EM energy scale has been reproduced within 6%. The result of discrepancy between the D and A layer provides an independent confirmation of a significant result, that could be related with problems in the inter-calibration procedure. This should be checked in collisions data in future work.

5.8 Azimuthal energy response

The main advantage of the TMF is that the reconstruction only depends on the Tile Calorimeter signal and for that reason this method is more adequate to access the full coverage in ϕ. The ID-track method provides only a partial coverage which is due to the requirement of a reconstructed track in the inner detector. When separating the data among many ϕ slices, it is necessary to ensure that each slice has enough statistics to provide a meaningful measurement of the 1% truncated mean. So a requirements of at least 100 events is placed on each slice.

Figure 5.19 shows the ϕ uniformity using the ID-COMM stream and calculating the energy loss per module (slice in ϕ) using the TMF algorithm. The top of these figures shows the normalized energy loss the bottom part its ratio with Monte Carlo. The results show that there are some biases in the method that cancel when comparing with simulated data. So the ϕ uniformity in this analysis is limited by these systematics. It is also evident that although the uniformity for energy loss results are within a window of ± 5%, and that the uniformity

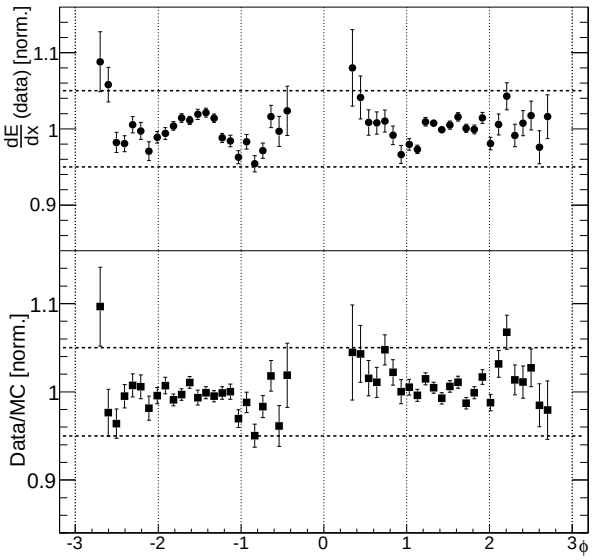

Figure 5.19: Energy loss for the radial layer A using ID-COMM stream data and ratio with Monte-Carlo simulated data.

Data stream	Layer	# modules	< > ± rms [MeV/mm]
RPC	A	64 (100%)	1.30 ± 0.05
	BC	50 (78%)	1.26 ± 0.06
	D	40 (62%)	1.33 ± 0.06
ID-COMM	A	49 (76%)	1.32 ± 0.04
	BC	47 (73%)	1.30 ± 0.04
	D	46 (72%)	1.38 ± 0.05

Table 5.8: Long barrel uniformity results for the RPC data stream and the ID-COMM stream.

of the data/MC ratio is considerably better, the coverage in ϕ is incomplete.

So two factors contribute to a limited coverage in ϕ: the algorithm as is the case of the IDtrack and the physics stream. In order to achieve a full coverage in the uniformity study, the RPC data stream is used.

In Figure 5.20 the uniformity results are presented for the three radial layers for the LB partitions. The results from the LBA and LBC partitions are combined to improve statistics. For all radial layers the data points are within the ± 5% window. The corresponding histograms are in Figure 5.21 for data. The values entering the histogram are weighted with the statistics of each ϕ slice. The numbers are all collected in Table 5.8.

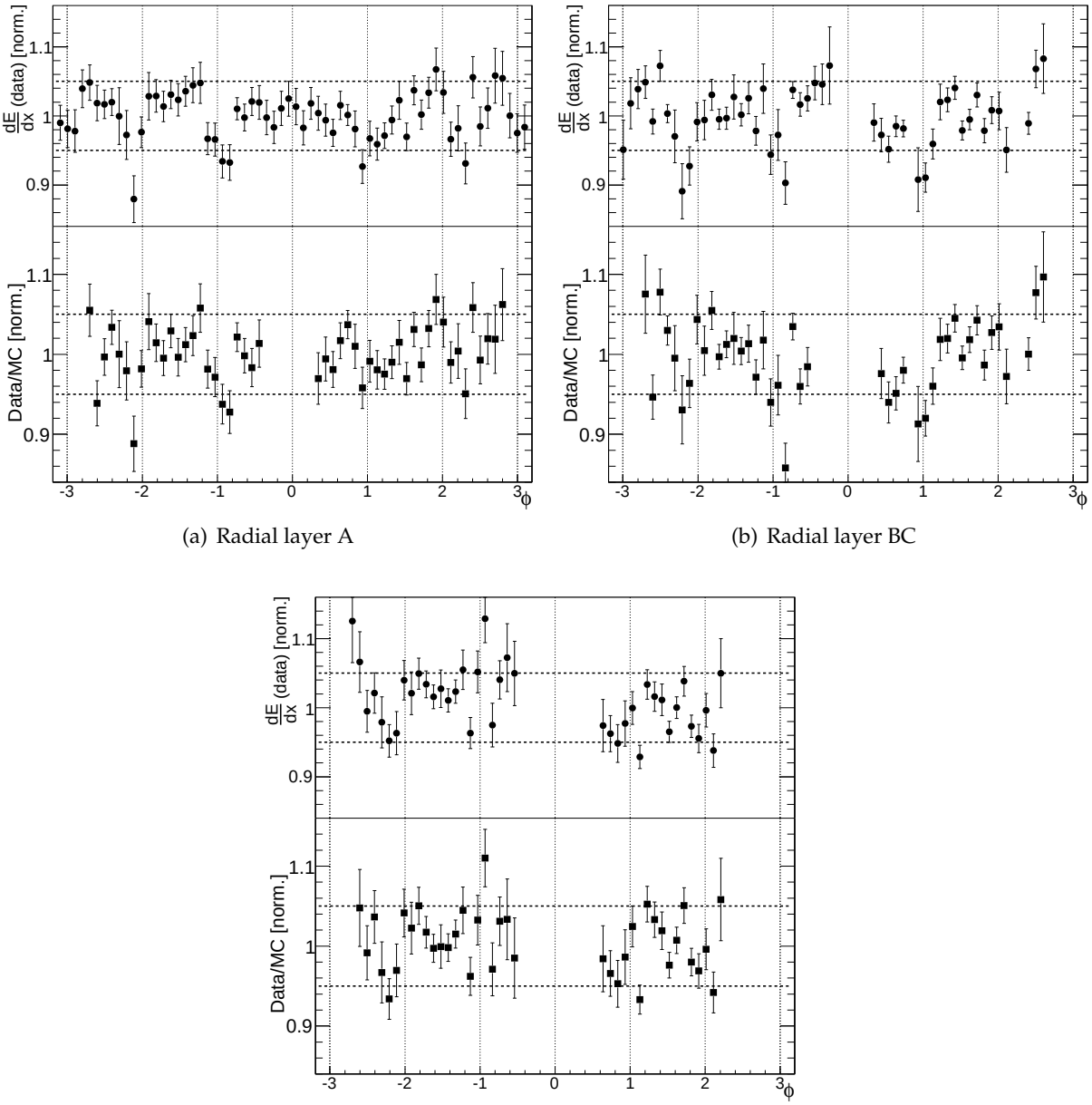

(a) Radial layer A

(b) Radial layer BC

(c) Radial layer D

Figure 5.20: Uniformity in ϕ of the energy loss for the three radial layers of LB. The results combine the two LB partitions LBA and LBC. This option is to compensate for low statistics. The ratio of data points with Monte-Carlo are also given for each radial layer. The Monte-Carlo, as mentioned before, only uses the TRT volume which explains that not all data points have a correspondent data/MC value.

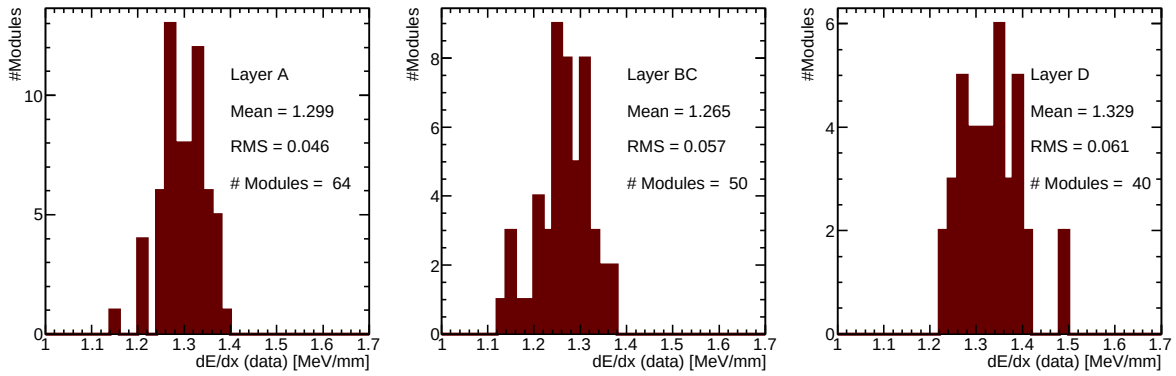

(a) RPC data stream

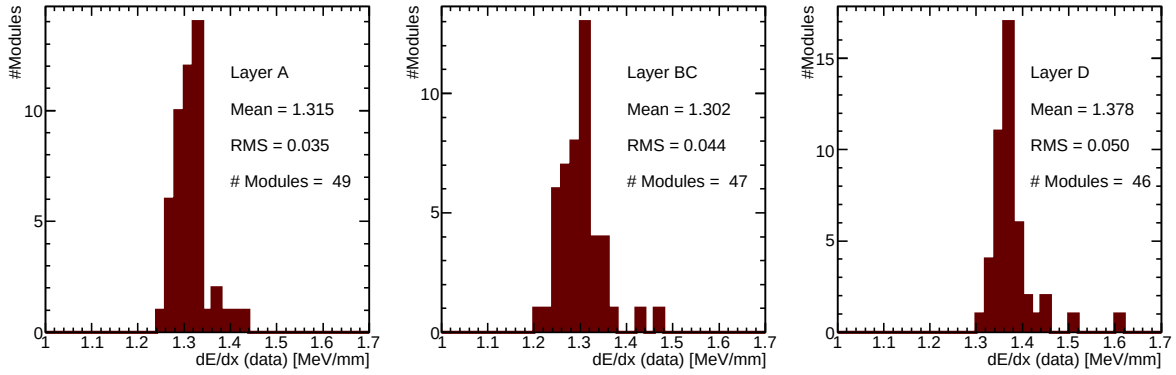

(b) ID-COMM stream

Figure 5.21: Weighted average module energy loss for each radial layer of the LB. The results combine the two LB partitions LBA and LBC. This option is to compensate for low statistics. The results for the two physic stream are presented for comparison.

Data stream	Layer	# modules	< > ± rms [MeV/mm]
RPC	A	60 (94%)	1.35 ± 0.05
	BC	47 (73%)	1.29 ± 0.06
	D	40 (62%)	1.32 ± 0.07
ID-COMM	A	18 (28%)	1.19 ± 0.05
	BC	23 (36%)	1.24 ± 0.06
	D	27 (42%)	1.22 ± 0.05

Table 5.9: Extended barrel uniformity results for the RPC data stream and the ID-COMM stream.

For the RPC data stream each radial layer the *rms*/*mean* are calculated giving 0.035, 0.045 and 0.045 for the radial layer A, BC and D respectively. A uniformity that is better that 5% is measured for the RPC data stream. For the ID-COMM stream the corresponding *rms*/*mean* values are 0.026, 0.034 and 0.036 for the radial A, BC and D layers respectively. For the ID-COMM stream the uniformity is better than 4%. Only for layer A the population is larger for the RPC data stream, for the other two radial layers ID-COMM is able to pair or overcome in population.

For the EB partitions the results are in Figure 5.22. As before EBA and EBC results are combined. All radial layers the data points are set within the ±5%. The histograms are in Figure 5.23 and numbers are collected in Table 5.9. For the RPC data stream each radial layer the *rms*/*mean* ratios are calculated giving 0.034, 0.045 and 0.051 for the A, BC and D layers respectively. A uniformity that is better that 5% is measured for the RPC data stream data stream. For the ID-COMM stream the corresponding *rms*/*mean* values are 0.044, 0.047 and 0.037 for the A, BC and D layers respectively. For the ID-COMM stream the uniformity is again better than 5%. For the extended barrel partitions is in fact clear that the larger population is achieved when using the RPC data stream.

Concluding the uniformity is ϕ measured with the TMF algorithm is better than 5%. This is within the detector requirements where a 10% uniformity is required [15].

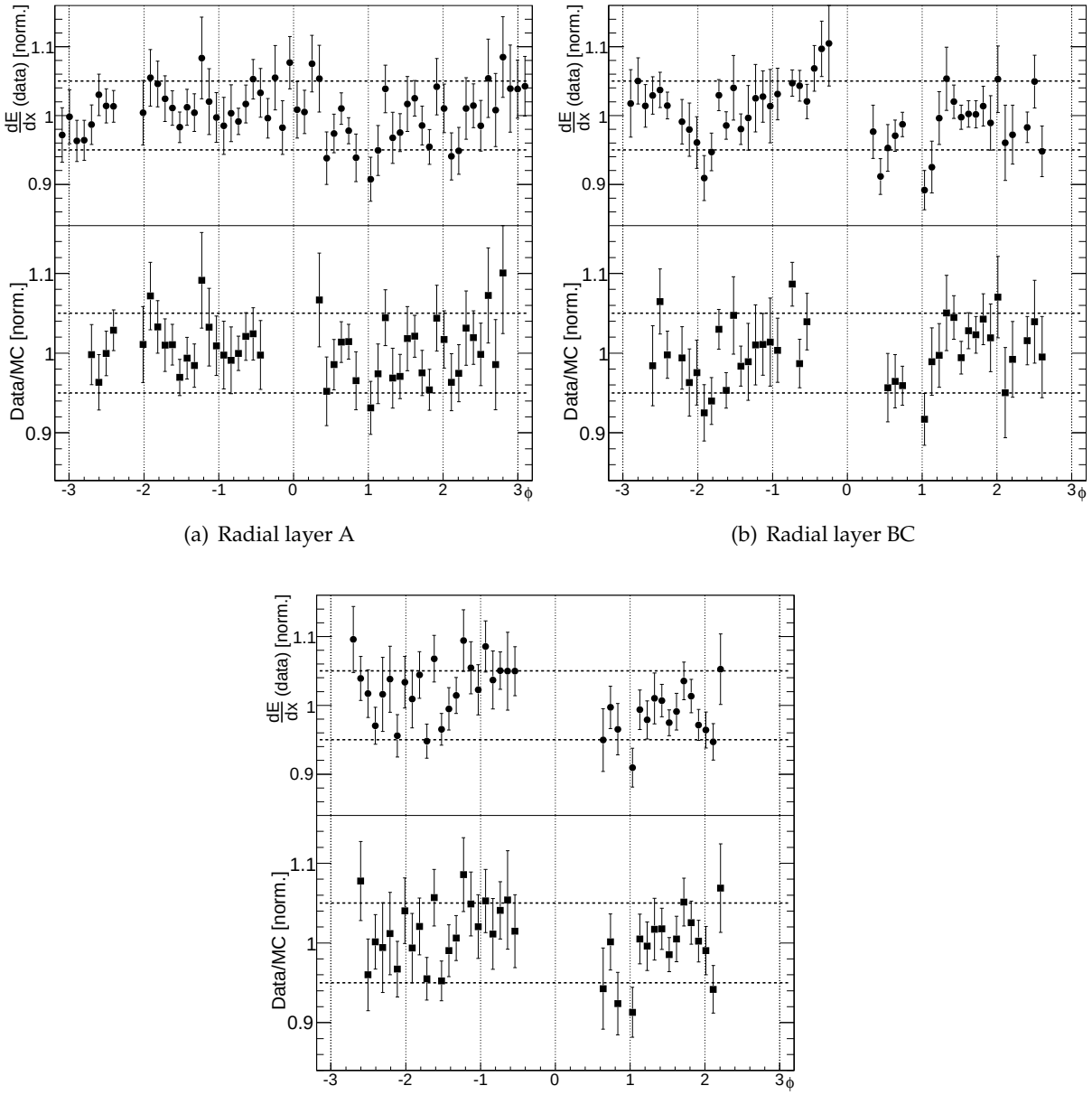

(a) Radial layer A

(b) Radial layer BC

(c) Radial layer D

Figure 5.22: Uniformity in ϕ of the energy loss for the three radial layers of EB. The results combine the two EB partitions EBA and EBC. This option is to compensate for low statistics. The ratio of data points with Monte-Carlo are also given for each radial layer. The Monte-Carlo, as mentioned before, only uses the TRT volume which explains that not all data points have a correspondent data/MC value.

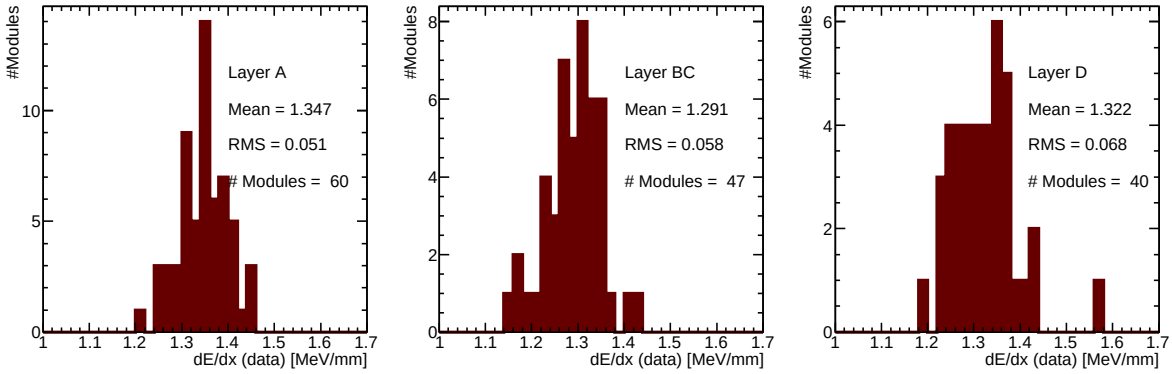

(a) RPC data stream

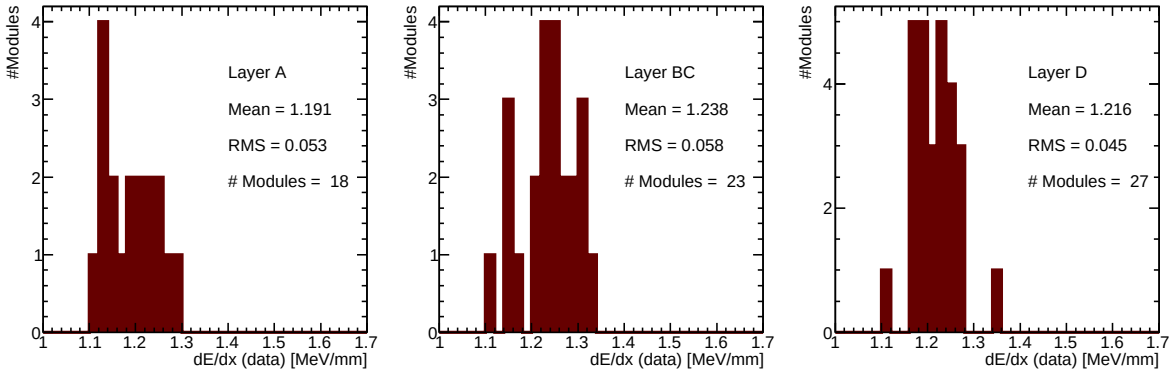

(b) ID-COMM stream

Figure 5.23: Weighted average module energy loss for each radial layer of the EB. The results combine the two EB partitions EBA and EBC. This option is to compensate for low statistics. The results for the two physic stream are presented for comparison.

6 Synchronization of the ATLAS Tile Calorimeter with cosmic ray muons

6.1 TileCal Time Calibration

Laser system and timing

The laser system main purpose was described in Section 2.2.2. It has been used also to monitor the Tile Calorimeter time response and produce calibration constants to synchronize all channels. This procedure requires the usage of a high amplitude pulse in order to take advantage of the higher time resolution but at the same time the amplitude should avoid saturation that tends to distort the signal shape and deteriorate the time response [29].

The Tile Calorimeter channels synchronization is achieved in three stages: Intra-module calibration, Inter-module calibration and Inter-partition calibration.

The distribution of the 40 MHz sampling clock along a Tile Calorimeter module can arrive at different times to the different digitizers of a module (to each digitizer of a module are connected up to 6 photomultipliers). The corrections of these phases between and within digitizers is what is called the **Intra-module calibration**. This signal is distributed to the different modules through TTC fibers that have different lengths producing a time delay between the different modules. Differences of the order of 40 ns were measured in the early phase of the commissioning [29]. To these correction is called **Inter-module calibration**. Finally a global time shift should also be observed between partitions due to the different TTC fibers distribution and the correction of these shifts is the **Inter-partition calibration**.

Contributions from hardware to the Tile Calorimeter timing

The hardware components that can contribute to the channels time offsets are separated in three groups. In the first group are the contributions not corrected with the laser system, in the second group the contributions that are corrected by the laser system and in the third group the ones introduced by the laser system.

Not corrected with the laser system:

– *Propagation time in Tile Calorimeter optics*

This results from the difference of lengths of WLS fibers that read-out the scintillating tiles and transport the light signal from cells to PMTs. The fiber lengths varies between 73 cm and 232 cm [12] [14] [13]. The light guides are all of the same size and the differences in length of the scintillating tile is small when compared with the length of the WLS fibers. So, the contribution of scintillating tiles and light guides may be neglected when compared with the one from WLS optical fibers.

– *Particle's Time of flight*

The time of flight of particles to different regions of the calorimeter must be corrected for during the LHC data taking. This requirement is a consequence of the restriction to a single iteration of the optimal filter algorithm during LHC data taking. During the LHC operation there is an unique time reference that is the proton bunches crossing time at the interaction point (IP). All channels have a time of flight correction setting the time of all channels to zero for particles coming from the interaction point and travelling with a velocity close to the speed of light.

Corrected with the laser system:

– *Distribution of TTC signals to modules*

The TTC fibers lengths need to be of different sizes due to the dimensions of the detector and length differences up to 40 m are necessary. These were verified experimentally and main results were presented in Chapter 4. The resulting time differences must be taken into account and corrected to avoid delays in the

distribution of the 40 MHz clock and L1A signals.

– *Distribution of TTC signals inside a module*

The TTC signals arriving to each module are distributed to the different digitizers in a drawer. These signals enter each drawer through a Drawer Interface Card and have to travel a path that can go up to ~ 1.5 m resulting in differences on the arrival of TTC signals to the different digitizers in a module.

– *Propagation of the electric signal*

A difference of time between low gain (LG) and high gain (HG) signals of the order of 2 ns with a $\sigma_{LG+HG} = 0.38\ ns$ was measured. This time difference should be taken in account when comparing HG and LG measurements.

Introduced by the laser system

– *Distribution of the laser signal by clear fibers*

The clear fibers lengths and velocity of propagation of light must be known with an accuracy that does not compromise PMT's time delays measurements and corresponding calibration. These are sources of systematic uncertainties in the laser synchronization.

Correction of the channel time

The time calibration can be achieved using the laser system. This is done in three stages: within modules, between modules and between partitions. It makes use of the Tile Calorimeter internal clock delays either in the digitizers ADCs, for fine tuning in units of 104 ps, or in the TileDMUs, for coarse tuning in units of 25 ns. This allows us to implement the needed hardware corrections for the time calibration of front-end electronics (FEE) digitizers within modules, between modules and partitions [29]. These corrections produce a time calibration between digitizers which can hold up to 6 PMTs. To calibrate the individual PMTs the calculation of *residuals* is mandatory. The residuals are the time offsets for each PMT that cannot be corrected by adjusting hardware settings. These are calculated applying for each

PMT *i* of a digitizer *j* the next expression:

$$r_i^j = t_i^j - n_j^{pipeline} \times 25 - n_j^{digitizer} \times 0.104$$

with:

$\mathbf{r_i^j}$ Calculated residuals of PMT i of digitizer j;

$\mathbf{t_i^j}$ Time of PMT i that is coupled to digitizer j;

$\mathbf{n_j^{pipeline}}$ The units of coarse tuning are given by the integer part [1] of the digitizer time

$$t_j^{digitizer} = \frac{1}{n}\sum_{i=1}^{n} t_i^j$$

divided by 25 ns:

$$n_j^{pipeline} = \left\lfloor \frac{t_j^{digitizer}}{25} \right\rfloor$$

$\mathbf{n_j^{digitizer}}$ The units of fine tuning are given by the integer part of the digitizer time after applying the coarse tuning divided by 0.104 ns:

$$n_j^{digitizer} = \left\lfloor \frac{t_j^{digitizer} - n_j^{pipeline} \times 25}{0.104} \right\rfloor$$

The residuals, $n_j^{pipeline}$ and $n_j^{digitizer}$ are introduced in a calibration database and applied during the event reconstruction.

6.2 Measurement of the effective speed of light in the laser fibers

The characteristics of the optical fibers used to distribute the laser signal to the different photomultipliers – laser fibers – must be taken in account when doing the time intra-calibration of the Tile Calorimeter. In Table 6.1 and Table 6.2 the laser fibers lengths, for

[1] The integer part of a number is usually expressed by incomplete brackets like $\lfloor x \rfloor = max\{ n \in \mathbb{Z} \mid n \leq x \}$

each photomultiplier and digitizer are given [48]. In the third column in this table shows the time corrections that compensate the clear fibers length differences and are one of the elements necessary to synchronize a super-drawer. These time corrections are made relatively to the first channel of the super-drawer (the one with shorter fiber length) and are obtained from:

$$\begin{aligned} t^{v_{cf}}_{correction}(j) &= \delta T^{v_{cf}}(j) - \delta T^{v_{cf}}(1) = \frac{L_{cf}(j)}{v_{cf}} - \frac{L_{cf}(1)}{v_{cf}} \\ &= \frac{L_{cf}(1) - L_{cf}(j)}{v_{cf}} \end{aligned}$$

where,

$t^{v_{cf}}_{correction}(j)$ is the time correction for channel **j** using a speed of light of v_{cf}.

$\mathbf{L_{cf}(j)}$ is the length of the clear fiber connected to channel **j**.

$\mathbf{v_{cf}}$ is the speed of light in clear fibers.

The name for v_{cf}, speed of light, is used for simplicity. The average speed of the light in the fiber body is determined by other factors besides its refraction index. The path, depending if the fibers follow a straight path or a curved path, and dimensions, radius and length, or even defects in the fiber also have a contribution simply because of the increase in the number of reflections necessary for the light to travel across the fiber length. From the analysis with the single beam data it was observed that in each partition the synchronization with the laser system was achieved within 2 ns. This included a residual slope that is visible when plotting the time as function of z. An hypothesis was that the slope resulted from using a wrong speed of light in the laser calibration. The used value was $v_{cf} = 22.5\ cm\ ns^{-1}$ that had been obtained from rough estimates from the laser data itself.

6.2.1 Single beam measurements

Before exploring the hypothesis, just enunciated, it is necessary to say more about the measurements with the single beam. The single beam refers to muons produced by a LHC beam colliding in a collimator, and this was presented earlier in Section 4.5 and here only the

PMT		Length [cm]	Time Correction [ns]	Digitizer
1	2	167.1	0	
3	4	178.7	0.52	#1
5	6	190.3	1.03	
7	8	201.9	1.55	
9	10	213.5	2.06	#2
11	12	225.1	2.58	
13	14	236.7	3.09	
15	16	248.3	3.61	#3
17	18	259.9	4.12	
19	20	271.5	4.64	
21	22	283.1	5.16	#4
23	24	294.7	5.67	
25	26	201.9	1.55	
27	28	213.5	2.06	#5
29	30	225.1	2.58	
31	-	236.7	3.09	
-	34	248.3	3.61	#6
35	36	259.9	4.12	
37	38	271.5	4.64	
39	40	283.1	5.16	#7
41	42	294.7	5.67	
43	-	306.3	6.19	
45	46	317.9	6.70	#8
47	48	329.6	7.22	

Table 6.1: Clear fiber lengths for each photomultipliers of the Tile Calorimeter long barrel and corresponding relative time corrections.

PMT		Length [cm]	Time Correction [ns]	Digitizer
1	2	51.1	0	
3	4	62.7	0.52	#1
5	6	74.3	1.03	
7	8	85.9	1.55	
9	10	97.5	2.06	#2
11	12	109.1	2.58	
13	14	120.7	3.09	
15	16	132.3	3.61	#3
17	18	143.9	4.12	
21	22	167.1	5.16	
23	24	178.7	5.64	#4
29	30	213.5	7.21	
33	34	236.7	8.25	#6
37	38	271.5	9.28	
41	42	283.1	10.31	#7
43	44	294.7	10.83	

Table 6.2: Clear fiber lengths for each photomultipliers of the Tile Calorimeter extended barrel and corresponding relative time corrections.

details related with the analysis are presented. From the 2008 single beam data a selection of events was made, requiring events with a total energy per event below 500 GeV in order to avoid the events with very high multiplicity and a minimum energy per cell of 300 MeV. The average time measured for cells with the same z coordinate i.e. the average over 64 modules is referred in the following as the cell time. The measured cell time using single beam data is presented in Figure 6.1(a). The plot on the left represents the effective time i.e. the cell time obtained from the reconstruction of the physics signal. The collimator where the proton beam collided or scraped is located 140 m of the interaction point. The Tile Calorimeter has approximately $\sim$ 12 m in length (along z). For a particle travelling with a speed c there are cell time measurements that can differ up to ~ 40 ns. The length of the four partitions is roughly the same and of the order of 3 meters which results in time differences inside each partition up to 10 ns only due to the particles time of flight. This is confirmed by the measurements in this figure, where for each partition a difference of 10 ns is measured. Introducing the time of

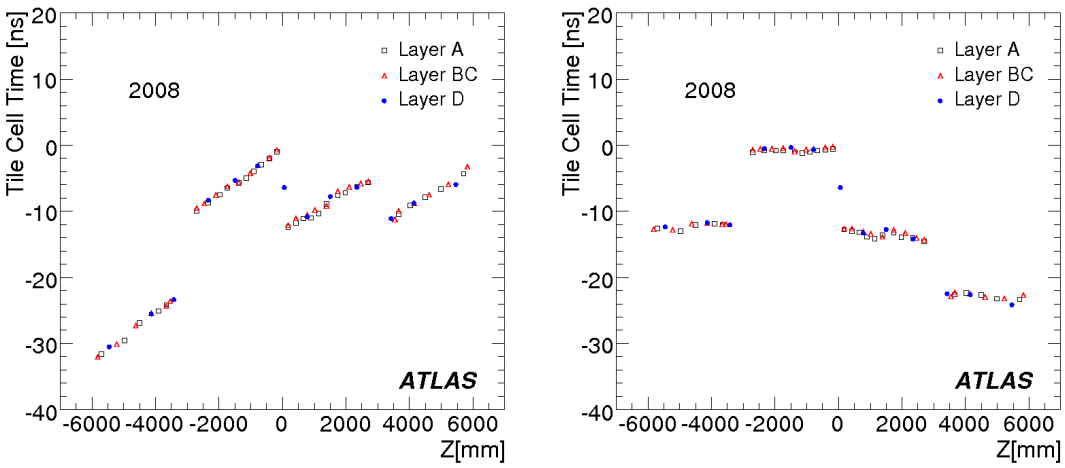

(a) Time of Tile Calorimeter cells

(b) Time of Tile Calorimeter cells with time of flight correction

Figure 6.1: Tile Calorimeter cells time measured with single beam 2008 data against the cell coordinate z: (a) Time measured showing slopes that result from the different distances to the collimator (b) Correcting for the time of flight of muons crossing the different calorimeter cells.

flight correction the cell time $T^{v_{cf}}(j,k)$ is obtained:

$$T^{v_{cf}}(j,k) = \frac{T^{v_{cf}}(j) + T^{v_{cf}}(k)}{2} + \frac{d_{cell}^{collimator}(j,k)}{c}$$

where:

- The first term is the average time between the two photomultipliers **j** and **k** that read a cell.
- The second term represents the time of flight (ToF) of the particle hitting the cell.

This is applied to all cells and results are presented in Figure 6.1(b), where It is seen that two partitions are equalized between themselves: EBC and LBA. For the other two an offset as large as 10 ns is measured. This was something expected since no inter-partition calibration was applied at that time (October 2008). Each partition is also characterized by a small residual slope.

The observed residual slopes in each partition have the following characteristics:

- A positive slope for the C-side i.e. $z < 0$.
- A negative slope for the A-side i.e. $z < 0$.
- The three radial layers have different radial positions in the detector. If the time of flight offset introduced above was not correct, then three lines with an offset between them should be seen for each partition, and an angular correction on the cell position would be necessary. This is not the case since the distance from the collimator to the tile cells is much larger than the height of a Tile Calorimeter module. The implemented time of flight correction is then precise enough.

The difference in slopes signal is an indication that in fact the origin of this slope can result from using a wrong velocity v_{cf}t in the laser synchronization. The laser signal is inserted for every module in the center of the long barrel and in the inner side of the extended barrels, and the systematic effect due to the distance travelled by the injected laser pulse should have this slope asymmetry.

6.2.2 Influence of v_{cf} in the synchronization of Tile Calorimeter cells

To test the hypothesis the natural procedure is to change the parameter v_{cf} and measure how the slope dt/dz is modified. In the measured time $T_{cell}(i)$ this correction is already built in for each PMT:

$$T^{v_{cf}}(j) = T(j) + \delta T^{v_{cf}}(j)$$

resulting for a cell readout by the pair (j,k) a correction $\delta T^{v_{cf}}_{cell}(j,k)$

$$\delta T^{v_{cf}}(j,k) = \frac{\delta T^{v_{cf}}(j) + \delta T^{v_{cf}}(k)}{2}$$

Finally, the contribution on time for different values of v_{cf} is given by:

$$T^{probe}(j,k) = T^{nominal}(j,k) - \delta T^{nominal}(j,k) + \delta T^{probe}(j,k)$$

where

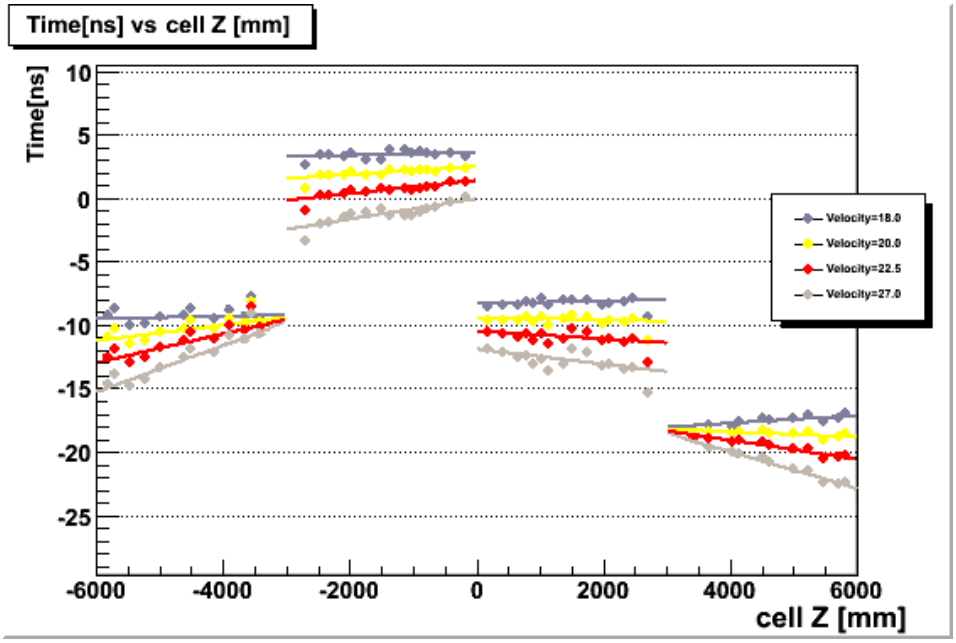

Figure 6.2: The cell time against the z coordinate of each cell for different values of v_{cf}.

$T(j,k)$ The cell readout by photomultipliers j and k.

$\delta T(j,k)$ The time difference between the two channels j and k of a cell.

The *nominal* means that a value $v_{cf} = 22.5\ cm/ns$ is used and *probe* means that a velocity different from nominal is used to test the hypothesis. In Figure 6.2 the tests done using four different values for v_{cf}

18.0, 20.0, 22.5 and 27.0 cm/ns

show that the variation of v_{cf} results on a variation of the slope dt/dz. This result confirms what was previously enunciated: for lower values of v_{cf} a smaller slope is obtained, and this is true all the four partitions. Since a fiber length is associated to a cell with coordinate z, these time measurements can be presented in a way which directly relates the three physical quantities that are the core of this analysis:

- The clear fibers length.
- The time measured for a given cell.
- The speed of light in the clear fibers v_{cf}.

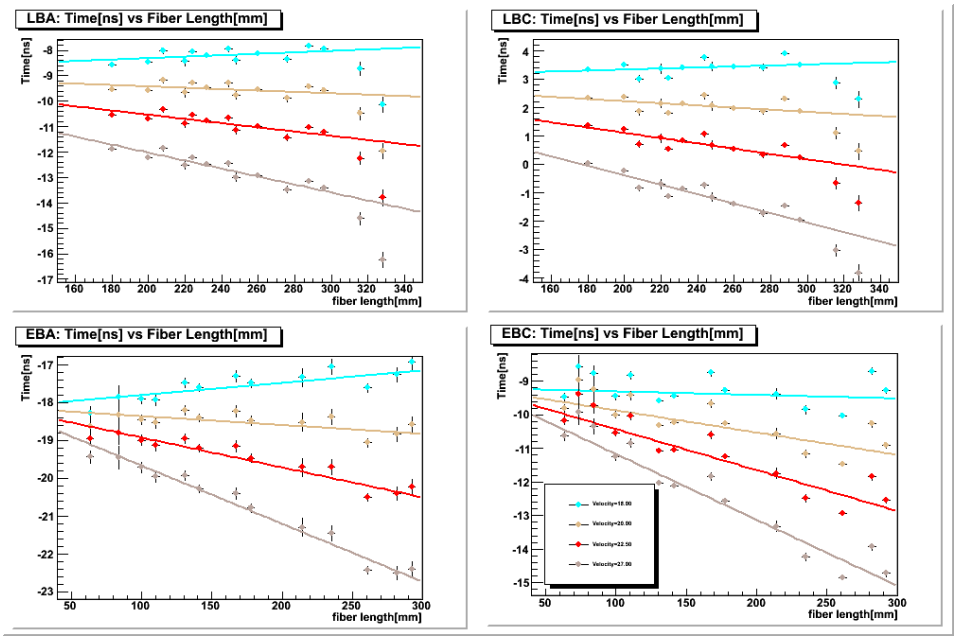

Figure 6.3: The cell time against the clear fiber length for different values of v_{cf}.

In Figure 6.3 the cell time is plotted against the clear fiber lengths for different values of v_{cf}. As before and as expected the same behaviour is observed, for a lower value of v_{cf} the difference between the cells time for the different clear fiber lengths is smaller i.e. the slope dt/dL is smaller.

The next step is to determine the v_{cf} value that for each partition results in a slope equal to zero. In the above figures it is seen that this optimum value must differ among partitions. Once more this shows that the speed that is measured is an effective speed that depends on the path length the light travels before reaching each cell. So a more detailed analysis using a larger number of velocities is made. The fine scan is done both for the dt/dz slope and dt/dL slope and the results are shown in Figure 6.4. For each approach in Figure 6.4 the values of v_{cf} for which the slope is equal to zero are between 17.1 cm/ns and 19.1 cm/ns as seen in Table 6.3.

in Table 6.3.

From the above results it can be concluded that the two approaches are compatible within 0.1 cm/ns for EBC, LBA and EBA and 1.5 cm/ns for LBC. For the average the agreement of the order of 0.3 cm/ns. Globally it can be stated that the speed of light in the laser fibers as used in the laser calibration is overestimated in approximately 4 cm/ns and that the hypothesis

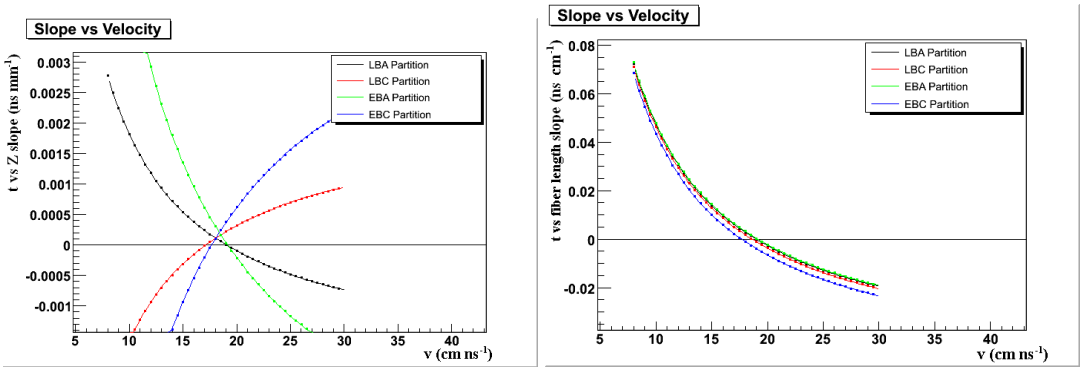

Figure 6.4: A fine scan on v_{cf}: (LEFT) The slope dt/dz vs v_{cf} (RIGHT) the slope dt/dL vs v_{cf}.

Partition	$dt/dz = 0$ Speed (cm/ns)	$dt/dL = 0$ Speed (cm/ns)
EBC	17.7	17.7
LBC	17.1	18.6
LBA	19.1	19.0
EBA	19.1	19.1
Average	18.3	18.6

Table 6.3: Speed of light in clear fibers in the four Tile Calorimeter partitions.

introduced in the beginning indeed solves the time residual lack of synchronization observed in the single beam measurements.

6.2.3 Systematics errors

In the measurement described in the above lines two sources of systematic errors are evident: distance between the collimator ($\sigma_{distance}$) and the Tile Calorimeter cell and the length of the clear fibers (σ_{length}).

Distance between the collimator and the Tile Calorimeter cell

The distance from the collimator should be different depending on the cell position in the Tile Calorimeter volume. The height of the tile calorimeter is 1500 mm and the distance of the collimator to the interaction point is 140000 mm. The difference between these two quantities limits the contribution of this error, since the time of flight to a cell is calculate using:

$$ToF = \frac{d}{c} = \frac{\sqrt{(d_{collimator} - z_{cell})^2 + d_{cell}^2}}{c}$$

where,

$d_{collimator}$ is the distance from the collimator to the ATLAS interaction point;

z_{cell} is the z-axis coordinate of the cell geometric center;

$d_{cell} = \sqrt{x_{cell}^2 + y_{cell}^2}$ is the distance to the z-axis of the cell geometric center.

The tile calorimeter height ($r_{out} - r_{in}$) and length are used to measure the maximum error introduced by the methodology described above. For this extreme case it is $d_{collimator}$ = 146000 mm and d_{cell} = 1500 mm. The value $d_{collimator}$ for the distance to the cell corresponds to a time-of-flight of 487.02 ns. Using the above equation where the position of the cell in the detector volume is considered a time-of-flight of 487.04 ns is obtained. A 0.02 ns difference between the two approaches is obtained.

Partition	$dt/dL = 0$ Speed (cm/ns)	Δv_{cf} (cm/ns)
EBC	17.4	-0.3
LBC	18.6	0.0
LBA	18.7	0.3
EBA	18.9	-0.2
Average	18.4	-0.2

Table 6.4: Speed of light in clear fibers in the four Tile Calorimeter partitions.

Recalculating the speed of light in the clear fibers as above, but using the new calculated length, it is verified that the impact of this systematic error is smaller than 0.1 cm/ns which is considered to be negligible.

Length of clear fibers

In order to study the effect of the uncertainty of the clear fibers length a random offset obtained from a gaussian distribution with a mean of 0 ns and a σ of 10 ns is applied to each clear fiber (10 ns would result from a difference of 2 m in the fiber length which is larger than what is expected). The procedure above was repeated to obtain the speed of light in the clear fibers per Tile Calorimeter partition and the results are summarized in Table 6.4. The comparison of the averages in Table 6.3 and Table 6.4 show a difference of 0.2 cm/ns.

Combining the errors

The final error in the measurement of v_{cf} is calculated by summing in quadrature the $\sigma_{length} = 0.2\ cm/ns$ and the maximum difference v_{cf} between partitions that is 1.4 ns, see Table 6.3. The final result for the measurement including systematic errors is:

$$v_{cf} = 18.6 \pm 1.4\ cm/ns$$

The result is consistent with values measured earlier using testbeam data [48]. As a follow up of this analysis and other measurements made using the laser system, measuring values

lower than 22.5 cm/ns, it was decided to update the value of v_{cf}, and use the value given by the producer i.e., $v_{cf} = 20\ cm/ns$

6.3 Method for time calibration using cosmic ray muons

The cosmic ray muons were the only high energy particles available for a long period of time and contrary to the laser they allow to test the full detection chain of the Tile Calorimeter: from the scintillating tiles to the signal reconstruction.

The method used to obtain the calibration constants or time offsets for each instrumental unit consists in two steps [49]. First for each event of a cosmic ray muons run it is computed the time difference between two instrumental units (IU) – a channel, a cell, a tower etc. – one at the TOP part of the cylinder ($\phi > 0$) and another at the BOTTOM part of the cylinder ($\phi < 0$). The difference between these two quantities, corrected by the time of flight between the IU's and averaged over all events, is compatible with zero if the detector is calibrated and otherwise different from zero. Combining the measurements from different Tile Calorimeter IU's a system of equations is built that has as unknowns the set of time calibration offsets, that from now on will be referred as time offsets, for that type of IU.

In this and the following sections are used designations that although common, it is advisable to clarify their usage in the present document. **Population** refers to the number of cells or measurements and **Efficiency** to their percentage relative to a reference number, verifying conditions detailed in the text. **Accuracy** is defined as the deviation of the measured mean from a reference value. If there is a large quantity of measurements the width that distribution is the **Precision**. The **Sensitivity** of a measurement evaluates how the output, our measurement, is capable to reproduce a change in the input data, the energy and time measured by the Tile Calorimeter cells. For all quantities that are presented only the statistical error is presented.

Instrumental unit (IU)	Quantities
Tower	ϕ, A or C side, $\|\eta\|$
Cell	ϕ, A or C side, $\|\eta\|$, Sampling
Channel	ϕ, A or C side, $\|\eta\|$, Sampling, left/right

Table 6.5: Number of quantities needed to identify an instrumental unit (IU) in Tile Calorimeter. Depending on the IU choice α and β must take in account these set of parameters to identify unambiguously the IU.

6.3.1 Time differences between two instrumental units

The calorimeter is calibrated in time if for any pair of instrumental units, identified by the greek letters α and β (see Table 6.5), the time difference $T^{\alpha} - T^{\beta}$ matches the corresponding time-of-flight $(ToF)^{\alpha}_{\beta}$ of the cosmic ray muon i.e.

$$\Delta T^{\alpha}_{\beta} = |T^{\alpha} - T^{\beta}| - (ToF)^{\alpha}_{\beta} \simeq 0\,. \tag{6.1}$$

This is calculated for each selected event and each pair of IUs. In the results presented in the next sections α is an IU with $y > 0$ and β an IU with $y < 0$ although it should be possible to extend this to a more general analysis where α and β are any two IUs. The measurement is trigger independent since time difference between two instrumental units, as used in Eq.6.1, compensates for non-uniformities in trigger latencies. For each IU pair the average of $\Delta T^{\alpha}_{\beta}$ over a set of n measurements (or events) is used:

$$< \Delta T^{\alpha}_{\beta} >= \frac{\sum_{i=1}^{n} \Delta T^{\alpha}_{\beta}(i)}{n} \tag{6.2}$$

and the corresponding standard deviation

$$\sigma^{\alpha}_{\beta} = \sqrt{\frac{\sum_{i=1}^{n} (\Delta T^{\alpha}_{\beta}(i) - < \Delta T^{\alpha}_{\beta} >)^2}{n}} \tag{6.3}$$

where n is the number of measurements obtained for each α,β pair. The time of flight of the cosmic ray muon between two points of the calorimeter is defined by dividing the distance

Reference position	$\phi > 0$			$\phi < 0$		
	A	BC	D	A	BC	D
Top of Tower	-	-	-	+	+	+
Center of BC cell	-	NA	+	+	NA	-

Table 6.6: Use of + or − signal in Equation 6.6 depending on the chosen reference position and the ϕ coordinate.

between these two points by the speed of light:

$$ToF_{\beta}^{\alpha} = \frac{d(\overrightarrow{r_{\alpha}}, \overrightarrow{r_{\beta}})}{c} \tag{6.4}$$

where $\overrightarrow{r}$ identify the IU in the ATLAS coordinates system (for cell the geometric center of the cell is used). The main objective is to calculate the time offsets for cells but preliminary studies were also done applying this method to towers. In what follows although the explanation is focused on cells, the differences for an analysis using towers as enunciated. It should be added that any extension to other IU's should be straightforward.

For a cell these quantities T_{cell}^{α} are the averaged reconstructed time of the *left* and *right* channels of each Tile Calorimeter readout system,

$$T_{cell}^{\alpha} = \frac{T_{channel(left)}^{\alpha} + T_{channel(right)}^{\alpha}}{2} \tag{6.5}$$

For towers the T_{tower}^{α} quantities must be the combination of typically 5 $T_{channel}^{\alpha}$ corresponding to the different channels that make a Tile Calorimeter tower. For this reason a time of flight correction with respect to a reference point must be introduced within each tower for each channel:

$$T'^{i}_{channel} = T^{i}_{channel} \pm \frac{d(\overrightarrow{r_{ref}}(\eta), \overrightarrow{r}(jpmt))}{c} \tag{6.6}$$

In the case of choosing the top of the tower as reference, should sum for $\phi < 0$ and subtract for $\phi > 0$ – see Table 6.6 where another case is also presented. A new quantity named T_{tower}^{α}

that represents the energy weighted time is defined as

$$T^{\alpha}_{tower} = \frac{\sum_{i=1}^{n} T'^{i}_{channel} \cdot E^{i}_{channel}}{E^{\alpha}_{tower}} \tag{6.7}$$

where

n is the number of channels in a tower;

$E^{i}_{channel}$ the reconstructed energy for a channel;

$T^{i}_{channel}$ the reconstructed time for a channel;

E^{α}_{tower} the summed energy contribution of all channels belonging to a tower:

$$E^{\alpha}_{tower} = \sum_{i=1}^{n} E^{i}_{channel}$$

where n is the number of cells in a tower.

The measured time differences $< \Delta T^{\alpha,\beta} >$ (Equation 6.2) and associated standard deviations σ^{α}_{β} (Equation 6.3) are combined in a system of equations as:

$$\frac{< \Delta T^{\alpha}_{\beta} >}{\sigma^{\alpha}_{\beta}} = \frac{t_{\alpha} - t_{\beta}}{\sigma^{\alpha}_{\beta}} \quad \forall \alpha, \beta \tag{6.8}$$

with α and β the set of indices necessary to identify the two compared IUs. The t_{α} and t_{β} are the time offsets of the α and β IUs, i.e. the unknown variables of the system of equations. The system of equations has a solution if the number of equations is larger than the number of IUs and this may limit the application of the method. However thanks to the random distribution of the incoming cosmic ray muon trajectories a number of IU pairs much larger than the number of unknowns can be reached. The σ^{α}_{β}, that expresses the precision of each time difference measurement, is used as a weight of the time differences as seen in Equation 6.8.

Cut ID	Quantity	Symbol	Cut
1	Tile Muon Fitter reconstruction	–	Yes
2	Cell energy threshold	E_{cell}^{min} E_{cell}^{max}	>= 200 MeV < 20 GeV
	Tower energy threshold	E_{tower}^{min} E_{tower}^{max}	>= 400 MeV < 20 GeV
3	Time difference of cell channels	T_{diff}	< 6 ns
4	Number of events per pair of cells	$N^{\alpha,\beta}$	> 5
5	Standard deviation	σ_{β}^{α}	< 5 ns

Table 6.7: Instrumental units selection cuts.

6.3.2 Data selection

Energy and time cuts are used to select the cells for which the $\Delta T_{\beta}^{\alpha}$ is calculated. After calculating all this values a second selection is done over the averages $< \Delta T_{\beta}^{\alpha} >$. These cuts are summarized in Table 6.7.

Individual cells selection

Quality cut An event is accepted if it has a cell with energy above 250 MeV for $\phi > 0$ and $\phi < 0$, in which case a track is reconstructed using the TileMuonFitter [42] algorithm. This algorithm is based on the Hough Transform that minimizes the contribution of noisy cells when reconstructing the track. In practice the selection is done by requiring at least one identified track using in ROOT:

$$\text{TileCosmicsHT\_fitQuality} = 1$$

Cell time and energy A minimum energy threshold $E_{cell}^{min} = 200\ MeV$ for a cell is set to reject noise events. To remove very high energy deposits that can appear due to data corruption, bremsstrahlung or nuclear interactions, an upper threshold $E_{cell}^{max} = 20\ GeV$ is also set. When using towers a minimum and a maximum energy are also set and are named $E_{Tower}^{min} = 400\ MeV$ and $E_{Tower}^{max} = 20\ GeV$ respectively. The time difference between the two readout channels of a

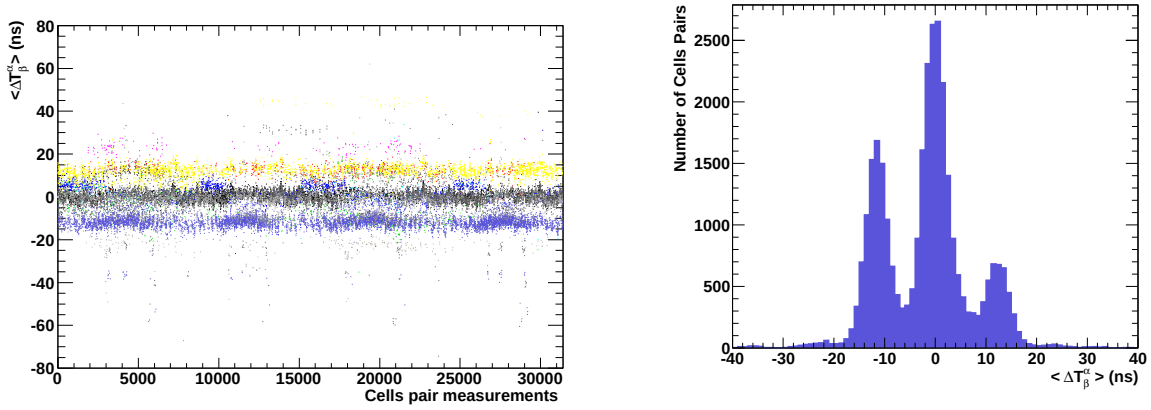

(a) Selected $< \Delta T^{\alpha}_{\beta} >$

(b) Projection in the y-axis

Figure 6.5: The selected $< \Delta T^{\alpha}_{\beta} >$. The individual cells have an energy above 200 MeV and the time difference between readout channels of a cell is below 6 ns. The cells pairs were required to have more than 5 measurements and a standard deviation lower than 5 ns.

cell is required to be below 6 ns. This is a quality cut that contributes to separate the physics signal from pedestal as described in Ref. [31]. The D^0 cells are read-out by a channel in LBA partition and a channel in the LBC partition, so if a large time offset exists between the two partitions an increase of the rejection efficiency for these cells is observed. Then for these 64 cells the time difference cut is not applied.

Pair of cells selection

The cells verifying the cuts 1-3 from Table 6.7 can be used to calculate $\Delta T^{\alpha}_{\beta}$ values. The resulting averages per cell pair $< \Delta T^{\alpha}_{\beta} >$ are selected using cut N^o4 which requires the number of events to be at least 5 and cut N^o5 which sets a limit to the standard deviation to 5 ns (Table 6.7). In Figure 6.5 the $< \Delta T^{\alpha}_{\beta} >$ obtained using a set of these cuts can be depicted. It is seen a distribution that is characterized by offsets different from zero implying that the detector is not calibrated in time. The different cells pairs are inspected and the selection is enforced by imposing a minimum number of events for the same pair of cells. As the statistics increase these cuts can be reinforced e.g. by increasing the limit on the number of events. The $< \Delta T^{\alpha}_{\beta} >$ remaining after these cuts are used in the system of equations.

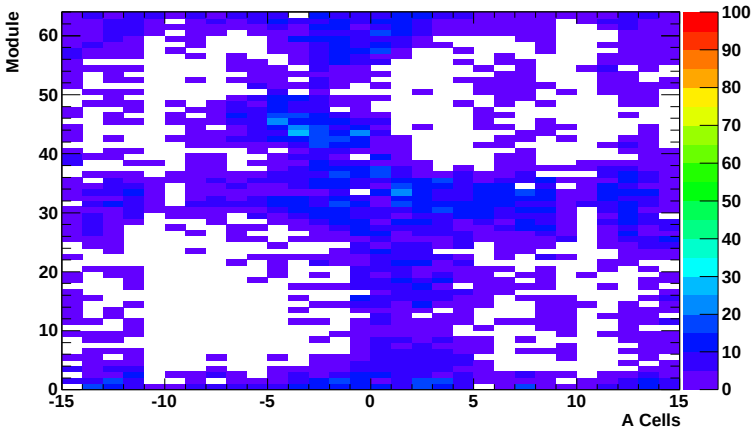

(a) A Cells

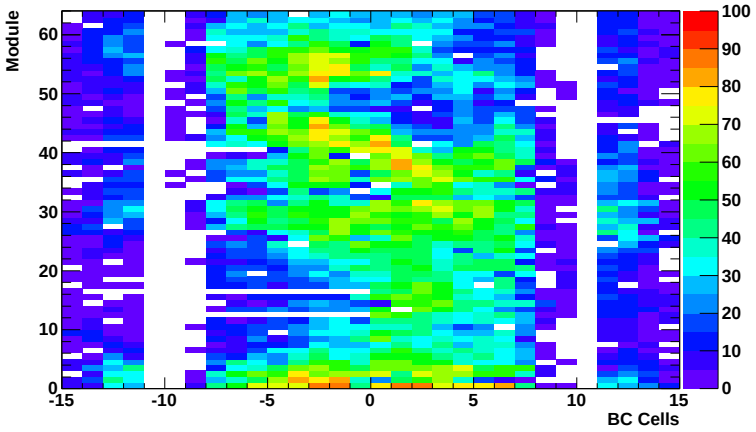

(b) BC Cells

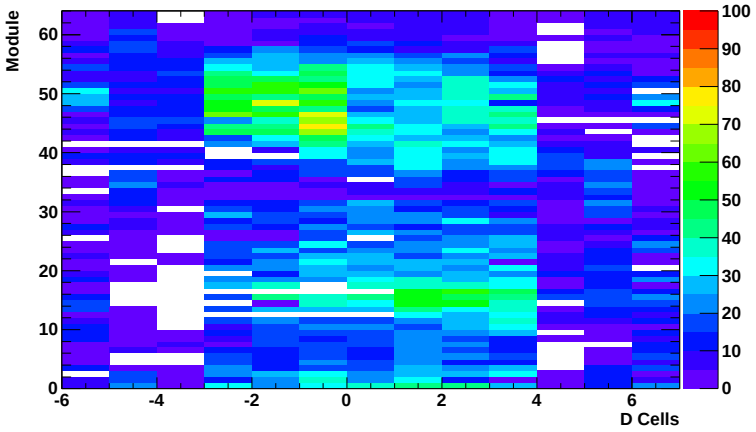

(c) D Cells

Figure 6.6: Number of measurements per cell (x-axis) and module (y-axis) (a) First radial layer (A cells) (b) Second radial layer (BC cells) (c) Third radial layer (D cells).

In Figure 6.6 the number of measurements for each cell are distributed as function of the cell index and the module number. There are a considerable number of cells that only have 5 measurements. It is seen that the typical population for A cells is below 25 measurements, with the lowest population for the TOP modules (1-32) in the LBC partition. For BC cells the region without any measurements corresponds to the C10 cell that is included in the EB's second layer. The limits of the LB barrel for this layer, cells BC8 and B9, have very few modules with measurements in more than 5 cells. For the D cells those cells with no measurement are distributed randomly. It is seen that the LB partitions have more measurements than the EB partitions. It is also seen a larger population for the BOTTOM modules in the LBC partition and the TOP modules in the LBA partition. In average ~ 20 measurements are found for cells in LB modules and ~ 7 for cells in EB modules. More statistics would be necessary to achieve a full, or at least wider, coverage.

6.3.3 Time offsets calculation

In this section the algorithm used to obtain the solutions of the system of equations is introduced following a discussion on the observed limitations of its application. For last a presentation and discussion over the technicalities that overcome these limitations is introduced.

Singular value decomposition (SVD) method [51]

Equation 6.8 can be written as a relation between matrices:

$$M\,t \;=\; \Delta T$$

where M is a matrix with a dimension $k \times (m+n)$, t is the vector of unknowns (time offset for each IU) with a dimension $m+n$ and ΔT the vector of measurements with a dimension k. The solutions of the system of equations are then obtained by applying a method called Singular Value Decomposition (SVD) as implemented in the ROOT package [50]. The method is based

on a theorem stating that any matrix M with a dimension $m \times n$ with $m \geq n$ can be written as:

$$M_{m\times n} \;=\; U_{m\times n}\, W_{n\times n}\, V^{T}_{n\times n}$$

where

$U_{m\times n}$ such as $U^{T}\, U \;=\; 1$

$W_{n\times n}$ is a diagonal matrix

$V_{n\times n}$ such as $V^{T}\, V = \; V\, V^{T} \;=\; 1$

The properties of matrices resulting from the decomposition enables the following transformation:

$$M\, t = \; \Delta T \qquad \rightarrow \qquad U\, W\, V^{T}\, t \;=\; \Delta T \qquad \rightarrow \qquad t \;=\; V\, W^{T}\, U^{-1}\, \Delta T$$

To have an unique solution the matrix must be overdetermined. In this case the SVD method will calculate the vector of solutions that minimizes $\| M\, t \;-\; \Delta T \|$.

The option for using this methodology comes from its capacity to deal with singular matrices i.e. matrices with null determinant and for which an inverse does not exist. The matrix M used in the measurement of the cells time offsets is made by setting for each row (with 4608 columns using as IUs the Tile Calorimeter cells Table 6.8) two values different from zero, that correspond to the pair of cells as explained in Section 6.3.1. Resulting in a sparse[2] matrix that can be close to the condition of singularity. The SVD method is also able to show a result for the case where the number of rows is smaller than the number of lines. These characteristics set the SVD method as ideal to obtain the time offsets for the Tile Calorimeter cells.

Matrix dimension challenges and implementation limitations

In Table 6.8 are detailed the quantities that define the dimensions of the matrix M or the size of the system of equations. The number of cells for which the time offsets must be calculated

[2]Most entries equal to zero.

	Number of IUs	Number of IU pairs
Towers	2048	1.048.576
Cells	4608	5.308.416

Table 6.8: Maximum number of rows – equations – and maximum number of columns – unknowns. The number of rows corresponds to the number of possible pairs of cells. The number of columns to the number of cells. In this account the scintillators readout by the Tile Calorimeter FEE are not included.

define the number of columns of matrix M. The number of cells pairs defines the number of equations or the number of rows in matrix M.

The selection cuts used in the analysis were already presented in a previous section and summarized in Table 6.7. In Figure 6.7 the number of selected cells are plotted versus the cell energy threshold, using two cuts on the number of measurements. To increase the method efficiency, the energy threshold was lowered down to 200 MeV which is still reasonable since the typical noise of the calorimeter cell is of the order of 60 MeV. As the energy threshold was decreasing the number of equations increased resulting in the discovery of limitations in the application of the method. It has been observed that by changing the cuts, or equivalently increasing the statistics, the computation requirements necessary to solve the system of equations exceeded the capacity of the used processing units resulting in memory allocation problems. Improvements in the algorithm implementation were applied but this problem remained. In Figure 6.7 for every point for which the number of selected cells is below 2000 the application of the method worked without problems using a single system of equations, this is named as 'Single Extraction' (SE). However when the number of cells is larger than 2000 a solution was not achieved without some modifications on the implementation of the method. The alternative that was found was to change the problem of solving one system of equations into the problem of solving a set of systems of equations, that in this case it is named as 'Multiple Extraction' (ME).

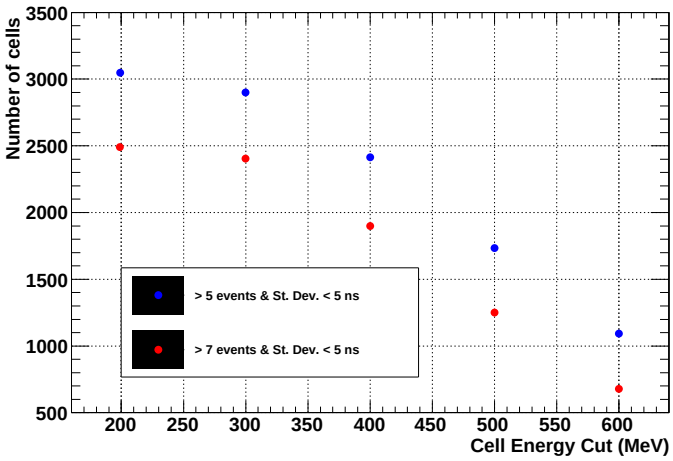

Figure 6.7: Number of cells with measured time offsets in function of the set of used cuts.

Tested solutions

In order to understand the better way to reduce a large problem in a set of smaller problems different solutions were tested. Although any of the next tested solutions could be valid for constructing the set of systems of equations the tests showed something different. Three options were tested and they are ordered in an historical order.

Geometric (GEOM) The new matrices are built based on the geometry of the event:

1. $\eta > 0$ cells with $\eta > 0$ cells i.e. (A side $\rightarrow$ A side);
2. $\eta > 0$ cells with $\eta < 0$ cells i.e. (A side $\rightarrow$ C side);
3. $\eta < 0$ cells with $\eta > 0$ cells i.e (C side $\rightarrow$ A side);
4. $\eta < 0$ cells with $\eta < 0$ cells i.e (C side $\rightarrow$ C side);

Cell Pair ID (CPID) It is necessary to save a cell pair ID in order to sum the contributions for the same cell pair for different events. The CPID is an integer that unambiguously identifies a cell pair and the set of four matrices results in a random distribution of cells pair measurements:

1. CPID divided by 4 has remainder 0 ;
2. CPID divided by 4 has remainder 1 ;

3. CPID divided by 4 has remainder 2 ;
4. CPID divided by 4 has remainder 3 ;

Counter (COUN) A counter that distributes evenly and randomly the measurements by four matrices.

A clear difference exists between the three listing options: GEOM and CPID or COUN. For the former, each cell can only be included in two lists, as for the latter two each cell can be include in any of the lists. The utilization of four matrices is an option but not necessarily a requirement. The ME methodology is comparable to the situation of having a different set of runs that are used to make the same kind of measurements, with no modifications of the setup, and must be combined to produce a final result. In the end the obtained solutions resulting from the four systems of equations are combined to produce the final result by calculating a simple average of the measurements obtained for the same cell.

Discussion

In Tables 6.9, 6.10, 6.11 the summary of the tests made over the three ME options are presented. The test starts by calculating:

- the time offsets difference between each list and the result of the combination of the set of lists.

- the time offsets difference between each list and a reference list.

The reference list is obtained using SE and corresponds to the set of cuts ($E_{threshold} > 400MeV$, number of measurements > 7 events, Std. Dev < 5 ns). For last the combined list of results is also compared with the reference list and these results are summarized in Table 6.12.

The first attempt was made using the GEOM separation that is based in Tile Calorimeter geometry (Table 6.9). Although resulted in precisions (Standard Deviation) below 1.5 ns, the accuracies (Average) showed values between 1.8 ns and 4.1 ns. The agreement with the reference list shows even worse results. The comparison the combined list with the reference

GEOM lists	Combined list Average (ns)	Combined list Std.Dev. (ns)	Reference list Average (ns)	Reference list Std.Dev. (ns)
1	1.8	0.7	5.7	1.5
2	3.0	1.4	2.2	1.2
3	3.1	1.2	1.7	0.8
4	4.1	0.6	5.9	1.6

Table 6.9: Comparison of lists of solutions with combined results (left) and reference results (right) for GEOM lists selection.

CPID lists	Combined list Average (ns)	Combined list Std.Dev. (ns)	Reference list Average (ns)	Reference list Std.Dev. (ns)
1	0.6	0.6	1.5	1.1
2	0.7	0.8	1.1	1.7
3	0.6	0.7	1.3	0.9
4	0.8	0.6	1.3	1.6

Table 6.10: Comparison of lists of solutions with combined results (left) and reference results (right) for CPID lists selection.

list are presented in Table 6.12 confirming these results giving an accuracy of 4.2 ns and a precision of 2.2 ns. These results were not satisfactory and required a new approach.

A second approach was using the CPID listing. In Table 6.10 the obtained results are presented. The comparison with the combined list gives an accuracy and a precision both below 1 ns. When comparing with the reference list worse accuracies and precisions are shown, but even so they are both below 1.5 ns and 1.7 ns respectively. From the comparison of the combined list with the reference list an accuracy of 1.3 ns and a precision of 1.3 ns are obtained (Table 6.12). These results represented a significant improvement relatively to our first option.

For last a solution based on a simple counter (COUN) distributing evenly the measured time differences between the different lists. In Table 6.11 the accuracy and precisions for this case are presented. The comparison with the combined list results in values comparable to the ones found for the previous case. However from the comparison with the reference list better results are obtained, showing accuracies better than 1 ns and precision below 1.5 ns.

COUN lists	Combined list Average (ns)	Combined list Std.Dev. (ns)	Reference list Average (ns)	Reference list Std.Dev. (ns)
1	0.6	0.6	0.9	1.0
2	0.7	0.9	0.9	1.3
3	0.7	0.9	1.0	1.5
4	0.7	0.8	0.8	0.8

Table 6.11: Comparison of lists of solutions with combined results (left) and reference results (right) for COUN lists selection.

Methodology	Average (ns)	Std.Dev. (ns)
GEOM	4.2	2.2
CPID	1.3	1.3
COUN	0.8	1.1

Table 6.12: Agreement of the combined list with reference list.

Comparing the combined results with the reference an accuracy of 0.8 ns and a precision of 1.1 ns are obtained (Table 6.12).

From the above results the preference went upon the CPID lists, because it was possible to obtain a measurement for 10% more cells and with a good accuracy and precision relatively to the reference list. It should be added that it was not identified a reason that justifies why the COUN and CPID methodologies show a difference in the number of cells with a time offset result. This is so for the used data, any other data could produce the opposite which could favor the COUN methodologies. Differences between these two methodologies are measured to be of the order of 1 ns which is quite reasonable showing that any of these two is a good option to obtain the time offsets of Tile Calorimeter cells.

6.4 Results

In 2006 the Tile Calorimeter was still running even in physics runs in a standalone mode. There were already some periods in which the LAr electromagnetic calorimeter and the Tile Calorimeter were included in the data taking at the same run. This was the case in October

2006 where a few long runs were made with the two calorimeters taking data, but using only 16 modules. The trigger in this period was still dependent on the trigger boards connected to the Tile Calorimeter towers described in Section 4.2. In this first period towers were used as the IUs. Approximately 80k events were used from runs 8037, 8035, 8055, 8051, 8077. The results are presented in Section 6.4.1.

During 2008 an updated version of the algorithm was developed in order to include all modules for all the four partitions. The conclusion of this development was achieved in two steps. In a first step the instrumental unit used were still towers. After the extension to cells of the algorithm was also made. In 2008 the trigger used was from the L1 trigger and in particular using the muon spectrometer RPCs. The trigger stream used was **CosmicDownwardMuons** that corresponds to cosmic ray muons triggered by the bottom sector. It were used ~0.5M events from run 91387 that had already the magnetic field on.

6.4.1 Time offsets for Tile Calorimeter towers

October 2006 data

As already mentioned there were only a few instrumented and fully operational modules: 8 modules in the bottom ($y < 0$) of LBA partition and 8 modules in the top ($y > 0$) on LBC partition. This configuration was chosen since it resulted in an higher statistics. Two of the modules were not included in the analysis. LBC16 tripped off very early during the data taking and LBC18 was not powered. In this period there was already laser data[3] used in the intra-module synchronization. This was the right time to measure the timing status using an independent source such as the cosmic ray muons. In Figure 6.8(a) the measured time offsets, including already the laser/led constants for the intra-module synchronization, are presented. The time offsets for each tower in the modules used in the data taking in this period are presented in Table 6.13. These numbers were afterwords used to correct the time constants in the Tile Calorimeter database [4]. The used runs were reconstructed using now the new time

[3] An alternative setup was used in this period since the laser system was not fully operational. The synchronization was done based on a LED (light emitting diode) light source.

[4] In this period the ATLAS database was not fully working and the constants used in the Tile Calorimeter synchronization were the content of a simple text file that was loaded and read during the events reconstruction.

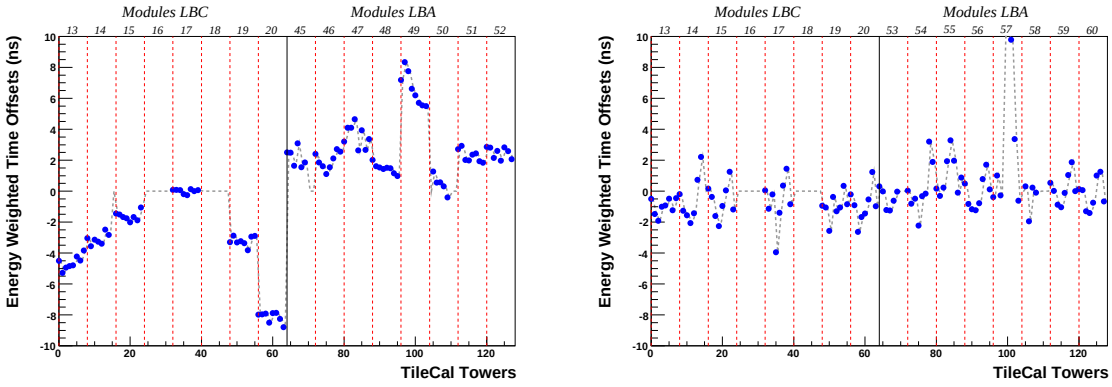

(a) Intra-module synchronization

(b) Inter-module synchronization

Figure 6.8: Tile Calorimeter towers inter-module synchronization done in the early commissioning using 2006 data (a) Intra-module synchronized using the laser/led system (b) Inter-module synchronization applied using 2006 cosmic ray muons data.

constants. After applying the method to this newly reconstructed runs the tower time offsets in the different modules are for most cases closer to zero as can be seen in Figure 6.8(b). In Table 6.14 the time offsets for each tower are presented. Comparing the two tables a clear difference is seen. All modules present now values closer to 0 ns except for module LBA49. The results per module are presented in Figure 6.9. The synchronization between modules was achieved with an accuracy of $\sim \pm 1$ *ns* for all the analysed modules except module LBA 49 for which the synchronization did not work out due to some problematic towers in this module.

October 2008 data

In 2008 the algorithm was updated to its final version including all the Tile Calorimeter modules. A working algorithm was first achieved using towers as the instrumental unit. In Figure 6.10 are presented the results for the long barrel partitions LBA and LBC. For each module is presented the averaged towers time offset, the standard deviation and the number of towers used in the measurement. It is seen that for most modules almost all the towers are used and the standard deviation for each module is below 3 ns. The mean values have a distribution that is characterized by a systematic effect correlated with the position of the

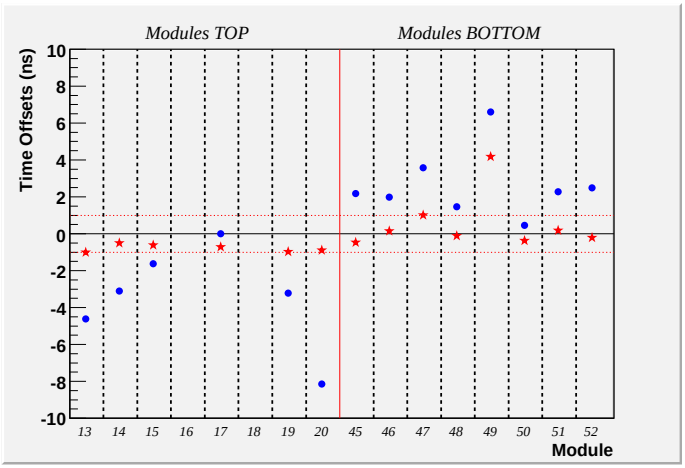

Figure 6.9: Modules average time from Tile Calorimeter inter-module calibration done in the early commissioning using 2006 data: • intra-module synchronized using the laser/led system and ⋆ inter-module synchronization applied using 2006 cosmic ray muons data.

Module	t_1 [ns]	t_2 [ns]	t_3 [ns]	t_4 [ns]	t_5 [ns]	t_6 [ns]	t_7 [ns]	t_8 [ns]
LBC13	- 4.5	- 5.3	- 4.9	- 4.9	- 4.8	- 4.2	- 4.5	- 3.8
LBC14	- 3.0	- 3.6	- 3.1	- 3.3	- 3.4	- 2.5	- 2.8	0.0
LBC15	- 1.4	- 1.5	- 1.7	- 1.7	- 2.0	- 1.7	- 1.9	- 1.0
LBC16	—	—	—	—	—	—	—	—
LBC17	0.1	0.1	0.1	- 0.2	- 0.3	0.1	- 0.0	0.1
LBC18	—	—	—	—	—	—	—	—
LBC19	- 3.3	- 2.9	- 3.3	- 3.2	- 3.4	- 3.8	- 2.9	- 2.9
LBC20	- 7.9	- 7.9	- 7.9	- 8.5	- 7.9	- 7.9	- 8.3	- 8.8
LBA45	2.5	2.5	1.6	3.1	1.5	1.9	0.0	0.0
LBA46	2.4	1.9	1.6	1.1	1.6	2.1	2.7	2.5
LBA47	3.2	4.1	4.1	4.7	2.6	3.9	2.7	3.4
LBA58	2.0	1.6	1.5	1.4	1.5	1.4	1.1	0.9
LBA49	7.2	8.3	7.8	6.6	6.2	5.7	5.6	5.5
LBA50	0.0	1.3	0.6	0.6	0.3	- 0.4	- 0.0	- 0.0
LBA51	2.7	2.9	2.0	1.9	2.4	2.4	1.9	1.8
LBA52	2.9	2.8	2.2	2.6	1.9	2.8	2.6	2.1

Table 6.13: Tower time offsets measured with cosmic ray muons 2006 data. Each column represents the time offset for a tower in a module. The index 1 refers to tower $\eta = 0.05$ and so forth.

Module	t_1 [ns]	t_2 [ns]	t_3 [ns]	t_4 [ns]	t_5 [ns]	t_6 [ns]	t_7 [ns]	t_8 [ns]
LBC13	- 0.5	- 1.5	- 2.0	- 0.9	- 0.8	- 0.4	- 1.0	- 0.5
LBC14	- 0.2	- 1.2	- 1.5	- 2.4	- 1.4	1.1	2.2	0.0
LBC15	0.2	- 0.4	- 1.6	- 2.2	- 0.9	0.2	1.4	- 0.0
LBC16	—	—	—	—	—	—	—	—
LBC17	0.1	- 1.1	- 0.2	- 3.9	- 1.3	0.5	1.6	- 0.7
LBC18	—	—	—	—	—	—	—	—
LBC19	- 0.9	- 1.0	- 2.5	- 0.4	- 1.1	- 1.0	0.5	- 0.9
LBC20	- 0.3	- 0.9	- 2.6	- 1.6	- 1.4	- 0.5	1.5	- 1.0
LBA45	0.3	- 0.1	- 1.2	- 1.3	- 0.7	- 0.2	0.0	0.0
LBA46	- 0.1	- 0.9	- 0.6	- 2.4	- 0.6	- 0.2	4.4	1.8
LBA47	0.1	- 0.4	0.2	1.8	3.1	1.8	- 0.4	0.8
LBA48	0.4	- 0.9	- 1.2	- 1.3	- 0.9	0.7	1.6	- 0.1
LBA49	- 0.5	0.9	- 0.4	9.9	10.3	10.5	3.3	- 0.7
LBA50	0.0	0.2	- 1.8	0.1	- 0.2	- 0.0	- 0.0	- 0.0
LBA51	0.4	- 0.1	- 1.0	- 1.1	- 0.2	0.9	1.7	0.5
LBA52	0.1	- 0.0	- 1.4	- 1.5	- 0.9	0.9	1.1	- 0.8

Table 6.14: Tower time offsets measured with cosmic ray muons 2006 data after correcting the time constants using the results from Table 6.13. Each column represents the time offset for a tower in a module. The index 1 refers to tower $\eta = 0.05$ and so forth.

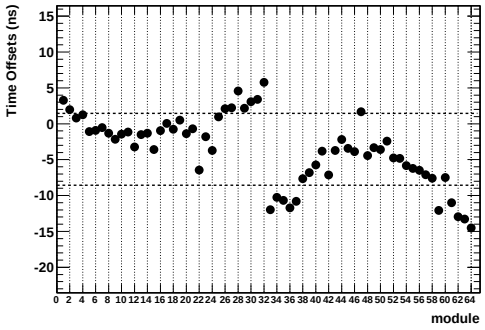

(a) Average LBA

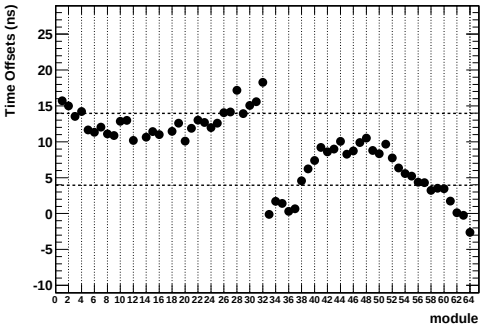

(b) Average LBC

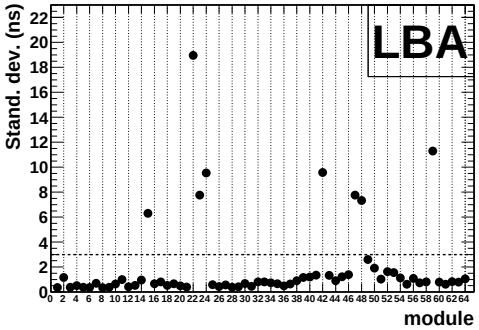

(c) Standard deviation LBA

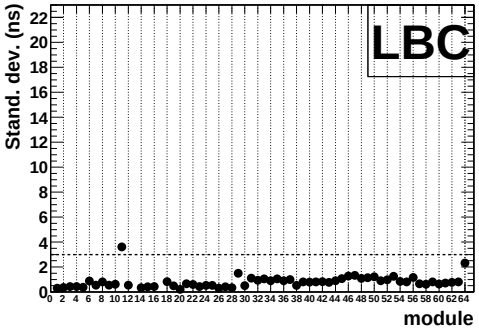

(d) Standard deviation LBC

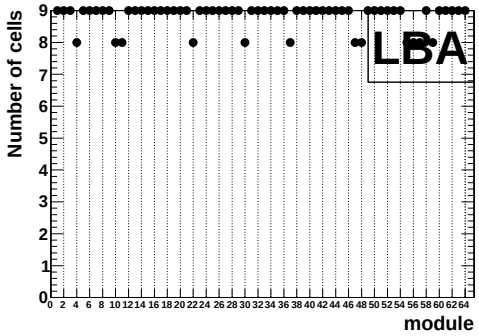

(e) Population LBA

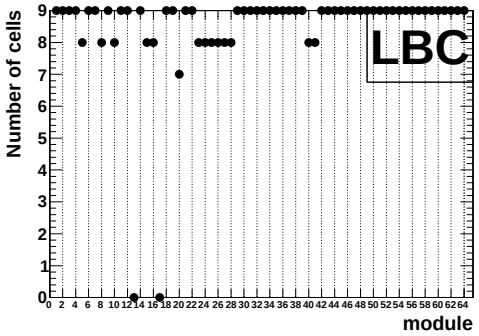

(f) Population LBC

Figure 6.10: Tower time offsets for 2008 Cosmic ray muons data: average, standard deviation and population (number of towers used in obtaining the statistical quantities).

	All modules		
	Top and Bottom	Top	Bottom
EBC	- 3.3 (6.7)	1.7 (6.5)	- 8.7 (6.8)
LBC	8.9 (4.9)	13.0 (4.5)	5.2 (5.3)
LBA	- 3.6 (4.8)	- 0.1 (4.3)	- 7.1 (5.2)
EBA	-13.7 (6.0)	- 9.9 (6.4)	-17.5 (5.6)

	16 modules			12 modules		
	Top and Bottom	Top	Bottom	Top and Bottom	Top	Bottom
EBC	- 3.3 (2.0)	- 1.5 (1.6)	- 5.0 (1.2)	- 3.2 (1.4)	- 1.7 (1.2)	- 4.6 (0.8)
LBC	9.9 (2.1)	11.7 (1.0)	8.1 (1.8)	10.1 (1.7)	11.5 (1.0)	8.6 (1.4)
LBA	- 2.9 (2.6)	- 1.8 (1.7)	- 4.0 (2.0)	- 2.6 (2.6)	- 1.7 (1.8)	- 3.4 (1.8)
EBA	13.2 (6.8)	-12.0 (6.4)	-14.3 (2.2)	12.0 (3.3)	-10.4 (2.6)	-13.6 (2.1)

Table 6.15: Average and RMS for tower time offsets using 2008 cosmic ray muons data in the Tile Calorimeter partitions. The 16 most vertical module span from module 9 to 24 on the top ($y > 0$) and from module 41 to 56 on the bottom ($y < 0$). Results are also shown selecting the 12 most vertical modules.

module in the cylinder. The most vertical modules (close to module 17 and module 48) show an agreement in the time offset measured per partition. As the module number approaches the ones closer to the horizontal a systematic offset is observed relatively to the most vertical modules, positive for top modules and negative for bottom modules. The same observations are valid for the extended barrel partitions EBC and EBA and the corresponding results can be seen in Figure 6.11.

In Table 6.15 the time offsets averages per partition are presented. Due to the systematic effect observed for the horizontal modules (modules 1 to 8, 25 to 40 and 57 to 64) additional columns excluding these module and including the results from the most vertical modules are built. Considering all modules in the Tile Calorimeter cylinder the standard deviation is considerably large of the order of 5-7 ns. This is worsen than the top or bottom modules alone and it is due to the difference between the top and bottom modules measurements. If modules closer to the horizontal plane (y=0) are not included the results improve considerably with standard deviations of the order of 2 ns. The agreement between the average value for the time offsets in the top and bottom also increases when considering only the most vertical modules. Differences of the order of 3 ns while before considering all the calorimeter modules

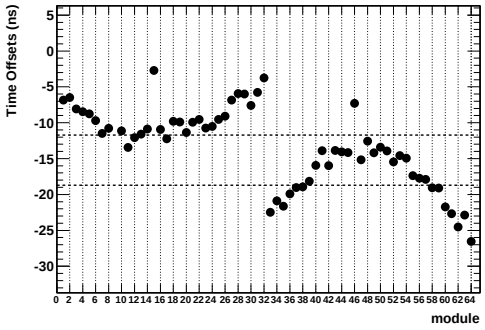

(a) Average EBA

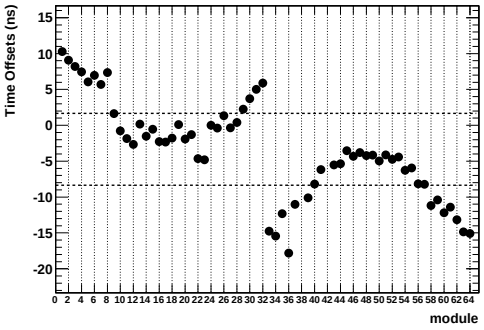

(b) Average EBC

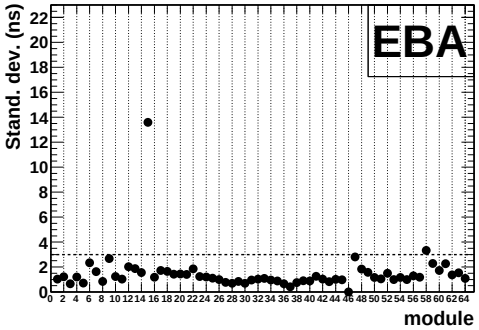

(c) Standard deviation EBA

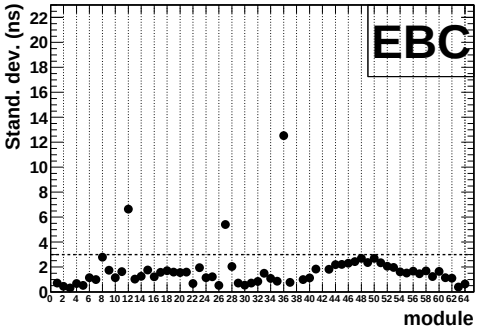

(d) Standard deviation EBC

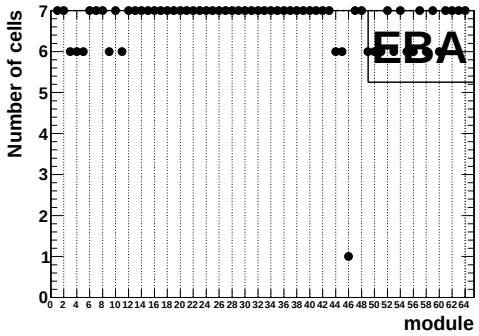

(e) Population EBA

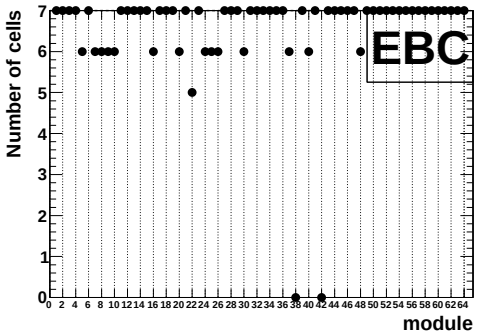

(f) Population EBC

Figure 6.11: Tower time offsets for 2008 Cosmic ray muons data: average, standard deviation and population (number of towers used in obtaining the statistical quantities).

	16 modules		12 modules	
Partition	Top	Bottom	Top	Bottom
EBC	-0.3 (1.2)	-1.6 (1.2)	-0.5 (1.3)	-1.1 (0.7)
LBC	0.6 (0.9)	-1.7 (0.8)	0.3 (0.8)	-1.3 (0.5)
LBA	-0.7 (2.1)	-1.5 (2.2)	-0.9 (1.9)	-0.7 (1.1)
EBA	-0.4 (2.3)	-2.3 (2.6)	-0.3 (0.8)	-2.1 (0.9)

Table 6.16: Time offsets difference between 2008 Single beam data and 2008 Cosmic ray muons data. The results are summarized per partition using only the most vertical modules as: mean (RMS).

the differences are of the order of 7 ns. Improvement is also seen when reducing from 16 to 12 most vertical modules, but the effect is already much lower.

To conclude a comparison with beam results in presented in Table 6.16. In this comparison are only included the most vertical modules in two sets as before: 16 modules and 12 modules. The obtained agreement is already of the order of 2 ns.

6.4.2 Time offsets for Tile Calorimeter cells

This section is subdivided in four parts. First the time offsets measurements per cell are presented with the details required for the analysis. A discussion follows. First on the obtained azimuthal and radial coverage and for last about the measured time offsets [47].

Presentation of time offsets measurements

Figures 6.12 and 6.13 present the time offsets averages, standard deviation and number of cells per module. These figures are organized in columns for easier comparison: the upper row presents the average, the mid-row the standard deviation and the lower row the number of cells for each module in each partition. Guide lines have been introduced in each plot: a window of 4 ns around the partition average, a 3 ns guide line for the standard deviation and half of the number of cells in each partition (11 for the LBs and 7 for the EBs).

In Table 6.17 the number of cells is detailed per partition and Tile Calorimeter radial layers. In parenthesis is given the corresponding efficiency as a percentage for this run. It shows that the efficiency is higher for the LB partitions reaching nearly 100% for the third

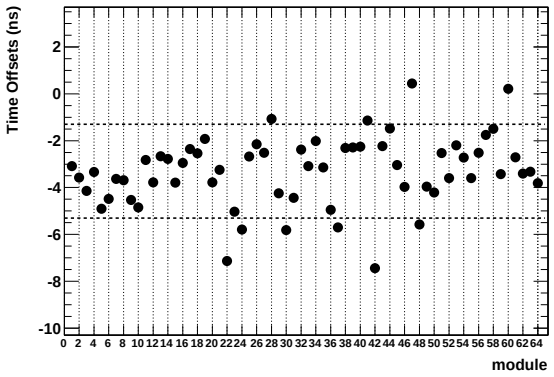

(a) Average LBA

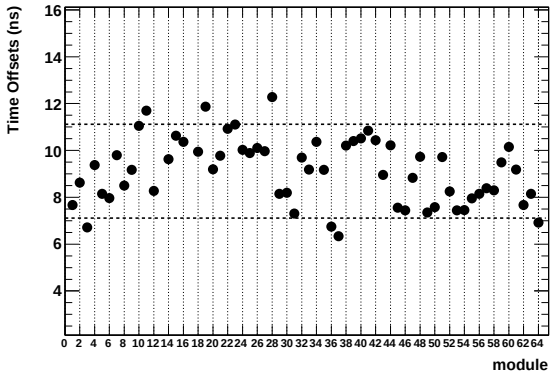

(b) Average LBC

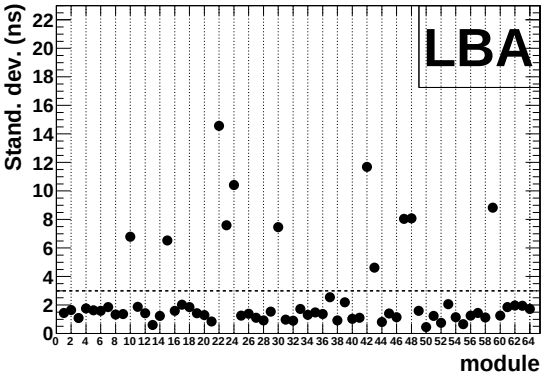

(c) Standard deviation LBA

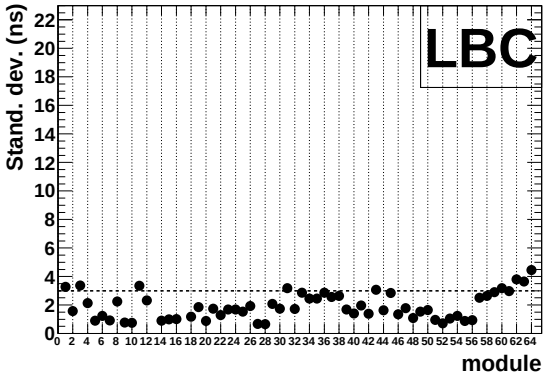

(d) Standard deviation LBC

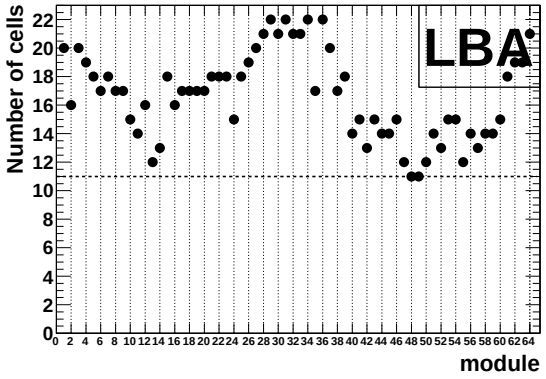

(e) Population LBA

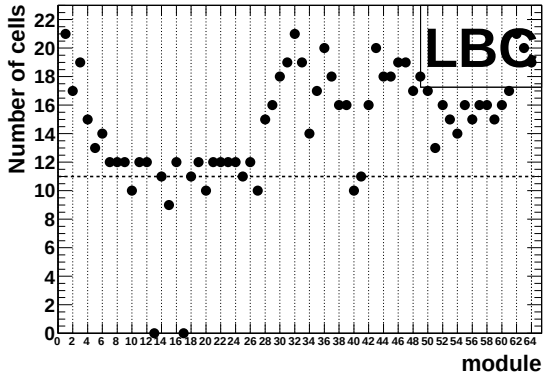

(f) Population LBC

Figure 6.12: Time offsets: average, standard deviation and population (number of cells used in obtaining the statistical quantities).

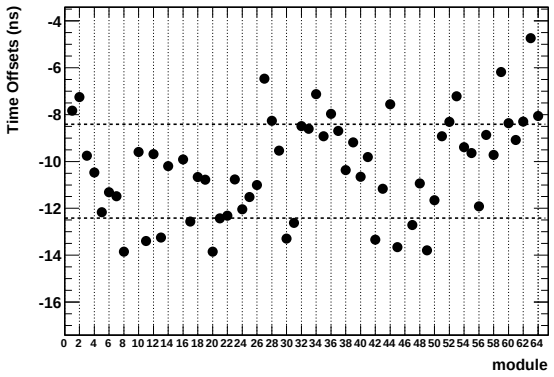

(a) Average EBA

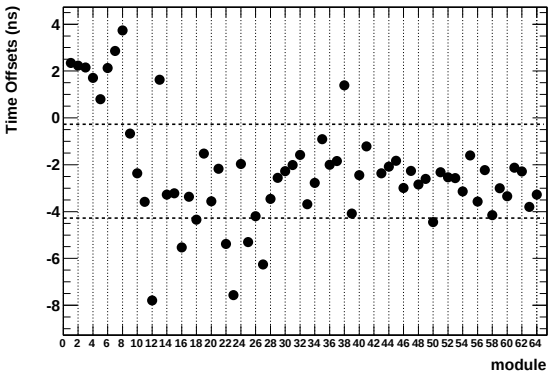

(b) Average EBC

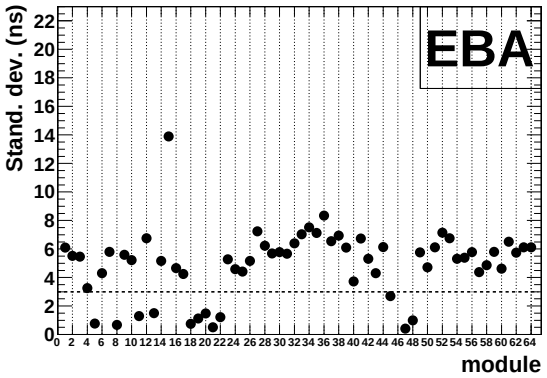

(c) Standard deviation EBA

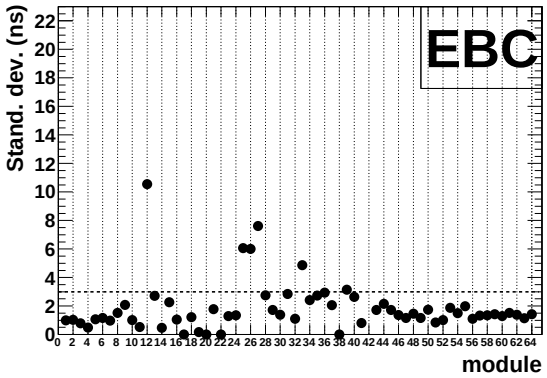

(d) Standard deviation EBC

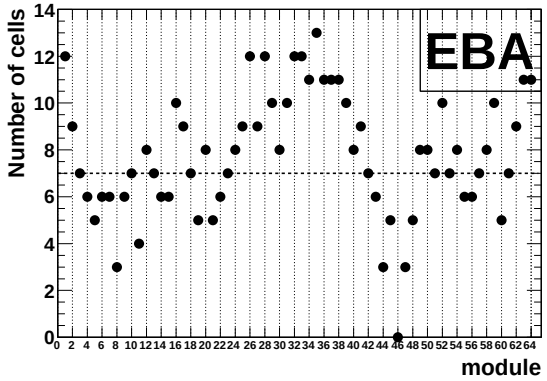

(e) Population EBA

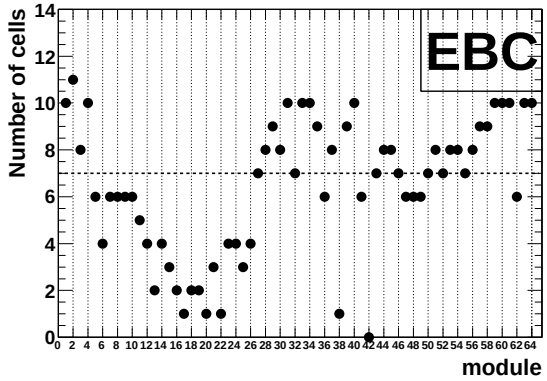

(f) Population EBC

Figure 6.13: Time offsets: average, standard deviation and population (number of cells used in obtaining the statistical quantities).

Partition	A Cells	BC Cells	D Cells	Total
EBC	95 (30%)	193 (50%)	123 (64%)	411 (49%)
LBC	265 (41%)	496 (86%)	175 (91%)	936 (49%)
LBA$^{(*)}$	285 (44%)	532 (92%)	249 (97%)	1066 (55%)
EBA	127 (40%)	229 (59%)	142 (74%)	498 (60%)
ALL	772 (40%)	1450 (75%)	689 (82%)	2911 (62%)

Table 6.17: Number of cells per partition and cell type for which time offsets were calculated. The total number of cells existing in the Tile Calorimeter are 1920 for layer A, 1920 for layer B/C and 832 for layer D. The scintillators are not included in these numbers. $^{(*)}$ For the D cells of LBA are also included the 59 D0 cells measured.

radial layer (D Cells). The first radial layer shows comparable efficiencies of the order of 40% for the 4 partitions. For the present data and sets of cuts it is possible to obtain the time offsets for 62% of the Tile Calorimeter cells.

From the Figures 6.12 and 6.13 it is seen that the global numbers, either module average or partition average, are characterized in some cases by high fluctuations that go up to 16 ns for individual modules. This requires the need of presenting the results with more detail. In Table 6.18 the results are detailed per radial layer. The D0 cell is placed in a separate column since it is readout by a channel of the LBA partition and a channel of the LBC partition. In Figure 6.14 the above results are summarized for each Tile Calorimeter partition. The corresponding average and standard deviation are in Table 6.19.

Azimuthal and radial distribution of measurements

Table 6.17 shows that ~ 60% of the cells of the Tile Calorimeter detector can be analysed. The coverage for this analysis is detailed per module for each partition in Figures 6.12, 6.13. The plot on the bottom in these figures shows the number of cells per module. All LB modules show populations (i.e. number of cells) where typically half of the cells in each module (11) have a measurement. The two EB show smaller populations but still many modules surpass the limit of half of the number of cells that for EB is 7. A ϕ dependence is visible which is characterized by a larger population for the most horizontal modules close to modules 1,32

A cells				BC cells			
Partition	#Cells	Average (ns)	Std.Dev. (ns)	Partition	#Cells	Average (ns)	Std.Dev. (ns)
EBC	95	-1.4 ± 0.4	3.6 ± 0.3	EBC	193	-2.7 ± 0.2	2.5 ± 0.1
LBC	265	7.2 ± 0.2	3.7 ± 0.2	LBC	496	9.3 ± 0.1	1.4 ± 0.0
LBA	285	-4.0 ± 0.2	2.6 ± 0.1	LBA	532	-2.8 ± 0.1	1.3 ± 0.0
EBA	127	-1.6 ± 0.5	6.0 ± 0.4	EBA	229	-12.8 ± 0.2	2.5 ± 0.1

D cells				D0 cell			
Partition	#Cells	Average (ns)	Std.Dev. (ns)	Partition	#Cells	Average (ns)	Std.Dev. (ns)
EBC	123	-1.4 ± 0.2	2.7 ± 0.2	EBC	59	4.6 ± 0.1	1.1 ± 0.1
LBC	175	10.4 ± 0.1	1.6 ± 0.1	LBC			
LBA	190	-1.9 ± 0.1	1.8 ± 0.1	LBA			
EBA	142	-11.7 ± 0.2	2.7 ± 0.2	EBA			

Table 6.18: Average time offsets detailed per radial layer.

and 64. It is also observed that for the C side the TOP modules (1-32), from the center to the left of the figures, have smaller efficiencies than the BOTTOM modules (33-64), from the center to the right. For the A side the opposite is observed. This is well depicted from the LB plots. For the EB plots, EBC also verifies this but EBA has high fluctuations that inhibit an equivalent conclusion in what respects this azimuthal asymmetry. It can be concluded that the modules populations are in agreement with what was observed in Figure 6.6.

In Figures 6.12, 6.13 the modules with no measurements are easily identified. This is the case of module 46 in EBA, module 42 in EBC and modules 13 and 17 for LBC. Other modules present a very small populations like modules EBC 17, 20, 22, and 38 with only one cell. It can be also added that globally the population is good for the LB, with almost all modules contributing with more than 50% of the number of cells per module. For the EB the performance is worse where many modules have low efficiencies especially in the EBC partition.

Partition	Average (ns)	Std.Dev. (ns)
EBC	-2.1 ± 0.2	3.3 ± 0.1
LBC	8.9 ± 0.1	2.6 ± 0.1
LBA	-3.3 ± 0.1	4.1 ± 0.1
EBA	-10.0 ± 0.3	6.9 ± 0.2

Table 6.19: Time offsets measured using cosmic ray muons data for each Tile Calorimeter partition.

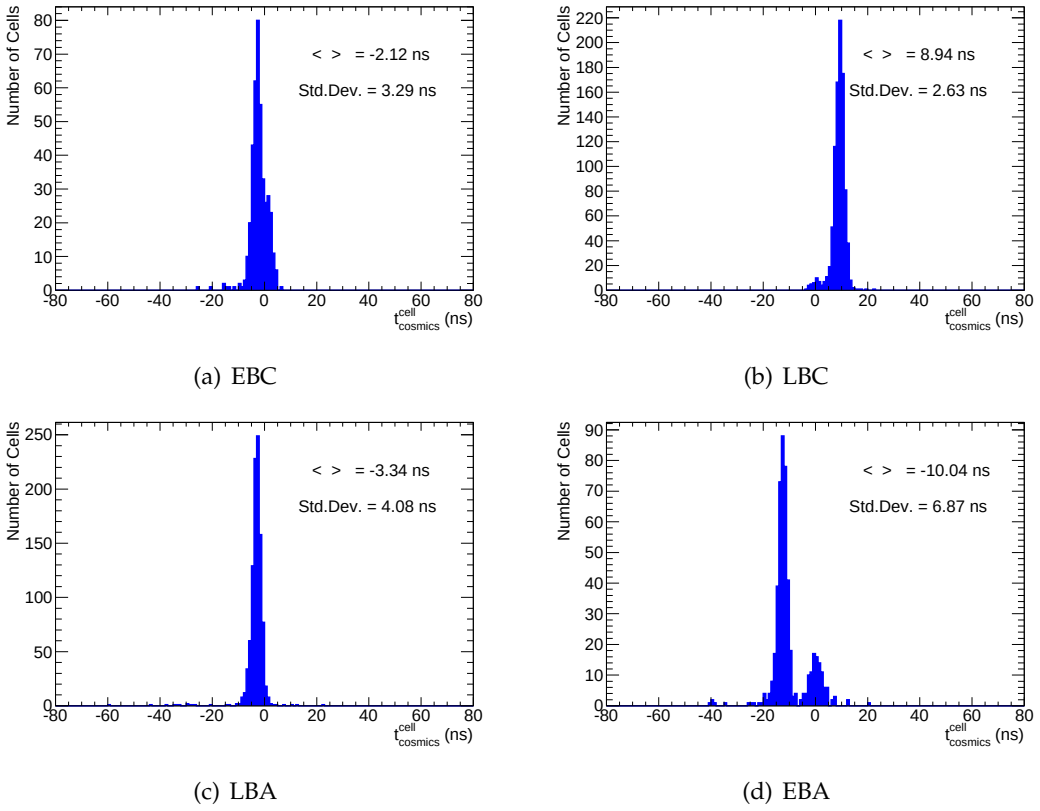

Figure 6.14: Time offsets measured using cosmic ray muons for each Tile Calorimeter partition.

Discussion of time offsets measurements

The obtained time offsets ($t^{cell}_{cosmics}$) have for three of the Tile Calorimeter partitions a well defined high statistics peak as can be seen in Figure 6.14; the exception is EBA that clearly shows two peaks well separated. It is also true that all histograms show cells that deviate from the main peak. For EBC the right tail shows a bump, for LBC the left tail extends and shows a distribution of cells around 0 ns. The results from these histograms are summarized in Table 6.19.

The partition averages shows that the cell averaged time calibration offset for EBC and LBA partitions are c-2.1 ns and -3.3 ns respectively. The LBC partition has a larger and positive time calibration offset of 8.9 ns. The EBA has also a large but negative time calibration offset of -10.0 ns. For EBA the standard deviation is of 6.9 ns which is two times larger than the one observed for EBC and LBC partitions, but the reason is evident from the histogram where a peak around 0 ns and another close to 10 ns are obtained; for LBA a standard deviation of 4.1 ns is measured. The differences between EBA and LBC partitions that mount up to 19 ns comes from the fact that for this data the inter-partition calibration was not carried out and reinforces the need of such a procedure. To identify the origin of the deviations from the main peak a detailed presentation is useful and given in the following lines. The results for the standard deviation of each partition per module can also be seen in Figures 6.12, 6.13. For the EBA partition most of the modules have values of 6 ns, which confirms that the 6 ns from Table 6.19 is in fact a dominant value and not due to some outliers from a small number of modules. Typically and for the remaining partitions, the modules standard deviation is of the order of 3 ns, but with some outliers. The LBA partition has 10 modules above 3 ns and the EBC has 4 modules in the same conditions. This differences are understood when the data is detailed per radial layer. This is summarized in Table 6.18. Within each LBA, LBC and EBC partitions all three layers agree within a interval of ±2 ns. The first layer of EBA is in strong disagreement with the second and third layers and this justifies the large standard deviation measured for the modules in this partition. From this table it can still be seen that for all partitions the first radial layer has the largest standard deviation.

Fake offsets (ns)	Measured offsets (ns)	Accuracy (ns)
5.0	4.98	0.02
2.0	1.99	0.01
1.0	0.99	0.01
0.5	0.49	0.01

Table 6.20: Sensitivity on the measurement of a time offset for a BC cell.

The D0 cell is read-out by a PMT in the LBA partition and a PMT in the LBC partition and for this reason it should be analysed in separate. The average value of 4.6 ns is in agreement with average values for the LBA and LBC partitions. The efficiency for this cell is 95% that is comparable with the other D cells of LB partitions as shown in Table 6.17.

From what was presented it is possible to explain better the distributions in Figure 6.14. For EBA the two peaks are explained from what was already said, the second peak at 0 ns includes the cells from the first radial layer. The small bump for LBC also close to 0 ns is also identified with cells of the first radial layer; for this partition and layer an average value of 7 ns, smaller that the one found for the second and third layer, and a standard deviation two times larger with a value of 3.7 ns, while for the other two layers is below 3 ns, can explain it. For EBC the bump observed in the right tail are undoubtedly associated with the first 8 modules that are set around a value of 2 ns and shifted from all other modules by ~ 6 *ns* as can be seen on the top right of Figure 6.13. These were modules for which the laser calibration did not work and these was also a result observed from 2008 single beam analysis as will be shown later. The other two contributions coming from module 13 and 38 are residual and come respectively from 2 and 1 cells as can be seen in the same figure.

6.4.3 Sensitivity, accuracy and precision

The measurement of the sensitivity, accuracy and precision is done with two approaches. In a first approach a fake time offset is added to the time of a single cell using values between 0.5 ns and 5 ns. In Table 6.20 the results obtained for a BC cell of the long barrel are presented. The results show that this method is sensitive to a fake offset up to 0.5 ns with an accuracy for

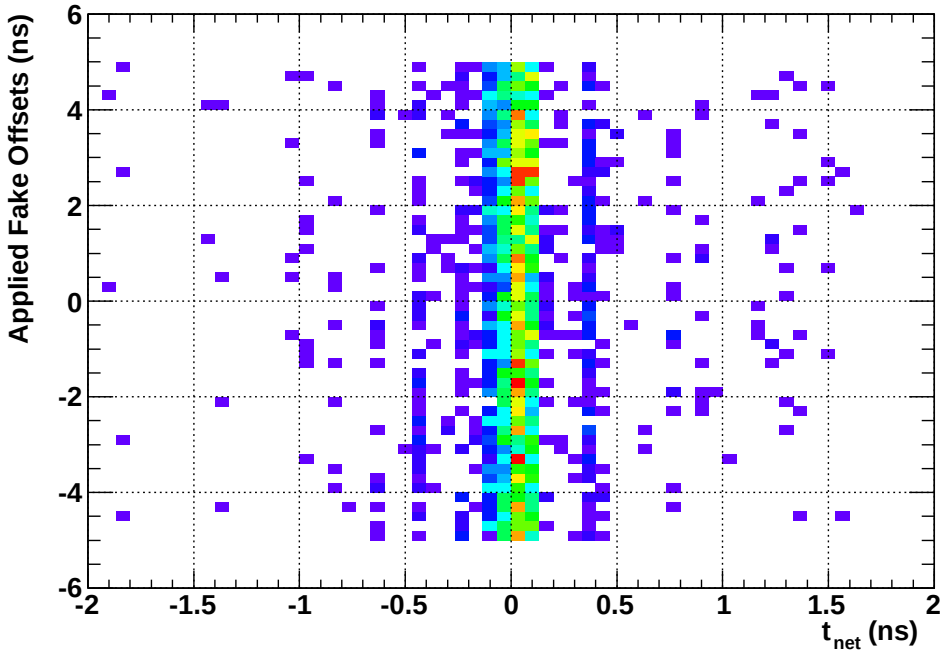

Figure 6.15: Correlation between the applied faked offsets in the vertical axis and the t_{net} shows the independence between the applied fake offset and the retrieved t_{net} that is used to account for the accuracy and precision of the method.

such offset of the order of 2%.

In order to have a global account of this quantities a second approach is used. Instead of a single cell all the available cells are used. The applied fake offsets come from an uniform random distribution within an interval $[-a,a]$. The net effect of this procedure in the measurement of the $t^{cell}_{cosmics}$ can be expressed as:

$$t_{net} = t_o - t_n + t_f \tag{6.9}$$

where

t_{net} is a measurement of the individual accuracy for a particular cell;

t_o is the offset before applying the fake offset;

t_f is the fake offset introduced before the resolution of the system of equations;

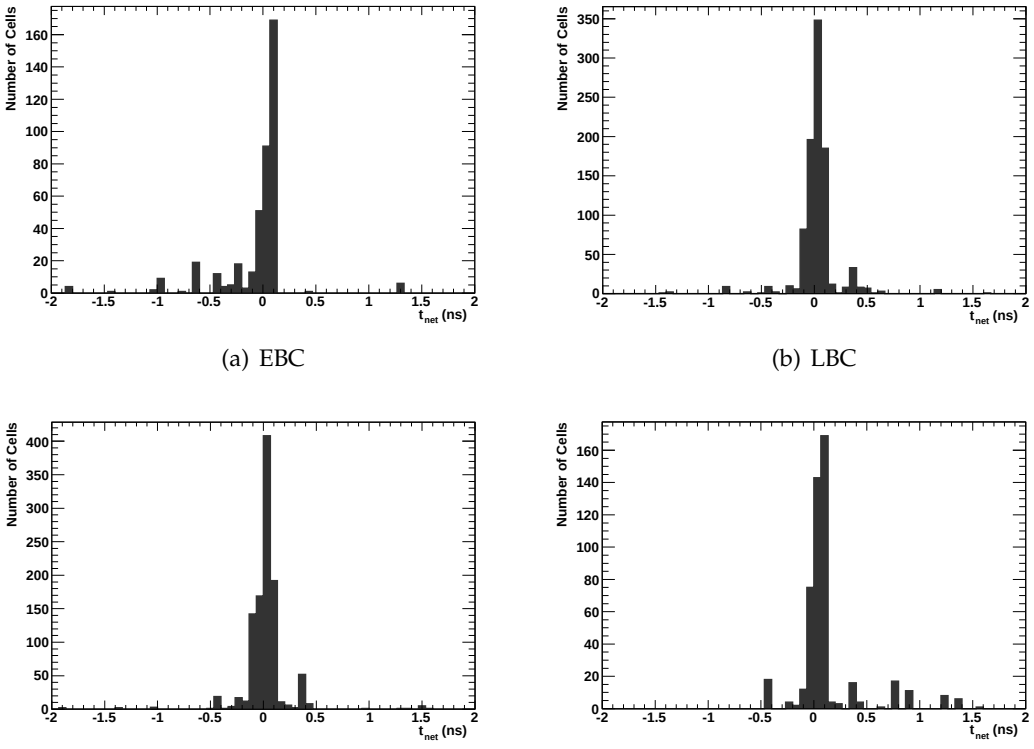

(a) EBC (b) LBC

(c) LBA (d) EBA

Figure 6.16: Precision and accuracy for measuring time offsets ($t^{cell}_{cosmics}$) using cosmic ray muons.

t_n is the cell time offset obtained in the solution of the system of equations after a fake offset t_f is applied;

The quantity t_{net} gives the precision and accuracy of the measurement. In Figure 6.15 the applied fake offsets are compared with the measured quantity t_{net}. It is seen that the measured quantity is independent of the applied fake offset. Even for very small fake offsets t_{net} is as sensitive as for larger fake offsets values. It is concluded that the method has a sensitivity enough to achieve a 1 ns synchronization and problems resulting in poorer accuracies should come from characteristics of the used data. In Figure 6.16 the results obtained for this quantity for the four Tile Calorimeter partitions are shown. In Table 6.21 the mean and average for each partition are presented. In Table 6.22 the results are detailed per radial layer. The results show that the achievable precision, given by the standard deviation of the distributions, for a random variation within an interval of 5 ns, is better than 0.4 ns and the corresponding

Partition	#Cells	$< t_{net} >$ (ns)	Std.Dev. (ns)
EBC	411	-0.05 ± 0.02	0.35 ± 0.01
LBC	936	0.04 ± 0.01	0.20 ± 0.00
LBA	1066	0.03 ± 0.01	0.22 ± 0.00
EBA	498	0.12 ± 0.01	0.31 ± 0.01
ALL	2911	0.04 ± 0.00	0.26 ± 0.00

Table 6.21: Accuracy and precision of the $t^{cell}_{cosmics}$ measurement using cosmic ray muons data per partition.

A cells			
Partition	#Cells	$< t_{net} >$ (ns)	Std.Dev. (ns)
EBC	95	-0.39 ± 0.06	0.61 ± 0.04
LBC	265	0.05 ± 0.02	0.36 ± 0.02
LBA	285	0.02 ± 0.02	0.39 ± 0.02
EBA	127	0.35 ± 0.05	0.53 ± 0.03

BC cells				D cells			
Partition	#Cells	$< t_{net} >$ (ns)	Std.Dev. (ns)	Partition	#Cells	$< t_{net} >$ (ns)	Std.Dev. (ns)
EBC	193	0.05 ± 0.00	0.05 ± 0.00	EBC	123	0.05 ± 0.01	0.07 ± 0.00
LBC	496	0.04 ± 0.00	0.06 ± 0.00	LBC	175	0.01 ± 0.00	0.06 ± 0.00
LBA	532	0.05 ± 0.00	0.11 ± 0.00	LBA	249	0.00 ± 0.01	0.09 ± 0.00
EBA	229	0.04 ± 0.00	0.04 ± 0.00	EBA	142	0.06 ± 0.01	0.14 ± 0.01

Table 6.22: Accuracy and precision of the $t^{cell}_{cosmics}$ measurement detailed per Tile Calorimeter radial layer and partition.

Partition	#Cells	Eff. (%)	$< t_{net} >$ (ns)	Std.Dev. (ns)
EBC	367	89	0.01 ± 0.01	0.13 ± 0.00
LBC	908	97	0.03 ± 0.00	0.12 ± 0.00
LBA	1044	97	0.02 ± 0.00	0.13 ± 0.00
EBA	450	90	0.04 ± 0.01	0.13 ± 0.00
ALL	2769	95	0.03 ± 0.00	0.13 ± 0.00

Table 6.23: Population and precision per partition for an accuracy between [-0.5,0.5] ns.

accuracy, given by the average of the distributions, is better than 0.2 ns. However these results are contaminated due to the existence of cells which are out of average. From the results evaluated per layer it is seen that the first radial layer shows the worst results although always below 1 ns both for the accuracy and the precision.

In Tables 6.23 the results of this study are presented for $t_{net} \in [-0.5, 0.5]$ ns. It is seen that more than 89% of the cells per partition have $t_{net} \in [-0.5, 0.5]$ ns with a precision better that 0.2 ns and an accuracy better than 0.04 ns. From Table 6.24 an interesting feature is observed in what refers to population. When choosing the mentioned window of accuracy the loss in population comes almost exclusively from the first radial layer. This was also the radial layer for which a larger standard deviation was seen for the measured $t^{cell}_{cosmics}$. The most important message to keep from this section is that the accuracy and precision of the method are better than 1 ns. A full account on the method precision would require an independent approach. This could be done by choosing any other run, using a different trigger and possibly away in time from the one used, and then comparing the time offsets from the two measurements.

6.5 Comparison with beam results

The time offsets were also calculated using the single beam data (SBD) [30] and are now compared with the numbers obtained from cosmic ray muons data (CMD). To produce this comparison a time correction and one additional quality cut are implemented. Since the SBD time offsets are obtained with reference to a specific cell, to produce a direct comparison

A cells				
Partition	#Cells	Eff. (%)	$< t_{net} >$ (ns)	Std.Dev. (ns)
EBC	51	53	-0.23 ± 0.03	0.19 ± 0.02
LBC	237	89	0.06 ± 0.01	0.22 ± 0.01
LBA	266	93	0.02 ± 0.01	0.24 ± 0.01
EBA	80	62	0.02 ± 0.03	0.29 ± 0.02
BC cells				
Partition	#Cells	Eff. (%)	$< t_{net} >$ (ns)	Std.Dev. (ns)
EBC	193	100	0.05 ± 0.00	0.05 ± 0.00
LBC	496	100	0.03 ± 0.00	0.06 ± 0.00
LBA	530	99	0.03 ± 0.00	0.05 ± 0.00
EBA	229	100	0.04 ± 0.00	0.05 ± 0.00
D cells				
Partition	#Cells	Eff. (%)	$< t_{net} >$ (ns)	Std.Dev. (ns)
EBC	123	100	0.06 ± 0.01	0.07 ± 0.00
LBC	175	100	0.01 ± 0.00	0.06 ± 0.00
LBA	248	99	0.01 ± 0.00	0.07 ± 0.00
EBA	141	99	0.05 ± 0.01	0.07 ± 0.00

Table 6.24: Population and precision per partition and radial layer for an accuracy between [-0.5,0.5] ns.

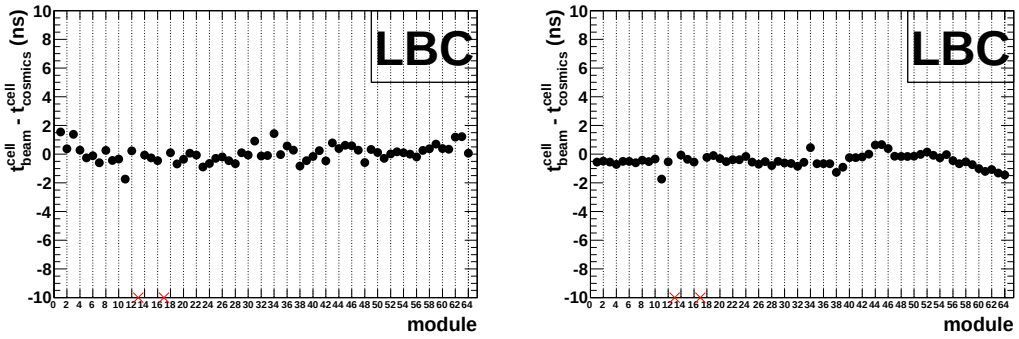

(a) Average offset over: all cells (LEFT) and all cells but cells from first radial layer (RIGHT).

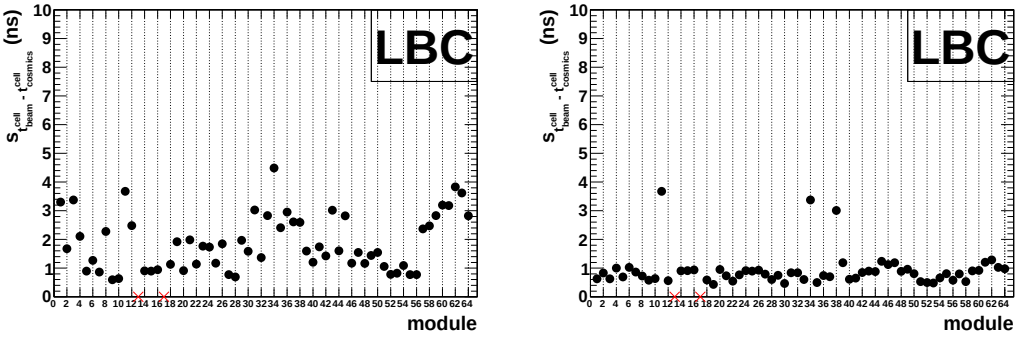

(b) Std. Dev. of offsets over: all cells (LEFT) and all cells but cells from first radial layer (RIGHT).

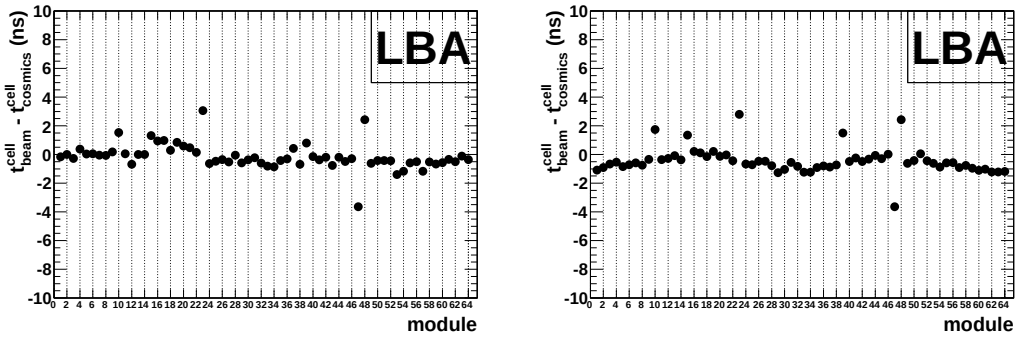

(c) Average offset over: all cells (LEFT) and all cells but cells from first radial layer (RIGHT).

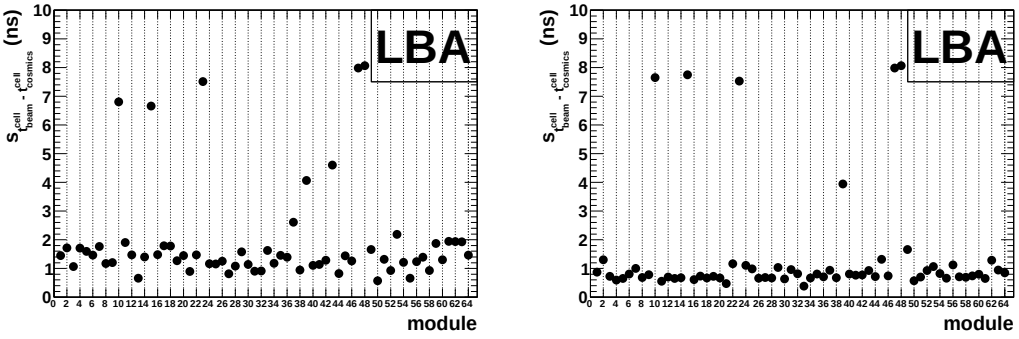

(d) Std. Dev. of offsets over: all cells (LEFT) and all cells but cells from first radial layer (RIGHT).

Figure 6.17: Long Barrel – Relative accuracy of cosmic ray muons and single beam: module average and standard deviation.

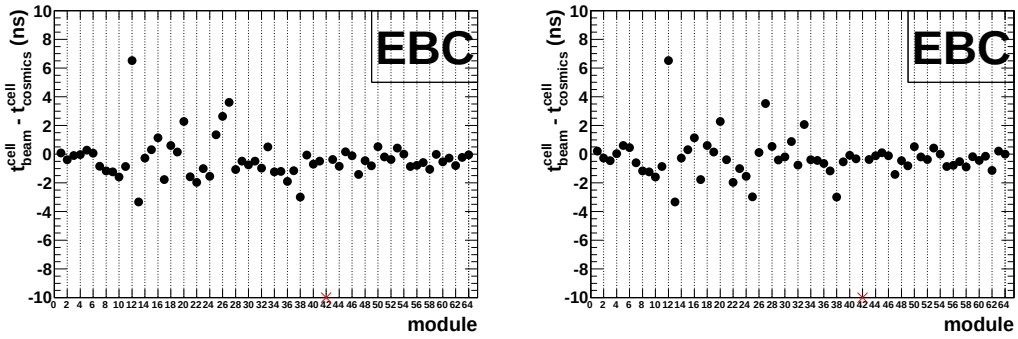

(a) Average offset over: all cells (LEFT) and all cells but cells from first radial layer (RIGHT).

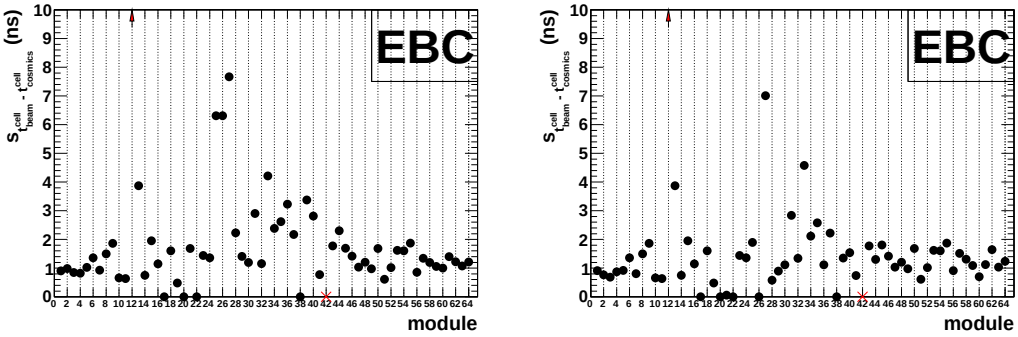

(b) Std. Dev. of offsets over: all cells (LEFT) and all cells but cells from first radial layer (RIGHT).

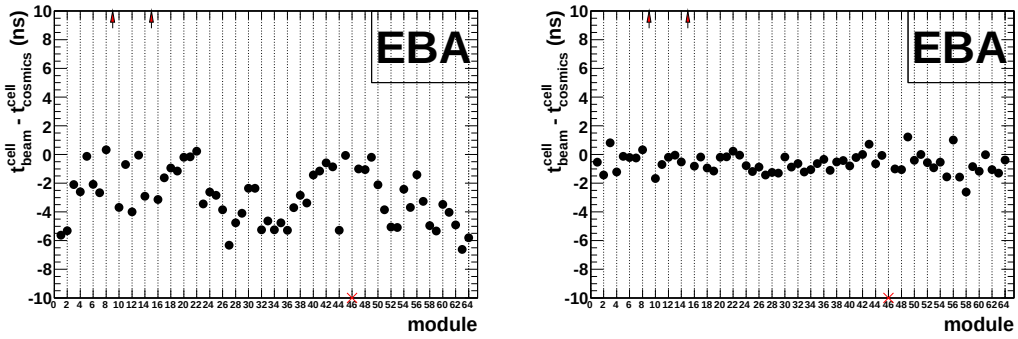

(c) Average offset over: all cells (LEFT) and all cells but cells from first radial layer (RIGHT).

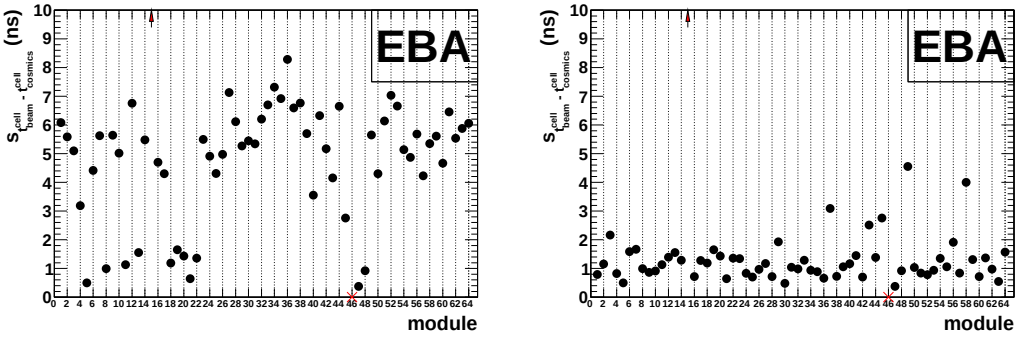

(d) Std. Dev. of offsets over: all cells (LEFT) and all cells but cells from first radial layer (RIGHT).

Figure 6.18: Extended Barrel – Relative accuracy of cosmic ray muons and single beam: module average and standard deviation.

Tile Calorimeter Layer	Total	CMD$^{(1)}$	CMD$^{(2)}$	SBD
A	1920	772 (40%)	453 (24%)	1547 (80%)
BC	1920	1450 (75%)	1268 (66%)	1724 (89%)
D	832	689 (82%)	610 (73%)	568 (68%)

Table 6.25: Number of cells per layer with a time calibration offset measurement. The CMD data are given for two sets of cuts (1) Number of measurements of $\Delta T_{\alpha}^{\beta} \geq 5$ and (2) Number of measurements of $\Delta T_{\alpha}^{\beta} \geq 7$. For both the standard deviation was required to be below 5 ns. The SBD was filtered using a $3 \times \sigma$ cut.

between the two measurements, this correction must also be implemented in CMD $t_{cosmics}^{cell}$. In order to remove residual outliers observed in the SBD a 3σ cut is implemented.

The comparison of these two quantities results in the measurement of relative accuracies and precisions, since a comparison between two indirect measurements is made. The absolute accuracies and precisions would result from the comparison with the laser/LED measurements made after these runs.

The number of cells per layer are summarized in Table 6.25 where for the SBD it is already taken in account the σ cut mentioned above. The table shows that for CMD the efficiency is small for A cells. For the other layers the results from CMD shows a much better efficiency reaching 75% but still below the 89% for CBD and for layer D reaches 82% which is 14% higher for SBD. In Table 6.26 the results from the difference of the two quantities:

$$\Delta_{beam}^{cosmics} = t_{beam}^{cell} - t_{cosmics}^{cell}$$

are summarized per partition. These results come from histograms in Figure 6.19. The same quantity is detailed per radial layers in Table 6.27.

In Table 6.26 it is shown that combining the results of cells from all partitions a $\Delta_{beam}^{cosmics}$ of -0.61 ns with a standard deviation of 3.71 ns is obtained. This is considered as a relative accuracy better than 1 ns and a precision better than 4 ns. Separating the results per partition it is seen that all agree with this statement, exception made for the EBA partition for which an accuracy of 3.1 ns and a precision of 6.5 ns are obtained.

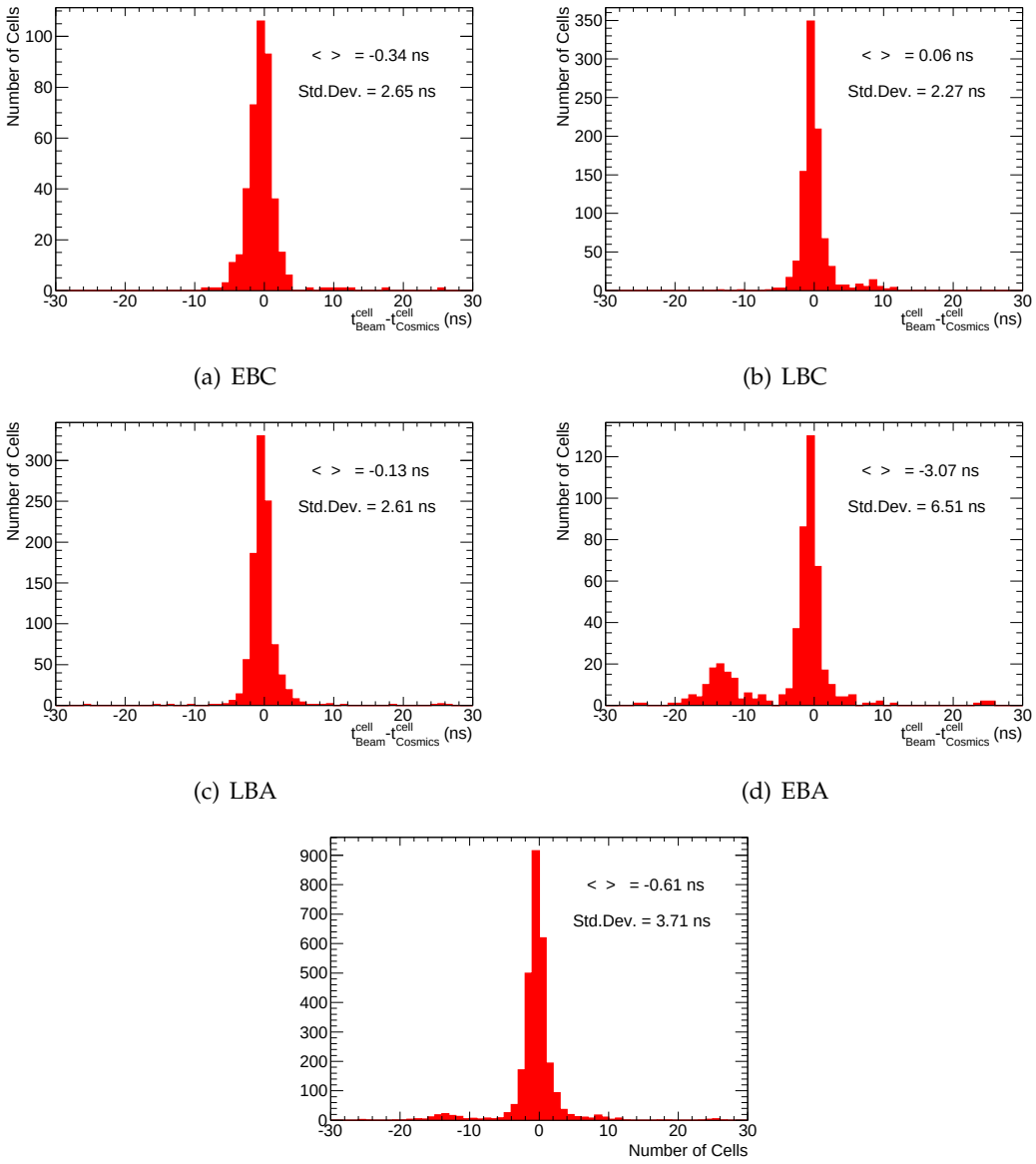

(a) EBC

(b) LBC

(c) LBA

(d) EBA

(e) All partitions combined

Figure 6.19: Difference of time offsets seen in the single beam and cosmic ray muons data for the Tile second and third radial layers for the four Tile Calorimeter partitions.

Partition	Cells	Average (ns)	Std.Dev. (ns)
EBC	408	-0.34±0.13	2.65±0.09
LBC	929	0.06 ±0.07	2.27±0.05
LBA	1003	-0.13±0.08	2.61±0.06
EBA	495	-3.07±0.29	6.51±0.21
ALL	2835	-0.61±0.07	3.71±0.05

Table 6.26: Relative accuracy of cosmic ray muons and single beam time offsets measurements.

6.5.1 Cosmics vs Beam results detailed per radial layers

If the results are detailed per radial layer as in Table 6.27 it is seen that the first radial layer of EBA cells has a relative accuracy of -10.8 ns and a precision of 6.6 ns which is not satisfactory. The remaining two radial layers show relative accuracies comparable with what is obtained for the radial layers of the other three partitions, all set within an interval of ± 2 ns. The relative precision of $\Delta_{beam}^{cosmics}$ has larger differences although still below 4 ns; in this comparison the first radial layer from EBA is not considered. For LBA the three layers show precisions around 2.5-2.7 ns. For LBC a precision of 3.4 ns is measured for the first radial layer but for the econd and third radial layers the precision is much better and around 1.0-1.2 ns. Finally for the EBC the worse precision is also for the first radial layer with a value of 3.2 ns, but the third radial with a value of 2.9 ns is not that good; the second radial layer shows a better precision with a value of 1.94 ns. All these differences are rather small and can be summarized in a statement: if the first radial layer of the EBA partition is excluded all other have accuracies better than 2 ns and precisions better than 4 ns.

In Figure 6.20 the $t_{cosmics}^{cell}$ is plotted against the t_{beam}^{cell} including and excluding the first radial layer for all partitions. It is seen that after excluding the first radial layer from all partitions the diagonal that establishes the correlation between the two quantities is enhanced although a few outliers are still visible.

The source of these outliers can be deduced looking at Figures 6.17 and 6.18 where the $\Delta_{beam}^{cosmics}$ is detailed per module and partition. For each partition are presented the average

A cells			
Partition	#Cells	Average (ns)	Std.Dev. (ns)
EBC	95	-0.80 ± 0.33	3.20 ± 0.23
LBC	261	1.57 ± 0.21	3.40 ± 0.15
LBA	283	0.66 ± 0.16	2.63 ± 0.11
EBA	127	-10.79 ± 0.58	6.57 ± 0.41
BC cells			
Partition	#Cells	Average (ns)	Std.Dev. (ns)
EBC	191	0.24 ± 0.14	1.94 ± 0.10
LBC	495	-0.24 ± 0.05	1.03 ± 0.03
LBA	525	-0.13 ± 0.12	2.71 ± 0.08
EBA	226	0.12 ± 0.24	3.66 ± 0.17
D cells			
Partition	#Cells	Average (ns)	Std.Dev. (ns)
EBC	122	-0.88 ± 0.27	2.94 ± 0.19
LBC	173	-1.35 ± 0.09	1.18 ± 0.06
LBA	195	-1.30 ± 0.12	1.73 ± 0.09
EBA	173	-1.35 ± 0.09	1.18 ± 0.06

Table 6.27: Relative accuracy and precision of cosmic ray muons and single beam time offsets measurements detailed per radial layer.

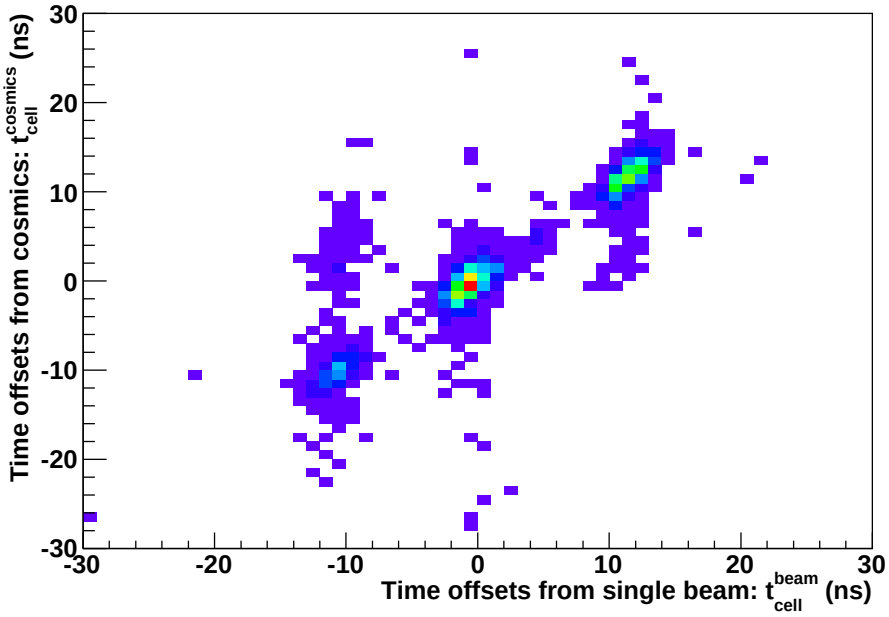

(a) BEFORE removing layer A cells

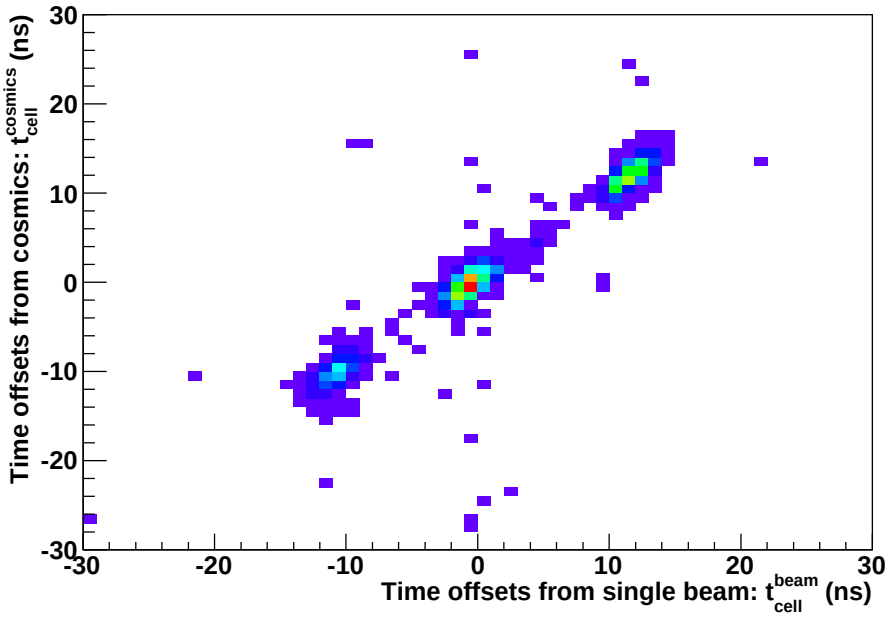

(b) AFTER removing layer A cells

Figure 6.20: Correlation between the time offsets measured with the 2008 single beam data and cosmic ray muons data from the same period.

Partition	Cells	Average (ns)	Std.Dev. (ns)
EBC	313	-0.20 ± 0.14	2.44 ± 0.10
LBC	668	-0.53 ± 0.05	1.18 ± 0.03
LBA	720	-0.44 ± 0.09	2.53 ± 0.07
EBA	368	-0.41 ± 0.20	3.80 ± 0.14
ALL	2069	-0.43 ± 0.05	2.48 ± 0.04

Table 6.28: Relative accuracy of cosmic ray muons and single beam time offsets measurements. Excluding the first radial layer – A cells – of each Tile Calorimeter partition.

and standard deviation including the first radial layer (LEFT) and not including the first radial layer (RIGHT). The first comment is that the benefit of removing the first radial layer is very large for the EBA partition. For the other LB partitions both accuracy and precision, improvements are seen. For the EBC partition the differences are residual and nothing can be advanced on any visible improvement in the relative accuracy and precision. The modules appearing out of average are the origin for the outliers still present in Figure 6.20 (b). In what follows the first radial layer – A cells – will be excluded and the above quantities recalculated. Is there a visible explanation on all the presented numbers that could give a stronger argument to this rejection is the question that may occur to the reader. The answer is that there are some hints that can partially do it:

- It was observed that the cells in this layer were the ones with less measurements (Cf. Figure 6.6).

- The A layer cells showed for all partitions also worse precision (Cf. Table 6.22).

- The signal to noise difference, that is small for the cells in the first radial layer.

But this are general comments over the data and do not justify the particular behaviour of the cells in the EBC partition. For now no final understanding was found for this misbehaving.

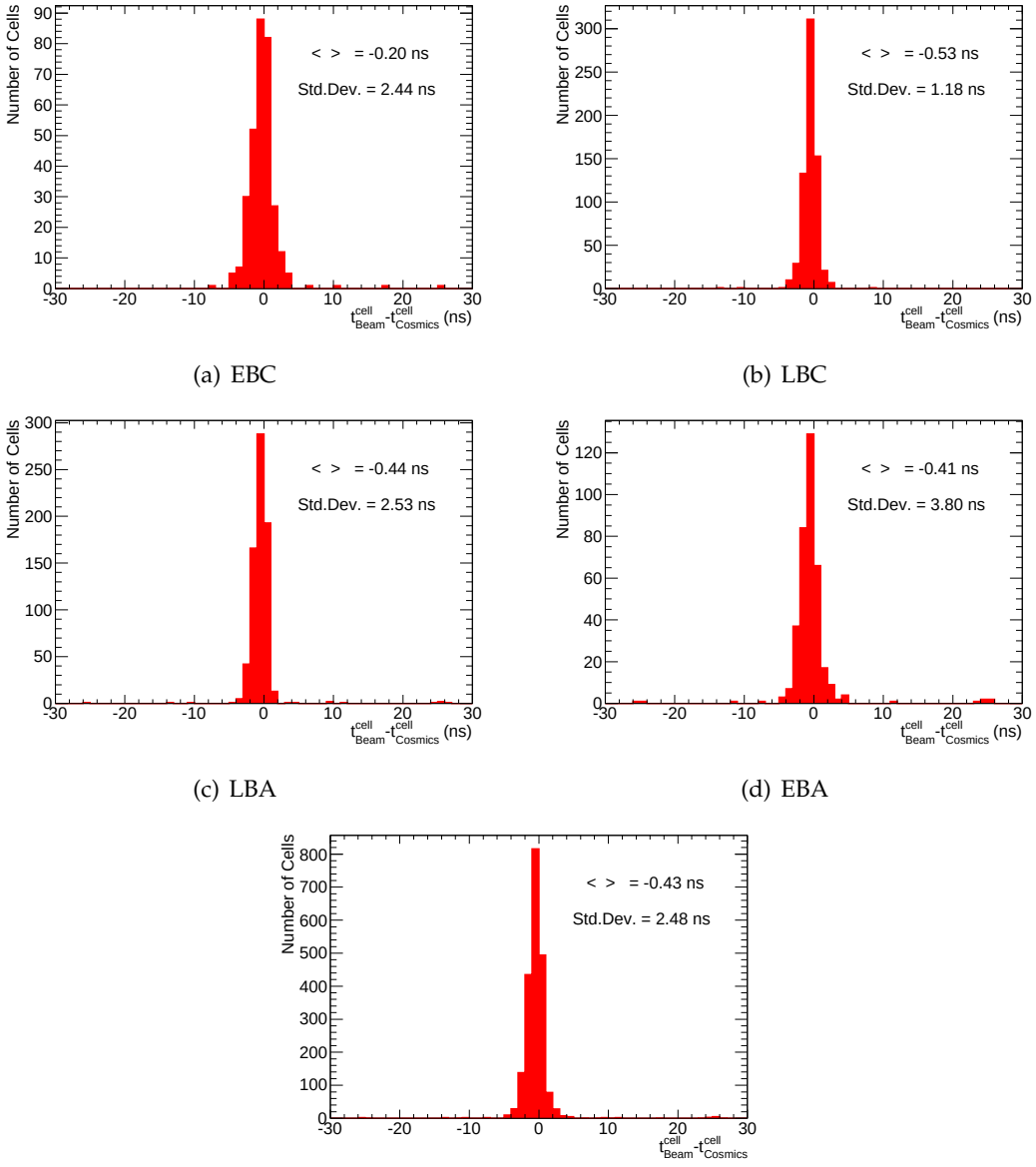

(a) EBC (b) LBC

(c) LBA (d) EBA

(e) All partitions combined

Figure 6.21: Relative accuracy of cosmic ray muons and single beam time offsets measurements. Excluding the first radial layer – A cells – of each Tile Calorimeter partition.

Partition	Eff.	Mean (ns)	σ (ns)	χ^2	NDF
EBC	308 (98%)	-0.37 ± 0.08	1.43 ± 0.08	11.16	6
LBC	665 (99%)	-0.49 ± 0.04	0.88 ± 0.03	20.30	5
LBA	710 (98%)	-0.57 ± 0.04	0.91 ± 0.03	25.39	6
EBA	358 (97%)	-0.69 ± 0.06	1.18 ± 0.06	14.81	7
ALL	2041 (98%)	-0.54 ± 0.02	1.02 ± 0.02	69.21	7

Table 6.29: Results from a gaussian fit between [-5,5] ns for the relative accuracy of cosmic ray muons and single beam time offsets measurements. Excluding the first radial layer – A cells – of each Tile Calorimeter partition.

6.5.2 Single beam vs Cosmics: Excluding the first radial layer

In Figure 6.21 and Table 6.28 are presented the results after excluding the first radial layer. It is seen now that all partitions have relative accuracies below 0.6 ns and precision better that 4 ns. Making use of Table 6.25 it can be accounted that these cells correspond to 78% of the BC and D cells, and 46% of the total number of cells. The expected distribution for this measurement must be gaussian for the correlated events and for this reason a gaussian fit using as fitting interval $[-5,5]$ ns is applied. The corresponding results are summarized in Table 6.29. From the fit and for the combination of cells from the four partitions a mean of (0.54±0.02) ns and σ of (1.02±0.02) ns are obtained. The two measurements agree within 2 ns on per cell level and refer to 98% of the measured time offsets for the second and third radial layers.

6.6 Re-evaluation of the Time Offsets

In the previous section it was shown that the time offsets measurements using cosmic ray muons and single have a strong disagreement that amount to about 10 ns for the first radial layer of the EBA partition. For the other partitions it is also for the first radial layer that large spreads are observed when comparing the two measurements. It can be concluded that the first radial layer should be looked in separate. However the other two layers show a very good agreement and for reasons of completeness this forces us to revisit the partition averages without the contribution of these cells. The re-calculated results are in Table 6.30. The removal

Partition	Average (ns)	Std.Dev. (ns)
EBC	-2.3 ± 0.2	3.1 ± 0.1
LBC	9.6 ± 0.1	1.6 ± 0.0
LBA	-3.0 ± 0.2	4.5 ± 0.1
EBA	-12.7 ± 0.2	4.4 ± 0.2

Table 6.30: time offsets measured using cosmic ray muons data for each Tile Calorimeter partition from cells of the second (BC cells) and third (D cells) radial layers.

of the first radial layer has an important effect on the precision, larger than or of the order of 1 ns, for the LBC and EBA partitions. The agreement with beam data in these conditions is now better than 0.5 ns for all partition.

6.7 Summary

A measurement of the time offsets of Tile Calorimeter was carried out with 0.5 M cosmic ray muon events, acquired in the 2008 ATLAS commissioning phase using the Muon Spectrometer RPC trigger. The measurements could be performed for 62% of all Tile Calorimeter cells, broken down into 40% of the A cells, 75% of the BC cells and 82% of the D-cells.

It was shown that the sensitivity of the measurement is adequate since even for a small offset of 0.5 ns an accuracy of 2%, obtained for a BC cell of the LB. A more general test was done by applying a [-5.,5.] ns random fake offsets to the current measurement. The global result was extremely good showing that the method's precision and accuracy are both better than 1 ns. A further validation was carried out with a detailed comparison with the single beam timing results.

The main results of this analysis can be summarized according to the component of the time calibration that they probe - inter-partition, inter-module and intra-module (as outlined in section 3):

Inter-partition The average offsets per partition were not expected to be the same since the laser system had not carried out this correction. The measured averages show significant

Partition	2008 Single Beam (ns)	Cosmic ray muons (ALL layers) (ns)	Cosmic ray muons (NO layer A cells) (ns)
EBC	-12.3	-12.0	-11.9
LBC	0	0	0
LBA	-12.0	-12.2	-12.6
EBA	-22.2	-18.9	-22.4

Table 6.31: Summary of time offsets measurements from single beam [30] and cosmic ray muons. For cosmics the time offsets are given for ALL radial layers and excluding the first radial layer (A cells).

discrepancies between the four partitions of Tile Calorimeter, of the order of 10 ns. Considering only the second and third layers, the results are in agreement within 0.5 ns with the measurements performed with single beam data.

In Table 6.31 the final results obtained for 2008 single beam data and cosmic ray muons data are presented. Only the partitions averages are presented and these are recalculated relatively to the LBC partition. This table shows that the inter-calibration offsets derived from cosmic ray muons are in full agreement with 2008 single beam data. When including all radial layers the mis-match is only important for EBA partition as could be expected from the results presented along this chapter.

Inter-module Within each partition, the spread of the module averages allow us to verify the inter-module calibration, that had been carried out with the laser system. For the Long Barrel partitions, the agreement is quite good, within $\pm 2ns$. It is slightly worse for the EBA partition, and shows a systematic offset of about 5 ns for the first eight modules of the EBC partition. This result is consistent whit what had been found for an equivalent measurement carried out with the single beam data [30]. Resulting this offset from a poor account for those modules of the length of the clear fibers.

Intra-module The quality of the intra-module calibration can be evaluated by the standard deviation of the measurements within each module, and of the differences of these measurements with respect to the single beam. The results show differences between the

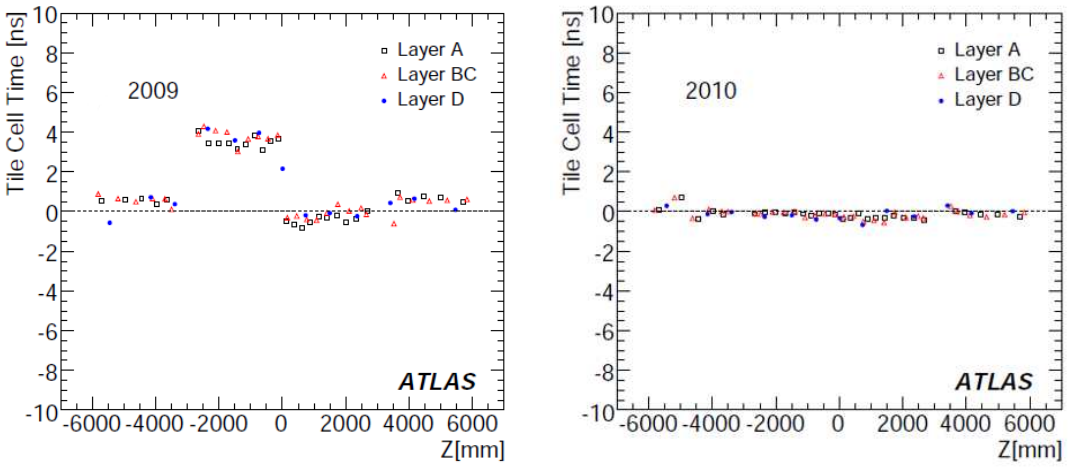

(a) 2009 (b) 2010

Figure 6.22: Tile Calorimeter cells time measurements from single beam data vs z : (a) single beam 2009 data (b) single beam 2010 data after using single beam 2009 for cells synchronization.

radial layers - apart from a few outliers, for the BC and D cells the intra-module calibration is established to about 1 ns for the Long Barrel and 2 ns for the Extended Barrel. The results are worse for the first layer, showing spreads of about 6 ns.

6.8 Present status of Tile Calorimeter synchronization

In the fall of 2009 with the start-up of the LHC new single beam runs were taken. The Tile Calorimeter took advantage of this by producing an update on the synchronization of cells. The procedure was the same as described in Section 6.2.1. The results of the time measurements with single beam data in 2009 are in Figure 6.22a. As before it is shown the distribution of the cell time for the three radial layers against the z_{cell} coordinate. Although with smaller offsets than the ones observed in 2008 the Tile Calorimeter cells still show an offset of 4 ns for the LBC partition and quite small but visible offsets in the other 3 partitions but not surpassing 1 ns. In order to synchronize all the calorimeter cells the 2009 measured offsets were used to correct the database time constants. In 2010 there was again the opportunity to collect data in single beam running mode. The cell time results are shown in Figure 6.22b. It

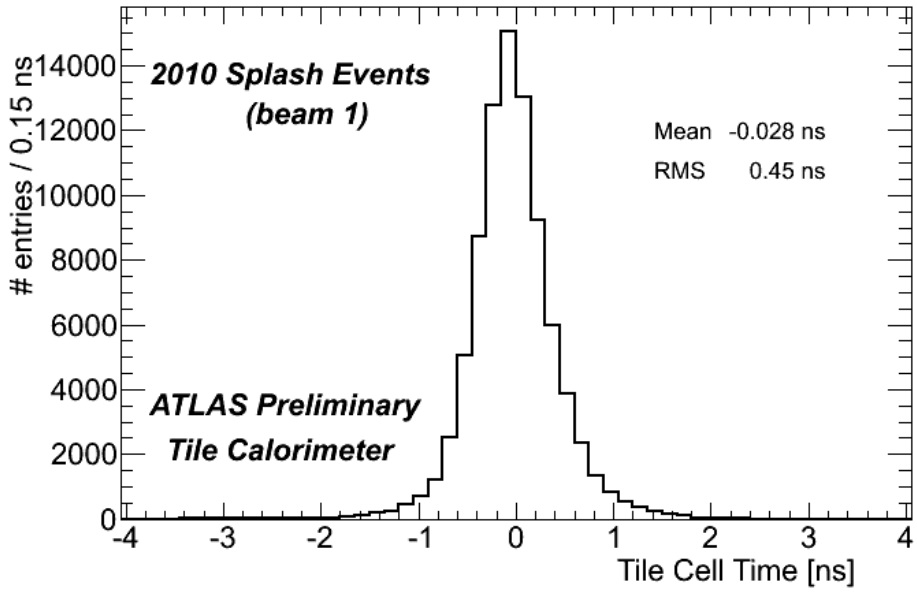

Figure 6.23: Tile Calorimeter cells time in 2010 after synchronization using single beam data from 2009. In this histogram 97% of the Tile Calorimeter cells are used.

is seen that the synchronization was successfully achieved using single beam 2009 data. All the Tile Calorimeter partitions have all cells within a window of ±1 *ns*. The distribution of the time measurements for all cells is draw. This is what can be seen in Figure 6.23. The measured accuracy of the cell synchronization is of 0.02 ns with a precision of 0.45 ns. This is better than what was achieved with 2008 data when 1 ns [30] was obtained for this quantity. Recently other methods for the synchronization are under study using particles from collision data, but when no beam is available the results with cosmic ray muons discussed in this chapter have shown to have a good precison for the measurements of the time offsets and synchornization of the Tile Calorimeter.

7 Conclusions

A new era in particle physics started this year, 2010, with the first 7 TeV p-p collisions at the Large Hadron Collider. The high quality of the first results, with a good match between data and Monte-Carlo predictions, would not have been possible without the intensive effort of the whole ATLAS collaboration during the commissioning of the detector between 2005 and 2009. The work of this thesis was a contribution to this phase of the ATLAS experiment, using data from cosmic ray muons and from the 2008 single beam.

In the initial commissioning period of the Tile Calorimeter, cosmic ray muons were used to monitor the operation of the detector, detect dead or noisy channels, evaluate the coarse trigger timing setup, test the reconstruction software, etc. For a considerable period, these data provided a contribution to the evaluation of the status of the calorimeter, complementary to the calibration systems. The main topic of this thesis is the certification of the Tile Calorimeter calibration, in terms of energy scale and synchronization.

The timing and energy response of TileCal will play an important role in the physics discoveries that are just around the corner. These are fundamental quantities in the jets and missing transverse energy reconstruction, to clean up the data from non-collisions events, for tests and searches in the standard model and to probe for new physics.

A preliminary result using cosmic ray muons to validate the energy scale was done in 2006 using 16 Tile Calorimeter modules. This was based on the energy response balance of the two channels the in read-out of each cell. The results showed a good response uniformity of $< 5\%$ for all investigated modules, and $< 1\ \%$ for those calibrated at testbeam. This was one of the earliest results of the Tile Calorimeter electromagnetic energy scale in the cavern.

After using the cesium system to calibrate the Tile Calorimeter energy response, it was

necessary to measure the electromagnetic energy scale using an independent method with high energy particles. Cosmic ray muons were the only available option for a source of such particles. The analysis described in this thesis uses the ratio of the energy deposited per crossed path length (for simplicity, referred to as energy loss, or dE/dx) in order to probe the energy scale settings and uniformity. In this analysis the track reconstruction is done with the TileMuonFitter (TMF) algorithm that only uses the information from the Tile Calorimeter. In previous analyses an inner detector track was required for the selection of a cosmic ray muon (IDtrack method). A comparison between the two analyses is made.

The energy loss results have shown an agreement between data and Monte-Carlo simulations within 5%. The systematic contributions to this measurement were investigated and their contribution was measured to be 7% for data and 5% for data/MC ratio. It should be noted that all contributions were assumed to be independent which overestimates the global systematic error. The TMF results showed that there is a discrepancy between the radial layer A and radial layer D. The results of TMF with a difference of the order of 3%, are consistent within the systematic errors with the 5% measured with the IDtrack method. Overall the global energy scale was validated with an independent technique.

The analysis is also focused on the uniformity in ϕ of the energy response of Tile Calorimeter. The energy loss uniformity was measured with the TMF method using two different data streams both triggered by the RPCs of the muon spectrometer: one selecting muons crossing the inner detector volume and the other accepting all triggered muons. Although statistics was limited, due to the separation of the data by modules, the usage of the large acceptance data stream allowed to increase the coverage for the A and BC cells. The response was consistent for both data streams and the uniformity was measured to be better than 5% for all three radial layers.

Cosmic ray muons were also used in the synchronization of the Tile Calorimeter. The first data analyzed was with the 2006 setup with only 16 Tile Calorimeter modules being used in the measurements. The first laser results had been applied to synchronize these 16 modules. Measurements from cosmic ray muons allowed to obtain a first inter-module synchronization within $\pm$ 1 *ns* using the time of a tower as the input to the analysis. With the progressing of the

installation of the detector in the ATLAS cavern, the previous method had to be re-designed to be able to measure the time offsets of all the calorimeter modules and calculate the time offsets per cell. The results showed that after the removal of the less accurate first radial layer measurements, this precision was of about 2 ns for the Long Barrel inter-module offsets, and for all intra-module offsets. The inter-partition average results agree with the single-beam measurements within 0.5 ns.

The results showed that, as a complement or alternative to the laser system, it is possible to measure the TileCal time offsets between beam runs using cosmic ray muons. The results have shown that, as a complement an alternative to the laser system, the Tile Calorimeter synchronization with cosmic muons is robust and accurate to be used during the LHC shutdowns or using data accumulated between beam runs.

So now it can be concluded that the main goals of this thesis, the energy scale and synchronization Tile Calorimeter, were achieved.

Bibliography

[1] The ATLAS Collaboration, G. Aad et al., **The ATLAS Experiment at the CERN Large Hadron Collider**, JINST 3 (2008) S08003

[2] L. Evans, P. Bryant, **LHC Machine**, Journal of Instrumentation, JINST 3 S08001 , 2008.

[3] K. Nakamura et al. **Particle Data Group** J. Phys. G 37, 075021 (2010)

[4] The ALEPH, DELPHI, L3, OPAL, SLD Collaborations, the LEP Electroweak Working Group, the SLD Electroweak and Heavy Flavour Groups, **Precision Electroweak Measurements on the Z Resonance**, Phys. Rept., vol. 427 2006 pg. 257 (hep-ex/0509008)

[5] `http://lepewwg.web.cern.ch/LEPEWWG/`

[6] The Tevatron Electroweak Working Group for the CDF and D^0 Collaborations, **Combination of CDF and D^0 results on the mass of the top quark using up to 5:6 fb^{-1} of data**, arXiv:1007.3178v1 [hep-ex], 19 Jul 2010

[7] CDF and DØ Collaborations, **Combined CDF and D0 Upper Limits on Standard Model Higgs-Boson Production with up to 6.7 fb-1 of Data** (hep-ex/1007.4587v1)

[8] T. Aaltonen et al., (CDF and DØ Collaborations), Phys. Rev. Lett. 104, 061802 (2010).

[9] ALEPH Collaboration, DELPHI Collaboration, L3 Collaboration, OPAL Collaboration and The LEP Working Group for Higgs Boson Searches **Search for the Standard Model Higgs boson at LEP** Physics Letters B Volume 565, 17 July 2003, Pages 61-75 (hep-ex/0306033)

[10] ATLAS Collaboration **Expected performance of the ATLAS experiment : detector, trigger and physics** (hep-ex/0901.0512) ; CERN-OPEN-2008-020

[11] A Gomes; A Maio; J Santos; M J Varanda **Cell geometry and fiber lengths of Barrel and Extended Barrel modules** ATL-TILECAL-2002-011.- Geneva : CERN, 2002

[12] David, M ; Gomes, A ; Maio, A ; Pina, J ; Tomé, B **15 years of experience with quality control of WLS fibres for the ATLAS Tile Calorimeter** ATL-TILECAL-PUB-2008-003

[13] Saraiva, J G ; Wemans, A ; Maneira, M J P ; Maio, A ; Patriarca, J **The aluminization of 600 k WLS fibers for the TileCal/ATLAS/LHC** 2004 - Published in : IEEE Trans. Nucl. Sci. 51 (2004) 1235-1241

[14] Cardeira, C ; Sá da Costa, J ; Gomes, A ; Gouveia, J ; Maio, A ; Pinhão, J **A Robot for Fiber Insertion in a Profile** ATL-TILECAL-PUB-2005-007 - 2005. - 9 p.

[15] ATLAS/Tile Calorimeter Collaboration **Technical Design Report** CERN/LHCC 96-42

[16] J Christiansen, A. Marchioro and P. Moreira **TTCrx Reference Manual: A Timing, Trigger and Control Distribution Receiver ASIC for LHC Detectors** CERN - ECP/MIC, Geneva Switzerland, March 1996, Version 1.2

[17] E Fullana, J Castello, V Castillo, C Cuenca, A Ferrer, E Higon, C Iglesias, A Munar, J Poveda, A Ruiz-Martinez, B Salvachua, C Solans, R Teuscher, J Valls, **Optimal Filtering in the ATLAS Hadronic Tile Calorimeter**, ATL-TILECAL-2005-001, CERN, Geneva; J Poveda et al, **Offline Validation and Performance of the TileCal Optimal Filtering Reconstruction Algorithm** ATL-TILECAL-INT-2009-001, CERN, Geneva.

[18] ATLAS Collaboration, **Readiness of the ATLAS Tile Calorimeter for LHC collisions**, ATLAS Publication Draft (submitted to EPJC 30.7.2010 `http://arxiv.org/abs/1007.5423`)

[19] H. Okawa `https://twiki.cern.ch/twiki/bin/view/Atlas/ApprovedPlotsTile` CERN, 2008

[20] João Pina, **The Atlas Detector Control System of the Tile Calorimeter**, Faculty of Sciences of the University of Lisbon, PhD Thesis, 2010

[21] R Alves, D Calvet, J Carvalho, R Chadelas, M Crouau, C Crozatier, R Febbraro, D Lambert, R Marchionini, R Oliveira, A Pereira, C Santoni, L P Says, F Vazeille and S Viret, **'ATLAS tile calorimeter laser calibration system'**, ATL-COM-TILECAL-2009-012 CERN, Geneva.

[22] J G Saraiva, **Studies on the Performance of the ATLAS tile calorimeter**, Master Thesis, Faculty of Sciences of University of Lisbon, 2005.

[23] Saraiva, J G ; Némécek, S ; Maio, A **Light yield Studies of the ATLAS Tile Calorimeter** ATL-TILECAL-PUB-2008-012 2005

[24] **A measurement of the energy loss spectrum of 150 GeV muons in iron** Z. Phys. C 73 (1997) 455-463

[25] E. Starchenko et al, **Cesium monitoring system for ATLAS Tile Hadron Calorimeter**, NIM A 494 (2002) 381-384

[26] TileCal Collaboration **Testbeam studies of production modules of the ATLAS Tile Calorimeter** Nucl. Inst. Meth. A 606 (2009) 362 - 394.

[27] T. Carli, M. Delmastro, T. Petersen, P. Speckmayer, K.J. Grahn, **Response and Shower Topology of 2 to 180 GeV Pions Measured with the ATLAS Barrel Calorimeter at the CERN Testbeam and Comparison to Monte Carlo Simulations**, ATLAS Internal Report, ATLAS-COM-CAL-2009-004 CERN, Geneva (Switzerland), 2009

[28] T. Barillari et al., Local Hadronic Calibration, ATLAS note, ATL-LARG-PUB-2009-001, CERN, Geneva (Switzerland), 2008

[29] C Clement, B Nordkvist, O Solovyanov and I Vivarelli, **Time Calibration of the ATLAS Hadronic Tile Calorimeter using the Laser System**, ATL-COM-TILECAL-2008-018 ATL-TILECAL-PUB-2009-003 CERN, Geneva.

[30] M Volpi, L Fiorini, I Korolkov, **Time inter-calibration of hadronic calorimeter of ATLAS with first beam data**, ATL-TILECAL-PUB-2009-008 CERN, Geneva 2009.

[31] B Meirose and R J Teuscher **'Time of Flight Analysis Using Cosmic Ray Muons in the ATLAS Tile Calorimeter'**, ATLAS-TILECAL-PUB-2008-004 CERN, Geneva.

[32] R Leitner, V. V. Shmakova, P. Tas **Time resolution of the ATLAS Tile calorimeter and its performance for a measurement of heavy stable particles** ATL-TILECAL-PUB-2007-002

[33] M. Fairbairn, A.C. Kraan, D.A. Milstead, T. Sjöstrand, P. Skands and T. Sloan **Stable massive particles at colliders** Physics Reports Volume 438, Issue 1, January 2007, Pages 1-63

[34] S. Tarem, S. Bressler, H. Nomoto, A. Di Mattia, **Trigger and reconstruction for heavy long-lived charged particles with the ATLAS detector** Eur. Phys. J. C (2009) 62:281-292

[35] S. Hellman, M. Johansen, R. Mackenorang, P. Mermod, D. Milstead, C. Ohm, A. Solodkov **Measuring the time-of-flight and identifying exotic stable massive particles with the ATLAS Tile Calorimeter** ATL-COM-TILECAL-2009-028

[36] R. Teuscher, **First ATLAS Events Recorded Underground**, Published in : ATLAS eNews, no. 200507 (200507), Issue No.30-31, 25 July 2005; Alison Wright, **First 'data' from LHC**, Nature, 14 July 2006.
http://www.nature.com/nphys/journal/vaop/nprelaunch/full/nphys005.html

[37] Status reports from LHC management team:
https://edms.cern.ch/nav/LHC-0000000861/LHC-0000000863
(public access)

[38] F. Tang et al **Stand-alone Cosmic Ray Trigger Electronics for the ATLAS Tile Calorimeter** 10th Workshop on Electronics for LHC and Future Experiments, Boston, MA, USA, 13 - 17 Sep 2004, pp.327-331

[39] J. Poveda et al (including J.G. Saraiva), **TileCal Barrel Read-Out and Trigger Optical Fiber Commissioning Tests and Validation**, ATL-TILECAL-INT-2007-001, 07 February 2007

[40] T. Davidek, R. Leitner **Parametrization of the Muon Response in the Tile Calorimeter** ATL-TILECAL-97-114 ; ATL-L-PN-114. - 1997.

[41] M. Sousa; J G Saraiva ; J Maneira ; A Maio et al **Energy scale and uniformity of the Tile Calorimeter using the TileMuonFitter** (note in preparation)

[42] J Maneira **TileMuonFitter : An algorithm for the reconstruction of cosmic muons with the ATLAS Tile calorimeter** ATL-TILECAL-INT-2007-003; ATL-COM-TILECAL-2007-007.- Geneva : CERN, 2007 - 8 p; L M A Filho **Detecção e Reconstrução de Raios Cósmicos Usando Calorímetria de Altas Energias** Março/2009 PhD Thesis (in Portuguese).

[43] P. Hough, C. Paul, **Method and mean for recognizing complex patterns**, United States Patent 3069654, 1962.; P. Hough, Proc. Conf. High Energy Acc. Instr., 1959.

[44] Richard 0. Duda, Peter E. Hart **Use of the Hough transformation to detect lines and curves in pictures** Comm. ACM. Vol 15 No. 1 pp. 11-15 (January 1972)

[45] M. Ohlsson, C. Peterson, **Track finding with deformable templates - the elastic arms approach**, Computer Physics Communications, pp. 77, 98, 1992.

[46] J. Illingworth, J. Kittler, **The Adaptative Hough Tranform**, IEEE Transactions, Patters Analysis and Machine Intelligence, v. 9, pp. 690 697, 1987

[47] J G Saraiva ; J Maneira ; A Maio ; M Aleksa ; M Stockner **Synchronization of the ATLAS Tile calorimeter with cosmic muon data** ATL-TILECAL-INT-2010-002

[48] T del Prete and I Vivarelli, **The timing of the Tile Calorimeter using laser events**, ATL-TILECAL-2003-009 CERN, Geneva.

[49] Private comunication from Martin Aleksa and Markus Stockner

[50] ROOT User's Guide

http://root.cern.ch/drupal/content/users-guide

[51] W H Press, S A Teukolsky, W T Vetterling, B P Flannery, **Numerical Recipes in C: The Art of Scientific Computing 2nd Edition**, Cabridge University Press 1997.